

**School of Civil & Mechanical Engineering
Faculty of Science & Engineering**

Modelling Human Upper-Airway Dynamics and Dysfunction

George A Tetlow

**This thesis is presented for the Degree of
Doctor of Philosophy
of
Curtin University**

August 2012

Declaration:

To the best of my knowledge and belief this thesis contains no material previously published by any other person except where due acknowledgment has been made.

This thesis contains no material which has been accepted for the award of any other degree or diploma in any university.

Signature:

Date:

Abstract

Repetitive closure of the upper-airway characterises obstructive sleep apnea. It disrupts sleep causing excessive daytime drowsiness, and is linked to hypertension and cardiovascular disease.

Previous studies simulating the underlying fluid mechanics of two-dimensional channel flow are based upon velocity-driven boundaries with symmetric positioning of the soft-palate. In the first part of the present work the two-dimensional work of Balint (2001) is extended to a pressure-driven model where the stability solutions space mapped for the soft-palate, symmetrically placed within viscous channel flow. As a result of this work the modelling of Obstructive Sleep Apnoea (OSA) it is proposed that modelling should focus on nasal breathing as the first indicator for the presence of OSA. Numerical simulations reveal the appearance of amplification of soft-palate displacement over several breathing cycles with asymmetric positioning of the soft-plate and for nasal breathing (single channel flow). Such events increase airway hydraulic resistance at the start of inhalation, a vulnerably period of the breathing cycle for collapse of the pharynx.

In the second part of the present work three-dimensional studies are conducted for duct flow and flow through an anatomically correct reconstructed geometry, supporting the findings of the two-dimensional work of the first part. Moreover, extending understanding of anatomical interactions, through development of a three-dimensional geometry reconstruction based on an airway at the end of inhalation. Here the geometry is reconstructed from quantitative data linked to the breathing cycle, captured via an *in vivo* method using an adapted endoscope technique. Simulations reveal flow mechanisms that produce low-pressure regions on the side walls of the pharynx and on the soft-palate within the pharyngeal section of minimum area. Soft-palate displacement and lateral pharynx-wall

deformations reduce further the pressures in these regions creating forces that would tend to narrow the airway owing to flow curvature. These phenomena suggest a mechanism for airway closure in the lateral direction as observed in an bronchoscope study conducted as part of this thesis.

Keywords: obstructive sleep apnoea, numerical modelling, pressure driven, 2-D soft-palate model, 3-D pharynx model, human upper-airway, biomechanical, stability solution space, viscous flow, turbulent model $k - \omega$ SST.

Nomenclature

A	stiffness matrix,
B	flexural rigidity (Nm),
C	convection term,
d	damping coefficient (N.s/m ³),
D	gradient matrix,
D_d	dimensional duct height (m),
D_h	hydraulic diameter (m),
E	elastic (Young's) modulus (N/m ²),
E_0	total energy at the beginning of the time series (Nm),
E_k	kinetic energy (Nm),
E_p	elastic (Young's) modulus (N/m ²) soft-palate,
E_s	strain energy (Nm),
E_t	total energy ($E_t = E_s + E_k$) (Nm),
E_w	elastic (Young's) modulus (N/m ²) side walls,
h	plate thickness (m),
$H1$	height of upper channel in the split segment (m),
$H2$	height of lower channel in the split segment (m),
$H3$	height of channel in the combined segment (m),
H_l	elemental height of the lower channel below the flexible plate (m),
H_u	elemental height of the upper channel above the flexible plate (m),
h'	element size (m),
L	plate length (m),
L_p	flexible plate length (m),
L_r	length of rigid segment (m),
M	mass matrix,
P_{D1}	driving pressure over the upper split channel segment (N/m ²),

P_{D2}	driving pressure over the lower split channel segment (N/m^2),
P_{D3}	driving pressure over the combined channel segment (N/m^2),
Q_1	flow rate upper split channel segment (m^3/s),
Q_2	flow rate lower split channel segment (m^3/s),
Q_3	flow rate combined channel segment (m^3/s),
Re	Reynolds number dimensionless,
T	shear-stress induced tension (N/m),
t	time (s),
t_ω	time for a single cycle oscillation (s),
U_1	x-velocity component (m/s),
U_{lid}	dimensional lid velocity (m/s),
U_{in}	the peak dimensional inlet velocity (m/s),
u'	element velocity (m^2/s),
W	work done on the plate (Nm),
w ,	plate displacement (m),
x	axial location (m),
x_a	x component of a node coordinate (m),
x_b	x component of b node coordinate (m),
y_a	y component of a node coordinate (m),
y_b	y component of b node coordinate (m),
\bar{E}_t	non-dimensional total energy,
\bar{F}_{plate}	non-dimensional plate restoring force,
\bar{t}	non-dimensional time,
\bar{U}_1	mean velocity upper split channel segment (m^2/s),
\bar{U}_2	mean velocity lower split channel segment (m^2/s),
\bar{U}_3	mean velocity combined channel segment (m^2/s),
$\bar{\delta p}$	non-dimensional pressure force,
\bar{H}	aspect ratio dimensionless,
\ddot{w}	plate acceleration (m/s^2),
δp_m	transmural surface pressure (N/m^2)($\delta p_m = p_{upper} - p_{lower}$),
Δt	time step (s),
\dot{V}	volumetric flow rate (m^3/s),
\dot{w}	plate velocity (m/s),
ℓ	half the dimensional lid extent (m),
Γ	stiffness ratio dimensionless,
$\hat{C}_{\alpha\delta}^k$	the element convection matrix,

§ Hilbert space,

List of Publications

The following outputs are based upon the research conducted within, or closely related to the work of this thesis.

0.1 Journal papers

Lucey, A., King, A., Tetlow, G., Wang, J., Armstrong, J., Leigh, M., Paduch, A., Walsh, J., Sampson, D., Eastwood, P. & Hillman, D. (2010). Measurement, reconstruction and flow-field computation of the human pharynx with application to sleep apnea, *Transactions on Biomedical Engineering*, 57, 2535-2548.

Tetlow, G. A. & Lucey, A. D. (2009). Motions of a cantilevered flexible plate in viscous channel flow driven by a constant pressure drop, *Communications in Numerical Methods in Engineering*, 25, 463-482.

0.2 Conference papers

Tetlow, G.A., & Lucey, A.D. (2006). Motions of an offset flexible plate in viscous channel flow: A model for flutter of the soft palate, *World Congress on Medical Physics & Biomedical Engineering*, Seoul, South Korea, 27 August–1 September, ISSN 1727-1983, ISBN 3-540-36839-6.

Wang, J., Tetlow, G.A., Lucey, A.D., Armstrong, J.J., Leigh, M.S., Paduch, A., Sampson, D.D., Walsh, J.H., Eastwood, P.R., Hillman, D.R. & Harrison S.

(2006). Motions of an offset flexible plate in viscous channel flow: A model for flutter of the soft palate, *World Congress on Medical Physics & Biomedical Engineering*, Seoul, South Korea, 27 August–1 September, ISSN 1727-1983, ISBN 3-540-36839-6.

Tetlow, G.A., Lucey A.D. & Balint, T.S. (2006). Instability of a cantilevered flexible plate in viscous channel flow driven by constant pressure drop, ASME Paper; PVP 2006 / ICPVT11-93943, *2006 Pressure vessels & piping conference & the eleventh international conference on pressure vessel technology*, Vancouver, British Columbia, Canada, 23–27 July.

Wang, J., Tetlow, G.A. and Lucey A.D. (2007). Flow-Structure Interaction in the Human Upper Airway: Motions of a cantilevered flexible plate in channel-flow with flexible side walls, *16th Australasian Fluid Mechanics Conference*, Gold Coast, Australia, 2–7 December.

Tetlow, G., Lucey, A. & Wang, J. (2008). Zolotarev & Horacek (ed.), Analogue computational modelling of upper airway dynamics, *Proc. of 9th International Conference on Flow Induced Vibrations - FIV*, Institute of Thermomechanics ASCR, Prague, 30 June – 3 July.

0.3 Presentations

Tetlow, G.A. (2006). A numerical model for further understanding of obstructive sleep apnoea, *Curtin Engineering Faculty Research Colloquium*, Curtin University of Technology, 14–November.

Tetlow, G.A., Wang, J. & Lucey, A.D. (2006). Numerical modelling – adding fundamental understanding to dysfunctions of the upper airway, *Australian Society for Medical Research, Medical Research Week Symposium*, The University of Western Australia, 9–June.

0.4 Posters Presentations

Tetlow, G.A., Wang, J. & Lucey, A.D. (2006). Dynamics of the Upper Airway, *Poster presentation at Curtin Science and Engineering Research Forum*, Curtin Engineering Faculty, 30–August.

Acknowledgements

First and foremost I thank Tony Lucey my supervisor. I am sure that those who know Tony will agree he is an incredibly productive researcher and an absolute pleasure to work and interact with. During my three years as a full-time PhD student having such a knowledgeable researcher, only a cigarette away, was a valuable resource and a reliable person for interesting discussions, if the constant references to obscure literature could be overlooked.

This work has benefited from the collaboration with Professor David Sampson (University of Western Australia) and Drs Peter Eastwood and David Hillman (Sir Charles Gairdner Hospital, Western Australia) in regard to the 3-D modelling and sleep study involvement. This contact provided valuable insights into the medical problem which was greatly enhanced by actually seeing and manipulating actual airways. The camaraderie shared with the fellow PhD students and research fellows at Curtin and the memorable antics perpetrated will always be remembered.

I thank Curtin University for granting an extension owing to my part-time study activity to finalise the thesis within other work commitments. I also acknowledge the support through the Curtin University Postgraduate Awards Scheme for my 3 years as a full-time research PhD student. Moreover, the support of the Department of Mechanical Engineering and the number of names it had over the years, for the additional income; teaching, marking and research allowing the mortgage to be paid each month. My subsequent period of part-time research was greatly assisted by my work colleagues who allowed me the flexibility to continue the research around work commitments. Of course special thanks go to all the family and friends who constantly enquired on research progress, occasionally showed some interest in contemporary findings and offered encouragement to stay the

course over the extended duration. Also to all I have not seen much of in 2011, owing to completion taking up every spare waking hour through Q1 & Q2 2011, I will enjoy catching up over a beer or two.

One of Tony's less esoteric literature quotes was apparently from one of the first book ever recorded, "The Epic of Gilgamesh" Circa 1500 BC. The story apparently tracks an individual's journey both over a long physical distance and time with the message being that the journey is often more important than the destination and how each of the obstacles encountered is overcome. In the case of research looking over the course of events it appears especially true; engaging with the new and novel, interesting encounters along the way changing the way a problem is approached, making the best use of the resources at your disposal and finding the motivation to continue when all is against you.

Contents

Abstract	iii
List of Publications	v
List of Publications	viii
0.1 Journal papers	viii
0.2 Conference papers	viii
0.3 Presentations	ix
0.4 Posters Presentations	x
Acknowledgements	xi
1 Introduction	1
1.0.1 Sleep disordered breathing	2
1.1 Obstructive Sleep Apnoea	2
1.2 The Medical Imperative	3
1.2.1 Numerical modelling	4
1.3 Research Objectives	5
2 Literature Review	9
2.1 Fluid Structure Interaction	10
2.2 Unbounded Flow	10
2.2.1 Infinite plates	11

2.2.2	Finite plates	11
2.3	Bounded Flow	13
2.3.1	Finite plates	13
2.4	Collapsible Tubes	14
2.5	Obstructive Sleep Apnoea; Treatment	15
2.6	Anatomy and action of the upper-airway	16
2.7	Physiopathology of obstructive sleep apnoea events	18
2.8	Bio-Mechanical model of the upper-airway	21
2.8.1	Flutter of the soft-palate	21
2.8.2	Pharyngeal stability	23
2.9	Motivation	25
2.9.1	Obstructive sleep apnoea; possible causes	25
2.9.2	Rationale for present modelling	26
I	Two-Dimensional Channel Flow	30
3	Simplified 2-D Model	31
3.1	Introduction	33
3.1.1	Assumptions	33
3.2	Theory	35
3.3	Structural solver	35
3.3.1	Linear elastic deformation of a thin plate	37
3.3.2	Structural boundary conditions	40
3.4	Finite Element Method for incompressible flows	41
3.4.1	Discretisation of the fluid domain	42
3.4.2	Galerkin Approximations	44
3.4.3	Weak form of the Navier-Stokes equations	46
3.4.4	Explicit formulation	49
3.4.5	Pressure driven	50

3.4.6	Inlet velocities for steady state solution	51
3.4.7	Inlet velocities for transient solution	55
3.5	Full coupling	56
3.5.1	Coupled fluid–structure interaction	57
3.5.2	Energies	58
3.5.3	Nondimensional analysis	59
3.6	Geometry and Materials of the upper-airway	63
3.6.1	Simulation Breakdown Structure	65
3.7	Validation	66
3.7.1	Fluid code	67
3.7.2	Flexible-plate code	67
3.7.3	Full coupling	70
3.7.4	Boundary conditions	77
3.8	Results	80
3.8.1	Numerical experiment methodology	80
3.8.2	Velocity-driven versus Pressure-driven model	82
3.8.3	Breathing cycle	95
3.8.4	Expanded pressure-driven model	103
3.8.5	Effect of channel boundary conditions	113
3.8.6	Dimensionless scheme	124
3.8.7	Solution space for a 2-D flexible-plate in channel flow . . .	131
3.9	Summary	134

II Three-Dimensional Duct Flow And Anatomically Correct Geometry **138**

4	Anatomically Correct 3-D Model	139
4.1	Introduction	141
4.2	Preliminary 2-D model with the inclusion of flow curvature	142
4.3	Analogue 3-D model with compliant palate and pharynx	144

4.4	Anatomical 3-D model developed from CT scans	152
4.5	Anatomically accurate 3-D reconstructed geometry using anatomical optical coherence tomography (<i>a</i> OCT)	157
4.6	Flow-field modelling of a reconstructed human pharynx	165
4.6.1	Reconstructed human pharynx modelling method and validation	166
4.6.2	Reconstructed human pharynx modelling results and Discussion	170
4.6.3	Reconstructed 3-D human pharynx modelling - conclusion	182
4.7	Summary	184
5	Application To Obstructive Sleep Apnoea	186
5.1	Airway geometry	186
5.2	Future biomechanical related work	189
5.2.1	Anatomical understanding	189
6	Conclusions & Future Work	192
6.1	2-D modelling	193
6.2	3-D anatomically correct modelling	194
6.3	Future work: 2-D modelling	195
6.4	Future work: 3-D modelling	196
	References	198
III	Appendices	207
A	Bronchoscope Images Of Forced Snores	208
B	Simulation Parameter Data Set	213
B.1	Solved cases within the viscous range	213
B.2	Un-Solved cases with stability points in the turbulent range . . .	219
C	Dimensionless Scheme Derivation	224

List of Tables

3.1	Non-Dimensional Parameters.	63
3.2	Physical variables held constant.	64
3.3	Physical variables varied.	65
3.4	Hydraulic diameters a comparison between 2-D and 3-D models with $\varepsilon = 0.33$	75
3.5	Hydraulic diameters a comparison between 2-D and 3-D models with $\varepsilon = 0.25$ and 0.33 respectively	75
3.6	Comparative Pressure drop and Velocities used.	83
3.7	Dimensionless Group Values for Figure 3.40. Note the table is grouped in row order, for example a-c are the cases in row 1 Figure 3.40.	125
3.8	Relative stability for a range of model composition variations with two channel flow. The reference base case stable oscillation is noted as ‘=’ with increasing instability from boundary condition changes qualitatively indicated with ‘+’ where the greater the number the more unstable.	137
3.9	Relative stability for a range of model composition variations for single channel flow for the configuration examined herein. Again increasing instability owing to boundary condition changes is qual- itatively indicated with ‘+’ where the greater the number the more unstable	137
B.1	Parameter data set expanded descriptions	214

B.2 Parameter data set expanded descriptions	220
--	-----

List of Figures

1.1	Development of 2-D model of the soft-palate from anatomical mid-sagittal view.	5
1.2	Development of 3-D model showing the critical region modelled within a schematic of the upper-airway and the orientation of soft-palate and pharynx motion.	6
2.1	Schematic representation of the anatomy of the human upper-airway.	17
2.2	Development of 3-D model of the soft-palate and pharynx walls within a rectangular duct.	28
3.1	Schematics presented. Upper for the Balint (2001) velocity-driven model, where maintaining constant inlet velocity results in the pressure necessarily varying with time. Lower the Tetlow <i>et al.</i> (2006) pressure-driven approach, where constant P_D was achieved through time and magnitude varying inlet velocities. The velocity boundary conditions on the walls and inlet outlet otherwise remain unchanged between the differing approaches. The pressure-driven model also lends itself more faithfully to asymmetric positioning of the soft palate which is highlighted through an example range of placements where differing magnitude inlet mean velocities for the oral and nasal inlets are depicted.	36
3.2	Schematic of the compliant plate.	39
3.3	Schematic of the fluid discretisation including an enlarged example of velocity and pressure node numbering.	43

3.4	Schematic of the parameters used in the calculation of \bar{U} . Upper presents the parameters of Eq. (3.52) when split between the two inlet channels and the combined segment. Lower provides a graphic on the summation performed in Eqs. (3.53) & (3.54) . . .	53
3.5	Schematic of the parameters used in the dimensionless scheme. . .	62
3.6	The first six mode displacement cycles of a cantilevered plate in vacuo.	69
3.7	Various pressure loads and deflections of a cantilevered: a) linearly decreasing pressure $P_0 = 0.00336$ Pa, b) linearly increasing pressure $P_L = 0.00336$ Pa, c) a point load positioned at the mid point of the cantilever $P_p = 0.000017$ N, b) linearly increasing pressure $P = 0.001$ Pa.	70
3.8	Flexible-plate tip deflections comparing 2-D and 3-D models for a range of flexible-plate E_p values: a) $E_p = 400$ Pa, b) $E_p = 800$ Pa and c) $E_p = 2800$ Pa.	74
3.9	Flexible-plate tip deflections comparing 2-D and 3-D models: a) $E_p = 400$ Pa, b) $E_p = 800$ Pa. Note 3-D $\varepsilon = 0.33$ & 2-D $\varepsilon = 0.25$	76
3.10	Schematic of the modelled base case and the set of variable boundary conditions that neutrally stable solutions were not sought. These boundary conditions were examined to yield relative stability compared to the base case.	81
3.11	Soft-palate tip displacement pressure-driven versus velocity-driven for inhalation.	85
3.12	Soft-palate tip displacement and upper channel flow rate versus time for inhalation, case L16_h2_01_H2.	86
3.13	Normalised flowrate versus non-dimensional time for pressure-driven numerical simulations.	87
3.14	Non-dimensional total energy versus non-dimensional time for a set of inhalation cases comparing the response of the two models; pressure-driven and velocity-drive.	89

3.15	Snapshots of pressure contours during a cycle of plate oscillations. Comparison for pressure-driven versus velocity-driven models for $\varepsilon = 0$ during inhalation.	90
3.16	Soft-palate tip displacement pressure-driven versus velocity-driven for exhalation.	92
3.17	Normalised flowrate versus non-dimensional time for exhalation pressure-driven numerical simulations.	93
3.18	Non-dimensional total energy versus non-dimensional time for a set of exhalation cases comparing the response of the two models; pressure-driven and velocity-drive.	95
3.19	Pressure contour plot pressure-driven versus velocity-driven $\varepsilon = 0$ for inhalation and exhalation.	97
3.20	Pressure contour plot pressure-driven versus velocity-driven $\varepsilon = 0.25$ for inhalation and exhalation.	98
3.21	Pressure contour plot pressure-driven versus velocity-driven $\varepsilon = 0.5$ for inhalation and exhalation.	99
3.22	Flexible-plate oscillations, initial condition shown as the thick line with 0.02 seconds between successive snapshots of motion. Note: PD = pressure-driven model and VD = velocity-driven model, rows and columns also marked for reference. These are also consistent in the following enlarged views.	100
3.23	Enlarged view of Figure 3.22 showing Rows 1 and 2, Columns 1 to 3.	101
3.24	Enlarged view of Figure 3.22 showing Rows 3 and 4, Columns 1 to 3.	102
3.25	Split section Mass flux with flexible-plate tip position versus time for inhalation for a variety of cases comparing inhalation and exhalation. Plate tip position solid line, Lower channel flowrate dashed line, Upper channel flow rate dotted line.	105
3.26	Enlarged view of Figure 3.25 showing Rows 1 and 2, Columns 1 to 3.	106

3.27	Enlarged view of Figure 3.25	107
3.28	Contributions of thin plate equation terms Eq. (3.1) presented for a number of cases. These show one time step with nodal contributions distributed along the flexible-plate. The flexible-plate position displayed in solid black, the flexural rigidity term $B\nabla^4 w$ solid magenta, the $\frac{\partial T}{\partial x} \frac{\partial w}{\partial x}$ component of tension green dashed, the $T\nabla^2 w$ component of tension green dotted and the total tension term $\frac{\partial}{\partial x} (T \frac{\partial w}{\partial x})$ solid green, with the pressure term δp_m presented in solid blue.	108
3.29	The same information is presented as for Figure 3.28 now with the temporal totals of terms being presented in bar chart form. The bar chart portion presents contributions over the whole simulation of each of the thin plate equation terms in Eq. (3.1). The magnitude of scale is uniform throughout. Each bar chart in green presents with the same order left to right being; $B\nabla^4 w$, $\frac{\partial T}{\partial x} \frac{\partial w}{\partial x}$, $T\nabla^2 w$ & δp_m	110
3.30	Enlarged view of Figure 3.29 showing Rows 1 and 2, Columns 1 to 3.	111
3.31	Enlarged view of Figure 3.29	112
3.32	Non-Dimensional plate tip deflections and flow rate versus Non-Dimensional time. Plate tip position solid line, Lower channel flowrate dashed line, Upper channel flow rate dotted line. Note the magnitude of P_D was held constant (0.04 Pa) for means of comparison.	114
3.33	Enlarged view of Figure 3.32 showing Rows 1 and 2, Columns 1 to 3.	115
3.34	Enlarged view of Figure 3.32	116
3.35	Flexible-plate oscillations over an idealised breathing cycle, in support of Figure 3.32. Plate initial position thick line normally unperturbed, displacement scale held constant in each case presented. Note the magnitude of P_D was held constant (0.04 Pa) for means of comparison.	118

3.36	Enlarged view of Figure 3.35 showing Rows 1 and 2, Columns 1 to 3.	119
3.37	Enlarged view of Figure 3.35	120
3.38	Schematic of the linkage between flowrate Q for dual (top) and single (bottom) channel flow as the rigid splitter section moves within the channel from top to bottom.	121
3.39	(a) Snapshots of soft-plate deflection and pressure contours (red=high to blue=low) for a typical inhalation using a constant applied pressure drop with the lower channel closed. Adapted from Tetlow et al. (2006), (b) & (c) Snapshots of soft-plate deflection at maximum deflection into the upper open channel during exhalation (flow from right to left) and pressure contours (light-magenta=high to Green=low) for initial soft-palate position denoted by broken line at, (b) undeflected and (c) the end of a previous inhalation. .	123
3.40	Flexible-plate oscillations. Variation of parameters, to demonstrate that dimensionless groups characterise palatal evolution. The relative importance of each dimensionless group to overall stability is also shown. Each row represents a set of dimensionless groups for comparison to determine the relative the importance of each. Cases (e, h and k) are for cases where Reynolds Number Re and of stiffness ratio Γ where varied showing significant changes to response. See Table 3.7 for specific dimensionless group values. Plate initial position thick line, displacement scale as shown in each case presented. Base cases for cases (a-i) considered neutrally stable oscillations and cases (j-l) unstable oscillations. . . .	127
3.41	Enlarged view of Figure 3.40 showing Rows 1 and 2, Columns 1 to 3.	128
3.42	Enlarged view of Figure 3.40	129

3.43	Stability space of Reynolds number Re versus stiffness ratio Γ . For numerical investigations of an undamped cantilevered, flexible plate, with one end fixed, symmetrically positioned in a 2-D channel subject to viscous fluid flow. Data points presented are for individual cases at or approaching stable conditions with red solid line of best fit and equation presented. The dotted and dashed lines represent two cases where plots for simulations with energy loss and gain to the fluid are also added. Below the solid red line energy is extracted by the flexible plate from the fluid, above loss of energy from the plate to the fluid. Note data points are coloured according to the dimensionless group of mass ratio Θ	132
3.44	Development of 2-D model from anatomical midsagittal view. . .	135
4.1	Two-dimensional calculation of the motion of the soft palate with a rigid anatomically valid upper-airway geometry during (a) inhalation, and (b) exhalation. (with the red peak values being 9.1 and 6.4 m/s, and blue indicating less than 1.5 and 1 m/s, in (a) and (b) respectively.) Adapted from Gray (1918a) "Anatomy of the human Body" online.	143
4.2	Upper-airway models, (a) 3-D analogue computational model, and (b) Anatomically correct reconstructed geometry (flexible regions circled in blue). Red arrows indicate principal directions of flexible-boundary motions.	145
4.3	Illustrative simulation of the flow-structure interaction; (a) generation of a 10-second time series and centreline flow at final equilibrium, (b) pressure contours, and (c) velocity magnitude. . . .	147
4.4	Dynamic response of palate tip and wall under various E_p - soft-palate stiffness, pharyngeal wall stiffness $E_w = 200$ Pa throughout. (a) Palatal response, (b) Pharyngeal Wall response & (c) Mass flux for a single case with $E_p = 400$ Pa.	149
4.5	Dynamic response of palate tip, demonstrating effect of side-wall stiffness on tip motion for three different soft-palates: (a) $E_p=200$, (b) $E_p=800$, and (c) $E_p = 2800$ N/m ²	150

4.6	Soft-palate tip deflection versus time. Response of soft-palate asymmetrically positioned subject to sinusoidally varying pressure applied drop, $E_p=800$ and $E_w=1600$ N/m ² . Lower channel blocked as an example of the most extreme case of calibre imbalance. Note - increasing deformation of soft-palate over cycle.	151
4.7	Schematic representation of a mid-sagittal view of the human head and neck highlighting the relevant upper-airway anatomy. The gold-coloured surface was the actual geometry that reconstructed in Section 4.5 using other methods to generate the geometric data.	153
4.8	Computed flow field for inhalation only through the nasal inlet, (a) Three-dimensional plot of velocity vectors for standard case, (b) Pressure field for standard case, and (c) Pressure field for a case with the soft-palate slightly deformed, relative to the standard case, towards the posterior of the pharynx. (Note velocity and pressure scales are respectively in mm/s and dynes/mm ² .)	154
4.9	Computed flow field for inhalation through both oral and nasal inlets for standard case, (a) Three-dimensional plot of velocity vectors, and (b) Pressure field. (Note velocity and pressure scales are respectively in mm/s and dynes/mm ² .)	155
4.10	Typical <i>a</i> OCT apparatus including mask to capture breathing related information and the catheter taped in position.	159
4.11	Series of slides generated by the <i>a</i> OCT system. Each slide captures geometry, location in breathing cycle and spacial information. Note an enlarged slide is included with in 4.12 demonstrating how the information was transposed into a 3-D model.	160
4.12	Progression from <i>a</i> OCT data acquisition to building an anatomical model of the upper-airway: (a) CT scan showing the locus of the catheter, (b) one <i>a</i> OCT geometry slice, (c) probe shown in the catheter, (d) one <i>a</i> OCT data set fitted to the catheter locus based on orientation and position from datum point, (e) 46 <i>a</i> OCT data sets added to the locus with the outline of the reconstructed geometry evident, (f) two images of velocity plots within the meshed model.	161

4.13	Various views of the upper-airway solid model at the end of inhalation (minimum volume): (a) from side, (b) from above, (c) from below, (d) from front.	162
4.14	Various views of the upper-airway solid model at the end of exhalation (maximum volume): (a) from side, (b) from above, (c) from below, (d) from front.	163
4.15	Computed flow field for the measured geometry in the velopharynx and upper oropharynx for inhalation through the nasal inlet, hence airflow direction is from top to bottom: (a) centerline velocity vectors, and (b) pressure values in five cross-sections of the airway, Note that the pressure legend denotes values of pressure divided by air density, (p/ρ) , in $(\text{m/s})^2$	167
4.16	Comparison of the pressure fields in the measured pharyngeal cross-section of area of minimum area predicted by different flow models. For the standard streamwise domain length depicted in Figure 4.14 and utilized throughout Figures 4.17 and 4.18: (a) unsteady laminar flow, and for turbulent flow, (b) $k - \omega$ SST model, (c) $k - \varepsilon$ model, and (d) using the $k - \omega$ SST model for a domain extended by 30% in both upstream and downstream directions.	169
4.17	Summary of variations to airway geometry generated by the model of soft-palate deflection; Case 0 is the actual (un-deformed) geometry measured.	172
4.18	Summary of variations to airway geometry generated by the model of side-wall deflection; Case 0 is the actual (un-deformed) geometry measured.	173
4.19	Computed flow field in the airway section of Figure 4.15 but with the soft-palate displaced into the velopharynx giving Case P4 of Figure 4.17: (a) centerline velocity vectors, and (b) pressure values in five cross-sections of the airway, Note that the pressure legend denotes values of pressure divided by air density, (p/ρ) , in $(\text{m/s})^2$	174

4.20	Computed flow field in the airway section of Figure 4.15 but with the side walls of the velopharynx deformed inwards giving Case W4 of Figure 4.18: (a) centerline velocity vectors, and (b) pressure values in five cross-sections of the airway, Note that the pressure legend denotes values of pressure divided by air density, (p/ρ) , in $(\text{m/s})^2$	175
4.21	Effect of airway deformation on magnitudes of non-dimensional pressure drop (P'_D), and pressures on the side-wall (p'_{lat}) and the soft-palate (p'_{pal}) surfaces, at the site of minimum cross-sectional area, due to: (a) non-dimensional soft-palate displacement, (Δd_y) , and: (b) non-dimensional side-wall displacement into the airway, (Δd_x) . The data points plotted as circles in (a) indicate results obtained at higher breathing rates of 50.4 l/min.	178
4.22	Non-dimensional logarithmic plot of the dependence of required pressure drop (P'_D) to maintain quiet breathing in an airway deformed due to soft-palate deflection characterised by non-dimensional hydraulic diameter (D'_h) and area (A'), and side-wall deformation characterised by non-dimensional area, at the site of minimum cross-sectional area in the velopharynx.	179
4.23	Variation of the magnitude of non-dimensional pressure on the lateral extremes of airway side-wall (p'_{lat}), and the soft-palate surface (p'_{pal}), with the non-dimensional minimum cross-sectional area (A') in the velopharynx varied by (a) soft-palate displacement, and (b) side-wall displacement into the airway. Broken lines indicate predictions based on a inviscid theory and mass continuity approach.181	

CHAPTER 1

Introduction

Once viewed as a defensive mechanisms during sleep to scare off predators and described even before medicine, snoring and obstructive sleep apnoea (OSA) have been known, liked and disliked throughout the ages. While ideas, theories and remedies have undergone significant revision over time, we still lack the knowledge to reliably obviate the ill-effects.

While the jury may still be out as to whether snoring is an unfortunate side effect of evolution, or design, there is little debate on the significant morbidity and potential mortality associated with this phenomenon.

Currently the dysfunction of OSA has not been satisfactorily classified on the basis of various causal modalities linked to treatments. In practical terms, current classifications tend to describe individual dysfunctions too broadly for the treatments available, resulting in low success rate for interventions. Treatment success rates for example central OSA, are around 50%. Currently the state-of-the-art for OSA diagnosis and treatment is informed by medical studies predominately developed from a body of heuristic research. However, in an attempt to overcome some of the drawbacks of purely medical studies, biomechanical modelling has been pursued. This modelling seeks to give further understanding of the underlying physics associated with, and leading to OSA. Thus far, no reliable cure has emerged and only a treatment for the symptoms has been developed, namely nasal Continuous Positive Airway Pressure (nCPAP) which remains the gold standard treatment eliminating much of the morbidity associated with OSA though only during continued use.

1.0.1 Sleep disordered breathing

Snoring is the precursor of several other diseases under the heading of sleep disordered breathing which contains two distinct subcategories:

1. Abnormalities of central respiratory drive or central sleep apnoea
2. Obstruction and narrowing of the upper-airway

Sleep disorders of the first kind are rare and not well suited to mechanical modelling as the dysfunction is with the body's feedback and control systems regulating breathing and oxygen levels. The second kind, including OSA, contains three subcategories:

1. Upper-airway resistance syndrome: characterised by frequent arousal from sleep due to increased upper-airway resistance
2. Hypopnoea: partial obstruction of the upper-airway associated with a reduced tidal volume
3. Obstructive sleep apnoea: characterised by repeated obstruction of the upper-airway and cessation of breath, associated with increased inspiratory effort and frequent arousal from sleep

Due to the close association of obstructive sleep apnoea and hypopnoea these are commonly referred to under one name as obstructive sleep apnoea-hypopnoea (OSAH). Sufferers of obstructed breathing generally but not always snore, though not all snorers suffer from obstruction. This is an important observation, that while snoring is linked, it is not the cause of obstruction. Many have focused their research with snoring as the precursor to be obtained for validation of their method, for example, to achieve a palatal vibration of 100Hz.

1.1 Obstructive Sleep Apnoea

Symptomatic OSA syndrome was estimated by Pierce & Worsnop (1999) to be present in 4% of men and 2% of women, with up to 20% of the adult population snoring habitually Huang (1995). More than just an inconvenience to partners,

the British Lung Foundation (1999) and Pierce & Worsnop (1999) and a wide variety of other sources publish lists of the numerous symptoms OSA sufferers exhibit, some of which are; daytime sleepiness while driving or reading or other periods of physical inactivity, general irritability, reduced concentration while also being associated with impotence, cardiovascular disease, stroke and nocturia. Huang (1995) cites higher natural and accidental death rates for OSA sufferers, the result being the community pays a large price for our inability to treat this syndrome. The financially quantifiable portion the Australian community payed for loss of productivity associated with sleep disturbances was estimated to be of the order of \$3-7 billion in 2004 alone (The Boston Consulting Group, 2003). The immeasurable loss resulting from the accidental death of loved ones resulting from OSA symptoms is also truly significant.

1.2 The Medical Imperative

The present research directs attention to the heart of the problem for clinicians: How to deal most effectively with each presented case of OSA. Numerous medical experimental studies have been conducted such as Hukins *et al.* (2000) and Hudgel (1998) to find answers to the problem of how to improve methods for diagnosis and treatment for OSA. The one finding common to all these studies is the inability to distinguish between the three modes of dysfunction; flutter of the soft-palate, collapse of the pharynx, and a combination of the palatal flutter and pharyngeal collapse followed by the difficulty in determining the site of obstruction.

This uncertainty in diagnosis, affects treatments through success rates as low as 40% to 66% (Hudgel, 1998). Currently there exists only one generally recognised successful medical treatment as stated by the British Lung Foundation (1999) this being nasal CPAP. Rather than being a permanent fix, nasal CPAP purely maintains airway calibre while in use. To receive any benefit, the OSA sufferer must endure wearing the mask and associated noise of the machinery to maintain airway patency. Nasal CPAP treatment has numerous side effects with long-term use, such as pressurisation of the stomach, and requires ongoing increase of the operating pressure over the sufferer's lifetime to maintain effectiveness.

Clearly, research directed towards understanding the fundamental causes of OSA

will be of great benefit to a large number people. This benefit will be realised through advances in the reliability of diagnosis and subsequent enhanced targeting of surgical interventions.

1.2.1 Numerical modelling

Typically numerical studies of OSA can be grouped into 3 broad categories with little or no overlap:

1. Investigations into flutter of the soft-palate in channel flow. Generally applying *inviscid* potential flow theory with a flexible beam or plate symmetrically positioned in the flow modelled by 1-dimensional Euler beam theory Howell, Lucey, Carpenter & Pitman (2009) and Huang (1995). Or above with the soft-palate assumed to rest on the tongue and move as one body Huang *et al.* (2007)
2. Starling resistor or collapsible tube studies Jensen (1990), Luo & Pedley (1998) and Bertram (2003) where the pharyngeal wall is examined for flutter and collapse phenomena. This work generally assumes only the nasal inlet is open to reduce complexity of the flow solution
3. Neuromuscular effects on the pharyngeal wall, with the model consisting of a channel with a spring backed compliant insert to incorporate the neuromuscular action Huang *et al.* (2001)

Clearly separation of the types of approaches fails to address adequately any interactions between the groups. While for some conditions this may be an acceptable assumption the low success rate for intervention point towards a lack of understanding when a combination of effects are at work. More recently studies such as Chouly *et al.* (2006), Chouly *et al.* (2008), Sun *et al.* (2007), Sung *et al.* (2006) and Mihaescu *et al.* (2007) have presented preliminary efforts to bridge one or more of these categories as three-dimensional models are developed.

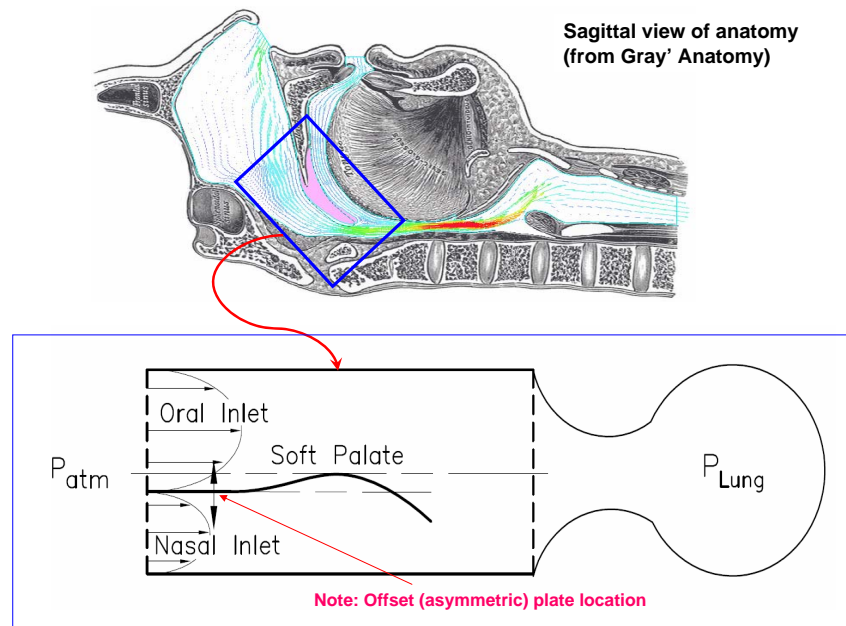


Figure 1.1: Development of 2-D model of the soft-palate from anatomical midsagittal view.

1.3 Research Objectives

This fundamental research will contribute towards a sound scientific understanding of the upper-airway dynamics of the human respiratory system see Figure 1.1. The benefits from this research will flow from a new understanding of the region of stability of a flexible-plate contained within a channel subject to a two-dimensional unsteady laminar fluid flow and an array of parametric variations. The simple analogue model of the soft-palate, enables the fundamental physics of the problem to be understood giving insights to the stability implications this has on the upper-airway as a whole, in particular the pharynx. Moreover, the three-dimensional modelling presented in Part II uses the key findings from the two-dimensional modelling and extends these to the remainder of the OSA problem space and the core physics prescribing the three modes of dysfunction elucidating the influence of geometric and material properties on stability.

The research objectives were to further understanding of the two-dimensional fluid structure interaction problem of a flexible-plate submersed in channel flow

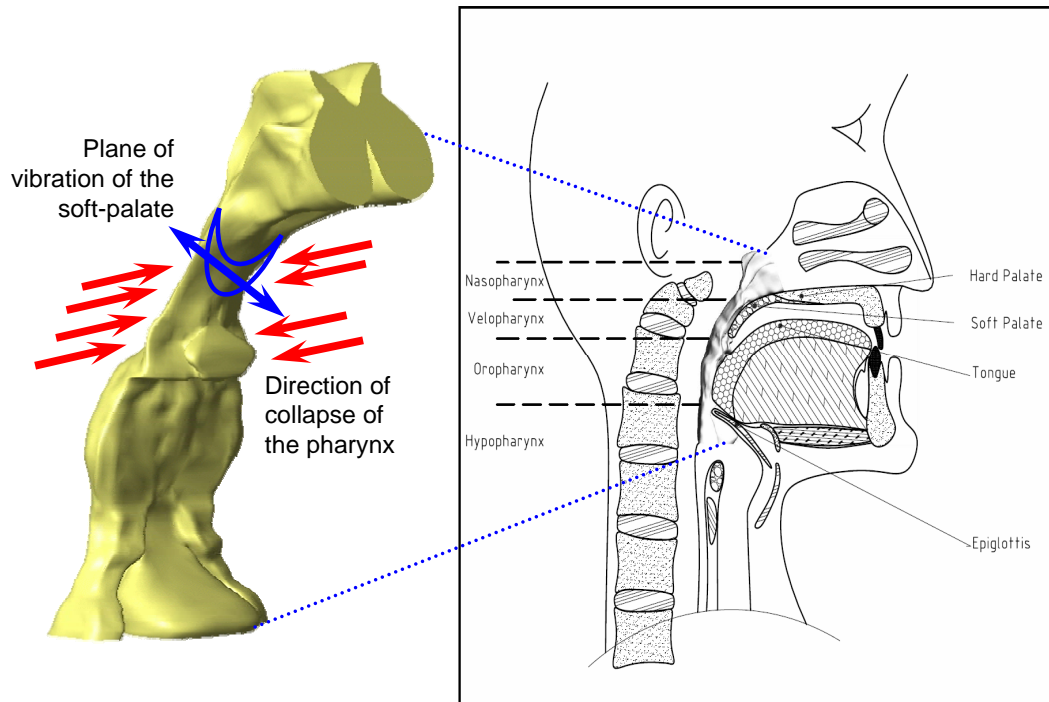


Figure 1.2: Development of 3-D model showing the critical region modelled within a schematic of the upper-airway and the orientation of soft-palate and pharynx motion.

utilising new modalities; modelling the flow using a pressure-driven approach rather than velocity-driven and include asymmetric positioning of the flexible-plate. This is followed by three-dimensional modelling which builds upon the two-dimensional findings with the inclusion of the orthogonal motion of the soft-palate and pharyngeal walls being simulated together see Figure 1.2.

Clearly these three broad objectives of 2-D modelling, 3-D modelling and application to OSA encapsulate a myriad tasks what follows is a summary of the key tasks undertaken in pursuit of the research objectives:

2D Modelling.

- Devised a non-dimensional scheme for the simplified two-dimensional fluid structure interaction problem
- Investigated the range of realistic parameter for consideration in simulations

- Developed pressure-driven flow through the domain, replicating the function of the lungs and accounting for varying upper-airway resistance
- Contrasted velocity-driven with pressure-driven models
- Incorporated the effect of the fluids's shear-stress induced tension term in the flexible-plate dynamics of the structural solver
- Reviewed contemporary modelling approaches for validity with medical literature, in conjunction with understood upper-airway function and structures
- Mapped parameter space for a flexible-plate symmetrically positioned in channel flow
- Considered stability implications of asymmetric positioning of the flexible-plate in the channel, with one channel closed and flow direction cycling, or a quasi respiratory cycle

3-D Modelling.

- Obtained clinical time-varying upper-airway geometric, pressure, flow and material properties from a subject for simulation and validation
- Developed a method capable of generating an upper-airway geometry at a specific point in a subject's breathing cycle
- Developed a method to reconstruct a geometry from data captured *in vivo*
- Investigated reducing complexity of geometry, compliant sections of pharyngeal walls and soft-palate motion
- Simulated quasi breathing cycle effects on upper-airway collapse
- Investigated the effect of incrementally varying the site of minimum area both laterally and in the anteroposterior plane
- Identified whether the findings from the 2-D modelling are applicable in a 3-D arrangement

Application to OSA.

- Reported on the findings from the 2-D and 3-D modelling and the significance of such to aid in the development of tools to better manage OSA
- Reported on the need to further investigate beyond the bulk geometry to the breaths immediately preceding apnoea
- Stressed the importance of collaborative efforts to deal with highly complex biological dysfunctions such as OSA

CHAPTER 2

Literature Review

The Literature under consideration for this thesis encompass two distinct areas of research. First the underlying physics of the fluid structure interaction between a flowing fluid and a flexible-plate in a channel, and second, contemporary approaches directed at understanding Obstructive Sleep Apnoea (OSA) from both medical and modelling points of view.

The first area of research focuses on the dynamics of plates in flow. The dynamics of plates were originally studied as a means to understand why a flag fluttered, (also an important aspect of aeroelastics). However, in the seminal aeroelastics books Bisplinghoff *et al.* (1956) and Fung (1955) very little is said on the aeroelastics of plates. This area of endeavour was comprehensively reviewed by Dowell & Hall (2001) and Dowell (1975) though dealt almost entirely with compressible and supersonic flows related to the contemporary topic of the day aeronautics. Since this time applications have diversified focusing on a large number of studies, motivated by applications in biomechanics Aurgan & Depollier (1995) and Huang (1995), the paper industry Watanabe, Isogai, Suzuki & Sugihara (2002) and Watanabe, Suzuki, Sugihara & Sueoka (2002), aerospace and nuclear engineering Guo & Paidoussis (2000). In recent times the literature on incompressible subsonic flows has been summarised in 2 volumes by Paidoussis (1998) and Paidoussis (2003), which has contributed to a substantial growth of research in the field. Of interest were the mechanisms leading to instability and under what boundary conditions, each mechanism was affected by the variety of configurations possible in bounded and unbounded flow.

The second area of research reviewed OSA and the associated challenges in diag-

nosis and treatment and the physical biological structures implicated with OSA. These later form the basis for modelling in the FSI section targeting the regions of instability and dysfunction. This thesis draws much from the medical literature of OSA, for constructing models of the human upper-airway, such that assumptions made were realistic within the constraints of numerical expense.

This chapter commences with a review of the biomechanical modelling of OSA and associated findings, concluding with a summary of the hitherto unexamined aspects from the medical and biomechanical literature for further investigation in the research area.

2.1 Fluid Structure Interaction

The interaction of a flexible surface or structure submerged within a flowing fluid gives rise to an number of physical phenomena of academic interest. Moreover, a large portion of this research is of a practical interest and impacts on a range of engineering application. For example, the stability and response of aircraft wings, instabilities due to flow of blood through arteries or air through the respiratory system, vibrations in heat exchanger tubes, the response of bridges, tall buildings to wind, the vibration of turbine and compressor blades, and the emerging areas of propulsion and renewable energy generation.

The phenomenology of the above can be categorised into three general groups. The first where the fluid moves around an essentially rigid body. In the second the structure moves without any feedback mechanism between the fluid and structure for example, a strummed guitar string, airplane wing or turbine blade. In the third and the focus of the present research there exists a energy transfer mechanism between the fluid and structure, impacting on the stability of the structure and flow-field characteristics.

2.2 Unbounded Flow

This area of literature studies the motion of compliant surfaces set into a flow hence the classification of, unbounded flow. Generally incompressible potential flow is adopted for the fluid domain. The classic problem, of a compliant flag

fluttering in a light wind where investigators seek to understand the fundamental question: why does a flag flutter, why is the drag of a fluttering flag much greater than a similar rigid body and what limits the amplitude of the flutter. This problem of the dynamic stability of an isolated flexible surface subjected to an unbounded uniform stream is old, dating back to Rayleigh (1879), who studied flapping of flags with little success. Thoma (1939) was among the first to revisit this problem and incorporated both the mass of the membrane and a constant tension force. This approach yielded a solution to the equations of motion in the form of a pair of travelling waves, which resembled that of a fluttering flag.

2.2.1 Infinite plates

Kornecki (1978) investigated infinite plates subject to incompressible potential flow subject to a range of geometries bounded and unbounded. The plate equation of motion included mass, damping and tension terms. Instability of infinite plates occurs initially as divergence then with increasing flow velocity neutral stability, until a flutter instability is reached. However with the inclusion of non zero damping for the boundary layer flows as in Carpenter & Garrad (1985) the system is dynamically unstabilised above the divergence threshold. This is referred to as a *Tollmien-Schlichting instability* where damping has a destabilising effect marked by a negative root on the Argand diagram for zero damping the root equals zero neutrally stable. The other flutter instability is *travelling wave flutter* where damping has a stabilising effect marked by a positive root on the Argand diagram.

2.2.2 Finite plates

Kornecki *et al.* (1976) conducted theoretical and experimental investigations of flexible-plates with two-ends-fixed and cantilevered configurations subject to a fluid flow. The unbounded flow perturbation pressures were determined by inviscid potential flow theory with the plate equations of motion including mass and spring stiffness terms. The resulting theoretical study of the two-end simply supported configuration showed that with increasing velocity firstly a divergence instability was reached followed by neutral stability then with increasing flow velocity flutter sets in giving a similar progression as for the infinite case.

Cantilevered arrangements with viscosity implicitly included through a Kutta condition at the free trailing edge with flow past one and two side/s showed instability to be solely flutter, but the critical velocity predicted by theory was lower than that obtained experimentally. This discrepancy was partly attributed to a underestimation of the *in vacuo* stiffness of the plate in the theory.

A concise literature review of the elastic and inertial nonlinearities in a cantilevered beam by Yandykin *et al.* (2001) and notes that most researchers approach this problem using linear plate theory, valid for small amplitude motion only. Numerical simulations were undertaken for a flexible-plate subject to an *inviscid* flow of constant velocity again with viscosity implicitly included with a Kutta condition at the free edge. When flow speed was increased above the critical velocity for flutter, oscillations become more violent and irregular (travelling-wave-type flutter) until a limit-cycle was reached. The inclusion of nonlinear terms allowed amplitude, frequency and drag coefficients at the limit cycle to be identified and presented as functions of the flow velocity. The numerical results were attained from one second of data, being sufficient to acquire confidence in the nature of the solution.

Yamaguchi *et al.* (2003) considered an industrial application with a thin sheet moving through air, between rollers, effectively clamped at each end. Again, a potential flow model was used, though analysis of the plate includes a tension term from the action of the rollers. This approach derived four governing parameters; tension/stiffness ratio, fluid force/tension ratio, reduced frequency and mass ratio. The flutter limits were seen to separate into three distinct relationships depending on the tension parameter. Watanabe, Isogai, Suzuki & Sugihara (2002) and Watanabe, Suzuki, Sugihara & Sueoka (2002) completed a similar study for an application in the paper industry.

Moretti (2003) estimates post critical flag (panel) flutter with the essential inclusion of structural stiffening due to induced tension. This theoretical work assumes the tension can be broken into two components these being; drag-induced tension and a time-averaged dynamically induced tension for incorporation into a potential flow solution. The plate model solves the classical thin plate equation of motion, with the full nonlinear equation of motion left for future work. These tension terms were found to be important if the bending stiffness was low.

An investigation with the aim to harvest energy from the vortices shed by a flow

passing over a bluff body was conducted by Allen & Smits (2001). Experimental work with several materials including polyurethane and the relatively more stiff piezoelectric material polyvinylidene difluoride were carried out. Flow visualisation showed for low Reynolds number flow, the polyurethane membrane acted as a splitter plate behind the bluff body. However, for high Reynolds number flow (Re of 20,000) a lock-in condition was reached where the membrane oscillated at the same frequency as the undisturbed wake behind the bluff body with the peaks and trough bounding the alternating vortices. At this condition the amplitude was also similar to the undisturbed vortex street being confined to the envelope of the wake behind the bluff body. This lock-in condition was only achieved in polyurethane as the stiffness of the piezoelectric material was too great.

2.3 Bounded Flow

This area of literature studies the motion of compliant surfaces set into a flow. Again mostly *inviscid* theory has been used to model the flow field however, now bounding channel walls effect the motion of the compliant surface. The classic problem is described by the Bernoulli effect where given a moving flexible surface the resulting cross-sectional area changes lead to transmural pressure changes. These fluid structure interactions are the focus of increasing research effort.

2.3.1 Finite plates

Guo & Paidoussis (2000) conducted theoretical investigations into the stability of plates held with various end connection configuration in *inviscid* channel flow. Both cantilevered and two-end-supported configurations were examined, with the flexible plate symmetrically positioned in the channel. Two-end-clamped configurations were examined for clamped-clamped and pinned-pinned end conditions. Clamped-clamped and pinned-pinned were found to be initially unstable through divergence then neutrally stable for increasing velocity until a critical velocity was reached, where the plate exhibited coupled-mode flutter.

Cantilevered plate configurations of pinned-free and clamped-free, found divergence can not occur, as the two branches of the first-mode imaginary eigenfrequency remains positive. For clamped-free plates, second-mode flutter is more prevalent

than first-mode whereas pinned-free configurations this is reversed. Looking at plates with free-clamped end conditions (or reversing the flow direction) shows the eigenfrequencies are conjugates of the clamped-free system for example divergence to be now possible.

Huang (1995) conducted numerical and experimental studies of cantilevered plates with free side edges, in channel flow. The numerical study used linear analysis of the plate motion, with motion being represented as a combination of *in vacuo* modes. Theodorsen's analytical solution of flow around airfoils was adapted to approximate the fluid-loading on the plate. Viscosity is explicitly excluded, but circulation around the plate is preserved by the Kutta-Zhukovskii condition. Simulations show no matter what the initial plate deflection was, after some transition period of modal realignment the plate assumes the same eigen-vibration. On a comparison of mass ratio and critical velocity (flutter) the fluid loading is relatively more destabilising when the density of the fluid is small. Additionally for long plates as velocity is increased to the critical limit there is a rapid onset of flutter while for short plates this onset is more gradual.

2.4 Collapsible Tubes

The review by Grotberg & Jensen (2004) describes advances to understand the mechanics involved with flow through a flexible-tube, the classical treatment of a flexible tube is the Starling resistor with the first experiments dating from 1912. The experiment comprises an elastic tube connected between rigid tubes where a pressure drop may be applied, this is then enclosed in a airtight chamber allowing a constant pressure to be exerted externally to the elastic-tube. Purely applying an external pressure to the elastic-tube causes the tube to buckle from circular to elliptical. Once buckled the tube becomes highly compliant with small pressure increases resulting in large cross-sectional area reductions. The addition of an applied pressure drop to the tube results in a constriction first towards the downstream end of the elastic tube where the pressure is predictably lower or the transmural pressure greatest. This configuration has been well characterised by Bertram (1986). The system exhibits spontaneous oscillations and arise in distinct frequency bands dependent on the rigid parts of the system. Highly nonlinear mode interactions and hysteresis between steady and dynamic states

are also apparent.

Theoretical 2-D models however consist of a channel with elastic segment added into one otherwise rigid wall. Subject to unbounded flows and the inclusion of spring backing of the elastic segment reveals multiple modes of instability that include Tollmien-Schlichting waves and travelling wave flutter. Travelling wave flutter relies on pressure and displacement at the wall being out of phase with one another for work to be done on the wall. Several modes of instability arise; long-wave instability for a developing flow and axial motions in the elastic segment have been identified in flows over gel-like viscoelastic surfaces as in Grotberg & Jensen (2004) and Davies & Carpenter (1997).

Bounded steady flows can become unstable to self-excited oscillations if the Reynolds number is sufficiently high or tension is low. Importantly the primary instability is sensitive to the choice of boundary condition, being more stable for prescribed velocity than pressure drop (Luo & Pedley, 2000).

2.5 Obstructive Sleep Apnoea; Treatment

An introduction into the significant morbidity associated with OSA was reviewed in Section 1.1 this present research directs attention to the heart of the problem for clinicians: How to deal most effectively with each presented case of OSA. Currently numerous medical experimental studies have been conducted Hukins *et al.* (2000), Hudgel (1998) and Pierce & Worsnop (1999) and Huang *et al.* (2001) to find answers on how to improve methods for diagnosis and treatment.

The one finding common to all these studies is the inability to distinguish between the three modes of dysfunction;

1. Flutter of the soft-palate
2. Flutter and collapse (divergence) of the pharyngeal walls
3. A combination of 1 and 2

Followed by the difficulty in determining the site of obstruction. This uncertainty in diagnosis, effects the treatments of sufferers leads to nasal CPAP treatment as the treatment. However, this treatment has numerous side effects with long-term

use, such as pressurisation of the stomach, and requires ongoing increase of the operating pressure over the sufferers lifetime to maintain airway patience. Nasal CPAP users often discontinue use within a year due to the significant sequelae (Pierce & Worsnop, 1999).

The dysfunction of OSA has not been satisfactorily classified on the basis of the various causes linked to treatments. In practical terms, current classifications tend to describe the causes of dysfunction too broadly, hence treatment suffers a reduced success rate. Treatments success rates for example central OSA, are around 50% within current classifications leading to the observations that current classification groups and treatments, are weakly linked. Currently the state-of-the-art for OSA diagnosis and treatment is informed from medical studies predominately of a heuristic nature with a number noted in Hudgel (1998). More recently however, biomechanical modelling has received greater attention in an attempt to understand the underlying physics behind OSA as in Lucey *et al.* (2010) and Chouly *et al.* (2008).

2.6 Anatomy and action of the upper-airway

The upper-airway extends from the soft-palate to the larynx see Figure 2.1, and serves two primary functions, namely swallowing and breathing. These functions require very different designed or evolved features. Operation is achieved by a collapsible tube normally held open, by muscular action pulling in appropriate directions on the pharyngeal walls. During swallowing these *pharyngeal dilator muscles* relax and allow the *pharyngeal constrictors* to propel the sustenance with a wave of activity. There are several muscles that contribute to maintaining the patency of the upper-airway. The muscles with direct dilator activity are the *genioglossus* (keeping the tongue forward), *levator veli palatini* (elevates the soft-palate from resting on the tongue), *styloglossus* and *stylopharyngeus* (works in combination with other muscles to open the lateral walls at the top of the pharynx) and the *thyrohyoid* (works in combination with other muscles to open the lateral walls at the bottom of the pharynx).

The most important feature in terms of upper-airway stability is the action of muscles to maintain airway caliber. The tongue is held in position in the direction of action of the *genioglossus* muscle, whereas the *styloglossus* and *stylopharyngeus*

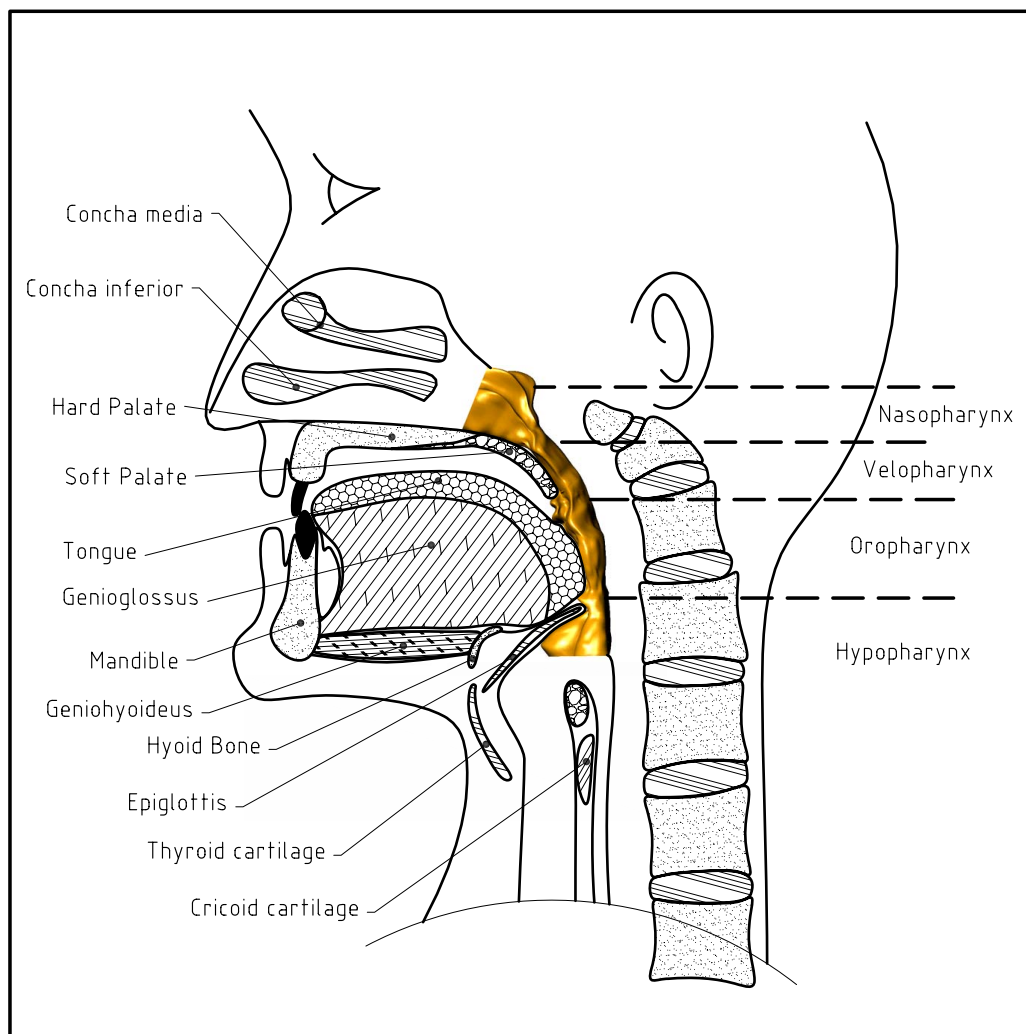


Figure 2.1: Schematic representation of the anatomy of the human upper-airway.

muscles in the pharyngeal lateral walls work in an orthogonal direction to these muscles line of action (White, 1995).

The pharyngeal tube itself is bounded to the anterior by the tongue and to the posterior by the spinal column, which are considered essentially rigid, leaving the pharyngeal lateral walls patency being solely maintained by an array of muscles working in concert, with the result being achieved in an orthogonal or transverse direction to their action.

Within one breath of falling asleep there is an abrupt reduction in *pharyngeal dilator muscle* activity. Within a few breaths of the initial decrease there is an increase in activity for the *genioglossus* (holding the tongue forward from the pharynx), whereas all other pharyngeal dilator muscles remain at lower activity levels (Pierce & Worsnop, 1999). Furthermore, when viewed from a mechanical perspective, due to the transverse action maintaining lateral wall patency, this would be the most susceptible area to collapse with any reduction in dilator muscle activity brought about by sleep.

The position of the head and neck effects the resistance of the upper-airway in individuals standing upright when compared to the supine position. This is due to increased blood flow to the nasal mucosa and gravity shifting the mandible posteriorly (Pierce & Worsnop, 1999). Opening the mouth also markedly reduces upper-airway resistance but heating, humidification and filtering of the inspired air is less efficient. In general it requires approximately 580-750ml/s of flow to necessitate the mouth and nose to be open together.

White (1995) reported on one interesting study that found that an externally applied vibration of 30Hz has been shown to activate upper-airway dilator muscles during sleep for normal subjects and OSA sufferers. Thus it may be possible that snoring serves a useful purpose as an early warning system of pharyngeal collapse which turns on protective mechanisms.

2.7 Physiopathology of obstructive sleep apnoea events

This section considers the elements of the literature that directly comment on the measurable changes which occur during apnoea or believed to be associated

with apnoea together with current treatments and the dysfunction modalities each attempts to remediate.

Woodson (2003) when reporting on a study of the OSA found that collapse and obstruction result in flow limitation and decreased ventilation and are marked by the following system recovery measures: increased ventilatory effort, hypoventilation, central nervous system arousal, sleep fragmentation and it is these that lead to the significant morbidity and mortality of OSA. Hukins *et al.* (2000) reported on radiofrequency tissue volume reduction as a means to stiffen and shorten the soft-palate by thermocoagulation scarring. The motivation for this technique stemmed from current techniques being associated with significant morbidity, for example uvulopalatopharyngoplasty, or methods requiring ongoing use rather than cure such as dental devices and continuous positive airway pressure, where patient compliance and acceptance is poor. This treatment was conducted on a sample group of 20 subjects, comprising successive application of the technique; on the middle third, upstream root (3 days later) and downstream tip (7 days later). At completion of the three applications, results showed 18 out of 20 subjects benefited from the treatment through a subjective snoring assessment, while only 8 reported an subjective improvement of 50% or greater. Quantitative assessment of sound intensity against baseline showed maximal sound levels increased after treatment, though the duration of time above 50 db reduced from 7% to 4% of sleep. Assessment of the individual treatments (between applications) was only conducted qualitatively with patients reporting greatest gains from the middle and upstream treatments. No quantitative findings were drawn from individual treatments. Moreover, response could not be predicted on the basis of demographic and several snoring/sleep indices to allow an informed decision as to who, and to what position, the treatment should be applied.

Hudgel (1998) conducted a major review of literature on surgical interventions for OSA and presented findings. An interesting finding for the most reported surgery, uvulopalatopharyngoplasty, statistically shows there were no differences in the preoperative clinical characteristics between surgery responders and non-responders, although non-responders tended to have worse OSA, one longitudinal study found weight gain in responders was associated with relapse of OSA while subsequent weight loss reversed this. This last finding was unsurprising as weight has been for a long time correlated with OSA.

Malhotra, Pillar, Fogel, Edwards, Ayas, Akahoshi, Hess & White (2002) compared the geometry of a representative male to that of a representative female with anatomic differences reported. The criterion used for selection of the non-OSA subjects was an apnoea-hypopnoea index of up to 15 events per hour. This high value was chosen as testing was undertaken with nasal pressure signal, which artificially increases events over conventional thermistors alone. Some data suggests the effects of OSA are evident in the range of 5-15 events per hour of sleep. Anatomic differences were normalised for body size including height; the pharyngeal airway length was 30% longer in men than women, the soft-palate cross-section in men was 45% larger than for women, the airway area of men was 40% greater than women. Importantly there existed no gender-related differences in pharyngeal fat distribution. The appropriateness of the normalising process and which metrics to normalise on was unclear, requiring further work.

Woodson (2003) explained OSA was not only implicated with inhalation, but also exhalation. The airway area in the region of the soft-palate was seen to be smaller during early and late expiration on obstructed, rather than nonobstructed breaths. Reductions in airway size on exhalation provide a mechanism for increased obstruction on subsequent inspiratory breaths. Data from various sources such as Saladin (2001) indicate that during sleep expiratory flow limitation increased airway resistance, however the reasons for this were not detailed. Moreover, the research indicated decreases in airway size occur, and are epochal leading to upper-airway obstruction. The model developed extended Starling resistor theory of a collapsible tube by using multiple segments with different properties to represent the upper and lower pharyngeal regions for nasal breathing. The model shows the upper-airway is not well represented by a conventional Starling resistor approach but rather with multiple segments (two elements in this case) and different or varying properties. This work compares clinically obtained pressure during expiration to that of the multi-segment model. The model demonstrates the applicability of lower airway pressure determining compliance in the retropalatal region (behind the soft-palate) during nonobstructed but no correlation existed for obstructed breaths as had been thought previously.

Neuromuscular failure is one possible cause of OSA where the delayed action on the upper-airway of the dilator muscles causes something comparable to negative damping. However, these cases are rare and associated with a primary neuromuscular problem such as brainstem lesions or myopathies. The pharyngeal dilator

muscles do have clear inspiratory phasic activity that contributes to upper-airway widening (Pierce & Worsnop, 1999).

White (1995) found over-weight to be linked with 40% of sufferers of OSA. MR imaging found fat preferentially deposited in the airways lateral fat pads. Furthermore, the pharyngeal airway in OSA patients is narrower laterally when compared to non-OSA sufferers.

2.8 Bio-Mechanical model of the upper-airway

Numerous medical studies of a qualitative or heuristic nature have investigated Obstructive Sleep Apnoea (OSA). However, few gains have been made increasing success rates for surgical intervention. These disappointing results have led to something of a sea change to quantitative methods. This change in focus is indicated by a growing number of studies based in physics over the last decades. The following reviews the two pre-eminent branches to the OSA condition of soft-palate stability and collapsible tube approaches.

2.8.1 Flutter of the soft-palate

Huang (1995) conducted a theoretical and experimental study of cantilevered plates with free side edges in channel flow. The numerical study employed linear analysis of the plate motion being represented as a combination of *in vacuo* modes. Potential flow was used to approximate the fluid-loading on the plate. Flutter instability was seen to be a combination of the first two *in vacuo* modes or, cross-mode coupling. This approach yielded two independent controlling parameters; a mass ratio and a velocity ratio. The physical interpretation of these two parameters in terms of a class of snorers were; those with long or less stiff soft palates, or those with small or narrow airways. These parameters as described, demonstrated a combination of parameters that can lead to greater risk of upper-airway obstruction. Huang (1995) cited use of an (at the time), new medical procedure that reduces the length of the soft-palate uvulopalatopharyngoplasty (UPPP) though *ergo propter hoc* the airway has proved significantly

more complex than this, resulting in disappointing success rates as noted above of 50% for the UPPP procedure.

Huang, White & Malhotra (2005) devised a 2-D model of the upper-airway utilising a midsagittal plane geometry with the mouth closed. Modelling considered the tongue and soft-palate to be compliant and essentially moving together in vibration and collapse. The geometry used was the average of 5 males (non-OSA sufferers) referred to as a “mean structure”. A genioglossal muscle contraction model was developed incorporating tonic and phasic activation. The fluid was modelled with laminar flow and the system modelled using the nonlinear dynamic analysis software, ADINA R & D. Results indicated flutter of the tongue and soft-palate at an applied pressure drop from nose to lower pharynx of 800Pa and collapse at 1300Pa.

Huang, Malhotra & White (2005) examined the effect of anatomic perturbations on an 2-D midsagittal model for nasal breathing obtained from signal averaged MRI of five male non-OSA sufferers, as described in Huang, White & Malhotra (2005). The anatomic perturbations modelled and reported on were mandibular advancement, palatal resection (removal) and palatal stiffening. All resulted in positive outcomes on the intramural pressure required to induce upper-airway collapse from a baseline of 1300Pa to 2100Pa, 1800Pa and 1700Pa respectively. The finite element method used applied pressure boundary conditions consistent with the function of the lungs and assumed laminar flow to reduce computational time. The advantage for clinicians to be gained from this type of research is all three methods can be trialed and the efficacy of each ascertained prior to any surgical intervention.

Balint & Lucey (2005) reports on the instability of a cantilevered flexible plate in viscous channel flow as an analogue for OSA. Findings indicating that the mechanisms leading to the various dysfunctions of the upper-airway to be flutter of the flexible-plate (soft-palate). Flutter is caused by a phase shift between the hydrodynamic forces, and the movement of the plate.

Aurgan & Depollier (1995) examined numerically and experimentally the vibrating frequencies of a flexible-plate using linear analysis of plate motion, in channel flow for Reynolds number of up to 3000. The range of frequencies seen in soft-palate snoring is 20–80Hz, the posterior and anterior wall of the pharynx having phasic oscillations in phase with the breathing cycle of the order of 1–2 seconds.

Therefore given the orders of magnitude in frequencies, an assumption of rigid posterior and anterior channel walls for the model was adopted. The model also assumed uniform inlet velocities and evaluates unsymmetrical positioning of the flexible-plate equating the results through the use of an equivalent height with some agreement for channel height variations. The experimental apparatus, however, functioned in a similar way to the lungs, in that inflow is achieved with a vacuum pump where the flow varies with upstream resistance. Aurgan & Depollier (1995) find snoring to be controlled by one dimensionless group in two parts: one the soft-palate characteristics; the other connected to the flow conditions. The physical interpretation of these two classes of snorers are those with long or less stiff soft-palates or those with small and narrow airways respectively. Importantly for the modelling method, the velocity required for the plate to become unstable or the *critical velocity* is lower than that seen experimentally, this finding has been made numerous times in the monograph reviewing FSI (Paidoussis, 2003) which includes many studies presenting similar findings.

2.8.2 Pharyngeal stability

Gavriely & Jensen (1993) examined the collapsible tube problem experimentally and theoretically. The theoretical model of the upper-airway, comprised a channel with the addition of a spring-backed plate set within the upper channel wall, subject to a flow of constant mean velocity. The pressure drop in the channel (or intraluminal pressure) for the fluid structure interaction was obtained for the two different compliance section as follows. For the rigid channel segments, a linear viscous flow resistance and for the collapsible section, a combination of viscous resistance and Bernoulli-effect were used. A force balance was then used to assess the plate dynamics with the fluid interaction. The study developed two independent parameters one a normalised head loss force, the second, an inertia force.

Shome *et al.* (1998) identified for a anatomically correct geometry of the human upper-airway (excluding the oral cavity) the spatial variation of Reynolds number for various flows. Findings show wholly laminar (Re 600) for low flows of 100 ml/s, laminar to transition (Re 1600-4500) for flows of 400 ml/s and wholly transition (Re 4000-9000) for flows of 800ml/s. Pressure drops were seen to increase by as much as 40% when turbulent effects were included. The effect of CPAP was then

considered for a single patient's airway monitoring; cross-sectional area, velocities and pressure drops, for an applied CPAP pressure below 1000Pa cross-sectional area changes were subtle.

Aittokallio *et al.* (2001) approached modelling the upper-airway with the so-called tube law or Starling resistor, in this case enhancing the model with the provision of tonic muscle activity and phasic muscle activity to more closely replicate reality. Jensen (1990) performs both experimental and theoretical studies to obtain explicit pressure-flow relations for a channel having one flexible wall, held in tension, subject to a *viscous* flow.

Huang & Ffowcs Williams (1999) proposed a lumped parameter model to study the effects of delayed neuromuscular activity and structural damping on the stability of the upper-airway. Airway pressure was found by the Bernoulli equation and identified a minimum condition for stability that the structural stiffness must be larger than the neuromuscular stiffness to avert collapse. The model showed that in the situation of structural stiffness being insufficient to withstand the intraluminal pressure, neuromuscular action is required to avert collapse. During sleep, significant delay occurs transforming the neuromuscular force into a negative damping effect that destabilises the pharyngeal wall.

In summary most research into soft-palate instabilities has considered a two-dimensional *inviscid* potential channel flow, with linear plate analysis. For these investigations the channel walls have been considered rigid. Correctly, lateral wall motion has been excluded in these two-dimensional studies owing to the orthogonal nature of the soft-palate and pharynx vibrations. Further, these studies have concentrated on symmetric positioning of the flexible-plate in the channel with a constant velocity entering each channel.

The investigations into pharyngeal collapse modelled by a collapsible tube considered purely nasal breathing (only one inlet) and has excluded the additional motion of the soft-palate. Also the upper-airway function was not driven by an inlet velocity but the pressure drop generated by the lungs, this was correctly implemented by some experimental approaches. Inhalation by the lungs produces an essentially constant pressure drop with the flow rate or inlet velocities being a function of this pressure drop. As a result the velocities are highly variable due to the nonlinear relationship between upper-airway resistance and the constant pressure drop.

2.9 Motivation

Medical practitioners are calling for a tool to assist with the following current issues

1. Identification of the localised site of obstruction
2. Surgical treatment is effective in a small number of patients but reliable recommendation is hampered by the inability to identify the point of narrowing and collapse or if other phenomena are at work
3. Treatment with CPAP is effective but is not a cure
4. Due to poor diagnosis potential beneficiaries are denied the opportunity for cure; while others are disappointed by the unsuccessful result of surgical intervention

Addressing these issues from an engineering perspective, requires a number of approaches to investigate the root causes of OSA, starting from a simple model then gradually building-in more functionality in line with increased understanding.

To date researchers have concentrated on understanding individual identified aspect of OSA, such as the motion of the soft-palate or pharynx. The literature shows a number of importance aspects associated with OSA. If the linkages between these are strong, while not appearing to be, then much of the underlying cause maybe masked. Clearly the way forward, owing to the lack of practical advancement, is to combine approaches as have Vos *et al.* (2007), Chouly *et al.* (2008), Sun *et al.* (2007), Sung *et al.* (2006) and De Backer *et al.* (2007) bringing a number of theories together, going beyond the superficial and attempting to understand the myriad causes or risks for OSA. This thesis attempts to further develop such multi-functional models, incorporating our already published contributions in Tetlow & Lucey (2009) and Lucey *et al.* (2010).

2.9.1 Obstructive sleep apnoea; possible causes

White (1995) cited medical literature indicating the tongue to be controlled well by the comparative active *genioglossus muscle* so is unlikely to be implicated

in pharyngeal collapse, whereas the action of the lateral wall dilator muscles is purely tonic and orthogonal to the line of action. Coupled with the associated lateral fat pad location, this is a site of potential instability.

OSA is not only implicated with inhalation, but also exhalation. The airway area in the region of the soft-palate is seen to be smaller during early and late expiration on obstructed, rather than nonobstructed breaths. Reductions in airway size on exhalation provide a mechanism for increased obstruction on subsequent inspiratory breaths. Data from various sources indicate that during sleep expiratory flow limitation increases airway resistance.

For cantilevered plate configurations of clamped-free, divergence cannot occur, as the two branches of the first-mode imaginary eigenfrequency remains positive. For clamped-free plates second-mode flutter is more prevalent than first-mode flutter. Considering plates with free-clamped end conditions (or reversing the flow direction) shows the eigenfrequencies are conjugates of the clamped-free system therefore divergence becomes possible.

The posterior and anterior wall of the pharynx has phasic oscillations in phase with the breathing cycle in the order of one to two seconds. Therefore given the orders of magnitude in frequencies, an assumption of rigid posterior and anterior channel is a reasonable assumption limiting for complexity.

Malhotra, Huang, Fogel, Pillar, Edwards, Kikinis, Loring & White (2002) assessed anatomic difference between non-OSA males and females normalised for body size implicated the following with OSA:

1. Pharyngeal airway length was 30% longer in men than women
2. Soft-palate cross-section was 45% larger in men than women
3. Airway area was 40% greater of men than women
4. No gender-related differences in pharyngeal fat distribution

2.9.2 Rationale for present modelling

Two-dimensional modelling see Figure 1.1 was developed to account for stability of the soft-palate and included a number of modalities associated with OSA that other researchers have omitted including the following.

1. Pressure-driven flow through the model to mimic the function of the lungs and permit flow to vary with channel resistance
2. Asymmetric positioning of the compliant, soft-palate can be rationally achieved with the implementation of item 1 above
3. The effect on stability of a range of airway, palatal material and geometric characteristics
4. the effect of breathing cycle including both inhalation and exhalation. There is much evidence pointing towards OSA developing over a number of breathing cycles
5. Airway response to increased respiratory effort resulting from restriction to maintain mass flow; this is subtly different to reverting to a velocity driven approach
6. Stability with one or two inlets open, mimicking breathing solely through the nose

With the above incorporated into a suitable numerical scheme, how reliable can this be applied to medical diagnosis? Clearly further questions are raised surrounding three-dimensional effects, pharyngeal wall motion and stability, scalability for treatment of individual sufferers and how geometric simplifications vary the outcome for an actual airway. While this two-dimensional model is a significant improvement from contemporary research these questions remain to be addressed.

The realistic inclusion of pharyngeal wall motion, orthogonal to that of the soft-palate shown in Figure 1.2, necessitates the progression to three-dimensional modelling. The simplest three-dimensional model comprises a flexible cantilevered soft-palate, rigid hard palate, tongue and anterior wall. The ability to capture collapse of the pharyngeal walls in a simplified rectangular geometry is overcome by modelling the pharynx walls as cantilevered flexible plates with free side edges in a similar manner to the soft-palate see Figure 2.2. This model allows the following additional modalities to be captured.

1. The interaction between the soft-palate and pharyngeal wall

2. Comparison of the previous 2-D simulations with the 3-D results to identify any significant trends

The final step is the development of a three-dimensional anatomically correct model with appropriate material properties, initially for the compliant soft-palate and pharyngeal walls. Clearly this step will allow study of individual sufferers. However, the intermediate step without implementing full FSI function allows a study of the airway with targeted deformations to ascertain pressure distribution variations.

Part I

Two-Dimensional Channel Flow

CHAPTER 3

Simplified 2-D Model

The initial development of the velocity-driven model used in this thesis was previously conducted by a University of Warwick PhD student. Balint (2001) undertook initial coding, implementation and validation of fluid and structure solvers including full coupling of the two. As such much of this previous work will be reviewed with the full detail referenced to the original thesis. The existing work comprised an explicit Navier-Stokes fluid solver suitable for laminar flow up to Reynolds number of approximately 1500. The structural-solver implementation used an implicit finite difference technique allowing arbitrary plate motions, in contrast to a truncated sum of orthogonal *in vacuo* modes. Explicit coupling of the fluid and structural solvers was achieved with the transmural pressure driving the plate's motion in-turn matching flow domain and boundary conditions with vertical displacement, velocity and acceleration of the plate.

This chapter details a review of Balint (2001) and the extension of this research to that of a pressure-driven flow, inclusion of significant structural terms and finer discretisation of the structural domain. Dimensional analysis of the resulting system is conducted to determine the modelled cantilevered plate's stability solution space. Validation was achieved through comparison with independent FSI solvers such as ADINA R & D. Inc (2006) and the Object-Oriented Multi-Physics finite element Library oomplib as in Elliott *et al.* (2010) for large-amplitude oscillations.

Following the theory and model implementation which comprises Sections (3.2) to (3.7) the key contribution from this chapter is the results presented in Section (3.8). Following a short introduction, a comparison of the originally developed

velocity-driven versus the newly implemented pressure-driven models are presented in Section (3.8.2). Here the advantages of the pressure-driven model are explored including the realistic manner in which asymmetric positioning of the soft-palate within the channel performs. The model allows varying inlet flow velocities as internal resistances change due to the flexible plate motion and position. However, this yields an overall steady mass flux through the combined section, typical of human breathing during inhalation.

Section (3.8.3) considers the dynamics of an idealised breathing cycle with results generated from each of the presented models. Here pressure field plots are presented as an extension to the energy transfer plots previously presented. The underlying mechanisms for the differing dynamics of Section 3.8.2 become clear as the pressure contours for the velocity-driven model have significant imbalances as a result of maintaining constant velocities, especially with asymmetric positioning of the flexible plate or flow reversal.

Section (3.8.4) concentrates on the pressure-driven model and further explores flow redistribution associated with asymmetric positioning of the flexible plate or flow reversal. Several cases are presented, which further showed that overall mass flux is maintained irrespective of a range of plate responses. The contributions of the constituent parts of the thin plate equation to plate stability were presented for a single time step and then summed over the simulation duration to give their total contributions. The purpose in particular was to identify the contribution of the two components of total shear stress induced tension. These were assessed to make very small contributions each time step however when summed over the entire simulation duration were significant though their magnitude were opposite moderating the overall result in most cases.

Section (3.8.5) again considers a breathing cycle however this time the flexible plate was initially unperturbed in each case which evolved into 1st or 2nd mode oscillations as a result of the boundary conditions and plate, flow parameters. Comparison was provided between dual and single channel flow with the latter being found to be significantly more unstable. This increased instability was again due to pressure imbalances associated with the closed channel, similar though not to the same extent to that associated with the velocity-driven model.

The complementary Sections of (3.8.6) and (3.8.7) then close out this chapter demonstrating the dimensionless scheme's usefulness in predicting outcomes and

providing general applicability of the solution space findings. The presented solution space and best fit line of neutral stability allow the maximum velocity for a set of parameters to be predicted for the base case boundary conditions considered. Defining the solution space of other boundary-condition combinations is left as future work, however this thesis provides a qualitative indication in terms of relative stability to how each of these would relate to this base case at the conclusion of the chapter.

3.1 Introduction

The literature review chapter when examined on the basis of what is realistic and how to most efficiently model OSA leads to a surprising finding; many approaches, perforce, fail to capture the essential features of OSA to allow any real significant advance state-of-the-art surgical interventions. These initial studies do serve to enhance readers' comprehension of the magnitude and complexity of the problem, and have guided research towards the ultimate goal of full three-dimensional modelling. This thesis first extends the two-dimensional analogue work of Balint (2001) for soft-palate flutter through several advances to more closely reflect reality: pressure-driven flow representing the lung action, asymmetric positioning of the flexible-plate and examination of breathing-cycle effects - given that obstruction or collapse potentially develops over several breaths. Motions of the soft-palate are considered in isolation from pharyngeal collapse in this analysis, although findings give a plausible hypothesis for this occurrence.

3.1.1 Assumptions

- Gravity is neglected
- The flow-field is two-dimensional
- The flow is within the laminar region
- The velocities are far less than the speed of sound, air is therefore considered incompressible
- The flexible-plate has a uniform cross-section and mass per unit width

- The flexible-plate is long compared to thickness, and rotary inertia and shear deformation are ignored
- The centre length of the flexible-plate is inextensible
- Plane sections before deformation remain plane after deformation
- Internal dissipation effects of the flexible-plate are neglected
- deflections of the flexible-plate are uniform in the width direction
- Inclusion of damping effects through dashpot-type damping is available
- The flexible-plate is held in a cantilevered arrangement with one end clamped the other free
- The flow is modelled using the unsteady Navier-Stokes equation with viscous effects fully incorporated in the flow
- The incoming flow is time varying to maintain constant pressure drop (for pressure driven cases)
- Vertical components of inlet and outlet velocity are set to zero, sufficient downstream channel length was allowed for appropriate flow development from the free end of the flexible-plate
- Classical thin-plate mechanics for the flexible-plate permit displacement in the vertical direction only
- The no-slip condition on the flexible-plate is applied at the displaced position by zeroing the horizontal component of fluid velocity; this linearisation was based upon small ratios of amplitude to wavelength in the flexible-plate, a further implication from adopting thin-plate mechanics
- No-slip and no-flux boundary conditions are enforced on all walls
- Plate instability is determined from the energy transfer to the plate in the time period investigated
- The flow medium properties are temperature independent and uniform

3.2 Theory

The modelling approach is of a pragmatic nature giving insight to the problem of OSA. The method devised is a standard, but flexible, approach able to capture the underlying physics required to investigate the operation and dysfunction of the upper-airway. While the method is not mathematically optimised for speed of computation, it delivers results of use and provides insights to the mechanics of OSA. The various numerical elements that together enable the chosen flow and geometry to be simulated, including the equations of motion and derivations as appropriate are presented. Firstly the compliant plate, representing the soft-palate, was developed. This is a classical application of thin-plate mechanics with the inclusion of shear-stress induced tension and permits simple dashpot-type damping within the model. The flow model was then developed, Galerkin approximations lead to the development of the weak form of the Navier-Stokes equations and explicit solution method. Discretisation of the domain utilised Taylor-Hood elements and the method developed to maintain a constant pressure drop then presented. With the individual structural and flow solutions presented the method of coupling the two is introduced followed by validation. The non-dimensional scheme for analysis of the geometry and materials of the upper-airway are then described.

Schematics of the original system by Balint (2001) and the subsequently extended version of Tetlow *et al.* (2006) are presented in Figure 3.1. Here the differences are highlighted graphically including the enhanced flexibility afforded by the pressure-driven approach.

3.3 Structural solver

The structural solver formulation solved by an implicit finite difference method, permits arbitrary deformation of the flexible plate allowing development of unstable behaviour to be studied as an initial-value problem.

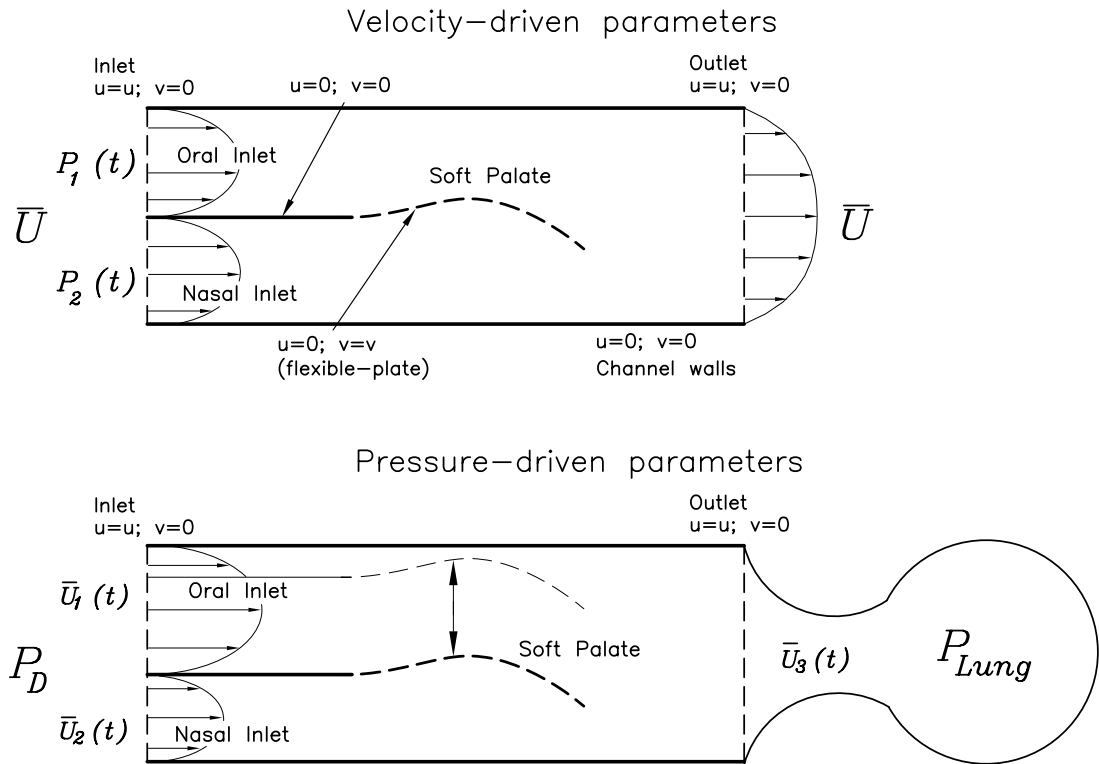


Figure 3.1: Schematics presented. Upper for the Balint (2001) velocity-driven model, where maintaining constant inlet velocity results in the pressure necessarily varying with time. Lower the Tetlow *et al.* (2006) pressure-driven approach, where constant P_D was achieved through time and magnitude varying inlet velocities. The velocity boundary conditions on the walls and inlet outlet otherwise remain unchanged between the differing approaches. The pressure-driven model also lends itself more faithfully to asymmetric positioning of the soft palate which is highlighted through an example range of placements where differing magnitude inlet mean velocities for the oral and nasal inlets are depicted.

3.3.1 Linear elastic deformation of a thin plate

A linear model was used to simulate the motions of the elastic plate, with the inclusion of the potentially significant non-linear term of shear-stress induced tension.

The general equation of motion for a inextensible flexible-plate with shear-stress induced tension, derived from Newton's Second Law Nowacki (1963), is given in Eq. (3.1).

$$\rho_m h \ddot{w} + d\dot{w} + \frac{\partial}{\partial x} \left(T \frac{\partial w}{\partial x} \right) + B \nabla^4 w = -\delta p_m \quad (3.1)$$

Where the flexural rigidity is given by, $B = (Eh^3)/(12(1 - \nu^2))$ and shear-stress induced tension T is a function of $(\ddot{w}, \dot{w}, w, t)$.

The equation of motion was discretised using an established finite-difference method. The finite-difference form of Eq. (3.1) at subsequent time steps $t + \delta t$, for the i^{th} nodal displacement can be written as

$$\ddot{w}_i^t = \frac{1}{\rho_m h} (-d\dot{w}_i^t(x, t) - \frac{\partial T}{\partial x} \frac{\partial w_i^t}{\partial x} - T \nabla^2 w_i^t - B \nabla^4 w_i^t - \delta p_m^t) \quad (3.2)$$

$$\ddot{w}_i^{t+\delta t} = \frac{1}{\rho_m h} (-d\dot{w}_i^{t+\delta t} - \frac{\partial T}{\partial x} \frac{\partial w_i^{t+\delta t}}{\partial x} - T \nabla^2 w_i^{t+\delta t} - B \nabla^4 w_i^{t+\delta t} - \delta p_m^{t+\delta t}) \quad (3.3)$$

Summing Eq. (3.2) and Eq. (3.3) and rearranging for $\ddot{w}_i^{t+\delta t}$ leads to the following

$$\begin{aligned} \ddot{w}_i^{t+\delta t} = & -\frac{B}{\rho_m h} (\nabla^4 w_i^t + \nabla^4 w_i^{t+\delta t}) \\ & -\frac{1}{\rho_m h} \frac{\partial T}{\partial x} \left(\frac{\partial w_i^t}{\partial x} + \frac{\partial w_i^{t+\delta t}}{\partial x} \right) - \frac{T}{\rho_m h} (\nabla^2 w_i^t + \nabla^2 w_i^{t+\delta t}) \\ & -\frac{d}{\rho_m h} (\dot{w}_i^t + \dot{w}_i^{t+\delta t}) - \ddot{w}_i^t - \delta p_m^t - \delta p_m^{t+\delta t} \end{aligned} \quad (3.4)$$

The tension coefficients in Eq. (3.4) additionally couple the fluid and structural sides of the system as the inputs are obtained directly from the flow solution

Section 3.4, as.

$$T(x) = \mu \int_L^x \left(\frac{\partial u(x')}{\partial y} \right) dx' \quad (3.5)$$

$$\left. \frac{\partial T}{\partial x} \right|_i \equiv \frac{T_{i+1} - T_{i-1}}{2dx} \quad (3.6)$$

The tension was evaluated over both sides of the plate, modelling the effect of skin-friction on the plate dynamics.

In Eq. (3.4) the finite-difference approximations at node i were given by

$$\nabla w_i \equiv \left. \frac{\partial w}{\partial x} \right|_i \equiv \frac{w_{i+1} - w_{i-1}}{2dx} \quad (3.7)$$

$$\nabla^2 w_i \equiv \left. \frac{\partial^2 w}{\partial x^2} \right|_i \equiv \frac{w_{i+2} - 2w_i - w_{i-1}}{dx^2} \quad (3.8)$$

$$\nabla^4 w_i \equiv \left. \frac{\partial^4 w}{\partial x^4} \right|_i \equiv \frac{w_{i+2} - 4w_{i+1} + 6w_i - 4w_{i-1} + w_{i-2}}{dx^4} \quad (3.9)$$

In addition to Eq. (3.1), the basis equations for the motion of any mass point within the discretised plate can be written of the form

$$w_i^{t+\delta t} \approx w_i^t + \frac{\delta t}{2} (\dot{w}_i^t + \dot{w}_i^{t+\delta t}) \quad (3.10)$$

$$\dot{w}_i^{t+\delta t} \approx \dot{w}_i^t + \frac{\delta t}{2} (\ddot{w}_i^t + \ddot{w}_i^{t+\delta t}) \quad (3.11)$$

Therefore, the system of equations to be solved (in finite-difference form) to obtain the displacement, velocity and acceleration was defined by Eqs. (3.4), (3.10) and & (3.11).

In these equations the term $-\delta p_m$ was the pressure forcing term obtained from the flow solution see Figure 3.2. For *in vacuo* simulations, or where no flow interaction was present and where pressure forces do not exist, its value was zero. When damping was not accounted for, the damping coefficient d was also zero.

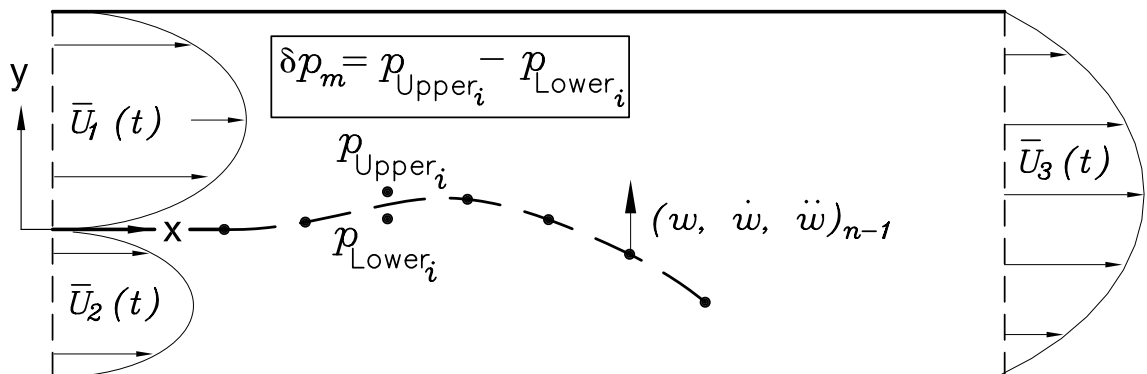


Figure 3.2: Schematic of the compliant plate.

3.3.2 Structural boundary conditions

The boundary conditions, defining the ends of the flexible-plate, admitted in this research, were *clamped* at the fixed end and *free* at the trailing end. Where the derivatives at the plate ends were set to zero (for example at $x = 0$), the conditions can be interpreted as the deflection ($w(0)$), the angle of inclination of the tangent of the deformed plate ($\partial w(0)/\partial x$), a quantity proportional to the bending moment ($\partial^2 w(0)/\partial x^2$) and a quantity proportional to the shear force ($\partial^3 w(0)/\partial x^3$). For arbitrary boundary conditions two of these conditions vanish.

For a clamped configuration the first node was stationary. In addition, the tangent of the deformed rod between the end node and the first node inside the domain was zero. The boundary condition were described as,

$$w_i = \frac{\partial w_i}{\partial x} = 0 \quad (3.12)$$

since

$$\frac{\partial w_i}{\partial x} = \frac{w_{i+1} - w_i}{\delta x} = 0 \quad (3.13)$$

the first derivative results in

$$w_{i+1} = w_i = 0 \quad (3.14)$$

For a free end configuration it follows that the bending moment and the shear force were zero at the last node, that is

$$\frac{\partial^2 w_i}{\partial x^2} = \frac{\partial^3 w_i}{\partial x^3} = 0 \quad (3.15)$$

Calculation of the finite difference operator using free end conditions requires knowledge of the displacement of two additional “dummy” points outside of the physical nodes of the plate. Displacement of the dummy nodes w_{i+1} and w_{i+2} were calculated from the known nodal displacement values of w_i and w_{i-1} . The first and second dummy point were calculated as

$$w_{i+1} = 2w_i - w_{i-1} \quad w_{i+2} = 3w_i - 2w_{i-1} \quad (3.16)$$

An additional “dummy” node for the tension term was required at the free end

T_{i+1} and was set to 0. A “dummy” node was also required at the clamped end T_{i-1} . This component of tension was found from T_i and T_{i+1}

$$T_{i-1} = 2T_i - T_{i+1} \quad (3.17)$$

3.4 Finite Element Method for incompressible flows

The motion of a fluid undergoing two-dimensional motion was described using the Navier-Stokes equations Eqs. (3.18), (3.19) & (3.20). The first two of which arise from Newton’s second law the third for the conservation of mass.

$$\rho \left(\frac{\partial u}{\partial t} + u \frac{\partial u}{\partial x} + v \frac{\partial u}{\partial y} \right) = -\frac{\partial p}{\partial x} + \mu \left(\frac{\partial^2 u}{\partial x^2} + \frac{\partial^2 u}{\partial y^2} \right) \quad (3.18)$$

$$\rho \left(\frac{\partial v}{\partial t} + u \frac{\partial v}{\partial x} + v \frac{\partial v}{\partial y} \right) = -\frac{\partial p}{\partial y} + \mu \left(\frac{\partial^2 v}{\partial x^2} + \frac{\partial^2 v}{\partial y^2} \right) \quad (3.19)$$

$$\frac{\partial u}{\partial x} + \frac{\partial v}{\partial y} = 0 \quad (3.20)$$

These equations were solved using the Finite Element Method (FEM). The finite element method utilised here is a process of numerical approximation to continuum problems, in which the unknown functions are replaced by an approximate trial set of functions involving a finite set of unknown parameters a , e.g.

$$\phi = \sum N_i a_i = \mathbf{N} \mathbf{a} \quad (3.21)$$

in which N_i were known functions of the independent coordinates. One further characteristic was required; the final set of approximating equations, derivable by a simple addition of contributions made by physically identifiable sub-domains of the whole region in which the solution was sought (Oden, 1975). The finite element method with origins in the 1950’s emerged as one of the most powerful methods devised for the approximate solution of boundary-value problems. Its variational method of approximation, making use of global or variational statements of physical problems and utilising the Rayleigh-Ritz-Galerkin philosophy

of constructing coordinate functions whose linear combinations represent the unknown solution. The domain under consideration was represented as a collection of geometrically simple subdomains (finite elements) connected together at certain nodal points. The variational problem is formulated approximately, for arbitrary boundary conditions, over individual subdomains, requiring simple local coordinate functions for each element (generally polynomials). The global model of the problem was then obtained by fitting the elements together to depict the domain, and summing the local element contributions. The strength of building a global approximation from a set of local ones was that a procedure for constructing coordinate functions for irregular geometries and boundary conditions could be achieved.

3.4.1 Discretisation of the fluid domain

The domain Ω was partitioned into a finite number (K) of subdomains $\Omega_1, \Omega_2, \dots, \Omega_K$ called finite elements see Figure 3.3. These elements were non-overlapping and, two-dimensional. The boundary $\delta\Omega$ of Ω was made up of straight segments, covering the entire domain with elements of a chosen geometry, quadrilateral, was best suited to this case. Every side of the element was either, part of, the boundary $\delta\Omega$ or another side of an element within Ω .

Certain points were identified in the subdomain, called nodes. Nodes were assigned to points of interest on elements such as vertices, constituting linear elements. However, with the introduction of further nodes the approximation maybe improved, for example a quadratic element, was obtained when a node was added to the mid-point in addition to the vertices of the sides of an element. The set of elements and nodes that make up Ω form the finite-element mesh. In practice discretisation of Ω was undertaken in conjunction with the desired element, to suit the purpose. One popular group of elements for approximating the Navier-Stokes equations are the Taylor-Hood family of elements. For a two-dimensional domain, quadrilateral elements have been compared to triangular elements Cuvelier *et al.* (1986) as

1. Only half the number of elements are required for rectangular meshes,

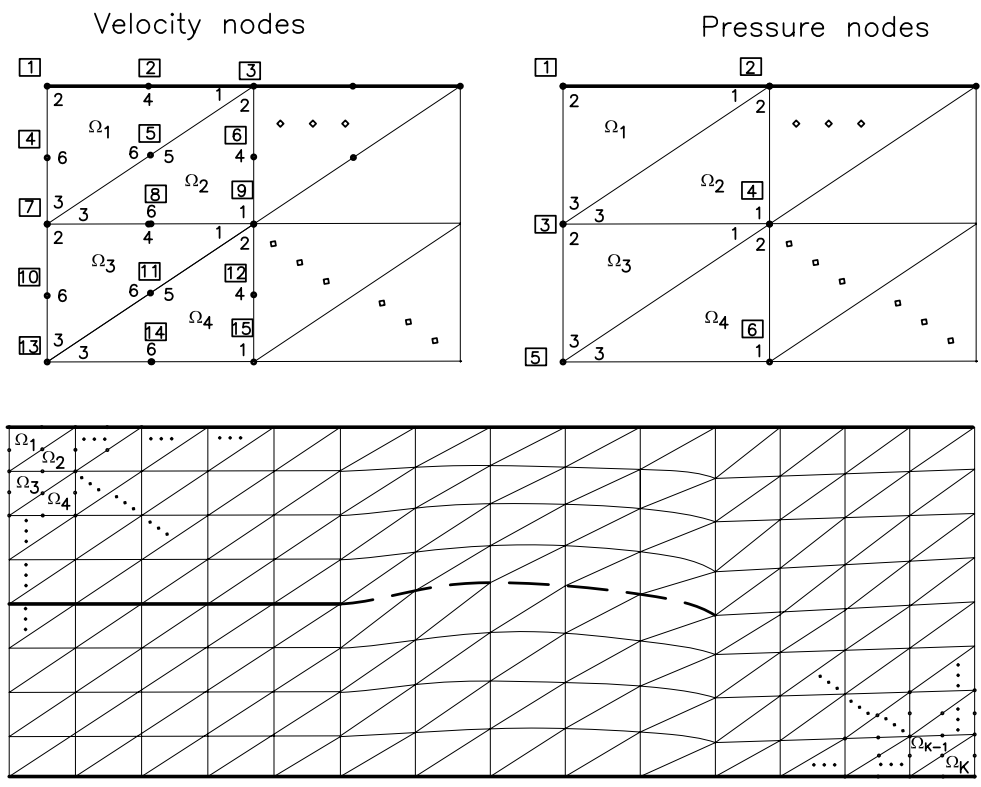


Figure 3.3: Schematic of the fluid discretisation including an enlarged example of velocity and pressure node numbering.

2. Triangular elements have been shown for numerical computations for convective-dominant flows, that the solution is sensitive to the direction of the diagonal when used to produce a rectangular grid and
3. Smaller element sizes are required for triangular elements to obtain a quality approximation

However the choice of meshing elements is also dependent on the Ω geometry, as a triangular cavity was used for validation in Balint (2001) triangular elements continue to be used for this analysis.

The 6-node quadrilateral Taylor-Hood element ($P_2 - P_1$) was used in the current formulation. These elements are characterised by the fact that pressure is continuous in Ω . The choice of nodal points allows both velocity and pressure to be continuous over the element boundaries, pressure nodes only on the vertices and velocity nodes on the vertices and mid-points. Taylor-Hood elements utilise quadratic polynomial basis functions for velocity and linear for pressure, with accuracy $O(h^3)$ for velocity and $O(h^2)$ for pressure. ($P_2 - P_1$) Taylor-Hood elements are only admissible with Dirichlet boundary conditions for velocity along the whole boundary, requiring other methods to achieve a pressure driven flow.

3.4.2 Galerkin Approximations

Galerkin (1915) proposed an elegant technique for the approximation of boundary-value problems. Galerkin's method results in a direct discretisation of the variational formulation of elliptic problems such as those described by the Navier-Stokes equations.

To illustrate the method, consider the abstract variational boundary-value problem of finding $u \in \mathfrak{U}$ such that

$$B(u, v) = l(v) \quad \text{for all } v \in \mathfrak{V} \quad (3.22)$$

Where $B(u, v)$ is a continuous bilinear form on $\mathfrak{U} \times \mathfrak{V}$, \mathfrak{U} and \mathfrak{V} being Hilbert spaces, which are vector spaces that are infinite dimensional complete inner product spaces. l is a linear function on \mathfrak{V} . Galerkin's method seeks solutions

to Eq. (3.22) when the variational problem involves only functions in certain finite-dimensional subspaces of \mathfrak{U} and \mathfrak{V} . Indeed, if

$$\mathfrak{U}_h \subset \mathfrak{U} \quad \text{and} \quad \mathfrak{V}_h \subset \mathfrak{V} \quad (3.23)$$

are two finite-dimensional subspaces of \mathfrak{U} and \mathfrak{V} , respectively then the Galerkin approximation of the solution u of Eq. (3.22) is the function $U(\mathbf{x}) \in \mathfrak{U}_h$ such that

$$B(V, U) = l(V) \quad \text{for all } V \in \mathfrak{V}_h \quad (3.24)$$

where the subscript h to these subspaces implies their properties are generally dependent on some real parameter h (such as mesh size). As h decreases, the dimensions of \mathfrak{U}_h and \mathfrak{V}_h increase and each tend to “fill up” \mathfrak{U} and \mathfrak{V} . The *quality* of the approximation U of u depends on the properties of the subspaces \mathfrak{U}_h and \mathfrak{V}_h . The finite-element concept provides a systematic method for constructing such subspaces which have several desirable properties.

Let \mathfrak{U}_h and \mathfrak{V}_h have the same dimension G . Let $\{\phi_i\}_{i=1}^G$ be a basis of \mathfrak{U}_h and $\{\psi_j\}_{j=1}^G$ be a basis of \mathfrak{V}_h . Then a solution $U \in \mathfrak{U}_h$ and $V \in \mathfrak{V}_h$ can be represented as a linear combination of the basis functions

$$U = \sum_{i=1}^G a_i \phi_i \quad \text{and} \quad V = \sum_{j=1}^G b_j \psi_j, \quad (3.25)$$

Where a_i and b_j are arbitrary. Equation (3.24) then becomes one of finding the specific collection of coefficients a_i , so that

$$B \left(\sum_{i=1}^G a_i \phi_i, \sum_{j=1}^G b_j \psi_j \right) = l \left(\sum_{j=1}^G b_j \psi_j \right) \quad (3.26)$$

or

$$\sum_{j=1}^G b_j \left[\sum_{i=1}^G a_i B(\phi_i, \psi_j) - l(\psi_j) \right] = 0 \quad (3.27)$$

With b_j arbitrary, gives a system of equations

$$\sum_{i=1}^G a_i K_{ij} = f_j \quad i = 1, 2, \dots, G \quad (3.28)$$

where K_{ij} is the stiffness matrix

$$K_{ij} = B(\phi_i, \psi_j) \quad (3.29)$$

and f_j is the forcing vector

$$f_j = l(\psi_j) \quad (3.30)$$

The stiffness matrix is bilinear on $\mathfrak{U}_h \times \mathfrak{V}_h$, and the generalised force represents a linear function on \mathfrak{V}_h . If K_{ij} is invertible, then

$$a_i = \sum_{j=1}^G K_{ij}^{-1} f_j \quad (3.31)$$

and the Galerkin approximate solution U assumes the form

$$U = \sum_{i,j=1}^G K_{ij}^{-1} f_j \phi_i \quad (3.32)$$

Often subspace \mathfrak{U}_h is referred to as the space of trial functions and \mathfrak{V}_h the space of test functions.

3.4.3 Weak form of the Navier-Stokes equations

The Navier–Stokes and Continuity equations Eqs. (3.18), (3.19) & (3.20), consist of a set of coupled, nonlinear, partial differential equations (PDE) in terms of velocity components and pressure. Thus for incompressible flow only these equations for the set of equations to be solved.

Eqs.(3.18), (3.19) & (3.20) presented in strong form, requiring evaluation of the integral which includes the highest order of derivative term in the differential equation. To yield a meaningful approximate solution to the differential equation, the integral must have non-zero finite values, requiring a trial solution that is twice differentiable and non-zero. So as to avoid these second order differentials this strong form can be transformed to obtain a weak form through integration by parts. This procedure permits trial solutions of a reduced order of differentiability to be used, for every strong formulation PDE there exists a weak formulation.

Using the constitutive equations and deformation-rate velocity relations Eqs. (3.18), (3.19) & (3.20) can be expressed compactly in terms of velocity components and pressure as shown,

$$\frac{\partial u_i}{\partial x_i} = 0 \quad (3.33)$$

$$\rho \left(\frac{\partial u_i}{\partial t} + u_j \frac{\partial u_i}{\partial x_j} \right) - \frac{\partial}{\partial x_j} \left[-p + \mu \left(\frac{\partial u_i}{\partial x_j} + \frac{\partial u_j}{\partial y_i} \right) \right] + \rho f_i = 0 \quad (3.34)$$

The next step is the formulation of the finite-element model from Eqs. (3.33) & (3.34), in which the weak forms are used to develop a natural formulation, termed *mixed model*. Where the term mixed is used as velocity variables are mixed with the force-like pressure variable, with both being retained within the single formulation Reddy (2001) and Reddy & Gartling (1994).

The weak form of Eqs. (3.33) (f_1) & (3.34) (f_2) is finalised by forming the weighted integral statements of these equations and carrying out an integration by parts. The weighted-intergral of the two equations over a typical element Ω_e are

$$\int_{\Omega_e} Q f_1 d\mathbf{x} = 0 \quad (3.35)$$

$$\int_{\Omega_e} \mathbf{w} \cdot \mathbf{f}_2 d\mathbf{x} = 0 \quad (3.36)$$

Where (Q, \mathbf{w}) are weight functions, which will be equated to the interpolation functions used for (P, \mathbf{u}) in the Rayleigh–Ritz–Galerkin finite element models.

To obtain the weak form of Eq. (3.34) integration–by–parts is used reducing the order of the resulting Eq. (3.37)

$$\int_{\Omega_e} Q \frac{\partial u_i}{\partial x_i} d\mathbf{x} = 0 \quad (3.37)$$

$$\int_{\Omega_e} \left[\rho \left(w_i \frac{\partial u_i}{\partial t} + w_i u_j \frac{\partial u_i}{\partial x_j} \right) + \frac{\partial w_i}{\partial x_j} \left(-p + \mu \left(\frac{\partial u_i}{\partial x_j} + \frac{\partial u_j}{\partial y_i} \right) \right) - \rho f_i \right] d\mathbf{x} = 0 \quad (3.38)$$

The substitution of appropriate trial functions and interpolation functions completes the development of the Rayleigh–Ritz–Galerkin finite element formulation Gresho & Sani (2000b). As these functions are restricted to the spaces of approximation functions used for the pressure and velocity fields. The dependent variables (u_i, p) can be approximated by

$$u_i(x, t) = \sum_{m=1}^{N^v} (u_i)_m(t) \psi_m(x) \quad (3.39)$$

$$P_i(x, t) = \sum_{n=1}^{N^p} (p_i)_n(t) \phi_n(x) \quad (3.40)$$

where N^v and N^p are the number of velocity and pressure nodes and $Q \approx \phi_n$, $\mathbf{w} \approx \psi_m$.

The finite element model in compact form is thus.

Continuity:

$$-\mathbf{D}^T \mathbf{u} = 0 \quad (3.41)$$

Momentum:

$$-\mathbf{M} \dot{\mathbf{u}} + \mathbf{C}(\mathbf{u}) \mathbf{u} + \mathbf{A} \mathbf{u} - \mathbf{D} \mathbf{P} = \mathbf{F} \quad (3.42)$$

where

$$\text{Mass matrix } M_{ij} = \int_{\Omega_e} \rho \Psi_i \Phi_j dx \quad (3.43)$$

$$\text{Stiffness matrix } A_{ij} = \int_{\Omega_e} \mu \frac{\Psi_i}{dx} \frac{\Phi_j}{dx} dx \quad (3.44)$$

$$\text{Advection matrix } C_{ij} = \int_{\Omega_e} \rho u_m \Psi_i \Psi_m \frac{\Phi_j}{dx} dx \quad (3.45)$$

$$\text{Coupling matrix } D_{ij} = \int_{\Omega_e} \frac{\Psi_i}{dx} \Phi_j dx \quad (3.46)$$

3.4.4 Explicit formulation

Traditionally explicit approaches suffer from a number of drawbacks. Foremost, they are only conditionally stable and the time step is limited by a Courant-Friedrichs-Lewy condition (CFL) or Δt_{cr} constraint. However, for this application where fluid and structural solvers were coupled a small time step has certain advantages. If a large time step were used this would require an additional iterative procedure facilitating the coupling to account for the potentially large motion of plate due to the increased time for motion and subsequent flow-field disruption. Thus, the explicit formulations ease of coding coupled with negating the requirement for an iterative coupling scheme between the structural and fluid solvers work to an advantage in this case.

The Navier-Stokes equations were discretised by the explicit Euler forward and used mass lumping. Detailed mathematical description of the method used can be found in many text books, for example in Reddy (2001), Bathe (1996) & Gresho & Sani (2000a) and Gresho & Sani (2000b). Combining the above results in the formulation used to model velocity and pressure conditions in a two-dimensional domain. The forcing term f is independent from velocity and pressure and is neglected in the present calculations.

Based on (a) the derived weak form of the Navier–Stokes equations, Eqs. (3.41) (f_1) & (3.42), (b) time discretisation using the conditionally absolute stable Euler Forward (Adams-Bashforth 1) scheme and (c) the Adams-Bashforth 3 based convection term Gresho & Sani (2000a) and Gresho & Sani (2000b), the final block form of the Navier–Stokes equations can be given as

$$\begin{aligned} & \begin{bmatrix} \frac{1}{Re}A + \frac{1}{\Delta t}M & 0 & -D_1 \\ 0 & \frac{1}{Re}A + \frac{1}{\Delta t}M & -D_2 \\ -D_1^T & -D_2^T & 0 \end{bmatrix} \begin{bmatrix} u_1^{n+1} \\ u_2^{n+1} \\ p^{n+1} \end{bmatrix} = \\ & \frac{1}{\Delta t} \begin{bmatrix} M & 0 & 0 \\ 0 & M & 0 \\ 0 & 0 & 0 \end{bmatrix} \begin{bmatrix} u_1^n \\ u_2^n \\ 0 \end{bmatrix} - \frac{1}{12}(23C^n - 16C^{n-1} + 5C^{n-2}) \end{aligned} \quad (3.47)$$

where Reynolds number (Re) represents suitable ρ and μ values. The convection term components, $C^q(q = n, n - 1, n - 2)$, were obtained from direct-stiffness

summation of

$$\sum_{\delta=1}^6 \left(\hat{C}_{\alpha\delta}^k \right)^q u_{g_\delta}^q \quad (3.48)$$

over k and α . The time step (Δt) used in the calculations was set only by the convection term.

The critical time step (Δt_{cr}) was found from the stability criteria (Gresho & Sani, 2000a) and (Gresho & Sani, 2000b).

$$\Delta t \leq \Delta t_{cr} = \min \left(\frac{h'_i}{u'_i} \right) \times 0.723 \times SF \quad (3.49)$$

where $SF = 0.9$ (safety factor) and

$$h'_b = \sqrt{(x_b - x_a)^2 + (y_b - y_a)^2} \quad (3.50)$$

$$u'_b = \frac{|(u_x)_b(x_b - x_a) + (u_y)_b(y_b - y_a)|}{\sqrt{(x_b - x_a)^2 + (y_b - y_a)^2}} \quad (3.51)$$

For two-dimensional channel flow, Dirichlet, or essential, boundary conditions are used, where the dependent (velocity) variables u and v are specified along the boundaries. Velocities u and v at the wall boundary nodes are zero due to the no-slip boundary condition. The velocities of the flexible-plate are purely in the y direction and are set as the v boundary conditions here. The *viscous* inlet velocity profile is parabolic based on the calculated mean inlet velocities. The inlet and exit flow has the normal flow component v set to zero. That is, at the outlet, only the x direction velocity components u exist.

3.4.5 Pressure driven

The numerical model developed uses inlet velocities as boundary conditions, most simply implemented with a constant velocity where no prior knowledge of variation exists. This arrangement of flow-driven by means of a constant velocity profile at the inlet does not reflect the actual physics of the respiratory system. During inspiration, the negative pressure generated within the lungs drives flow due to this pressure drop achieved between intra-alveolar and ambient pressure.

Thereby the velocities and respective flow rates through each channel are variables satisfying the available pressure drop. Therefore, to pursue study of this more realistic problem the development of a simple technique to adapt the existing solver to one with a rationally varying velocity was required. To this end a predictor-corrector approach was developed which predicted appropriate inlet velocities based on a Poiseuille calculation satisfying pressure drop over the domain.

The method for obtaining the inlet velocities was split into two sections satisfying the differing flow conditions. Initially a steady state solution was solved, while for subsequent time steps a transient solution was solved. Essentially the same predictor-corrector method was adopted for both flow conditions. The prediction being based on a Poiseuille flow approximation with subsequent refinement of the inlet velocities as required to achieve the desired pressure drop P_D within a prescribed tolerance. This enforcement of a temporally constant pressure drop over the domain, ensured that as the internal resistance changed with each time step so too would the mean flow rates in the upper and lower channels. Thus, at each time step the resistance of the system was evaluated and, in a self-consistent iterative procedure, determination of the mean upper and lower channel flow rates was achieved.

3.4.6 Inlet velocities for steady state solution

Finding a suitable predictor algorithm for the inlet velocities to satisfy a required pressure drop across the domain essentially entailed solving the Navier-Stokes equations for an incompressible flow given in Eqs. (3.18), (3.19) & (3.20).

However, several simplifications were made for a steady state solution as for a Poiseuille-flow approach.

- All time dependent terms = 0,
- There is no velocity gradient in the streamwise direction $\frac{\partial u}{\partial x} = \frac{\partial^2 u}{\partial x^2} = 0$,
- Flow is uniaxial $v = 0$ and
- As u does not vary in the streamwise direction, $\frac{\partial^2 u}{\partial y^2}$ becomes a total derivative $\frac{d^2 u}{dy^2}$

Integrating the resulting expression of Eqs. (3.18), (3.19) & (3.20) twice with the incorporation of the above simplifications and applying boundary conditions leads to an expression Eq. (3.52) with velocity in terms of pressure drop and channel geometry see Figure 3.4.

$$\bar{U} = \frac{P_D H^2}{12\mu L} \quad (3.52)$$

With a relation between P_D & \bar{U} derived, applying this to the geometry under consideration Fig. 3.4 was assessed. Parameters that needed to be considered included; two inlets of potentially different heights H_1 & H_2 , varying mean channel height in the flexible region and a recombination zone H_3 . Further examination of flow and pressure characteristics of this channel geometry lead to the following physical constraints.

- The flow through both inlets sum to the flow leaving $Q_1 + Q_2 = Q_3$,
- As the pressure at the tip of the flexible section is common between the upper and lower channels and the spanwise pressure gradient is small then, $P_{D1} = P_{D2}$ and
- The total pressure relation can be simplified in terms of one inlet pressure $P_D = P_{D2} + P_{D3}$

The need to account for time varying inlet channel heights H_1 & H_2 through the flexible plate region requires identification of appropriate mean channel heights. The height term in the Poiseuille equation (3.52) is squared therefore a mean height raised to this power is desirable. A summation of elemental heights H_u or H_l of dx length shown in Fig. 3.4 for the upper and lower inlets respectively was derived as, Eqs. (3.53) & (3.54) with the formulation raised to the second power faithfully incorporating plate motion, for use in the determination of suitable mean inlet velocities.

$$H_1^{SQ} = \frac{H_1}{n} \sum_{i=0}^n \frac{1}{H_{u_i}^3(x)} \quad (3.53)$$

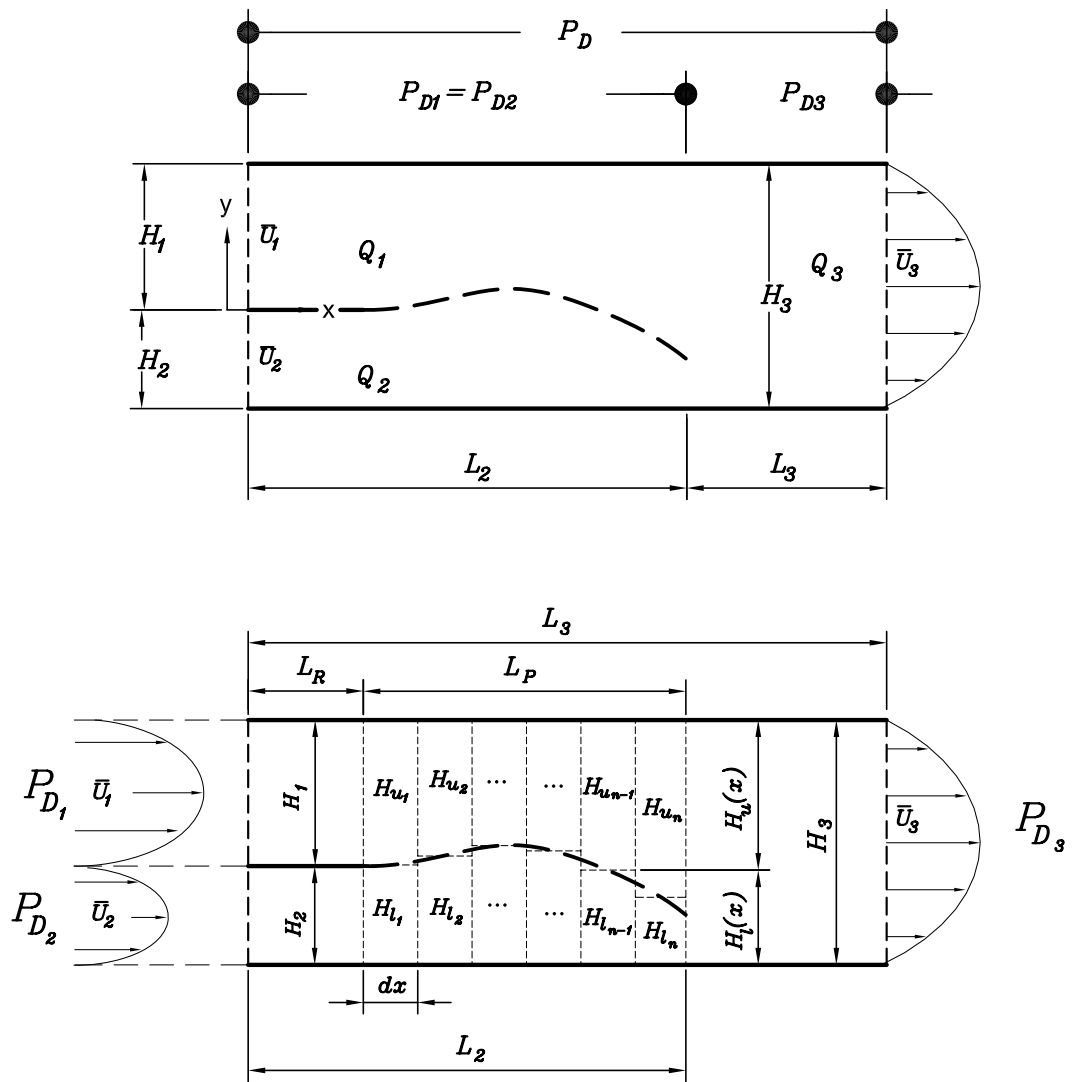


Figure 3.4: Schematic of the parameters used in the calculation of \bar{U} . Upper presents the parameters of Eq. (3.52) when split between the two inlet channels and the combined segment. Lower provides a graphic on the summation performed in Eqs. (3.53) & (3.54)

$$H_2^{SQ} = \frac{H_2}{n} \sum_{i=0}^n \frac{1}{H_{l_i}^3(x)} \quad (3.54)$$

Satisfying the above constraints and Eqs. (3.53) & (3.54) gives Eqs. (3.55) & (3.56) that predicts the inlet velocity for steady state flow conditions.

$$\bar{U}_1 = \left(\frac{H_2^{SQ}}{H_1^{SQ}} \left[(L_2 H_2^{SQ}) + \left(\frac{H_2^{SQ} L_3 H_1}{H_1^{SQ} H_3^3} \right) + \left(\frac{H_2 L_3}{H_3^3} \right) \right]^{-1} \times \left[\frac{P_D}{\mu_{12}} \right] \right) \quad (3.55)$$

$$\bar{U}_2 = \left(\left[(L_2 H_2^{SQ}) + \left(\frac{H_2^{SQ} L_3 H_1}{H_1^{SQ} H_3^3} \right) + \left(\frac{H_2 L_3}{H_3^3} \right) \right]^{-1} \times \left[\frac{P_D}{\mu_{12}} \right] \right) \quad (3.56)$$

For the initial steady state solution this approach gives a good approximation of the inlet velocities for the desired pressure drop. If the actual pressure drop did not lie within an appropriate error tolerance ($\pm 0.5\%$ for most cases) a corrector algorithm was called. A complex relationship between the individual inlet sections existed with changes in one affecting the other. This connection, while problematic, settled out after a small number of iterations. Therefore, each inlet was accounted for separately. The modification Eqs. (3.57) & (3.58) was based on the previously obtained Eqs. (3.55) & (3.56) with P_D being replaced by the respective inlet pressure error P_{error} . This result was then added to the previous inlet velocities, to give the new inlet velocity $\bar{U}_{new} = \bar{U}_{old} + \bar{U}_{mod}$. Most would achieve a solution within the appropriate error tolerance following one or two modification iterations.

$$\bar{U}_{1mod} = \left(\frac{H_2^{SQ}}{H_1^{SQ}} \left[(L_2 H_2^{SQ}) + \left(\frac{H_2^{SQ} L_3 H_1}{H_1^{SQ} H_3^3} \right) + \left(\frac{H_2 L_3}{H_3^3} \right) \right]^{-1} \times \left[\frac{P_{error_u}}{\mu_{12}} \right] \right) \quad (3.57)$$

$$\bar{U}_{2mod} = \left(\left[(L_2 H_2^{SQ}) + \left(\frac{H_2^{SQ} L_3 H_1}{H_1^{SQ} H_3^3} \right) + \left(\frac{H_2 L_3}{H_3^3} \right) \right]^{-1} \times \left[\frac{P_{error_l}}{\mu_{12}} \right] \right) \quad (3.58)$$

The initial work to formulate the corrections Eqs. (3.57) & (3.58) and determine which parameters were required used a trial solution approach. This method

allowed a number of reduced parameter models to be studied for predictions of velocity required to achieve the desired pressure drop. These were compared over a set of *test geometric parameters* chosen from configurations that had proven difficult to achieve convergence previously. The most efficient corrector was the initial parameters and in the same combination as the original Poiseuille approach, this time with the pressure used being the difference between actual and desired pressure or P_{error} for the upper and lower channel.

3.4.7 Inlet velocities for transient solution

With the initial steady state solution obtained the time was set to $t = 0$, the plate was then released the first transient flow solution obtained using the previous time step inlet velocities ($t = 0$ here). Application of the steady state Poiseuille equations, Eqs. (3.57) & (3.58) adopted above were no longer a good approximation for appropriate inlet velocities, due to the transients now being significant. Simple techniques were tested such as modifying the inlet velocities by an amount proportional to P_{error} , with poor results often being highly unstable and susceptible to non-convergence. Again a trial solution approach was adopted. These trials led to an approximate method accounting for the now significant transient factors. The trial results showed the importance of the geometric variables, especially channel height, with the general trend of predictions being accounted for well in the Poiseuille solution. However, due to the transients, now the resulting predicted inlet velocities often lead to a overshooting non-convergent iteration. Clearly a mechanism to allow some iterative damping was required. Again trials were utilised to determine the dependence of a suitable convergence time, on various geometric variables, in developing this iterative damping or the correction term. A strong link was observed between the correction required and the respective inlet channel heights. One curve was developed for symmetrically positioned flexible-plate and two others for various offset ratios ε . This led to a correction being applied to the modified portion of the velocities, allowing convergence to be achieved see, Eqs. (3.59) & (3.60).

$$\bar{U}_{1mod} = \left(\frac{\frac{H_2^{SQ}}{H_1^{SQ}} \left[\left(L_2 H_2^{SQ} \right) + \left(\frac{H_2^{SQ} L_3 H_1}{H_1^{SQ} H_3^3} \right) + \left(\frac{H_2 L_3}{H_3^3} \right) \right]^{-1} \times \left[\frac{P_{error_u}}{\mu 12} \right]}{corr} \right) \quad (3.59)$$

$$\bar{U}_{2mod} = \left(\frac{\left[\left(L_2 H_2^{SQ} \right) + \left(\frac{H_2^{SQ} L_3 H_1}{H_1^{SQ} H_3^3} \right) + \left(\frac{H_2 L_3}{H_3^3} \right) \right]^{-1} \times \left[\frac{P_{error1}}{\mu_{12}} \right]}{corr} \right) \quad (3.60)$$

One finding from this work was for an offset flexible-plate Poiseuille-flow modification for simulations were a slightly less accurate prediction than for an equivalent symmetric geometry. This was due to the increased complexity of the flow field, generating increased internal losses, resulting from the joining of two flows of differing mean velocities. Convergence times were also impacted as the larger inlet had a dominant effect on the smaller channel's pressure drop. Essentially the larger channel would need to reach the correct inlet velocity to allow the smaller channel to adjust unopposed.

Upon starting the first transient time step the determined correction was used as an initial guess. To aid in convergence times for subsequent iterations, the correction value was adjusted through a suitable algorithm. The requirement to adjust the correction was to account for other geometric variables influencing convergence times and differing flexible-plate dynamics. These included plate dynamic effects that varied over an oscillation. The correction adjustments serve to reduced solution run times from up to 15 iterations to satisfy the pressure error tolerance for a poor initial correction, to normally between 1 and 4 iterations. Of further note was that each pressure evaluation, including those within a time-step iteration, includes the fluid inertial term so the approach yields a fully dynamic solution of the governing equations.

3.5 Full coupling

This section outlines the methodology for coupling the fluid and structural solvers. The coupling comprises two components, the first was the fluid solver. The velocity and pressure fields were initialised to zero and only the inlet velocity and no-slip boundary conditions were applied. A virtual time-stepping technique was used to achieve a quasi-steady-state condition, which was calculated, based on an RMS criterion. During this iteration an initial displacement shape is prescribed to the cantilevered flexible section, which is held static during this initial phase of the calculation. Once the quasi-steady-state condition had been attained the time series was reset to zero. For subsequent time steps the fluid solver was

preceded by the structural solver. At this point the velocity and pressure fields obtained were based on inlet and boundary conditions, while the flexible-plate nodal; displacements, velocities and accelerations were set to those calculated from the structural solver. The fully-coupled nature of the model was evident from Eqs. (3.47) & (3.1).

3.5.1 Coupled fluid–structure interaction

Implementation of full coupling of the fluid and structure requires the existing fluid and structural solvers to be combined. The coupled solvers operate through an initial start-up phase, where a quasi-steady-state solution was found, there after operated in a transient mode. During coupling it was ensured that the time-averaged v nodal wall velocities, calculated in the wall code, were the same as the corresponding nodal velocities in the fluid code. The final nodal displacements from the wall code were used to re-mesh the fluid domain. The nodal acceleration values of the wall code were calculated from the time derivative of the time-averaged nodal velocity. Since the fluid code uses the same time-averaged nodal velocity values for the cantilevered plate as the ones calculated in the wall code, the nodal acceleration terms will also match. Due to the higher discretisation of the structure than the fluid the structural solver requires a smaller time step than the more computationally expensive fluid solver. To minimise run times the structure uses a smaller time step or *critical time step* T_{cr} (Bathe, 1996) as defined by,

$$T_{cr} = \frac{T_n}{10} \quad (3.61)$$

where

$$T_n = \frac{20\pi}{\beta^2 \left(\sqrt{\frac{B}{\rho_m h}} \right)} \quad (3.62)$$

and

$$\beta_n = \frac{2n-1}{2}\pi \quad n \text{ is the number of nodes} \quad (3.63)$$

To retain consistency between the fluid and structural solvers the final displacement and the time-averaged velocity for each nodal positions were used in the subsequent fluid time step. As the fluid time steps were sufficiently small no iteration between the structural and plate solvers were undertaken. For each time step ΔT the domain was re-meshed, based on the wall displacement boundary

conditions, which were obtained from the wall code. This results in a change of flow area for the affected elements, and introduces a systematic error, since the velocities are not adjusted at the displaced nodal locations. However, as the incremental change in flow areas was very small this could be neglected. For example, one time step results in a less than 0.2% flow area change.

Let us assume that at $t = 0$ (quasi-steady-state) the velocity field inside the domain was known. The cantilevered plate displacement was given from the structural solver, while the nodal plate velocities are set to zero. From this, the fluid solver can calculate the velocity and pressure fields at $t = t + \Delta t$. At this point the structural solver was called, using the nodal velocities (v), displacements (w) and transmural surface pressure ($p_{upper} - p_{lower}$) values across the plate, to calculate the new displacements and time-averaged velocities at $t = t + \Delta t$. The new nodal displacement was used to re-mesh the domain, while the velocity values were used as boundary conditions in the fluid solver. From this, the new velocity and pressure values were calculated at $t = t + 2\Delta t$, starting the time iteration loop again. The time series stops when the time reaches the end-time specified in the input file.

3.5.2 Energies

For a cantilevered plate with unit width in the transverse direction the strain (E_s), kinetic (E_k), and total ($E_t = E_s + E_k$), energies can be calculated at each time step of simulations. The dimensional energy terms were defined by the following discretised expressions:

$$E_s = \frac{1}{2}B \int \left(\frac{\partial^2 w}{\partial x^2} \right)^2 dx \approx \frac{1}{2}B \sum_{i=1}^N \left[\frac{w_{i+1} - 2w_i + w_{i-1}}{\delta x^2} \right]^2 \delta x \quad (3.64)$$

$$E_k = \frac{1}{2}\rho_m h \int \left(\frac{\partial w}{\partial t} \right)^2 dx \approx \frac{1}{2}\rho_m h \sum_{i=1}^N (\dot{w}_i)^2 \delta x \quad (3.65)$$

The work done on a plate of unit width given in discretised form is,

$$W = \int \int \left(-\Delta p \frac{\partial w}{\partial t} dx \right) dt \approx - \sum_{t_{start}}^{t_{end}} \left(\sum_{i=1}^N \Delta p_i \dot{w}_i \delta x \right) \delta t \quad (3.66)$$

3.5.3 Nondimensional analysis

Nondimensional analysis gives generality to results generated from the relatively small domain permitted within numerical limits (Douglas, 1969). Dimensional analysis also provides guidance as to which combinations of physical variables should be varied within the dimensionless parameter groups to generate results and subsequent graphical representation of the results mapping out the solution space for the FSI system. Despite the advantages of nondimensional analysis, there exists one major drawback: The need for some prior knowledge of the system to make choices as to how the dimensionless groups were formed. Aiding in this understanding of the system, a degree of trial and error was required to find situations where prior knowledge was restricted. This was required to a greater degree as the complexity of the problem increased, for example, with the addition of pressure driven boundary conditions. Some interplay was required between the numerical model and confirming the particular relations born out of the dimensional analysis as the velocity parameter was being substituted by pressure. As alluded to earlier only by working with the dimensionless scheme gives the increased knowledge of how the various physical variables relate and interact, thereby allowing some insight as to how the groups should express themselves. For a detailed derivations of the dimensionless groups see Appendix C.

The governing equations of motion for a viscous fluid are given in Eqs. (3.18), (3.19) and (3.20). By choosing appropriate length L , speed \bar{U} & time $T = \frac{L}{\bar{U}}$ scales allows the distances, velocities and times to be converted to a non-dimensional form,

$$\bar{u} = \frac{u}{\bar{U}} \quad \bar{v} = \frac{v}{\bar{U}} \quad \bar{t} = \frac{t}{\frac{L}{\bar{U}}} \quad \bar{x} = \frac{x}{L} \quad \bar{y} = \frac{y}{L} \quad (3.67)$$

Substituting Eq. (3.67) into Eqs. (3.18), (3.19) & (3.20) and simplifying gives,

$$\frac{\partial \bar{u}}{\partial t} + \bar{u} \frac{\partial \bar{u}}{\partial \bar{x}} + \bar{v} \frac{\partial \bar{u}}{\partial \bar{y}} = -\frac{\partial \bar{p}}{\partial \bar{y}} + \frac{1}{Re} \left(\frac{\partial^2 \bar{u}}{\partial \bar{x}^2} + \frac{\partial^2 \bar{u}}{\partial \bar{y}^2} \right) \quad (3.68)$$

$$\frac{\partial \bar{v}}{\partial t} + \bar{u} \frac{\partial \bar{v}}{\partial \bar{x}} + \bar{v} \frac{\partial \bar{v}}{\partial \bar{y}} = -\frac{\partial \bar{p}}{\partial \bar{y}} + \frac{1}{Re} \left(\frac{\partial^2 \bar{v}}{\partial \bar{x}^2} + \frac{\partial^2 \bar{v}}{\partial \bar{y}^2} \right) \quad (3.69)$$

$$\frac{\partial \bar{u}}{\partial \bar{x}} + \frac{\partial \bar{v}}{\partial \bar{y}} = 0 \quad (3.70)$$

$$\text{Where } \bar{p} = \frac{p}{\rho \bar{U}^2} \quad \text{and} \quad Re = \frac{\rho \bar{U} H_3}{\mu} \quad (3.71)$$

The flexible-plate equation of motion excluding the smaller nonlinear tension terms for small-amplitude oscillations is

$$\rho_m h \frac{\partial^2 w}{\partial t^2} + d \frac{\partial w}{\partial t} + B \frac{\partial^4 w}{\partial x^4} = -\delta p \quad (3.72)$$

Utilising the existing non-dimensional system with the addition of,

$$L = L_p \quad \bar{w} = \frac{w}{L_p} \quad (3.73)$$

And substituting into Eq. (3.72) and rearranging for the non-dimensional pressure \bar{p} gives,

$$\left(\frac{\rho_m h}{\rho H_3} \right) \frac{\partial^2 \bar{w}}{\partial \bar{t}^2} + \left(\frac{d}{\rho \bar{U}} \right) \frac{\partial \bar{w}}{\partial \bar{t}} + \left(\frac{B}{\rho \bar{U}^2 L_p^3} \right) \frac{\partial^4 \bar{w}}{\partial \bar{x}^4} = -\delta \bar{p} \quad (3.74)$$

Clearly the three groups of physical variables in Eq. (3.74) (within brackets) are non-dimensional parameters of the system and where these variables were drawn from shown in Figure 3.5. These three are a combination of flow and structure variables. A further non-dimensional parameter can be found in Eqs. (3.68) & (3.69) namely the Reynolds number. So far only the flexible-plate and fluid

influences have been considered. For completeness, the inclusion of channel walls and ability to asymmetrically position the flexible-plate within the flow, place further geometric control parameters on the system. Eccentricity and an aspect ratio can be accounted for as follows,

$$\varepsilon = \frac{2\kappa}{H_3} \quad \bar{H} = \frac{H_3}{L_2} \quad (3.75)$$

To account for pressure drop P_D being the physical variable driving flow rather than velocity \bar{U} one needs to perform a substitution; clearly the following appeared appropriate.

$$\bar{U} = \sqrt{\frac{P_D}{\rho}} \quad (3.76)$$

However, pressure-driven further complicates the system as for a given P_D the flow rate and hence velocity was dependent on the resistance of the channels, this resistance being a function of a number of factors see the above section on pressure driven implementation in particular Eqs. (3.55) & (3.56). In fact to adequately represent \bar{U} would require inclusion of a Poiseuille type term overly complicating and interlinking the non-dimensional terms. Hence it was necessary to maintain the use of \bar{U} though its magnitude would be revealed following completion of the simulation for an applied P_D .

Figure 3.5 shows the parameters forming the non-dimensional scheme and their origins; flexible-plate, fluid or geometric. Noting the above discussion on the relationship between \bar{U} and P_D , Figure 3.5 shows P_D under the geometric parameters as P_D in combination with the geometric variables sets the system velocity \bar{U} . The complete non-dimensional parameter set to describe the system is shown in Table 3.1 comprising one flow, three flow-structure and two geometric parameters.

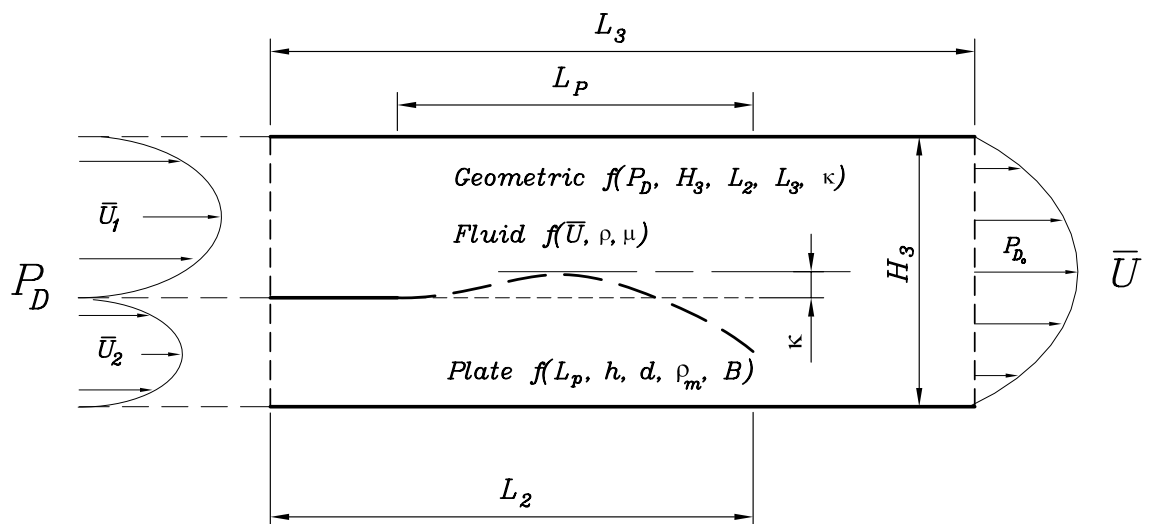


Figure 3.5: Schematic of the parameters used in the dimensionless scheme.

Table 3.1: Non-Dimensional Parameters.

Reynolds Number	$Re = \frac{\rho \bar{U} H_3}{\mu}$
Mass Ratio	$\Theta = \frac{\rho_m h}{\rho L_p}$
Damping Ratio	$\xi = \frac{d}{\rho \bar{U}}$
Stiffness Ratio	$\Gamma = \frac{B}{\rho \bar{U}^2 L_p^3}$
Eccentricity	$\varepsilon = \frac{2\kappa}{H_3}$
Aspect Ratio	$\bar{H} = \frac{H_3}{L_2}$

3.6 Geometry and Materials of the upper-airway

Prior to conducting validation it is useful to consider how the upper-airway was to be approximated in the present model. The physical problem of palatal snoring occurs during inspiration. Air is drawn into the lungs, conveyed through the upper-airway. Should a critical flow condition be reached vibrations of the soft-palate and surrounding tissue will ensue. These vibrations are the result of a fluid-structure interaction with the coupling being two-way. Two-way refers to changes in the plate geometry affecting the flow field and hence the pressure distribution on the plate which causes further motion of the plate. These motions are driven by a transfer of energy between the flow and structure. While these energy transfers can be complex over the cycle a shift of energy can be seen to the plate (amplitude growth unstable) or to the fluid (plate amplitude decay - stable) or for specially chosen cases no net transfer (neurally stable).

The medical literature indicates several physical variables associated with OSA; the length of the soft-palate, palatal stiffness and the size of the airway. Given the dimensional analysis of Section 3.5.3 perhaps these were unsurprising obser-

Table 3.2: Physical variables held constant.

Physical Variable	Constant Value	Reference
Domain length	40.5 mm	
Damping d	0 Ns/m	
Density of the plate ρ_m	1000 kg/m ³	
Elastic Modulus E	8800 Pa	(Huang, White & Malhotra, 2005)
Density of the fluid ρ	1.1774 kg/m ³	20 °C & 101 kPa
Dynamic viscosity μ	1.98×10^{-5} m ² /s	20 °C & 101 kPa
Poisson ratio ν	0.3	

vations. Dimensional analysis was crucial for this aspect of research as varying too many physical variables would lead to an array of data, where no meaningful conclusions could be drawn. Further, a sound understanding of the clinical problem informed which variables were most likely to be subject to variation and those that would remain essentially constant. The length of the soft palate was the highest order variable and scales flexural rigidity and the total height of the channel. With these relations examined, a picture forms of how subsequent testing may be carried out and what variables to vary. Of the physical variables used in the dimensional analysis to describe the problem several were assumed to remain constant. In reality these would vary little between individuals and are listed in Table 3.2 with the value assigned.

In addition to the physical variables held constant in Table 3.2 the geometric ratio of domain length to split section length (L_3/L_2) was maintained at 1.76 or all the plates ended at the same point in the channel see Figure 3.5. This was to maintain consistency as far was possible of the inlet velocities, with the pressure-driven model being sensitive to changes to this ratio. However as the P_D term was not used in the final dimensionless scheme this is of less importance as velocity \bar{U} better self accounts for these variations in geometry. The remaining physical variables were varied over a range of values selected to cover variations that could be expected in reality. The flexural rigidity B was a function of the thickness of the plate h , with values listed accordingly in Table 3.3. Only undamped compliant plates were considered in the present work.

Table 3.3: Physical variables varied.

Physical Variable	Range of Values
Total Channel Height H_3	10, 5 & 15 (mm)
Plate Thickness h	0.5, 1.0 & 0.1 (mm)
Flexural Rigidity B	8.2×10^{-7} , 1×10^{-7} & 8.2×10^{-10} (Nm ²)
Length of flexible-plate L_p	4, 6, 8, 10, 12, 14 & 16 (mm)
Pressure drop P_D	variable to solve for stability

3.6.1 Simulation Breakdown Structure

The simulation breakdown structure (SBS) refers to the coding given to each numerical experiment allowing a compact framework for referring to each case without the necessity for a lengthy relisting of parameters used. However, the simulation breakdown structure developed over a period and has several legacy non-intuitive conventions whereby the magnitude of variables does not necessarily correlate with the order of the various descriptors. Nevertheless the simulation breakdown structure was used to manage the number of combinations during the numerical simulations. The SBS code is decoded as follows;

Plate length _ Plate thickness _ 01 _ Total channel Height.

- Plate length was represented as L followed by the length in mm. In the below example L10 and L16 are 10mm and 16mm respectively.
- Plate thickness was represented as h1, h2 or h3 being 0.5, 1.0 or 0.1mm respectively.
- The 01 identifier was not used and is of no significance.
- Total channel height was represented as (Blank), H2 or H3 being 10, 5 or 15mm respectively.

To illustrate this the examples below would indicate a plate 10mm long 0.5mm thick in a channel 10mm high or 16mm long 1mm thick in a channel 15mm high respectively.

L10_h1_01

L16_h2_01_H3

The above applies to the base case in which the flow is inhalation and the compliant soft-palate positioned symmetrically. The following listing relates to the boundary conditions imposed for asymmetric and exhalation cases and are added to the above SBS codes.

- `-flow` following the SBS code indicates an exhalation case.
- `_S1` following the SBS code indicates an asymmetric case with $\varepsilon = 0.25$
- `_S2` following the SBS code indicates an asymmetric case with $\varepsilon = 0.5$

Note a `VD_` preceding the SBS code indicates the run is a velocity-driven model otherwise the solution is based on a pressure-driven approach.

Pressure drop P_D was the independent variable chosen to vary within the laminar region, to achieve a state of stable oscillation for a set of physical variables, if possible. The flexible-plate was symmetrically positioned in the flow for the bulk of research, though some indicative results were generated for asymmetric positioning.

It should be noted that no attempt was made to develop an average physical data set with, for example, palatal frequencies of 100 Hz. The approach was to choose a spread of physical parameters to appreciate how stability was affected over the problem space. The result of this leads to some extreme conditions, however, of importance was the trends away from the middle ground.

3.7 Validation

The following two Sections 3.7.1 & 3.7.2 were previously reported in Balint (2001), what follows is a summary of the validation undertaken. However Section 3.7.3 was extensively revisited and expanded in this thesis and hence reported here in greater detail.

3.7.1 Fluid code

Development of a numerical algorithm for implementation in a working code requires the algorithm's accuracy and efficiency to be demonstrated through computational experiments. One such validation method is to compare the pressure drop over the domain to that of the Poiseuille equation, for which the results were found to be in good agreement Balint (2001). Using the lower part of the 2-D split entry domain of Figure 3.1 for the pressure-driven model, typically Poiseuille equation over estimates velocities by 1-3% as the viscous effects were neglected where the two flow streams combine. The particular physical problem for which the code is to be validated against is based on one utilising similar physics for which experimental data exists. There are a wide variety of such test problems available. The following section outlines the validation cases employed by Balint (2001). It includes the triangular and rectangular cavity driver flows, backward and forward facing steps and flow around a vertical wall for laminar flow. The code development and validation addressed stokes flow before transitioning to the Navier-Stokes problem for simplicity and debugging. This included implementation of critical time step satisfying the convection term. The study included spatial and temporal convergence assessments with the comparison flow features, number of vortices and location from Reddy & Gartling (1994) being evident in each validation case. Importantly for the most demanding validation case the flow around a vertical wall as Reynolds number was increased not only were the re-circulation zones either side of the vertical wall (or fence) evident but the opposing back-flow re-circulation zone bordering the main flow stream on the downstream side was evident demonstrating the robustness of the code.

3.7.2 Flexible-plate code

In the numerical simulations of the flexible-plate code, firstly the flexible-plate was displaced using various initial eigenfunction based displacement shapes. From this plate displacement position the plate was "released", then the nodal displacement, velocity and acceleration values were calculated through the time series. The accuracy of the calculations was measured by how well the analytical and numerical solutions matched after a predefined time. A numerical prediction was considered 'accurate', if the nodal displacements matched within 1% of the

analytical solution at the end of the time series. The code was validated using fundamental *in vacuo* modes, though uniform or non-uniform damping and pressure distribution along the plate were permitted together with arbitrary initial flexible-plate displacements. Displacement cycles for the first six eigenmodes are shown in Figure 3.6, where the consecutive frequencies of vibration are also given. It was found that the results matched the analytical solutions within the 1% error tolerance.

An additional test was performed whereby plate deflections were compared to theoretical solutions for a series of idealised loading situations. These comprised uniformly distributed loads and point loads acting on the flexible-plate. The computed predictions of the displacement of the free end of the flexible plate were compared to analytical results Gere & Timoshenko (1999) Eqs. (3.77), (3.78) & (3.79), (3.80).

Tip deflection w_t for linearly decreasing pressure see Figure 3.7 (a).

$$w_t = \frac{\Delta P_0 L^4}{30EI} \quad (3.77)$$

Tip deflection w_t for linearly increasing pressure see Figure 3.7 (b).

$$w_t = \frac{11\Delta P_L L^4}{120EI} \quad (3.78)$$

Tip deflection w_t for a point pressure (acting over one element) at $\frac{L}{2}$ see Figure 3.7 (c).

$$w_t = \frac{5\Delta P_p L^3}{48EI} \quad (3.79)$$

Tip deflection w_t for uniform pressure see Figure 3.7 (d).

$$w_t = \frac{\Delta P L^4}{8EI} \quad (3.80)$$

Where; ΔP is the pressure across the plate, ΔP_0 is the maximum pressure at the fixed end, ΔP_L is the maximum pressure at the free end and ΔP_p is a point load

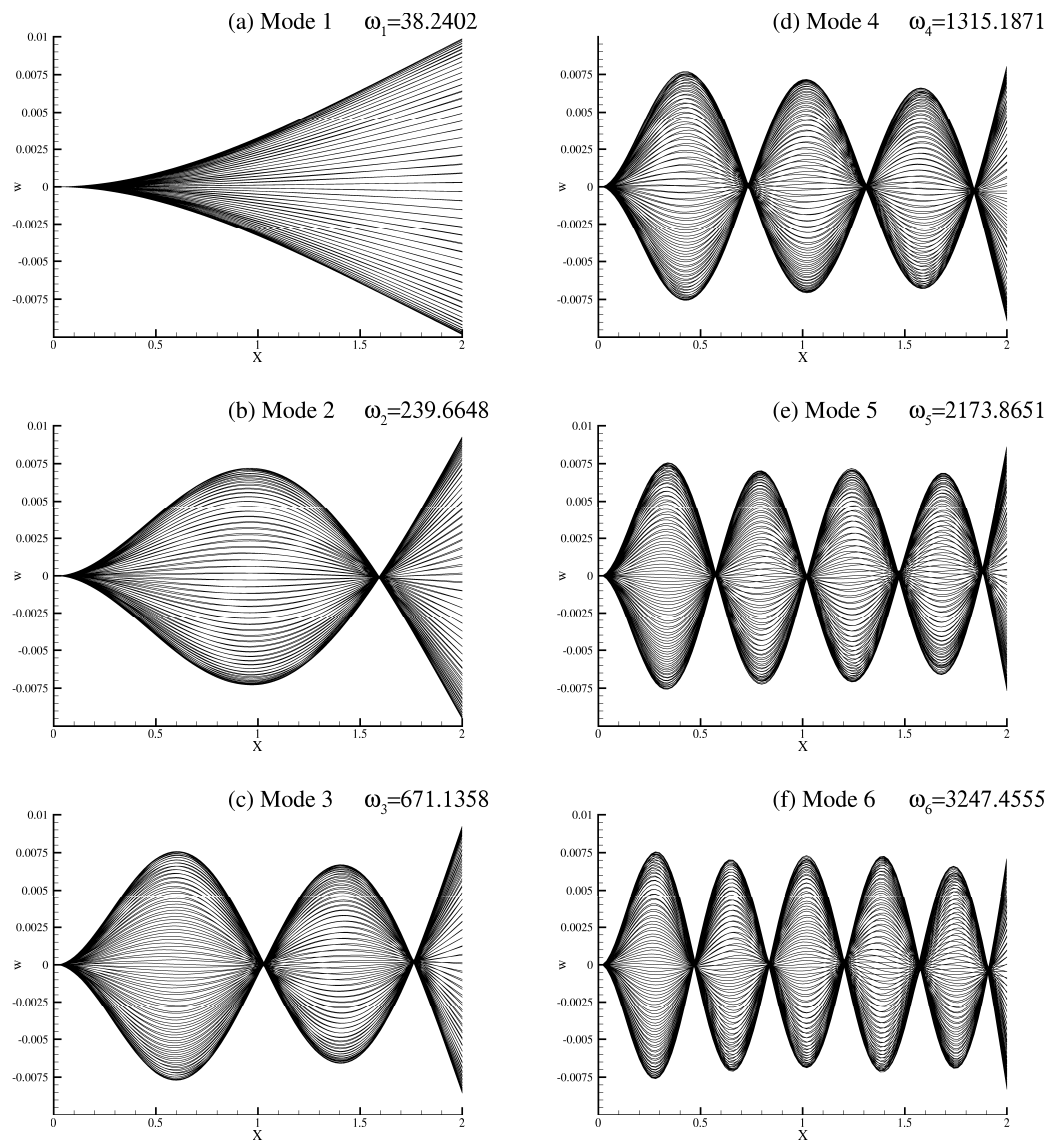


Figure 3.6: The first six mode displacement cycles of a cantilevered plate in vacuo.

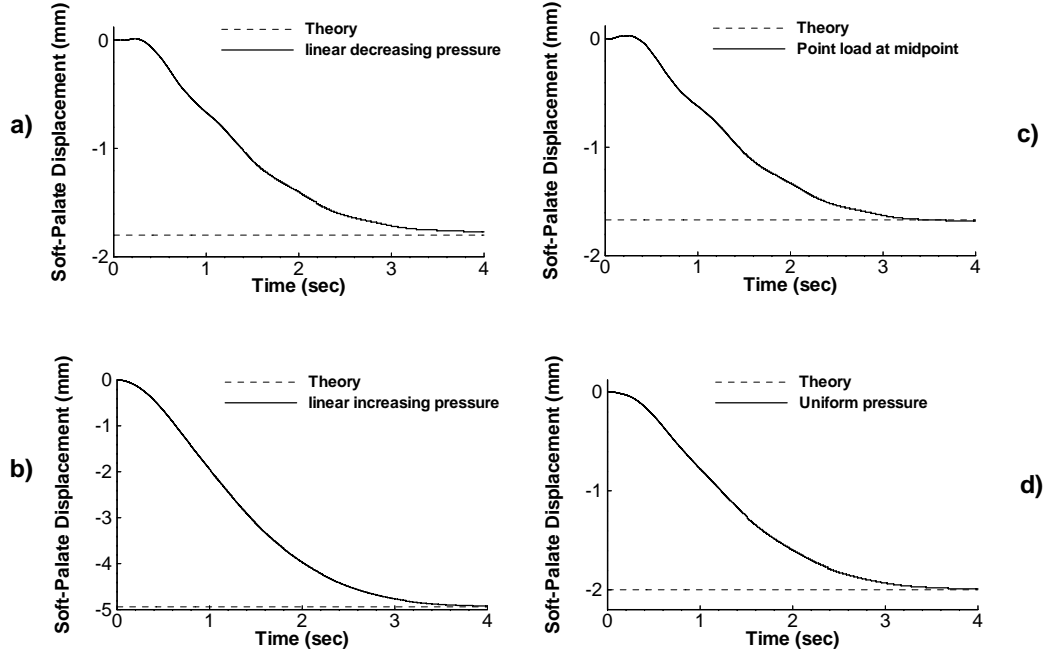


Figure 3.7: Various pressure loads and deflections of a cantilevered: a) linearly decreasing pressure $P_0 = 0.00336$ Pa, b) linearly increasing pressure $P_L = 0.00336$ Pa, c) a point load positioned at the mid point of the cantilever $P_p = 0.000017$ N, b) linearly increasing pressure $P = 0.001$ Pa.

acting over one element.

Figure 3.7 (a-d) shows the tip deflections w_t under four different loadings conditions together with the theoretical predicted results. The simulated results were within 1% of theory for each of the four loading conditions demonstrating the robustness of the code for steady state conditions. Note that damping of 1 N.s/m^3 was included to reduce run times damping oscillations around the resulting new stable deflected point. These results confirm that pressure distribution obtained from the fluid solver indeed lead to the plate deflecting in line with theory, an essential test prior to coupling the plate motion the fluid solver transients.

3.7.3 Full coupling

In addition to the work of Balint (2001) further validation was undertaken for the flow and structural solvers Sections 3.7.1 & 3.7.2. This ensured the important

features of the pressure field were correctly determined in the fluid solver and correct displacements were predicted by the structural solver. Typical validation procedures for fluid solvers can be somewhat qualitative concentrating on characteristic flow features of velocity as would be done for *inviscid* modelling. However, in this case further validation of the pressure field in a qualitative manner was possible for simple cases of Poiseuille flow and the structural solver correctly predicted natural frequencies and various external pressures loads as could be expected under coupled loading condition; see Section 3.7.2.

The fluid and structural solvers were validated separately by comparison with benchmark simulations, experimental results and analytic relations. However a further level of validation was required for the combined fluid-structure system. For this independent results either experimental or an independent computational model could be used. An independent computational model using the commercially available software ADINA R & D. Inc (2006) was chosen for independent computational simulation rather than experimental methods, for the following reasons;

- Numerical simulation has the advantage over experimental approaches that parameters could be accurately predetermined such as pressure drop and material properties where mechanical devices and real materials properties are subject to fluctuation over time
- Reduced uncertainty of external factors such as temperature differentials, wear and other issues associated with longitudinal experimental testing
- Commercial FSI solver capabilities and computational resources have increased
- Reduced uncertainty obtaining results and interpreting when the system has been simplified
- Minimal experimental resources available
- Ability to modify simulations quickly as new phenomena are encountered
- Project management issues are minimised with research not dependent on outside timetabling and competing influences

- ADINA gives a degree of reliability from being a commercial code plus can be readily validated against using standard spatial and temporal discretisation checks

To establish the accuracy of the 3-D model solution by ADINA, entailed a discretisation study where a high-resolution preliminary simulation comprising 250,000 fluid tetrahedral elements and 30,000 solid brick elements was used to approach the actual solution. Since displacements of soft-palate tip were found to be small, adaptive meshing was not needed. Accordingly, simulation run time were reduced with the level of discretisation down to 40,000 fluid plus 3,000 solid brick elements resulting with just a 3% reduction to the calculated maximum deflection of the soft-palate.

Further simulations considered the effect of assumptions that the vertical velocity component at the exit were could be adopted and also minimise the length downstream of the tip of the flexible-plate. This was also completed in ADINA repeating the investigations of Balint (2001) with an identical finding of insensitivity to this assumption with channel lengths increased by 30% to current levels.

One difficulty common to all independent testing methods was to solve the same problem in the same way. ADINA's solution method involves a period of ramp-up of the fluid load where the flexible-plate moves. Moreover, the initial displacement of the flexible-plate was not readily permitted, and would require an additional set of temporary plate loadings to impose a contoured shape, whereas, the computational method developed herein, based on Balint (2001) performed this task with the plate position fixed until a fully converged flow field solution was reached, within error constraints. Clearly, for symmetrically positioned flexible-plates where an initial prescribed position was required to obtain results, subsequent transient analysis will show little similarity.

One test where a meaningful comparison could be made was the problem of an offset flexible-plate, where the deflected steady condition reached will be independent of initial conditions. Here the boundary conditions were simplified as the plate was released from an undeflected position. While the load application procedures differed, the flexible-plate approached the new steady deflected position allowing comparisons of the interactions between the plate and fluid codes to be made.

Full coupling extends the above work from a steady state fluid interaction where the pressure exerted by the fluid on the flexible-plate was constant over time, now including the interaction where energy may be exchanged between the fluid and plate, in a spatial and temporal sense.

For the validation results flow stability calculations allowed for 100×10^{-5} second time steps in the 2-D model, which was coarser than that normally used of 5×10^{-5} seconds. Numerical simulations were run until a stable condition was reached. For the fluid code the fluid (air) density was set to $\rho = 1.1774 \text{ kg/m}^3$, based on 300 K air temperature. The corresponding dynamic and kinematic viscosities were $\mu = 1.98 \times 10^{-5} \text{ N.s/m}^2$ and $\nu = 1.68 \times 10^{-5} \text{ m}^2/\text{s}$, respectively. For the wall code the elastic modulus was set to either $E_p = 400, 800$ or 2800 N/m^2 . The Poisson ratio was $\nu = 0.3333$, the plate density was $\rho_{wall} = 1000 \text{ kg/m}^3$, with a plate thickness of $h = 0.0005 \text{ m}$ and length of plate $L_P = 17 \text{ mm}$.

Figure 3.8 (a-c) shows for each case of comparison between 2-D and 3-D of $\varepsilon = 0.33$ the 2-D tip deflections were approximately 20-25% greater than that of the 3-D mode prediction. Clearly there was a fundamental difference between the two models that needed to be accounted for to allow meaningful comparison to be made. 3-D effects account for the deflection variations between the 2-D and 3-D models, owing to side-wall effects. Here side-wall friction effects becomes an important factor influencing the pressure distribution between the split section and the combined sections. This difference results from hydraulic diameter changes between the two inlet channels and the combined section. In the 2-D model an assumption of unit width (channel 1m wide) was made. Here side-wall effects were negligible and the hydraulic diameter being more strongly a function of channel height owing to the contribution in the *Area* term, where the computation for the *Perimeter* term remains essentially constant owing to the large width contribution. The hydraulic diameter was calculated using $D_h = 4 \cdot \text{Area} / \text{Perimeter}$.

Analysis of Table (3.4) allows the differences in the hydraulic diameters to be compared between 2-D and 3-D models where $\varepsilon = 0.33$. The ratios of H_1 to H_2 between the upper and lower channel hydraulic diameters between models was around 20%, with the 2-D model having the greater flow differential. This then allows the potential for greater transmural pressure gradients in the 2-D model at $\varepsilon = 0.33$, where as the 3-D model at $\varepsilon = 0.33$ was more comparable to a 2-D

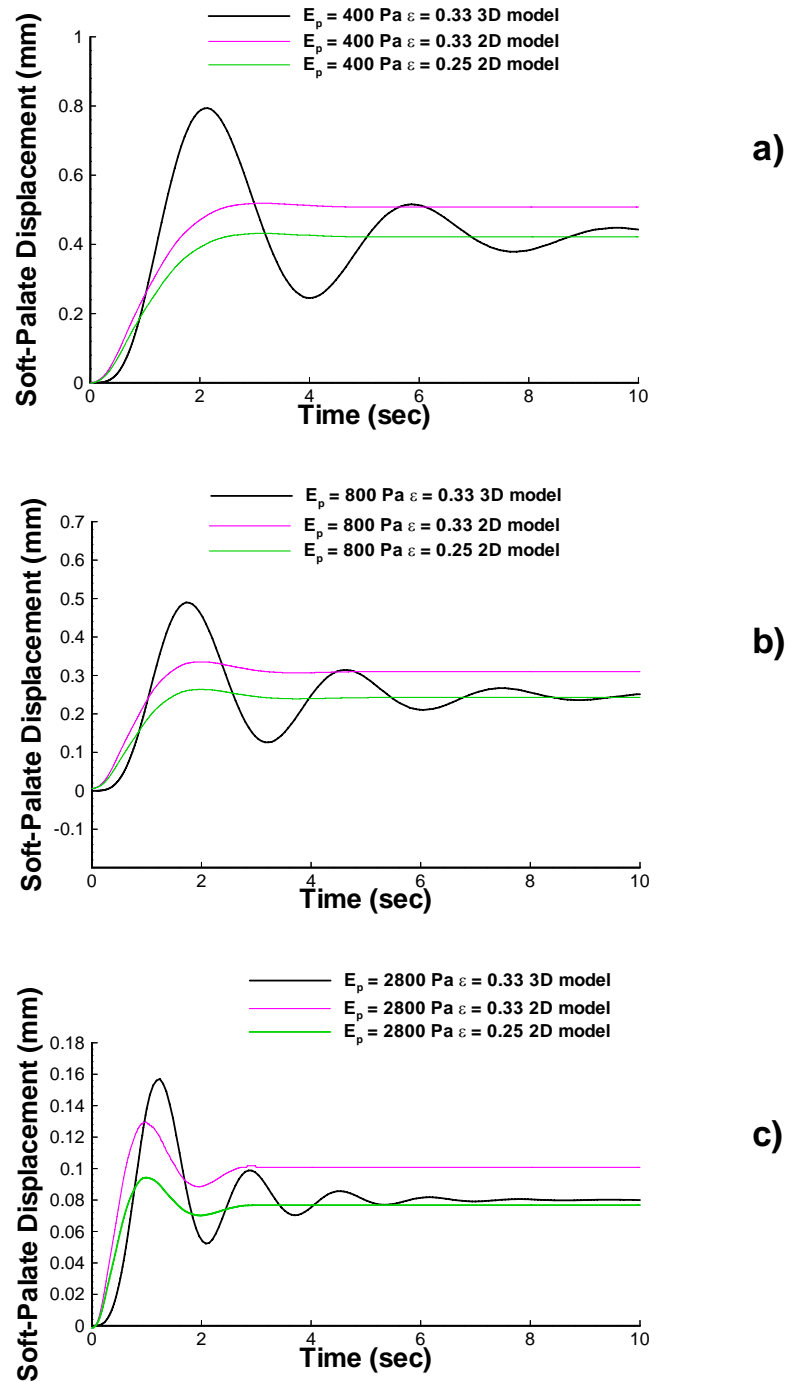


Figure 3.8: Flexible-plate tip deflections comparing 2-D and 3-D models for a range of flexible-plate E_p values: a) $E_p = 400$ Pa, b) $E_p = 800$ Pa and c) $E_p = 2800$ Pa.

Table 3.4: Hydraulic diameters a comparison between 2-D and 3-D models with $\varepsilon = 0.33$

Location	2-D model D_h (mm)	3-D model D_h (mm)
Upper channel H_1	9.5	7.2
Lower channel H_2	19.2	11.8
Combined channel H_3	28.8	15.0
Ratio of H_1 to H_2	0.49	0.61

Table 3.5: Hydraulic diameters a comparison between 2-D and 3-D models with $\varepsilon = 0.25$ and 0.33 respectively

Location	2-D model D_h (mm)	3-D model D_h (mm)
Upper channel H_1	11.2	7.2
Lower channel H_2	18.6	11.8
Combined channel H_3	29.7	15.0
Ratio of H_1 to H_2	0.60	0.61

model of $\varepsilon = 0.25$ as shown in Table. (3.5) where these ratios of H_1 to H_2 were within 2%.

Additional cases were run for the 2-D model with $\varepsilon = 0.25$ and all other parameters left unchanged. These simulations confirm this result with the deflected flexible-plate tip displacement variation, now being reduced, to less than 3% see Figure 3.8 (a-c). The dominant feature in the computation was the ratio of upper to lower channels rather than the change in downstream hydraulic diameter owing to the relative sensitivity to pressure drop in the narrower channels.

As the 2-D simulations used damping to reduce simulation run times two examples at $E_p = 400$ Pa and $E_p = 800$ Pa were conducted over a longer duration with no damping. These replicated stable motions response in the 2-D and 3-D model approaches and the frequency content was also matched. Figure 3.9 shows that while the deflections were larger in the 2-D model, which was expected from the differing initial loading conditions, frequency content was very similar. Both examples also demonstrated similar stability between the 2-D and 3-D models as far as can be determined visually.

Further validation was indirectly performed in the non-dimensional analysis Sec-

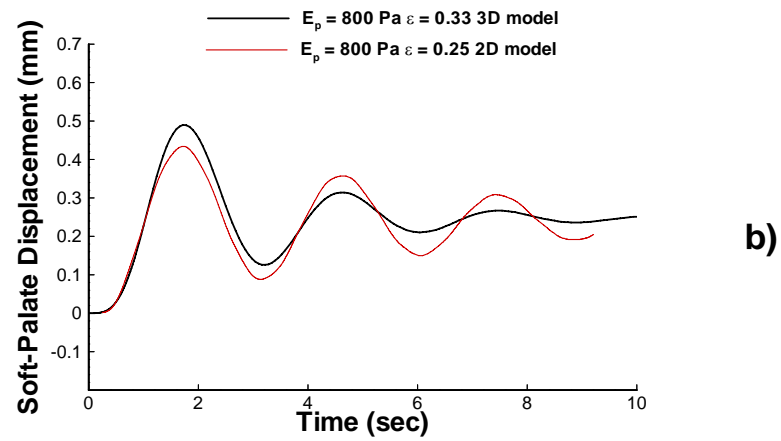
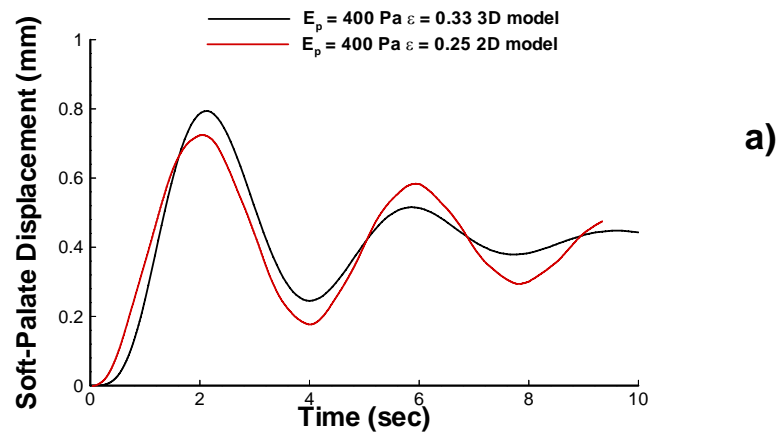


Figure 3.9: Flexible-plate tip deflections comparing 2-D and 3-D models: a) $E_p = 400 \text{ Pa}$, b) $E_p = 800 \text{ Pa}$. Note 3-D $\varepsilon = 0.33$ & 2-D $\varepsilon = 0.25$

tion 3.8.6. This section varied physical parameters producing similar dimensionless groups values, proving the dimensionless scheme for stable and unstable cases, add further confidence levels to the results obtained.

3.7.4 Boundary conditions

Owing to the similarities of the system considered in this thesis to that of collapsible tubes for example the Starling-resistor problem and studies of channels with flexible inserts Luo & Pedley (1998), Luo & Pedley (2000), Luo & Pedley (1996) & Huang *et al.* (2001) it is useful to examine the various boundary conditions adopted, for which a summary is provided. These types of problems were also sensitive to the system's boundary conditions. For a given geometric configuration and physical properties of the constituents, Luo & Pedley (2000) summarises the three sets of conditions that can be applied to such systems. It was necessary to specify any two from three parameters, these being the external pressure the difference between entry and exit, and the flow-rate through the system. In a configuration with the walls bounding the fluid domain remaining rigid the external pressure was irrelevant. This reduced complexity to just two control parameters, the pressure drop between entry and exit (P_D), and the flow-rate (or inlet velocities) through the system, one of which must be prescribed while the other being the result of the numerical simulation. The conditions applied in this thesis' pressure-driven model correspond to BC(I) in Luo & Pedley (2000) when the entry profile, but not the mean (or maximum) velocity value, was assumed. Huang *et al.* (2001) made the assumption that the external pressure applied exactly matched that due to frictional effects of the mean flow and thus yields a two-parameter system such as presented herein. Interestingly, the dual inlet problem considered in this thesis has a 2-4% additional loss above that of frictional shear stress losses. This additional loss is from the recombination of the two flow streams not present in the single channel models, which would also need to be accounted for. Huang chose to prescribe the flow-rate but recognised that the associated parallel, parabolic, profile for the total velocity could be imposed at either the entry or the exit to the channel to yield different system dynamics. Huang termed these 'blowing' and 'suction' flow conditions respectively. The description of the latter arose from the controlled action of the lungs that broadly serves to maintain constant flow from the downstream end of the tube. The

contrasting velocity-driven model Balint & Lucey (2005), also examined in this thesis, corresponds to Huang's blowing flow. The flutter illustrated in Section 3.8 comprises a coupling of first and second *in vacuo* mode effects as found in Huang *et al.* (2001). However, the pressure-driven model differs from Huang's suction-flow case that required flow leakage at its inlet when the system volume changed due to deformation of the membrane. This promoted upstream influence and Huang *et al.* (2001) showed that it caused a marked change to system instability with single-mode flutter replacing the coupled-mode flutter of the blowing-flow condition. Huang's upstream flow leakage is effectively replaced in the model developed in this thesis by the process of mean-flow re-distribution between the upper and lower channels, which occurs during oscillation of the flexible surface as the respective channel resistances vary.

The length of the rigid plate upstream of the flexible-plate, L_R , was a variable in the present investigation to ensure the channel length, L_3 , between its trailing edge and the channel exit remained uniform as L_2 was allowed to vary. For the related compliant-insert problem, Luo & Pedley (1998) showed that the latter did not exercise a qualitative effect on the system dynamics. Previous investigations of Balint & Lucey (2005) of the velocity-driven case gave the same conclusion for the present flow-structure system; the same value of L_3 was used in Balint & Lucey (2005), for which an increase of 25% generated only a 0.1% change to the fluid-loaded oscillation frequency of the flutter mode found therein. The length of the upstream rigid plate, L_R , (and external channel walls) was varied, though to ensure fully developed Poiseuille flow existed in each of the upper and lower channels a parabolic flow profile was applied at split section openings. For a channel with flexible walls, Larose & Grotberg (1997) showed that a long-wave instability exists where the boundary-layer is thin in the developing region; this can probably be associated with the divergence of compliant coatings in open flows where the boundary layer-thickness has a very significant effect on the instability as explained in Carpenter *et al.* (2001). The requirement for the minimum length of L_R was mitigated against by the imposed parabolic flow profile at inlet ensuring flow was fully developed before it reaches the flexible-plate; thus the instability of Larose & Grotberg (1997) was excluded from the system studied in this thesis.

For the pressure-driven model, parabolic profiles, were applied at entry to each of the upper and lower channels with their mean values being time dependent.

This was not a necessary constraint and could have equivalently extended the rigid-channel upstream domains and applied uniform flow profiles, thus allowing the flow to develop, but this would incur added computational cost and as such was excluded.

3.8 Results

This section commences with a review of the methodology adopted detailing the programmatic specificity concerning the numerical experiments. Variations and similarities associated with the two numerical approaches of velocity-driven and pressure-driven models are then presented. Further results for the pressure-driven model are then presented describing a wider set of numerical experiments. A range of stability cases were explored together with the effects of; asymmetric positioning of the compliant splitter insert, single channel flow and representative characteristics for inhalation verses exhalation. Findings concerning the dimensionless scheme deployed are then detailed. Completing the results is a presentation of the stability solution space for the two-dimensional problem at hand.

3.8.1 Numerical experiment methodology

In a flow field an oscillating flexible-plate generates unsteady aerodynamic forces. Fluid loading and plate responses can couple and cause phase shifts between the motion of the plate and the pressure acting on it. The velocity and the pressure of the flow affects the work done on the flexible-plate as energy exchanges between the plate and flow stream. At a critical flow speed, the work done on the plate equals the energy extracted by the flow and the plate movement neither amplifies nor decays. At flow speeds greater than this critical velocity, the energy extracted from the flow amplifies the plate movement resulting in an unstable response, flutter. At flow speeds less than the critical value the plates motion is damped and attenuated. Aerodynamic forces are a function of the applied pressure drop or velocity, fluid properties and the geometry of the system, while, elastic forces are solely dependent on the properties of the flexible-plate.

The methodology to identify the system pressure drop and hence critical velocity required for neutrally stable oscillations was an initial guess with later refinement to determine a suitable pressure drop for each case. The numerical expense of this approach was necessary in the absence of *a priori* knowledge. As will be seen later this approach can be simplified through the use of an experimentally developed stability criterion. This initial set of simulation, (the base case configuration see Figure 3.10) allowed a baseline for an appropriate pressure drop for each cases'

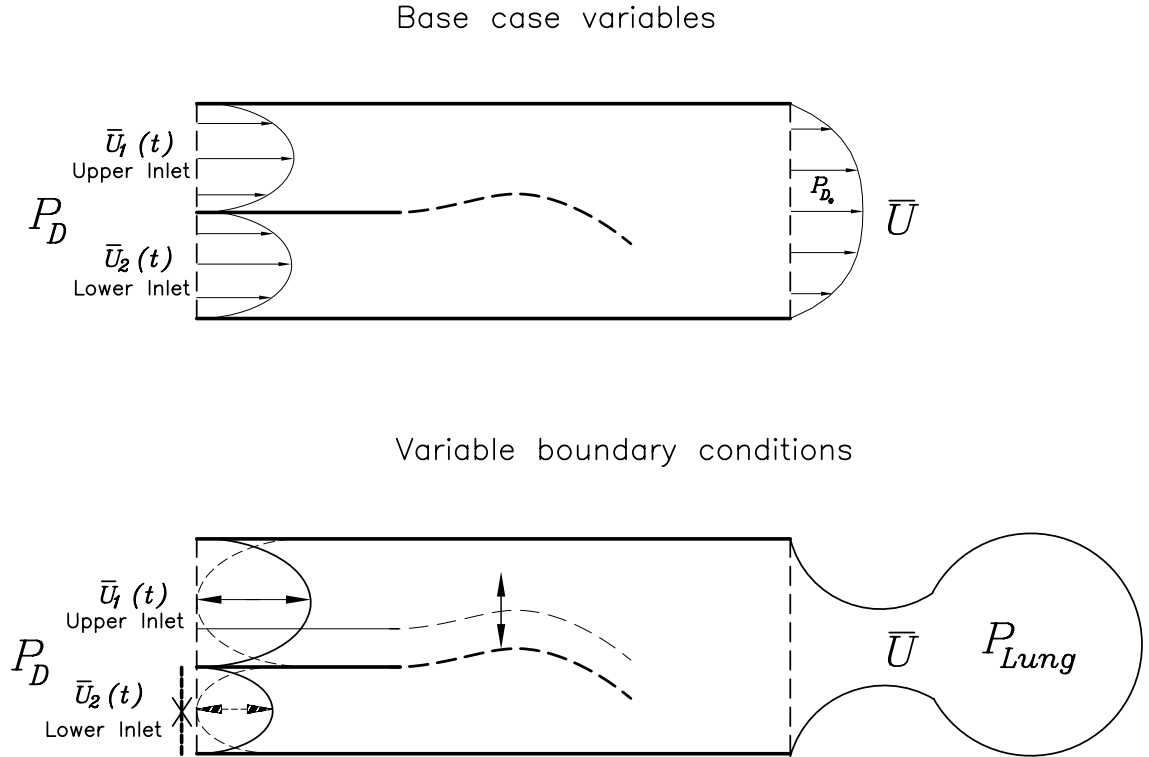


Figure 3.10: Schematic of the modelled base case and the set of variable boundary conditions that neutrally stable solutions were not sought. These boundary conditions were examined to yield relative stability compared to the base case.

stability. The base case configuration was inhalation only, with a symmetrically ($\varepsilon = 0$) positioned undamped compliant cantilevered plate or soft-palate, see Figure 3.10. During this iterative process several cases violated the laminar-flow stability regime assumption, these are presented in Appendix B. as greyed out rows, typically flexible plates with lengths less than 10 mm were within this region.

From the findings of the base case for which neutral stability was sought, the set of variable boundary conditions (see Figure 3.10) of flow direction, single channel flow and asymmetry ($\varepsilon = 0.25$ & 0.5), were explored. To avoid the additional numerical expense of iterating for individual cases stability points for these sets, the pressure drops used values based on the base case numerical experiments with some reduced by an appropriate factor to allow meaningful comparison. Clearly this approach precludes presentation of solution space stability plots for these

additional variable boundary condition cases. However, relative comparison with the base cases' stability delivers insights to how the stability region would be modified.

Further numerical experiments were developed to report the dimensionless scheme as a predictor for variations of physical parameters. Put simply, this served as a check on the dimensionless scheme ensuring that for other cases the predicted critical velocity was indeed achieved. Here individual cases' parameters were carefully modified ensuring the governing dimensionless values remained unchanged, allowing comparison of the resulting palatal responses. On completion, stored data was post-processed and typically non-dimensionalised, lending general applicability to findings presented herein where the assumptions remain valid. Appendix B. provides a detailed set of all simulations carried out and aids identification of parameters used linking through the Simulation Breakdown Structure (SBS) code as detailed in Section 3.6.1.

3.8.2 Velocity-driven versus Pressure-driven model

The results in this section present a comparison between pressure-driven and velocity-driven models. Average mass flux over the domain for the pressure-driven model was first determined through numerical experiment and was then used as the basis for inlet velocities in the velocity-driven model. Mass flux provided a quantitatively meaningful starting point to compare the two competing modelling approaches as mass flux remains relatively constant over the domain. This section highlights the potentially stark differences brought about by considering essential, real global influences, such as the breathing cycle and asymmetric positioning of the soft-palate $\varepsilon \neq 0$, on airway stability, hitherto not extensively examined in the literature.

An undamped plate L16_h2_01_H2 (a member of the base case) was used as an exemplar of stable oscillations to compare soft-palate stability for pressure versus velocity model type and three soft-palate positions. Firstly the stability characteristics of the six boundary conditions for inhalation are described followed by an examination of the exhalation dynamics.

The properties together with natural frequencies and dimensionless parameters of

Table 3.6: Comparative Pressure drop and Velocities used.

PSBS code	Value	Unit
L16_h2_01_H2	3.8	Pa
L16_h2_01_H2_S1	1.0	Pa
L16_h2_01_H2_S2	0.5	Pa
VD_L16_h2_01_H2	3.69	m/s
VD_L16_h2_01_H2_S1	1.09	m/s
VD_L16_h2_01_H2_S2	0.62	m/s

L16_h2_01_H2 are listed in Appendix B. The pressure drop P_D required for stable oscillation was found to be approximately 3.8 Pa. Table 3.6 lists the chosen values for pressure drop and prescribed velocities for each of the cases examined. The velocities were determined following completion of the pressure-driven numerical experiments as described above using the mass flux as a means of attaining standardisation between the two approaches. The split section velocity values (prescribed for inhalation or exhalation) were based on the combined end velocity from the pressure-driven case. Moreover, for offset cases $\varepsilon \neq 0$ the pressure drop P_D (for pressure-driven cases) no longer represents an attempt to approach stable oscillation conditions, but was chosen to ensure that large-amplitude unstable motions were not reached too quickly. This was a necessary departure from maintaining uniformity of boundary conditions to allow increased run times for cases with increasing values of ε and exhalation breathing conditions.

Initial soft-palate displacement conditions were identical for each case, each comprised a combination of 1st and 2nd modal content. The decision against an initial condition of a pure 1st or 2nd mode was made on the basis of the wide ranging parameter set, where an appropriate P_D for stable oscillations was being sought. The parameter set could lead to 1st or 2nd mode dominated stable oscillations over the solution space. A combination of modal content reduced simulation run times in the extreme cases as there was comparatively less modal readjustment required.

Figure 3.11 shows the tip displacement evolution of the six cases detailed in Table 3.6. Note the non-dimensional tip position is based on the undeflected neutral position and the starting value of -1 owing to the starting position being deflected into the lower channel. The neutrally stable pressure-driven base case of L16_h2_01_H2 consisted predominately of a first-mode oscillation, noting the

non-dimensional time scale is based on the period of the 2^{nd} *in vacuo* mode. Flow redistribution is evident in case L16_h2_01_H2 Figure 3.12, furthermore, flow redistribution was in phase with plate tip motion as the whole plate moves into each channel in turn. In this case the magnitude of oscillation of flow redistribution for inlet flow rates was 8% owing to the greater differential in resistances in the split channel sections. Considering the overall airway flow rate calculated at the combined end of the domain for inhalation, Figure 3.13, despite the large cross channel fluctuations seen in Figure 3.12 the overall mass flux remains essentially uniform. This steady flow rate fits well with lung function, regulating a constant flow rate as seen in tidal volume plots. The velocity-driven approach leads to a similar outcome of normalised flowrate equal to 1, though the mechanism used to achieve this could be described as suboptimal as variations to flow path resistances cannot be accounted for.

The VD_L16_h2_01_H2 case Figure 3.11 precludes this flow redistribution due to variations in split channel resistances resulting in a strongly 2^{nd} mode type oscillation, noting that for the comparative velocities representing the same mass flux as the previously discussed L16_h2_01_H2 base case though now leads to an unstable oscillation. Luo & Pedley (2000) also found this situation with stability being sensitive to the choice of either velocity or pressure-driven models. However, considering a starling resistor problem the effect was different, more stable for prescribed velocity than pressure drop, opposite to the finding herein. Of course the problem was different so this is unsurprising, though for flow reversal as will be shown late, the results align with those of Luo & Pedley (2000) as the mechanisms have a similarity in that the velocities are constant and the varying compensating pressure field has a stabilising effect. Clearly in the case VD_L16_h2_01_H2 a transition point has been reached where for $\varepsilon = 0$ a velocity-driven approach gives an underestimation of the critical velocity to achieve stable oscillations. Previous findings from Tetlow & Lucey (2009) that considered a shorter stiffer plate with $\varepsilon = 0$ concluded the velocity-driven method was an appropriate predictor for critical velocity. The difference in these findings was solely attributable to the stable mode being predominately first-mode which a velocity-driven approach fails to capture in as robust a manner as the pressure-driven model. To summarise: for 2^{nd} or higher order symmetrical stable oscillations, a velocity-driven approach yields similar results to that of pressure-driven flow. However, for first *in vacuo* mode oscillations the inability

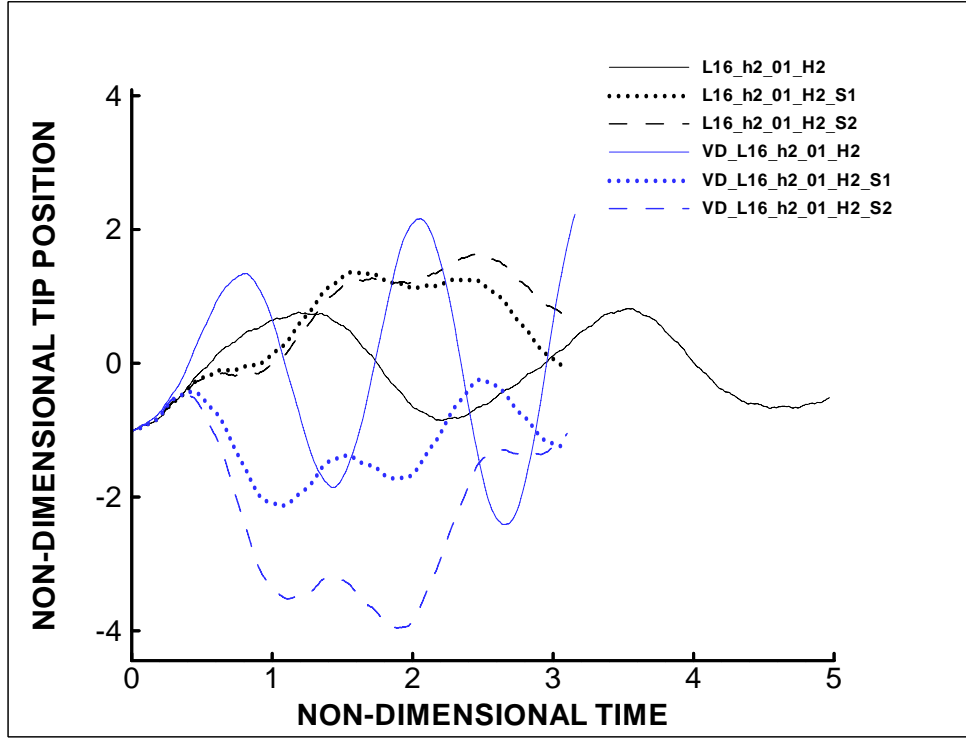


Figure 3.11: Soft-palate tip displacement pressure-driven versus velocity-driven for inhalation.

to compensate for flow redistribution, and thus velocity-driven approaches fail to capture realistic motions, and an over-estimation of energy transfer to the flexible-plate as compared with the pressure-driven methods for inhalation is the outcome.

The tip-displacement evolution with $\varepsilon \neq 0$ are considered together as clearly there is a fundamental difference between the VD_ series evolutions and the pressure-driven. L16_h2_01_H2_S1 & L16_h2_01_H2_S2 move into the upper channel whereas VD_L16_h2_01_H2_S1 & VD_L16_h2_01_H2_S2 move into the lower channel otherwise the frequency content of each were very similar after a period of modal readjustment, consistent with a subcritical stable type response. Note here the reduced P_D and inlet velocities limited the amplitudes for the offset cases.

The irreversible energy exchanges which occur between the fluid and the flexible-plate drive these motions as seen in Figure 3.14 for inhalation cases. The initial source of strain energy was the finite strain energy present in the applied deforma-

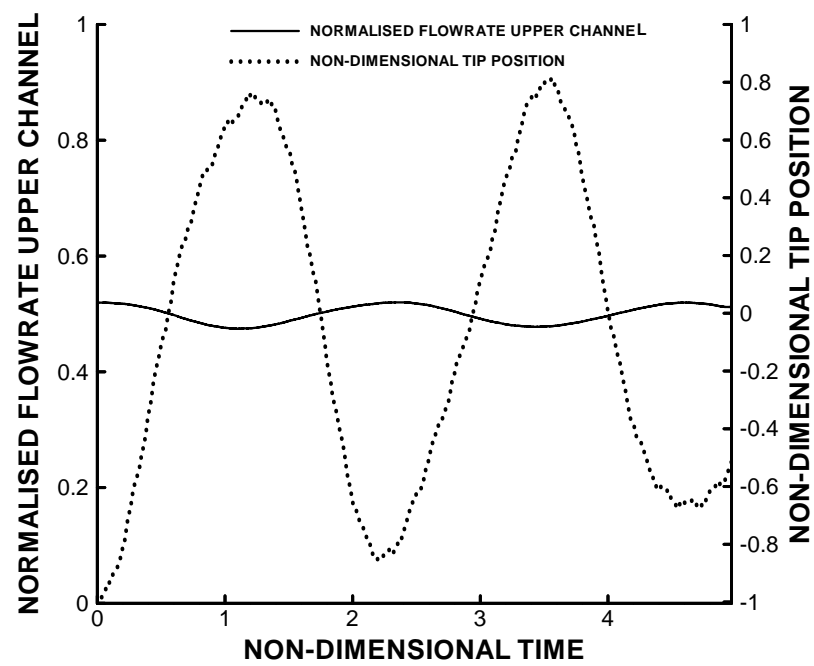


Figure 3.12: Soft-palate tip displacement and upper channel flow rate versus time for inhalation, case L16_h2.01_H2.

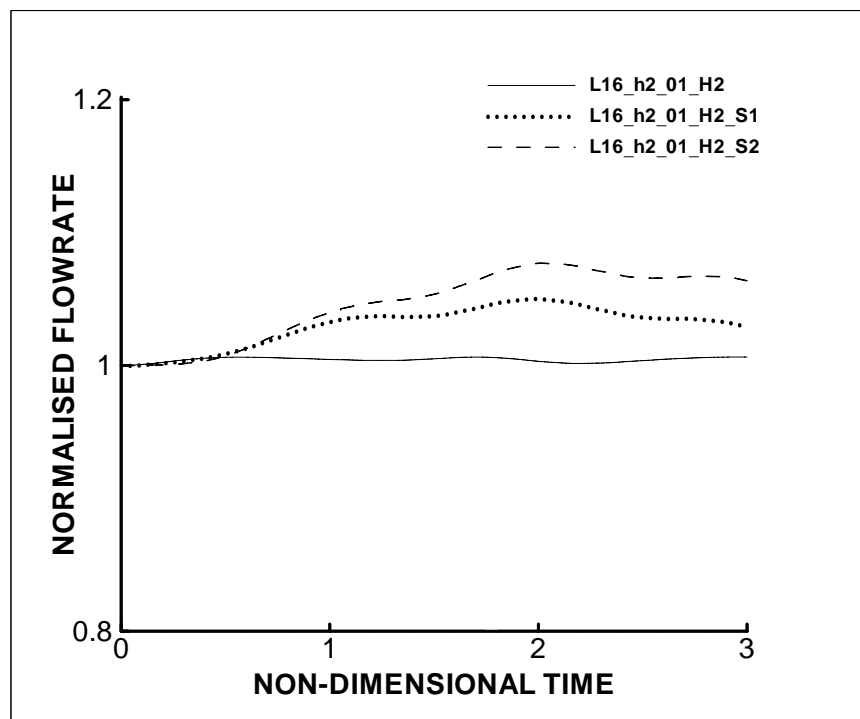


Figure 3.13: Normalised flowrate versus non-dimensional time for pressure-driven numerical simulations.

tion to the soft-palate and the basis for non-dimensionalisation. Releasing from this position within the viscous flow permitted energy gain or loss. These represent nearly neutrally stable cases with little gain or loss of energy with respect to that originally applied apart from VD_L16_h2_01_H2. Given a predominantly first-mode response was recorded for L16_h2_01_H2 and energy cycling around unity it was likely the pressure drop chosen was slightly lower than required for truly neutrally stable motion.

Tetlow & Lucey (2009) considered a more extreme comparison between the competing methods with flows well away from the point of neutrally stability. This showed the velocity-driven model predicted a greater loss of energy to the flow and thus plate oscillations were damped more quickly than for the pressure-driven model. The matching unstable comparison was also made with the velocity-driven model over-predicting energy growth, lending to the finding the velocity-driven model over-predicts the rate of energy transfer between the plate and fluid for both stable and unstable oscillation of the flexible plate when compared to the pressure-driven model.

Closer inspection of Figure 3.14 indeed demonstrates this same finding where the velocity-driven VD_L16..._S1 /& _S2 cases have a greater spread between them than that L16..._S1 /& _S2 which was the comparative case recalling that the velocities and pressure drops presented in Table 3.6 were not chosen to yield a neutrally stable response, more to limit excessive amplitude growth. Also the VD_L16..._S2 was prone to a far greater increase in energy due to modal realignment as noted by the amplitude at time 0.5 seconds, which the other cases did not exhibit.

The fundamental difference between the two competing models is highlighted through pressure plots of Figure 3.16. In these plots for L16_h2_01_H2 versus VD_L16_h2_01_H2 the essential inadequacy of the velocity-driven approached is clearly evident. The inlet pressures of the L16_h2_01_H2, series are uniform whereas, VD_L16_h2_01_H2 deviated from uniformity indicating a pressure imbalance at the inlets and across the split domain. This decreases pressure for one inlet and increases the other, maintaining constant mass flux through each split channel, while resistance varies. The colour spectra in the pressure plots represent the pressure-driven limits in this case ranging 3.8 Pa to 0 Pa. Both plots are presented with identical colour spectra, saturation beyond these values

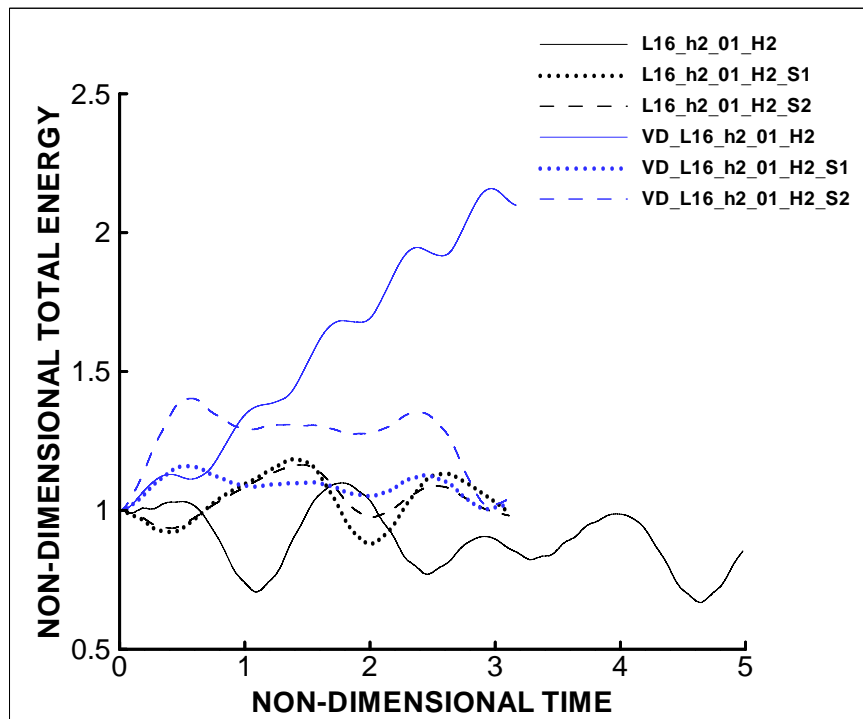


Figure 3.14: Non-dimensional total energy versus non-dimensional time for a set of inhalation cases comparing the response of the two models; pressure-driven and velocity-drive.

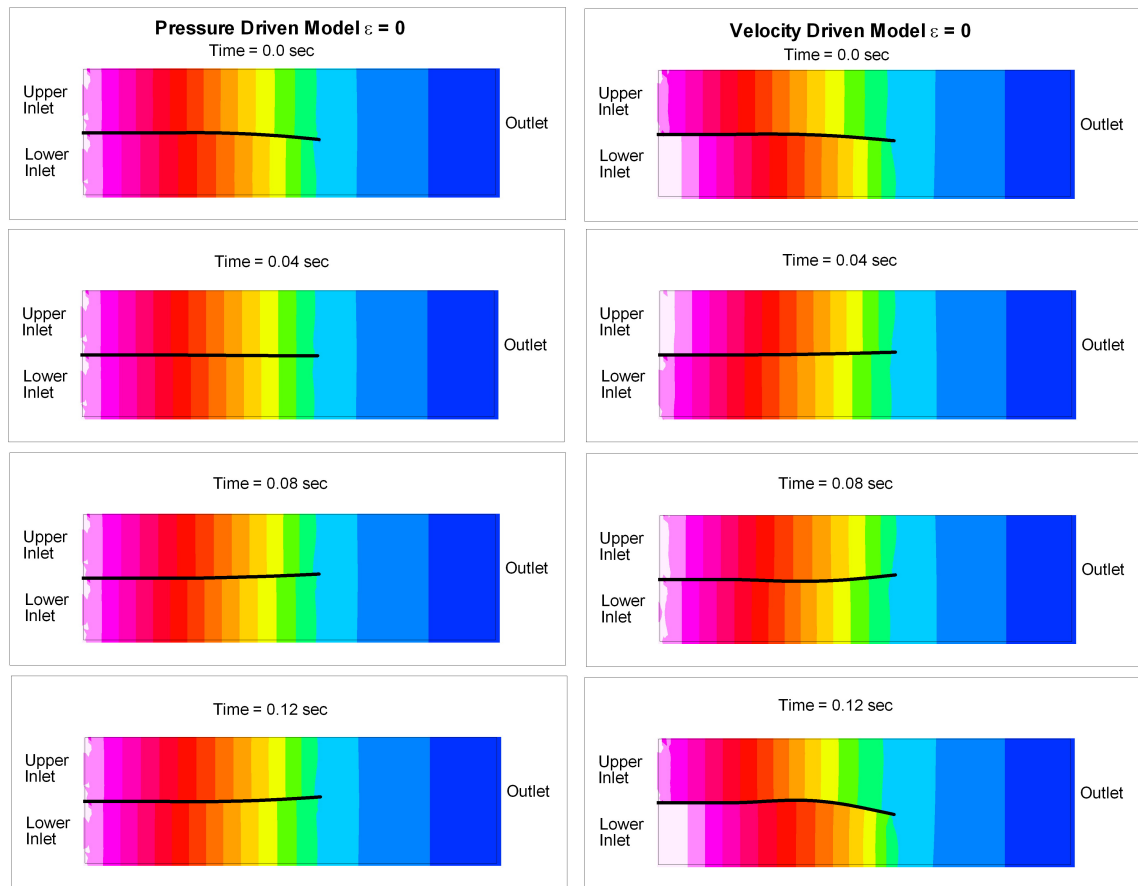


Figure 3.15: Snapshots of pressure contours during a cycle of plate oscillations. Comparison for pressure-driven versus velocity-driven models for $\varepsilon = 0$ during inhalation.

was shown as light magenta.

Reversal of flow gives further insights to the stability of the human upper-airway. To permit comparison with inhalation results, the data of Table 3.6 was used for exhalation now with `-flow` inserted into the SBS code. Figure 3.16 shows tip motion for exhalation. Note the scale for non-dimensional tip position is identical to that in Figure 3.11. Clearly the divergence type instability predicted by Guo & Paidoussis (2000) is evidenced with either motion into the upper or lower channel. Contrasting pressure-driven with velocity-driven cases leads to the following observations:

- Second-mode content was retained by the pressure-driven cases, as see from the periodic motion (albeit dominated by 1st mode content) but completely damped out in the VD_ cases, noting the tip motions track purely exponen-

tial paths

- L16_h2_01_H2-flow_S2 compared to VD_L16_h2_01_H2-flow_S2 was comparatively more stable, in fact for VD_ cases the relative stability of _S1 & _S2 appears reversed for the pressure-driven cases during the inhalation numerical simulations. However, this same effect may have been masked by a combination of initial conditions, modal realignment and choice of P_D being too close to the neutral stability point leading to an inconclusive result over the simulation interval
- Again $\varepsilon \neq 0$ cases are driven into opposite channels similar to that reported for the previous inhalation cases. However, for the same initial conditions the channel into which each was driven, reversed, to that found during the inhalation cases

The final observation is due to the breathing cycle itself exciting instability of the soft-palate. Reductions in airway size on exhalation provide a mechanism for increased obstruction on subsequent inspiratory breaths. Furthermore, this finding indicates a linkage between upper-airway occlusion and the preceding breaths, in the absence of muscular activity, damping or pharyngeal wall interaction which could have an unquantified effect ameliorating or exaggerating these effects. This finding correlates well with those reported by Woodson (2003) who explained OSA was not only implicated with inhalation, but also exhalation. Woodson reported on actual airways explaining the airway area in the region of the soft-palate was seen to be smaller during early and late expiration on obstructed, rather than non-obstructed, breaths. This fits well with the findings herein, even though only a simple 2-D geometry is considered, the effect may extend through to actual airways and be linked to Woodson's findings.

For clamped-free numerical experiments, it was recognised that variations to soft-palate initial conditions left the long-term response essentially unchanged. Plates with free-clamped end conditions, exhalation in this case, have eigenfrequencies that are conjugates of the clamped-free system as demonstrated by Guo & Paidoussis (2000) and thus for example divergence becomes possible. Moreover, the potential for either of two stable conditions exists, one for each outlet channel, being possible, given appropriately chosen initial conditions. This was demonstrated in Figure 3.16 where VD_ cases move to opposite channels purely as a function of initial conditions.

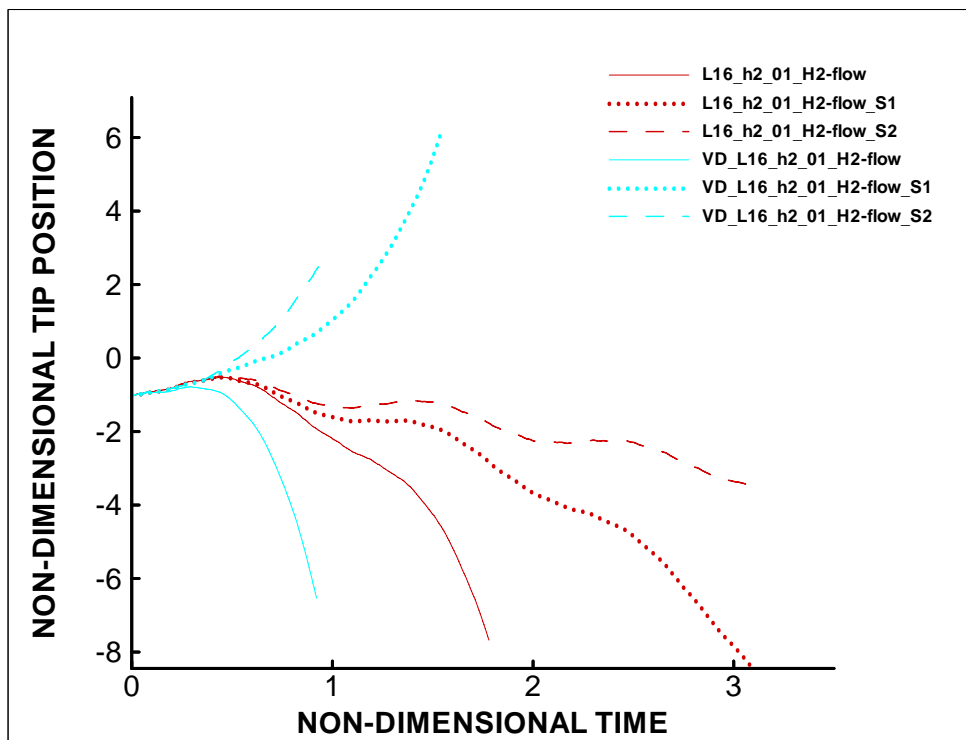


Figure 3.16: Soft-palate tip displacement pressure-driven versus velocity-driven for exhalation.

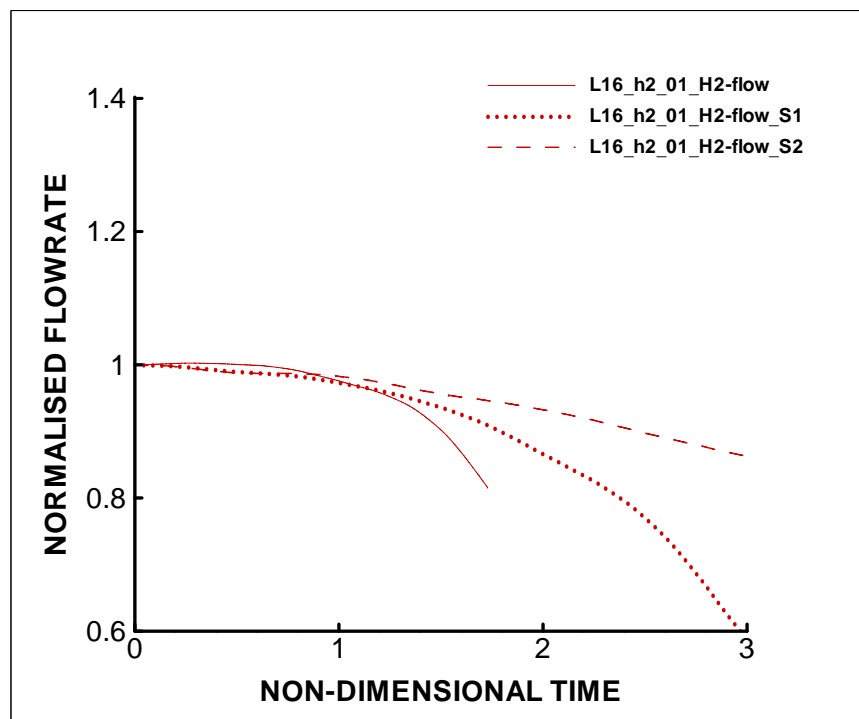


Figure 3.17: Normalised flowrate versus non-dimensional time for exhalation pressure-driven numerical simulations.

Figure 3.17 depicts normalised flowrates for the pressure-driven cases. The velocity-driven values were not shown as they remain constant throughout owing to the uniform inlet velocities inherent to the model. As overall channel resistance increased by means of predominantly first *in vacuo* mode palatal deformation there was a greater reduction in overall flowrate. Reductions correlate with tip position as shown in Figure 3.16. Of note was that during inhalation flow-rates increased with time, whereas during exhalation flow-rates decreased, indicating a tendency to move to a streamlined position during inhalation and a more restrictive position during exhalation. Should the biological system move to maintain a constant mass flux for exhalation, the required pressure drop to achieve this would be increased in relation to inhalation. This finding also tends to correlate well with the findings of Woodson (2003).

The concept of Huang *et al.* (2001) for ‘blowing’ and ‘suction’ flow conditions were useful here. However, a more faithful and realistic interpretation is developed purely considering a pressure-driven model. In simple terms ‘suction’ from the lungs relates to inhalation for the pressure-driven model and imposes tensile frictional forces through skin friction on the flexible-plate with the effect of applying a relatively constant flux out of the domain. By contrast ‘blowing’ from the lungs relates to exhalation for the pressure-driven model imposing compressive forces through skin friction on the flexible-plate. This compressive force on the flexible-plate aids buckling (divergence-type instability) ensuring higher overall resistance and thus leads to commensurately lower mass flux for a given P_D .

Figure 3.18 depicts unstable motions characterised by energy flowing from the fluid to the plate. This demonstrates that even for unstable cases, modal realignment can, for short periods, return energy to the fluid as in the case of the pressure-driven cases. However, for the VD_ cases the pressure or destabilising force content is an order of magnitude greater than the restorative forces for which the flexure term is foremost, leading to an unrelenting exponential increase. In all cases the velocity-driven approach predicts a higher transfer of energy from the fluid to the plate which was in line with the assessment made in Tetlow & Lucey (2009), though now broadened to cases where $\varepsilon \neq 0$. The pressure-driven responses were very different for each case with ε increasing and P_D reducing. There is a clear trend of relative stabilisation as the tip moved into the larger of the two channels. However this trend is not replicated in the velocity-driven cases, evidenced by the order of energy increase changing from

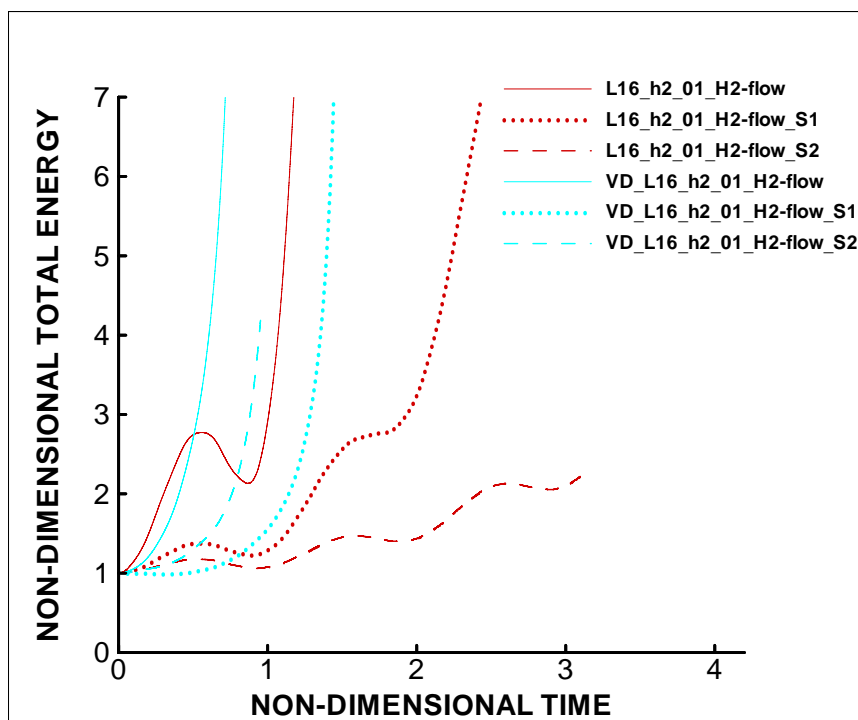


Figure 3.18: Non-dimensional total energy versus non-dimensional time for a set of exhalation cases comparing the response of the two models; pressure-driven and velocity-drive.

that of the pressure-driven result, potentially a result of sensitivity to initial conditions and rapid energy increase. These differences were a result of the tip moving into the high velocity narrow channel with the associated large transmural pressures (an essential feature ensuring constant velocity) despite the overall reductions in mass flux as ε increases.

3.8.3 Breathing cycle

An idealised breathing cycle is now considered, combining the constituent elements of inhalation and exhalation together. Idealisation is made in that the starting point for each case was not the flexible-plate deformations resulting from the previous half of the cycle. Also there was no gradual variation from inhalation to exhalation. Furthermore, the fluid-structure interaction in the upper-airway may well be dominated by complexities such as muscle tone and neuromechanical

interaction with both spatial and temporal variations, that were absent in the present modelling. Accordingly, the present study serves as an illustrative step towards the goal of obtaining understanding of soft-palate dynamics over the tidal breathing cycle. Firstly, model method variations were reviewed (pressure-driven and velocity-driven) and secondly variable stability characteristics explored. Figures; 3.19, 3.20 & 3.21 depict the variations for the cases considered previously. The figures were developed in the following configuration;

L16_h2_01_H2, VD_L16_h2_01_H2

L16_h2_01_H2-flow, VD_L16_h2_01_H2-flow

For each successive figure the value of ε increased and P_D changed according to Table 3.6 values. These figures show plate position for two time steps against a colour-contour background that represents the unsteady pressure-field. The colour spectra for the pressure plots depict the pressure-driven limits presented in Table 3.6 and are a common scale across the pressure-driven and velocity-driven plots. Saturation beyond the values of Table 3.6 were shown as light magenta or white depending on flow direction.

Figure 3.19 shows an idealised breathing cycle for $\varepsilon = 0$ comparing the predictions of pressure-driven and velocity-driven approaches. For inhalation some amplification of the flexible-plate motion was evident in the velocity-driven numerical simulation with the mode shape being principally second-mode. Comparison of exhalation amplification was evident in both cases, also noting the reduced end-time. However, both plates have a far greater contribution of first-mode content. These series highlight the oscillation of the flexible-plate brought about by alternating the flow direction. Interestingly the effect of sensitivity to initial conditions is shown in the exhalation cases, as both pressure-driven and velocity-driven models predicted deflection into the lower channel rather than opposite channels as was the case for $\varepsilon \neq 0$.

Figure 3.20 compares the predictions of pressure-driven versus velocity-driven approaches for asymmetric $\varepsilon = 0.25$ positioning of the flexible-plate. Amplification of the flexible-plate motion is not evident during inhalation with the mode shape for both being principally first-mode though the bulk motions for each were into opposite channels. For exhalation, amplification is evident in both cases again noting the reduced end-time. For this case both results show principally first-mode plate deformation due to the out-of-balance fluid forces resulting from breaking flow symmetry. Unlike the $\varepsilon = 0$ cases, the $\varepsilon = 0.25$ cases exhibit

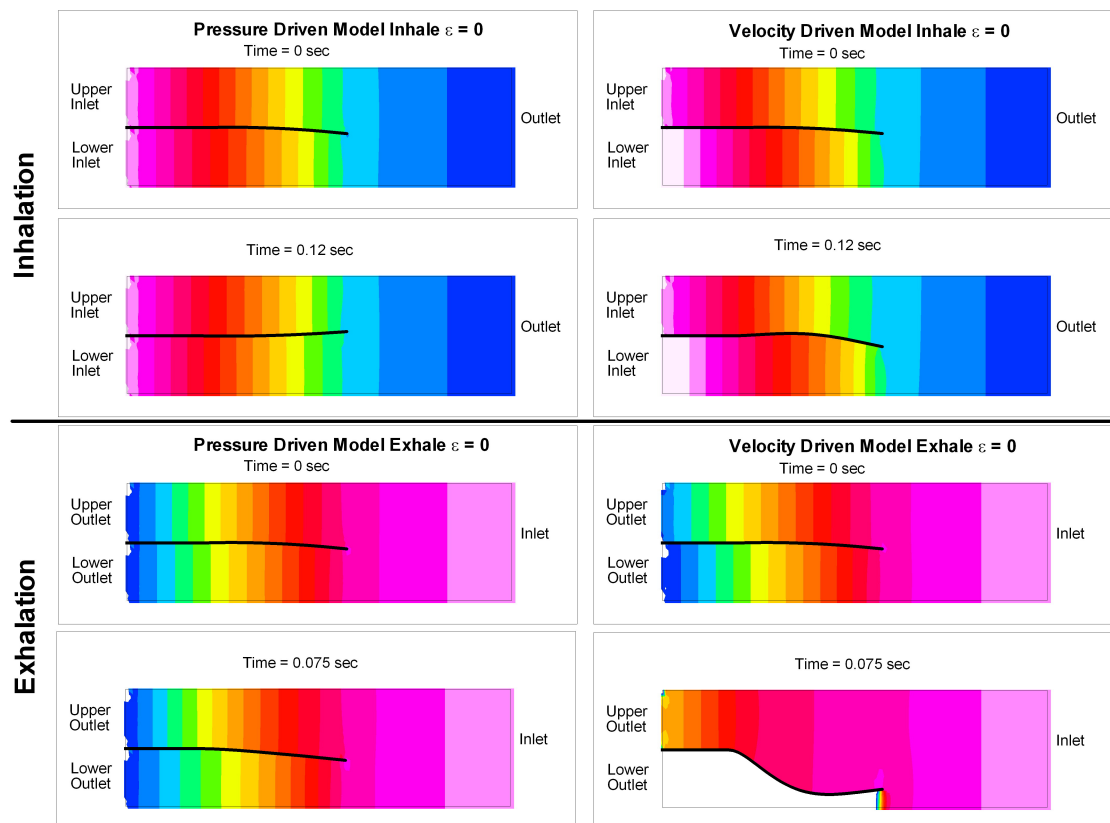


Figure 3.19: Pressure contour plot pressure-driven versus velocity-driven $\varepsilon = 0$ for inhalation and exhalation.

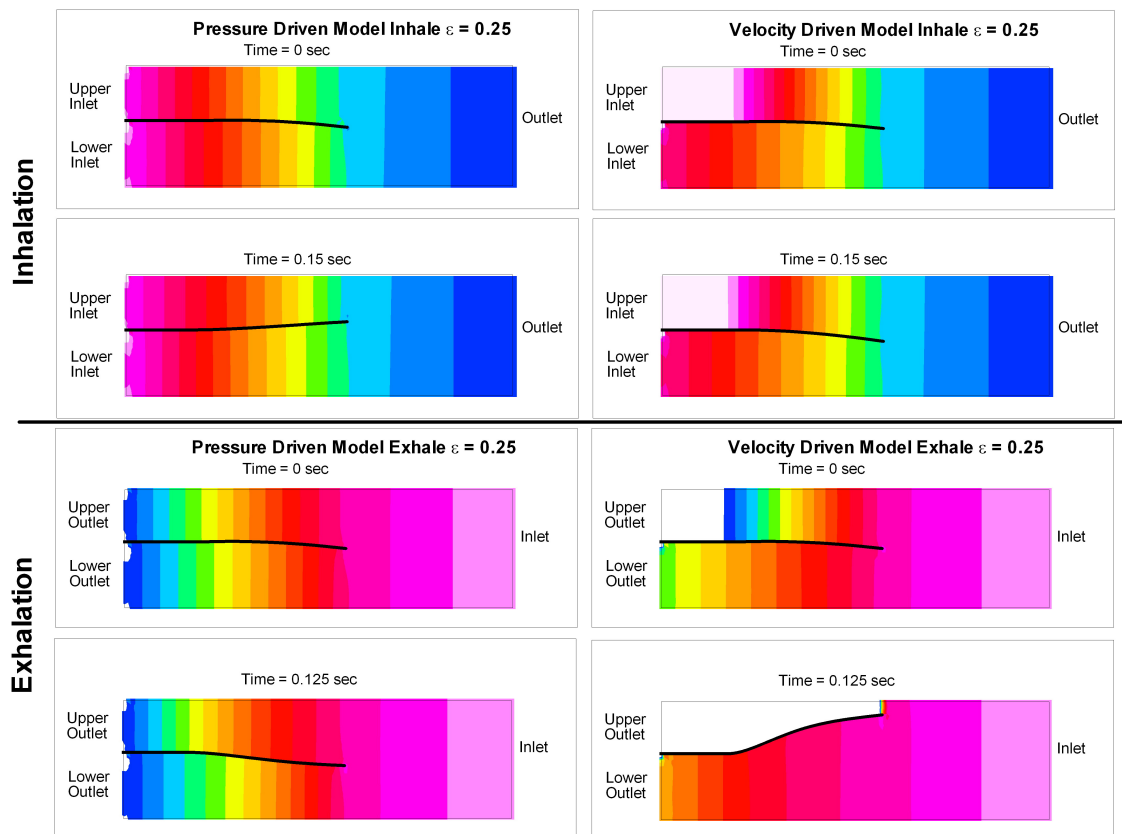


Figure 3.20: Pressure contour plot pressure-driven versus velocity-driven $\epsilon = 0.25$ for inhalation and exhalation.

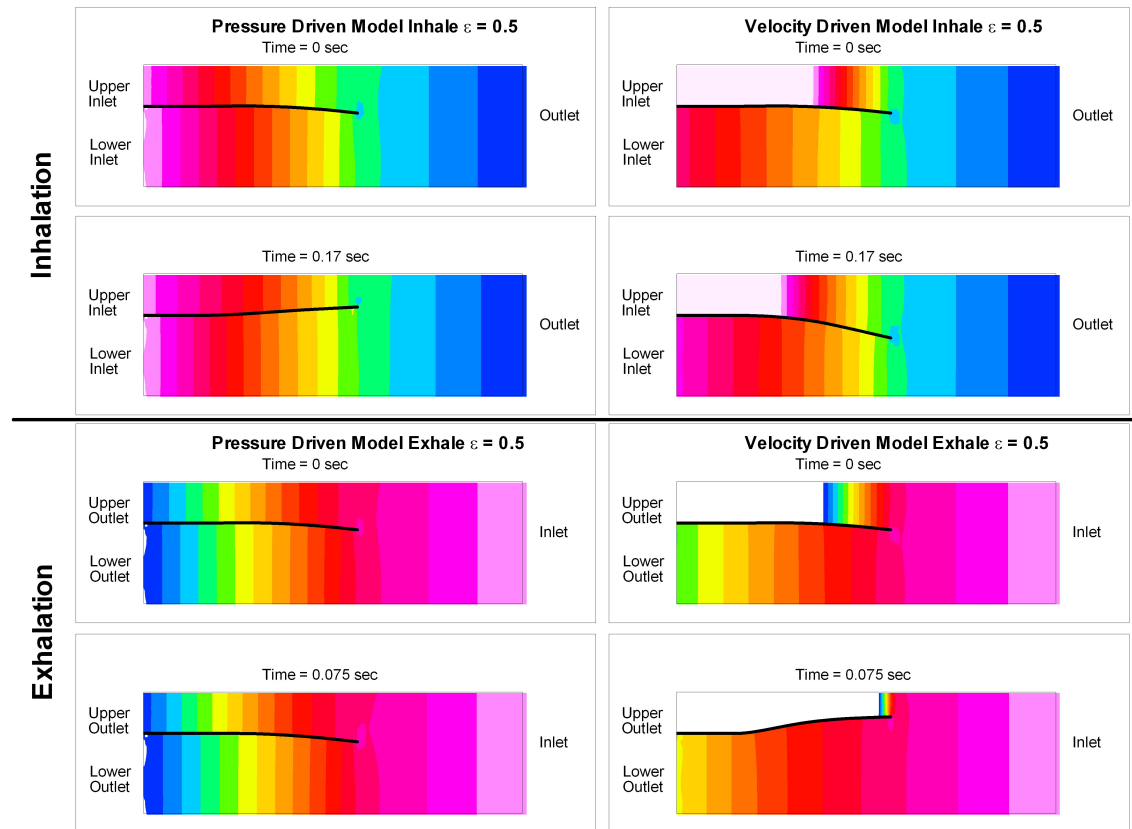


Figure 3.21: Pressure contour plot pressure-driven versus velocity-driven $\varepsilon = 0.5$ for inhalation and exhalation.

movement into opposite channels, a result of variable split channel pressures as evidenced in the very large saturated pressure areas for both the inhalation and exhalation of the velocity-driven cases. These abnormal pressures drive the motion in the velocity-driven series with the flexible-plate being deflected into the channel with the lower opening pressure (outlet or inlet depending on flow direction). The effect governing the pressure-driven motion is change in relative split section mass-flux and flow curvature effects owing to flow-field velocity changes, thereby locally lowering pressures in the case of inhalation or increasing them for the exhalation case.

Figure 3.21 produced results similar to Figure 3.20 with all trends observed for the latter applicable to the former. Note the increased region of saturated pressures at the commencement of the velocity-driven predictions compared to $\varepsilon = 0.25$ or 0.

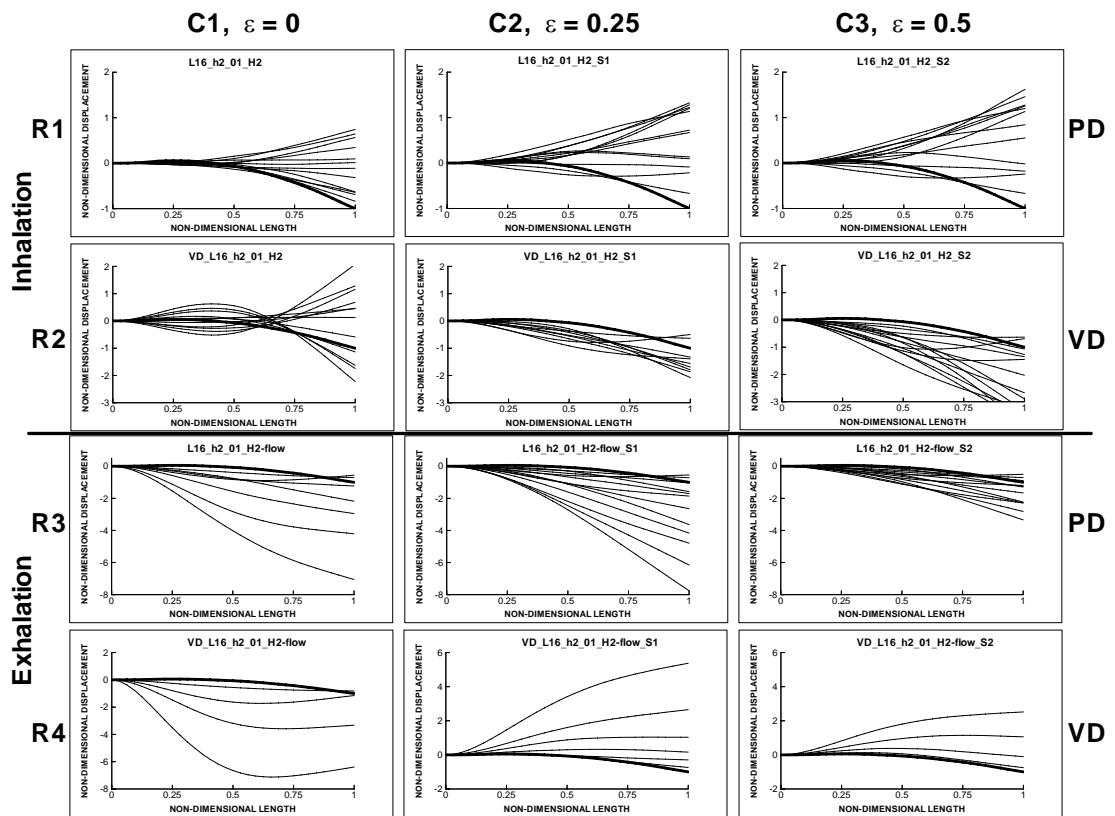


Figure 3.22: Flexible-plate oscillations, initial condition shown as the thick line with 0.02 seconds between successive snapshots of motion. Note: PD = pressure-driven model and VD = velocity-driven model, rows and columns also marked for reference. These are also consistent in the following enlarged views.

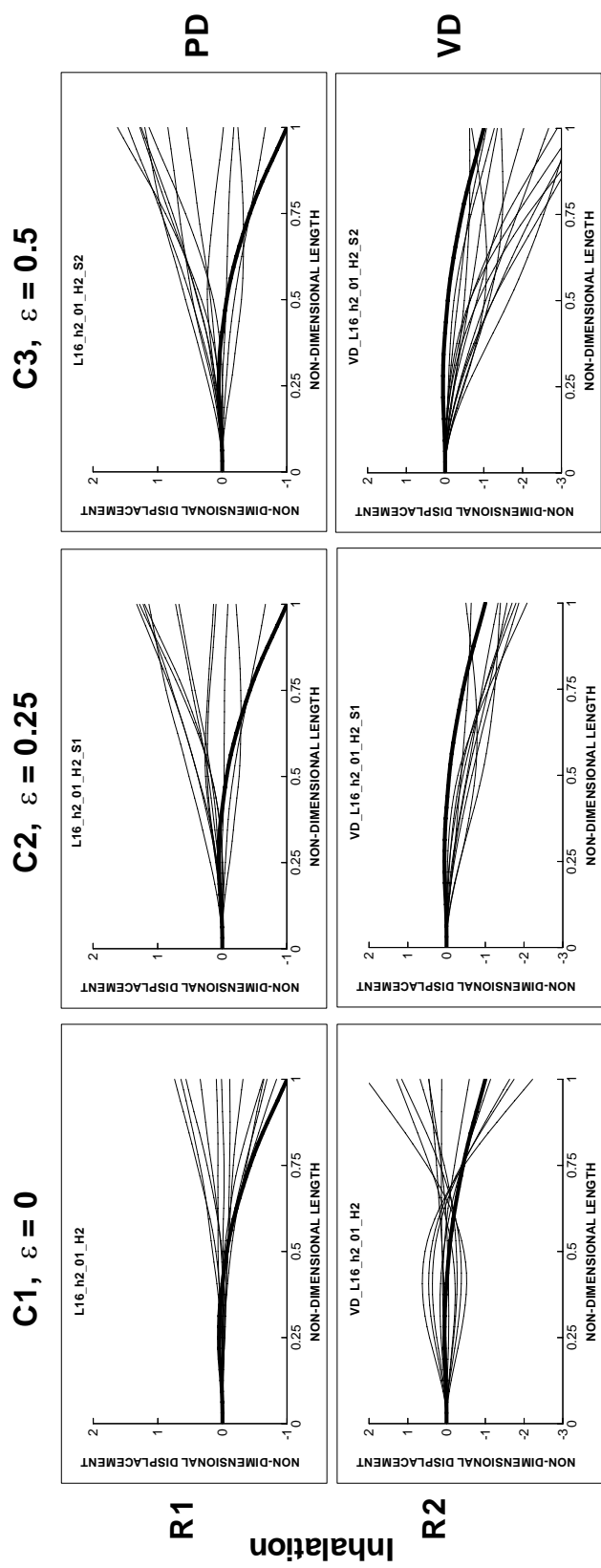


Figure 3.23: Enlarged view of Figure 3.22 showing Rows 1 and 2, Columns 1 to 3.

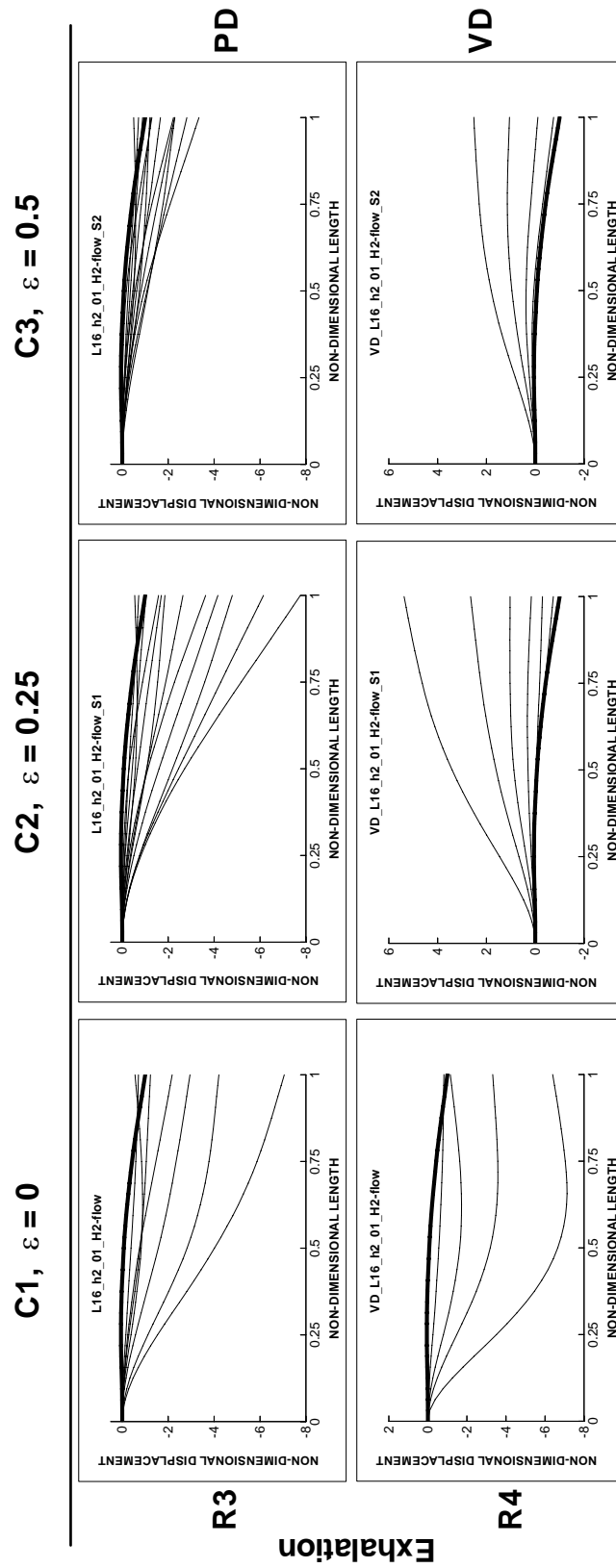


Figure 3.24: Enlarged view of Figure 3.22 showing Rows 3 and 4, Columns 1 to 3.

Figure 3.22, together with sub-Figures 3.23 and 3.24, show flexible-plate oscillations through a number of snapshots at uniform time gaps, of 0.02 seconds between successive plate position updates. This depicts modal content and gives an indication of relative rates of motion. The first column relates to $\varepsilon = 0$ cases. Note the displacement scales change from row to row and not all data points are recorded for the divergence type instabilities though this was accounted for by the reduced number of plate response updates.

Note: Data that is presented in a tabular figure format, have row and column numbering included. This provides for comparison of a number of cases and are also included in sub-figures. A row, column convention has been adopted to communicate locations within these tabular figures, for example, [R2, C1] refers to row 2, column 1 of the figure or sub-figure in question.

The centre column of Figure 3.22, 3.23 and 3.24 shows flexible-plate oscillations for $\varepsilon = 0.25$. Here dominant first-mode content is evident for all cases, though VD_L16_h2_01_H2_S1 [Row 2, column 2 or R2, C2] exhibits a remnant of second-mode content. Unlike the $\varepsilon = 0$ cases the $\varepsilon = 0.25$ cases [R3, C2 & R4, C2] exhibit movement into opposite channels, and the mode shape to be dominated by first-mode content.

The right column of Figure 3.22 shows flexible-plate oscillations $\varepsilon = 0.5$. Comparison of $\varepsilon = 0, 0.25$ & 0.5 for each case (Row) shows that in relative terms for inhalation [R1 & R2], peak flexible-plate tip amplitudes increased as $\varepsilon > 0$, while P_D values decreased. For exhalation [R3 & R4], peak flexible-plate tip amplitudes decreased as $\varepsilon > 0$. For visual comparison Figure 3.22 presents sub-figures within each row using the same ordinate scale to allow comparison.

3.8.4 Expanded pressure-driven model

Figure 3.25, together with sub-figures 3.26 and 3.27, further develops insights into the usefulness of the pressure-driven model accounting for mean-flow redistribution between the upper and lower channels, one aspect not fully developed in relationship to OSA. Variations of aspect ratio, eccentricity ε , flow direction and flexible-plate parameters, were explored to provide characteristics for comparison between limiting or extreme cases. Note, that the figure does not use

constant scales between plots as the overall responses were of primary interest for this section.

Figure 3.25, shows a series of cases comparing inhalation versus exhalation. [R1-2, C1-3] a for a single base case L12_h3_01_H3 with eccentricity increasing from left to right. A set of cases with varied parameter are shown in [R3-4, C1-3] where the responses show a more even balance between structural and fluid forces where palatal oscillations are retained for a longer period.

Row 1 of Figure 3.25 and sub-figure 3.26, shows ε increasing offset from left to right. This change in ε has the effect of dividing the mass flux unequally between the channels, biasing towards the large channel in line with the governing physics, the channel with least hydraulic resistance. The change is stark from evenly balanced [R1, C1] to almost entirely through the lower channel [R1, C3]. Also note the relative change in mass flux through the upper and lower channels versus tip position, while the magnitude change is small, flow increases with deflection of the plate tip into the upper smaller channel.

Row 2 of Figure 3.25 and sub-figure 3.26 is identical to Row 1 apart from the flow direction being reversed from inhalation to exhalation. The difference is the plate now deflects into the lower, larger channel, for $\varepsilon \neq 0$, the mass flux now decreases at an accelerated rate with plate tip deflection when compared to those of Row 1. Comparing the scales for tip position [R1, C3] versus [R2, C3], the latter deflection were around half the rate of the former. When relating these findings to actual breathing at a constant mass flux, during inhalation effort could be reduced whereas for exhalation, increased effort would be required which would lead to increased deflection of the soft-palate.

Rows 3 & 4 Figure 3.25 and sub-figure 3.27 present similar content though present different parameters for comparison. [R3, C1] contains an interesting mass flux distribution owing to particular mode containing some 3^{rd} order content as the plate passes its neutral axis, disrupting the normal channel crossover point at the inflection points of the plate tip position plot. The remaining plots [R3 & 4, C2 & 3] showed similar responses to those preceding, however, [R3 & 4, C3] oscillatory motion is maintained rather than being damped out due to the increased channel heights and stiffness of these plates.

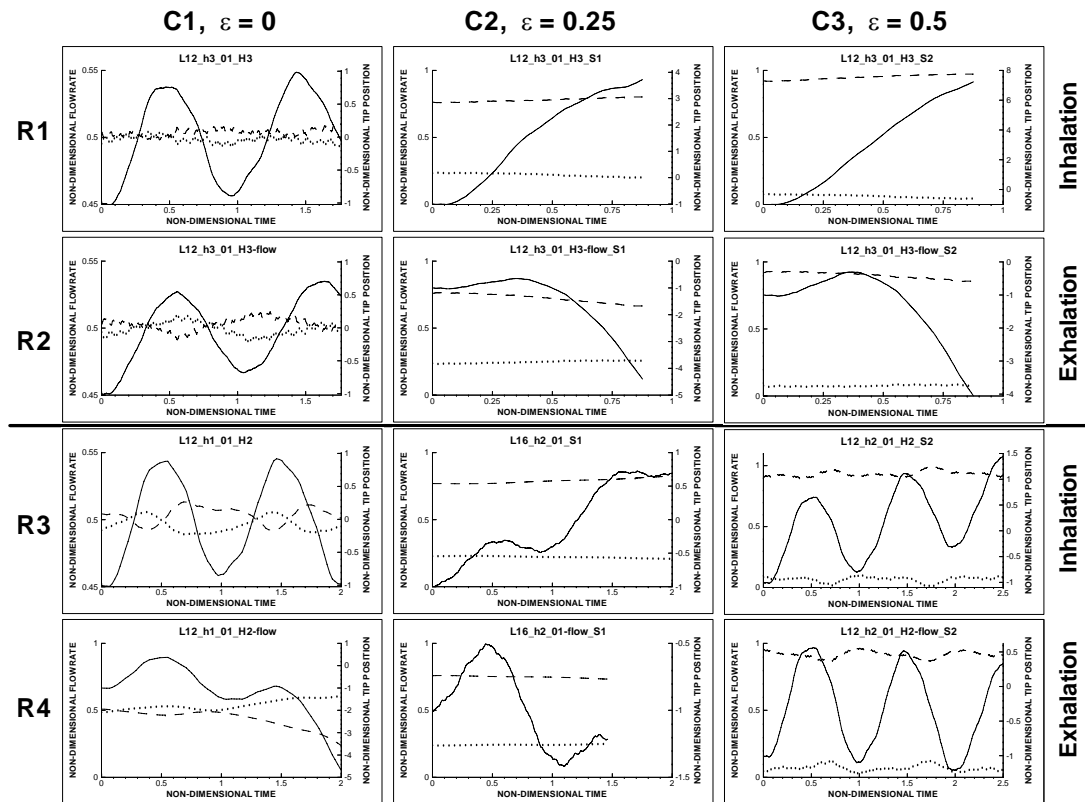


Figure 3.25: Split section Mass flux with flexible-plate tip position versus time for inhalation for a variety of cases comparing inhalation and exhalation. Plate tip position solid line, Lower channel flowrate dashed line, Upper channel flow rate dotted line.

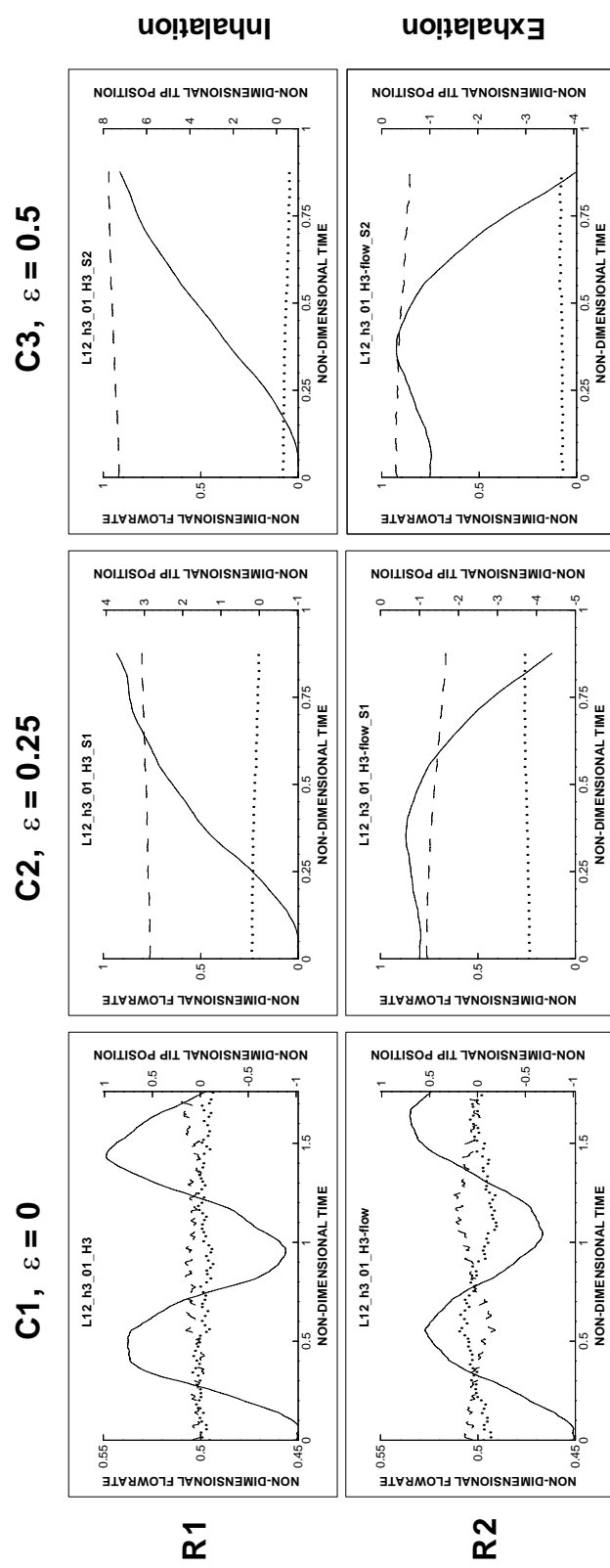


Figure 3.26: Enlarged view of Figure 3.25 showing Rows 1 and 2, Columns 1 to 3.

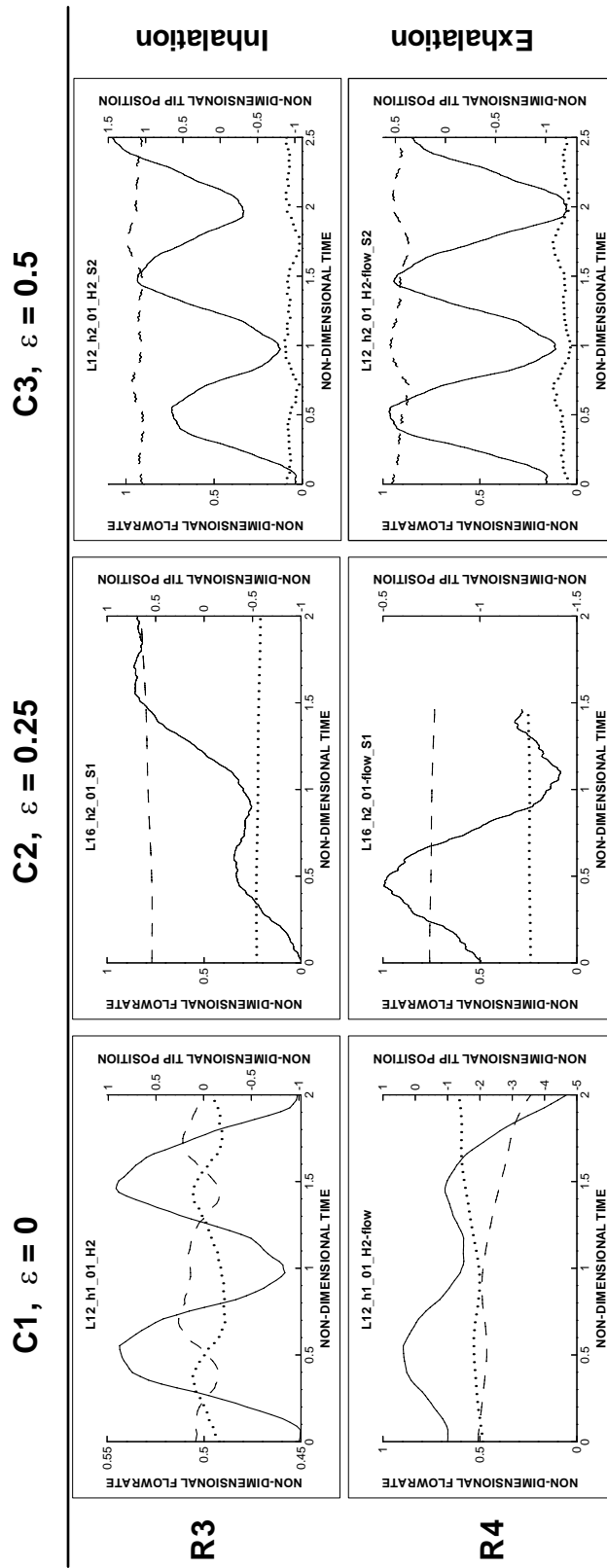


Figure 3.27: Enlarged view of Figure 3.25 showing Rows 3 and 4, Columns 1 to 3.

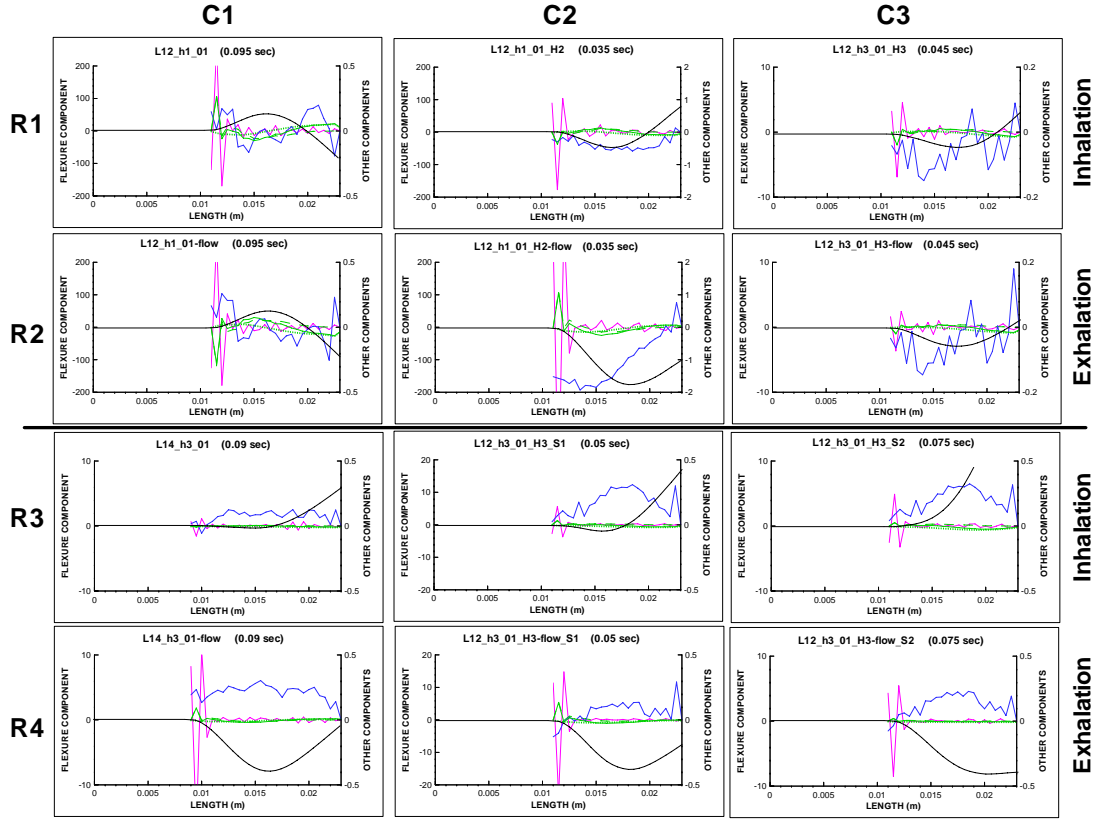


Figure 3.28: Contributions of thin plate equation terms Eq. (3.1) presented for a number of cases. These show one time step with nodal contributions distributed along the flexible-plate. The flexible-plate position displayed in solid black, the flexural rigidity term $B\nabla^4 w$ solid magenta, the $\frac{\partial T}{\partial x} \frac{\partial w}{\partial x}$ component of tension green dashed, the $T\nabla^2 w$ component of tension green dotted and the total tension term $\frac{\partial}{\partial x} (T \frac{\partial w}{\partial x})$ solid green, with the pressure term δp_m presented in solid blue.

Effect of structural and fluid-loading terms

Figure 3.28 captures the essential features of the 1-D plate equation Eq. (3.1). Here by considering one time-step and the nodewise contributions from the flexure term $B\nabla^4 w$ (scale on the LHS axis) and tension term $\frac{\partial}{\partial x} (T \frac{\partial w}{\partial x})$ including the contributions from the two components $\frac{\partial T}{\partial x} \frac{\partial w}{\partial x}$ & $T\nabla^2 w$ and pressure (on the RHS axis) the energy imbalance may be visualised. The remaining acceleration term not shown permits transfer to the fluid. In each case plots for a single time step are presented, the flexible-plate shape overlaid, shown in black.

Plots were chosen to cover a range of parameter variability from relatively stiff to

flexible plates, flow direction and channel heights, thereby giving an insight into some of the fundamental mechanisms associated with stability and instability. These individual time steps were principally characterised by a dominant temporal and spatial flexural rigidity contribution. However, as a general comment the flexure contribution tends to have a balanced contribution whereas the tension and pressure terms tend to have a net contribution rather than being evenly balanced, albeit at a reduced magnitude. The two components of the tension term were, as expected, minor for individual time steps and had a moderating effect on each other being opposite in magnitude. The pressure profile varied rapidly between time steps being dependent on plate motion. As seen in the plots there was no correlation between bulk plate position and motion. Note the pressure profiles [R3 & 4, C3] of Figure 3.28 which were similar despite opposing flexible-plate positions. Here the component not captured, specifically temporal plate motion, explains this. Note sub-figures for this same information are presented as part of Figure 3.29.

The actual point in the oscillation (position show in solid black) of the flexible-plate was around a maximum of motion, either just before or after. The lack of consistency in this respect was balanced against keeping consistency between time steps allowing comparison between palatal evolutions for each set. This decision precludes any significant comment on overall contributions to stable behaviour or otherwise although the presented individual snapshots were interesting in terms of the incremental contribution to the fluid-structure interaction and give additional insight such as to the magnitude of flexure term versus the other components. Moreover, the contributions of these terms vary widely throughout the oscillation of the flexible-plate and the transient dynamic nature of these fluid structure interactions is highlighted.

The prime motivation was to unlock the constituent contribution in a temporal sense. Figure 3.29, together with sub-figures 3.30 and 3.31, presents for each of the cases detailed in Figure 3.28 the total contributions for each term, plotted in bar chart form. An integration both spatially and temporally was performed to determine each term's total contribution over the entire simulation. While individual time-steps were principally characterised by a dominant spatial flexural rigidity contribution the overall contribution was balanced when temporal effects were accounted for, resulting in a more modest contribution from the flexure term. The contribution from the two components of the tension term were now

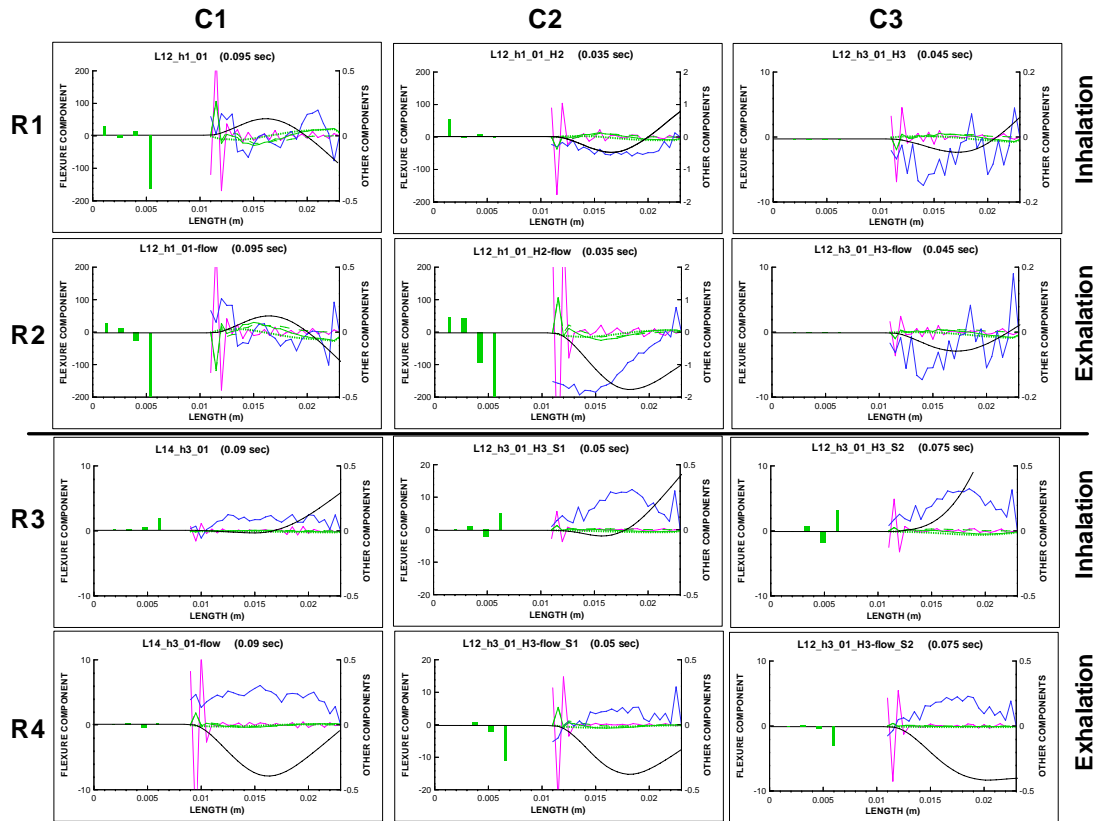


Figure 3.29: The same information is presented as for Figure 3.28 now with the temporal totals of terms being presented in bar chart form. The bar chart portion presents contributions over the whole simulation of each of the thin plate equation terms in Eq. (3.1). The magnitude of scale is uniform throughout. Each bar chart in green presents with the same order left to right being; $B\nabla^4 w$, $\frac{\partial T}{\partial x} \frac{\partial w}{\partial x}$, $T\nabla^2 w$ & δp_m .

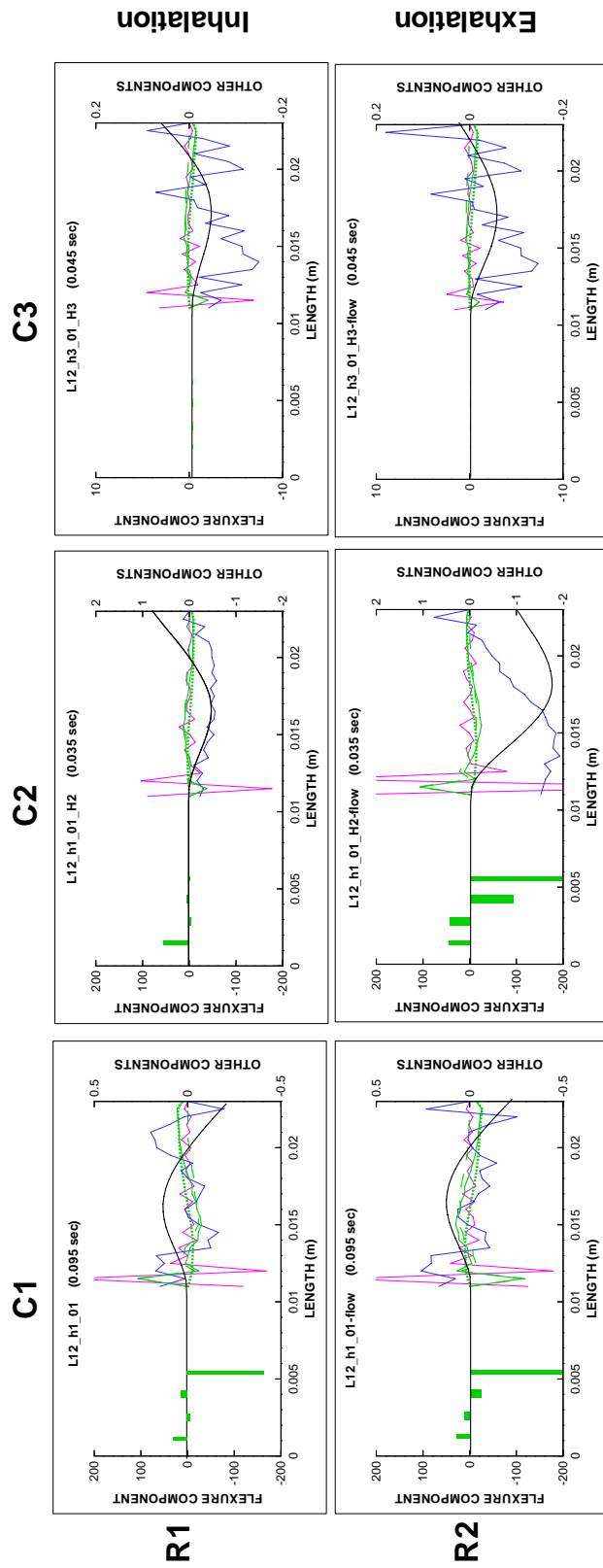


Figure 3.30: Enlarged view of Figure 3.29 showing Rows 1 and 2, Columns 1 to 3.

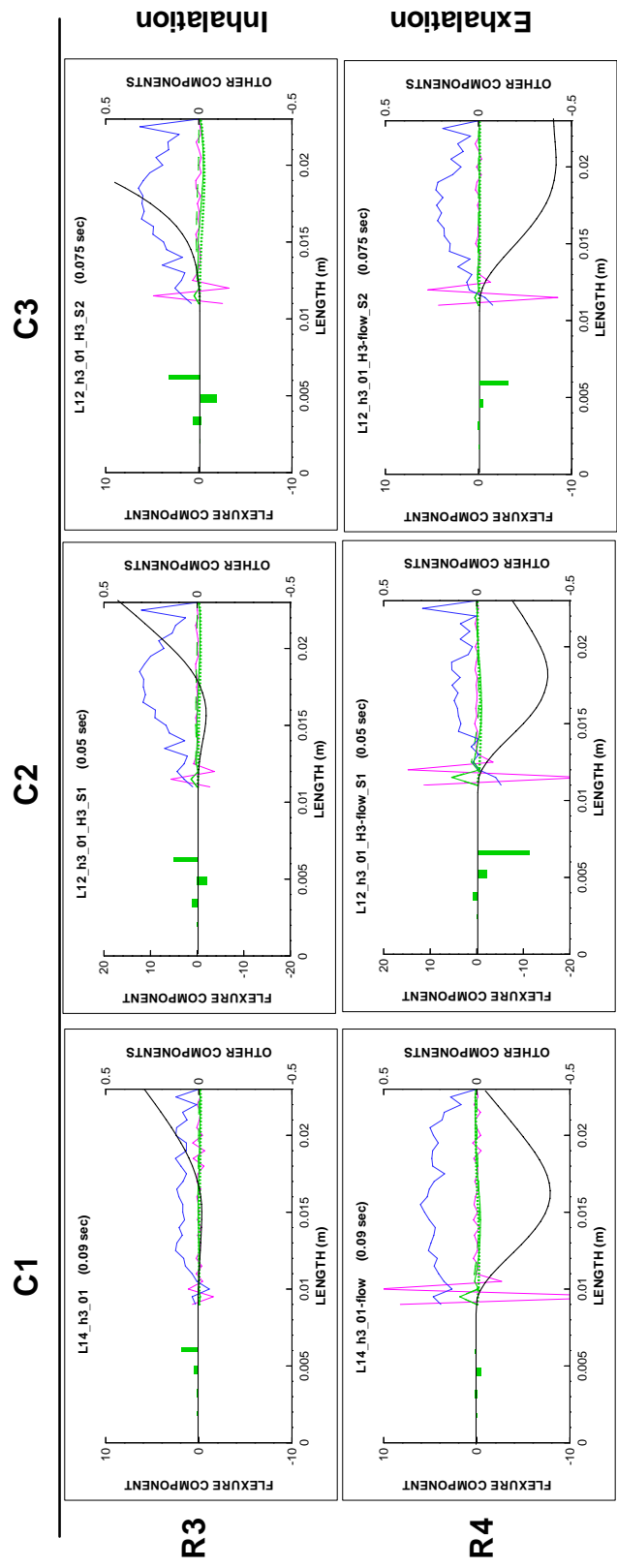


Figure 3.31: Enlarged view of Figure 3.29 showing Rows 3 and 4, Columns 1 to 3.

more significant although had a moderating effect on each other due to opposing directions and $\frac{\partial T}{\partial x} \frac{\partial w}{\partial x}$ being roughly half that of $T\nabla^2 w$ irrespective of flow direction and whether energy is being gained or lost by the flexible-plate. A *-ve* $T\nabla^2 w$ term correlated with energy being transferred from the fluid to the flexible-plate but not with flow direction.

Initially considering $\varepsilon = 0$, for inhalation and exhalation cases the flexure and pressure terms retain the same sign whereas the two tension terms alternate sign from inhalation to exhalation. This can be contrasted with $\varepsilon \neq 0$ where the two tension terms retained their same sign; this time pressure changed sign reflected by deflection into opposite channels.

Each term's temporal distribution was as follows: skin-friction induced tension and stiffness were largest at the fixed end of the flexible-plate and some small value at the free end. The pressure term was less predictable being a function of the fluid loading and plate displacement. The one pressure node known was the free tip which shared a common node so the transmural pressure was always zero. For some cases the integrated pressure term produced a net force, though no amplitude gain was viable, this was due to an uneven number of cycles where simple harmonic motions was being observed. A large pressure contribution was also seen in [R1, C1] which explained a large modal realignment from the initial perturbed shape with the frequency of oscillation reducing by 1.5 rad/sec from the *in-vacuo* second-mode. For the case shown in [R2, C2] clearly the large pressure contribution explained the divergence-type motion after a short period 0.035 seconds relative to the other presented cases.

The scale for the bar charts was uniform to enable visual comparison though no separate scale is provided, however, the physical limits were that of the two provided ordinate axis. Note the pressure components saturate on [R2, C1] and [R2, C2]. The decision not to re-scale allows the direction of the smaller contributors to be clearly seen and comparison made with the inhalation cases of [R1, C1] and [R1, C2].

3.8.5 Effect of channel boundary conditions

The series of cases in Figure 3.32, together with sub-figures 3.33 and 3.34, presents a study into the breathing cycle and the typical characteristics of a simplified

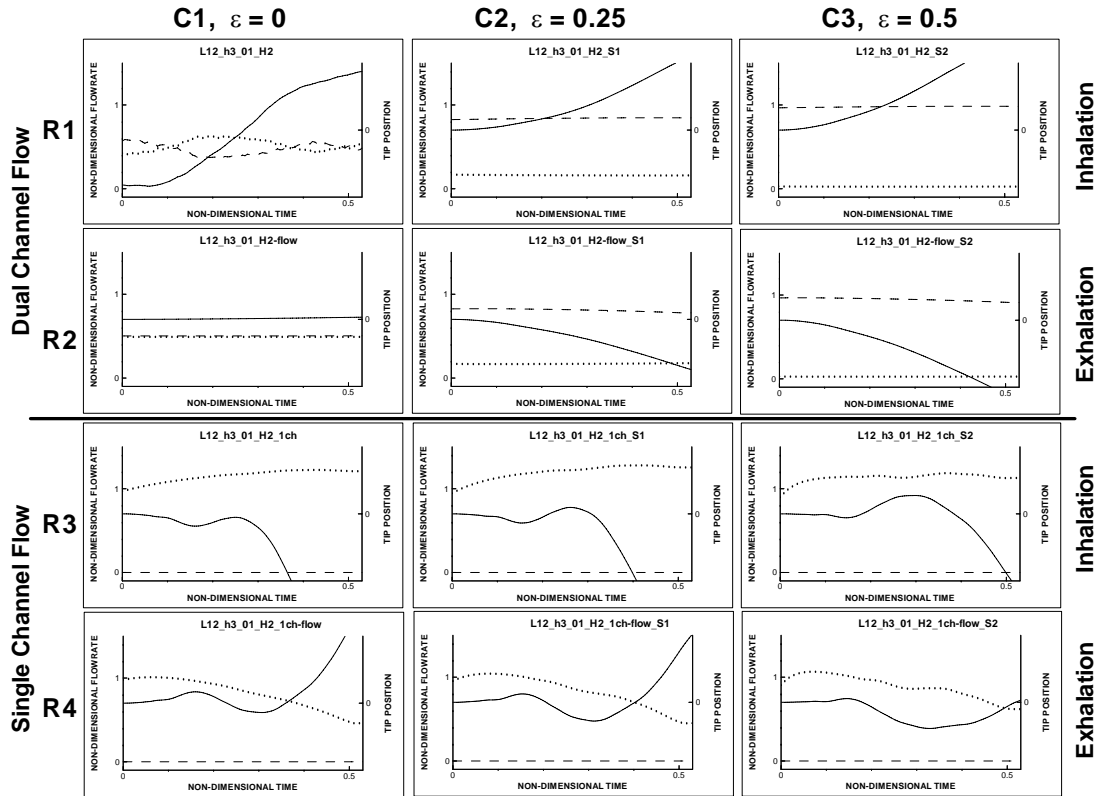


Figure 3.32: Non-Dimensional plate tip deflections and flow rate versus Non-Dimensional time. Plate tip position solid line, Lower channel flowrate dashed line, Upper channel flow rate dotted line. Note the magnitude of P_D was held constant (0.04 Pa) for means of comparison.

upper-airway. In this section single channel flow is included and these cases are Rows 3 & 4. The initial flexible-plate positions were unperturbed to give a relative measure of rate of motion without an extended modal realignment period. However one case [R1, C1] did have a standard perturbation assigned to it allowing a suitable tip scale to be determined for the other cases. [R2, C1] was left in the unperturbed state and underwent very little motion demonstrating the inherent stability of an unperturbed symmetric system when compared to the cases of Column 2 & 3 where symmetry was broken and large deflections ensue. Note for each of the cases presented the magnitude of P_D was held constant at 0.04 Pa for means of comparison.

Unsymmetrical cases with flow through both channels are presented in rows 1 & 2, and have very similar features to those of Figure 3.25, (note different time

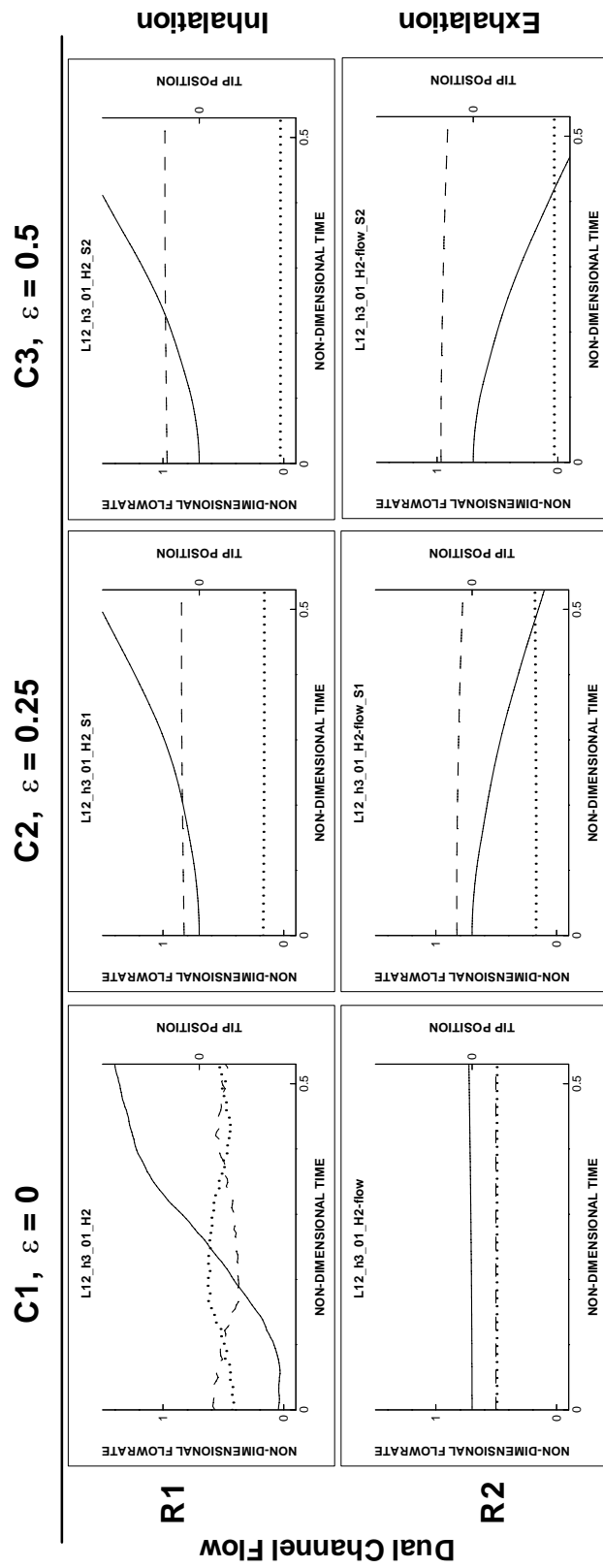


Figure 3.33: Enlarged view of Figure 3.32 showing Rows 1 and 2, Columns 1 to 3.

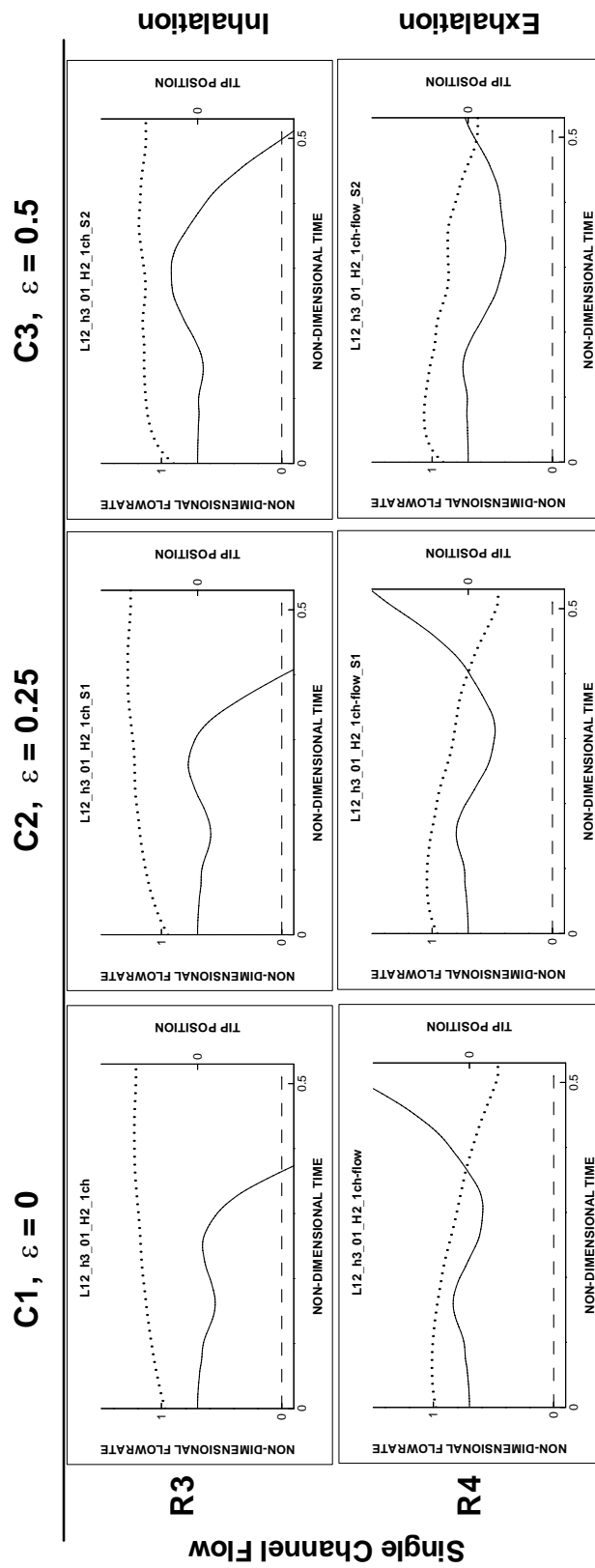


Figure 3.34: Enlarged view of Figure 3.32 showing Rows 3 and 4, Columns 1 to 3.

ranges) with the motion being a 2^{nd} mode type motion. For Row 1 responses due to the initial conditions in Figure 3.32 the response is dominated by 1^{st} mode content, though once motion established the 2^{nd} mode type patterns emerged. Row 2 maintained a 1^{st} mode divergence-type unstable response deflecting into the lower channel.

The foregoing results of Figure 3.32 Rows 1 & 2 represent breathing through, in a biological sense, the mouth and nose simultaneously. However quiet breathing would be generally through the nose only, owing to the biological drive to maximise efficiency. Pierce & Worsnop (1999) state that opening the mouth markedly reduces upper airway resistance but heating, humidification and filtering of the inspired air is less efficient. In general it requires approximately a 580-750 ml/s flowrate to necessitate the mouth and nose to be open together. Clearly this is not always going to be required during sleep. Rows 3 & 4 in Figure 3.32 examine the effect proposed by Tetlow *et al.* (2006) that single channel flow is actually the least stable breathing mode in terms of palatal stability and successive cyclic excitation. A set of cases with single channel flow utilising identical plate properties and pressure drops as Rows 1 – 2 are shown in Rows 3 – 4 isolating the response variations between single channel and dual channel flow.

Considering [R1-4, C1] responses were starkly different when one channel was blocked, flow through two channels had a stabilising effect while through one channel was very destabilising, though when looking at tip positions for [R3 & 4, C2 & 3] the tip responses actually reduced when compared to the $\varepsilon = 0$ case. The motion of the flexible-plate now resembles that of a divergence type instability see Figure 3.35, together with sub-figures 3.36 and 3.37, in rows 3 and 4 where a portion of the plate around $1/3$ to $1/4$ the length of the plate from the fixed end, is the first segment to rise, with the free end essentially holding position, leading to a classical divergence deformation. However for Row 3 cases the free end was drawn up after a short delay by a travelling wave type phenomena. Row 4 however, maintains the divergence shape with the plate tip moving up after an extended period almost in time with the leading region, maintaining the divergence type shape, to some extent suppressing the travelling wave to around $1/2$ the plate's length. For inhalation cases Rows 1 and 3 the initial motion emanates from this same portion of plate with motion propagating in a travelling-wave manner, extracting energy from fluid at the upstream end and returning to the fluid at the downstream end. Here the energy balance is greater in the former

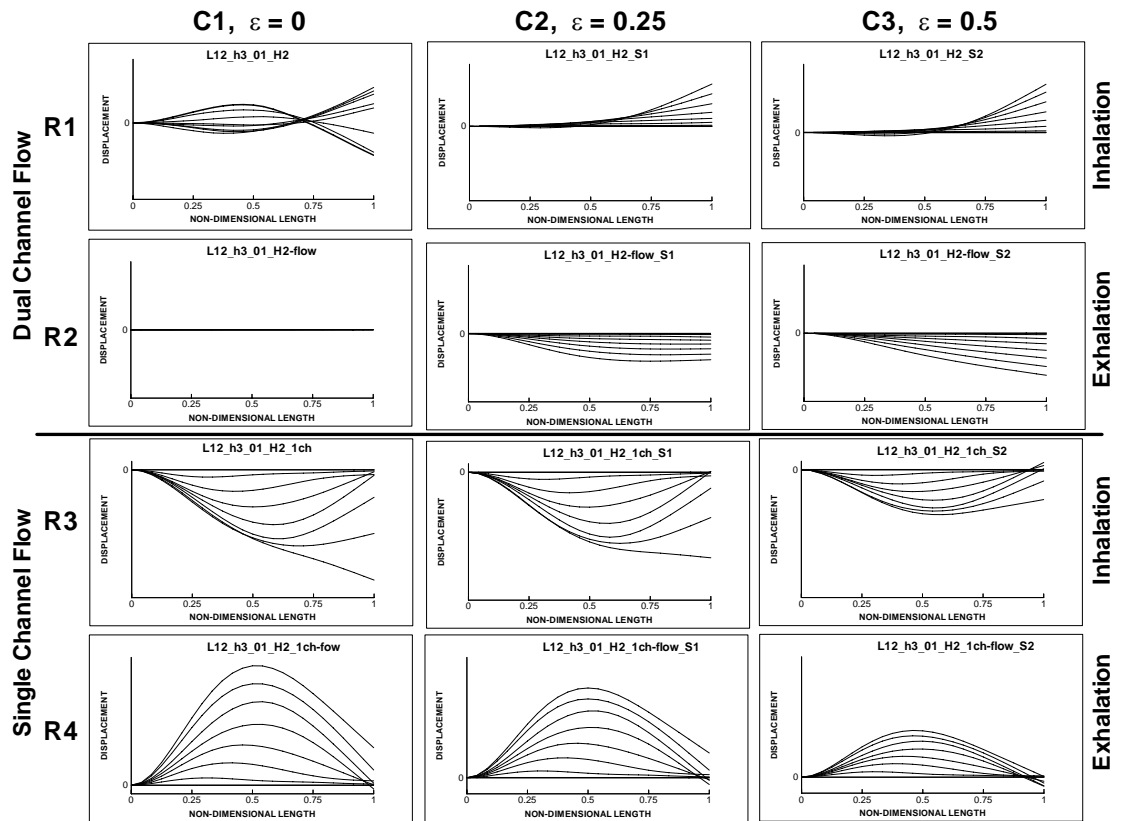


Figure 3.35: Flexible-plate oscillations over an idealised breathing cycle, in support of Figure 3.32. Plate initial position thick line normally unperturbed, displacement scale held constant in each case presented. Note the magnitude of P_D was held constant (0.04 Pa) for means of comparison.

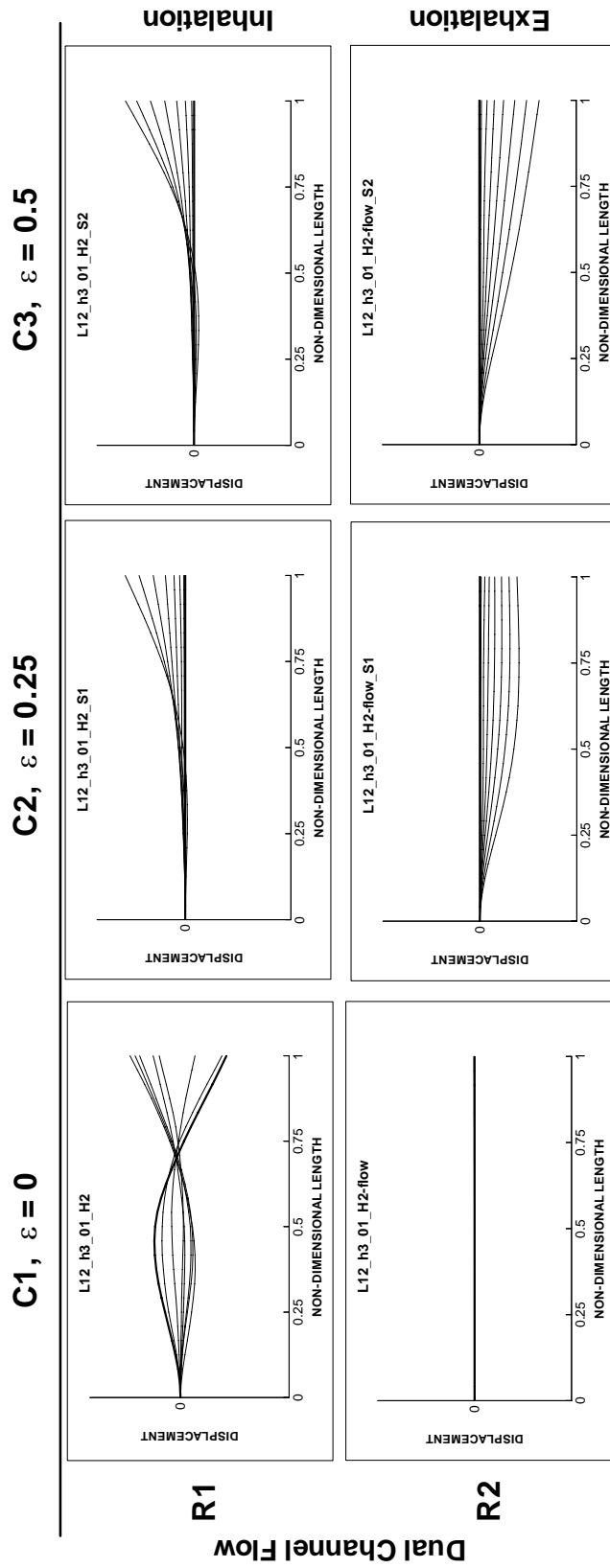


Figure 3.36: Enlarged view of Figure 3.35 showing Rows 1 and 2, Columns 1 to 3.

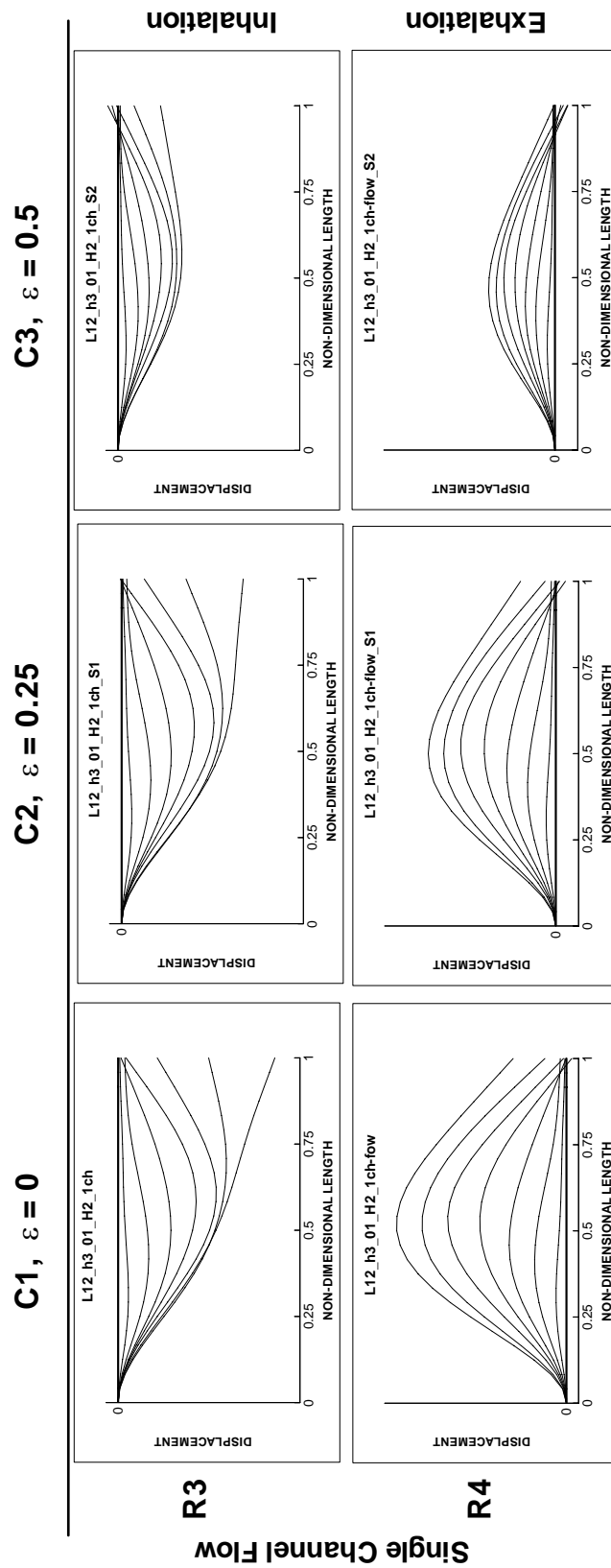


Figure 3.37: Enlarged view of Figure 3.35 showing Rows 3 and 4, Columns 1 to 3.

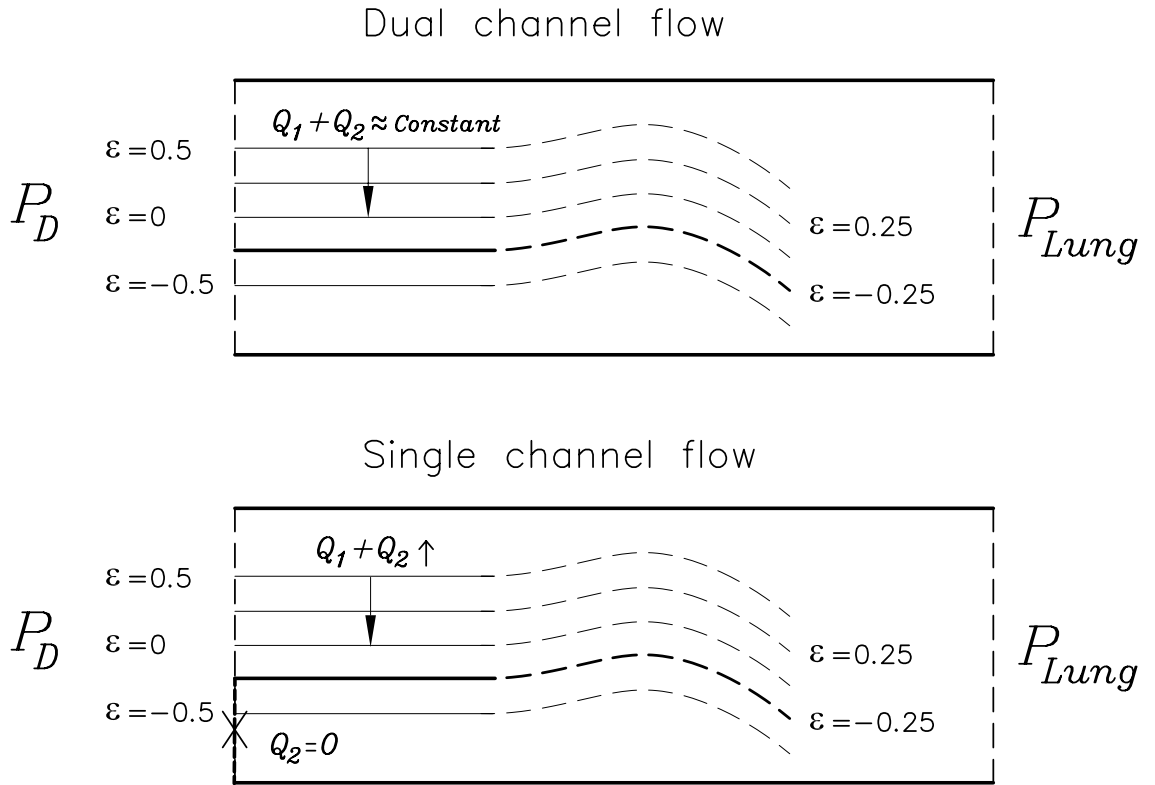


Figure 3.38: Schematic of the linkage between flowrate Q for dual (top) and single (bottom) channel flow as the rigid splitter section moves within the channel from top to bottom.

than the latter and so increased oscillation amplitude is exhibited. This travelling wave instability has its analogue in the flutter instability demonstrated by Huang *et al.* (2001) though here it is more pronounced, due to the free end condition, though travelling waves in the upstream direction, which are typically attributed with providing additional excitation disturbances, were far less visible due to this same free end condition. Note the closed channel for $\varepsilon \neq 0$ was the larger of the two channels thereby intensifying any hydraulic resistance differentials across the flexible-plate.

Viewing Row 3 plots within Figures 3.32 and 3.35, deflections decreased as ε increased while, mass flux increased due to the plate deforming out of the flowing channel. The mass flux increase is relatively greater than in the equivalent two-channel flow case of Row 1. This arises from the region in which the pressure drop occurs; as ε is increased a greater percentage of the finite hydraulic

loss occurred in the rigid splitter section leaving a smaller available transmural pressure across the flexible-plate. Figure 3.38 summarises the flowrate changes between dual and single channel flow with flowrate remaining essentially constant and highly variable respectively. It is this increased flowrate variation that led to the variable pressure drop distribution, under single channel flow conditions as flowrate reassignment between the two channel is not permitted.

Row 4 in Figures 3.32 and 3.35 demonstrated the same trend for smaller deflections as ε increased though this time the deflections were into the flowing channel see Figure 3.35 Row 4. The resulting mass flux decreases shown in Figures 3.32 Row 4 were the most restrictive seen, tending to choke off flow as a result of this deformation.

With one channel blocked, the trend found is that as the flowing channel was decreased in height the deflections reduced in magnitude. Conversely if the compliant plate was moved downwards increasing the upper flowing channel then the deflections would continue to increase until some limiting value was reached. This was due to the finite pressure drop over the domain remaining constant and being expended over the three sections as hydraulic resistance, the three sections being; split channel section comprising rigid and flexible-plate segments and the combined channel segment. In simple terms the pressure under the flexible-plate was a function of the pressure at the free end of the flexible-plate, so minimising pressure drop over the rigid split section maximised the net force exerted by the flow on the plate. The rigid section in the split channel in effect wastes some of the available pressure drop at varying rates depending on height. If the rigid section was not present then this would have potentially quite a material impact where the trend and peak deflections could be reversed and be found with the smaller rather than larger channel, an interesting finding for asymmetric loading (single channel flow) and asymmetric positioning of the compliant surface within. This sensitivity to minor changes in the composition of the model presents a great deal of material for further research even within this relatively simple model, with the aim of informing OSA research more broadly.

Figure 3.39 (a) shows the results of a typical inhalation period when a pressure drop was applied. The lower channel was blocked. The flow is from left to right and motion of the soft plate was initiated by deforming it into its second in-vacuo mode. At early times of the simulation, oscillatory motion occurs due to

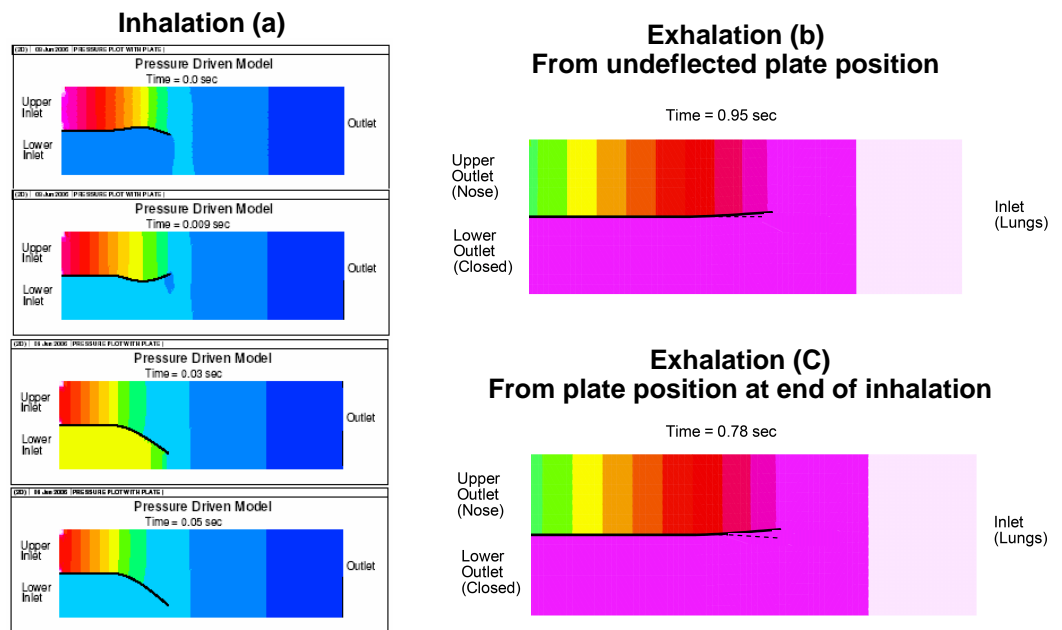


Figure 3.39: (a) Snapshots of soft-plate deflection and pressure contours (red=high to blue=low) for a typical inhalation using a constant applied pressure drop with the lower channel closed. Adapted from Tetlow et al. (2006), (b) & (c) Snapshots of soft-plate deflection at maximum deflection into the upper open channel during exhalation (flow from right to left) and pressure contours (light-magenta=high to Green=low) for initial soft-palate position denoted by broken line at, (b) undeflected and (c) the end of a previous inhalation.

the initially introduced presence of the second mode. This was damped by the fluid with the plate finally settling into the deformed position seen when $t=0.05$ s. Note that the pressure in the closed cavity must ultimately equal that at the tip of the flexible-plate as there is no external flow present with the channel closed. For the exhalation phase of the breathing cycle (b) is presented with the initial position being un-deformed. A constant pressure drop was applied with the lung-side pressure above atmospheric by 0.0014 N/m^2 . A snapshot of the soft-plate position at the time the tip reaches maximum deflected position into the open upper channel is shown in (b). Figure 3.39 (c) was based on (b) although now the initial position is deflected in to the closed channel as though it were a continuation from a previous inhalation breath. Note the increased deflection seen in Figure 3.39 (c) from (b) as a result of the initial conditions being varied to reflect a more accurate situation where the previous breathing cycles deformed flexible-plates position was included.

The presented results for single channel flow demonstrate that during the exhalation phase, the soft-palate deflects into the open channel, thereby increasing resistance for the start of the next inhalation breath. This would necessitate the lungs to apply greater inhalation effort to achieve a constant flow rate, thereby reducing the mean pressure in the airway. Importantly the effect of this would be to increase the pressure differential across the pharyngeal walls. Reduced airway pressure heightens the risk of apnoeic closure of the airway due to pharyngeal (side-wall) collapse. Moreover, these results show that the position of the soft palate at the start of the exhalation phase leads to increased deflections with the start of the next inhalation. In Figure 3.39 (c) the deflection into the upper channel by the flexible-plate was 0.20 mm , having commenced at -0.14 mm this exceeded the 0.17 mm reached in (b) when the starting point was from the neutral position. Over a number of breathing cycles, a significant increase to the resistance of the open channel could occur, necessitating progressively higher levels of lung suction during inhalation and thus an increased propensity to overall airway collapse.

3.8.6 Dimensionless scheme

Study of the solution space is presented in the context of the dimensionless scheme presented in Section 3.1. This work pertains to symmetrically positioned config-

Table 3.7: Dimensionless Group Values for Figure 3.40. Note the table is grouped in row order, for example a-c are the cases in row 1 Figure 3.40.

Fig label	ω (Rad/sec)	Re	Θ	Γ	stability
a	83	1700	42	0.0074	Neutrally stable
b	70	2410	42	0.0054	
c	100	2410	21	0.0054	
d	265	257	2.5	0.035	Neutrally stable
e	42	255	25	0.0088	
f	264	256	2.5	0.035	
g	100	2440	42	0.0052	Neutrally stable
h	100	2440	21	0.0053	
i	100	2410	42	0.0051	
j	42	247	2.5	0.00094	Unstable
k	15	514	15.0	0.00045	
l	13	242	25.0	0.00098	

urations for inhalation as identification of *stable* oscillations only, unsymmetrical configurations and exhalation cases were not considered.

With six dimensionless groups available to explain the underlying physics, this necessitated a means to further reduce complexity allowing a solution space to be presented in a straightforward and usable form. This section outlines the first step towards determining how best to present the stability space and how the complexity of a system governed by six independent dimensionless groups of parameters can be reduced.

The basis behind the dimensionless groups and relative importance of each was developed through a systematic investigation. Firstly parameter variation yielding identical dimensionless-group values was conducted validating the derived groupings. Secondly slightly changing each dimensionless group in turn allowed a feel of the relative importance of each to be developed. Upon studying the actual non-dimensional values in Table 3.7 where individual dimensionless groups were to be varied, not all other values could necessarily be maintained as constant. In order to permit testing to proceed, small variations were accepted when the primary varied dimensionless groups deviation was 30% or more, this was viewed as sufficient to give visually discernable difference to the response if any effect was to be detected.

Figure 3.40, together with sub-Figures 3.41 and 3.42, shows a number of plots

comparing identical or similar cases. The PSBS codes do not apply because the standard parameter values were not used and further appropriate parameter variations were required to achieve the same or similar dimensionless group values, parameters used are listed in Appendix B. Pursuant to this Table 3.7 lists the dimensionless groups values used that were varied as part of this study. Reynolds Number Re , mass ratio Θ and stiffness ratio Γ were all considered to be significant measures of stability with all three comprising fluid and flexible-plate parameters. Simplify this analysis the other dimensionless groups were held constant, Damping Ratio ξ affect was excluded by setting damping to zero, as has been the case throughout. Eccentricity ε was held constant at $\varepsilon = 0$ and finally the aspect ratio and \bar{H} were also held constant by maintaining the distance from the free end of the flexible-plate to the exit of the channel i.e. the summation of the lengths of the split section plus flexible-plate were held constant and the height of the channel was not changed within any Row of comparative cases. Moreover, the channel H was directly related to Re as velocity and P_D were related through Eq. (3.52).

This section demonstrates firstly, that the dimensionless scheme can be used to faithfully predict the result for equivalent cases comprised of variables of different magnitude though holding the respective dimensionless group values constant. Secondly, that the mass ratio term has little control over system stability though the systems frequency will be changed. Figure 3.40 shows four rows of figures where within each row variations of parameters values are presented to demonstrate the influence each dimensionless groups has. Rows 1-3 are for stable oscillatory motion and Row 4 for an unstable case with the findings being applicable for each, further validating the approach.

Cases (a-c) in Row 1 of Figure 3.40 establish neutrally stable oscillations for a number of plate and fluid parameter variations, including plate length. The slight deflection response differences in (a) were due to the stiffness ratio Γ and Reynolds number Re , in (a) being 15% and 30% lower or higher respectively than for cases (b-c). Note (c) has 1/2 the value of mass ratio Θ than (a & b) with only very minor change to response excluding frequency change shown in Table 3.7, which is accounted for here with non-dimensional time, Luo & Pedley (1998) and Tetlow & Lucey (2009) also find slight connection of mass ratio Θ to system stability.

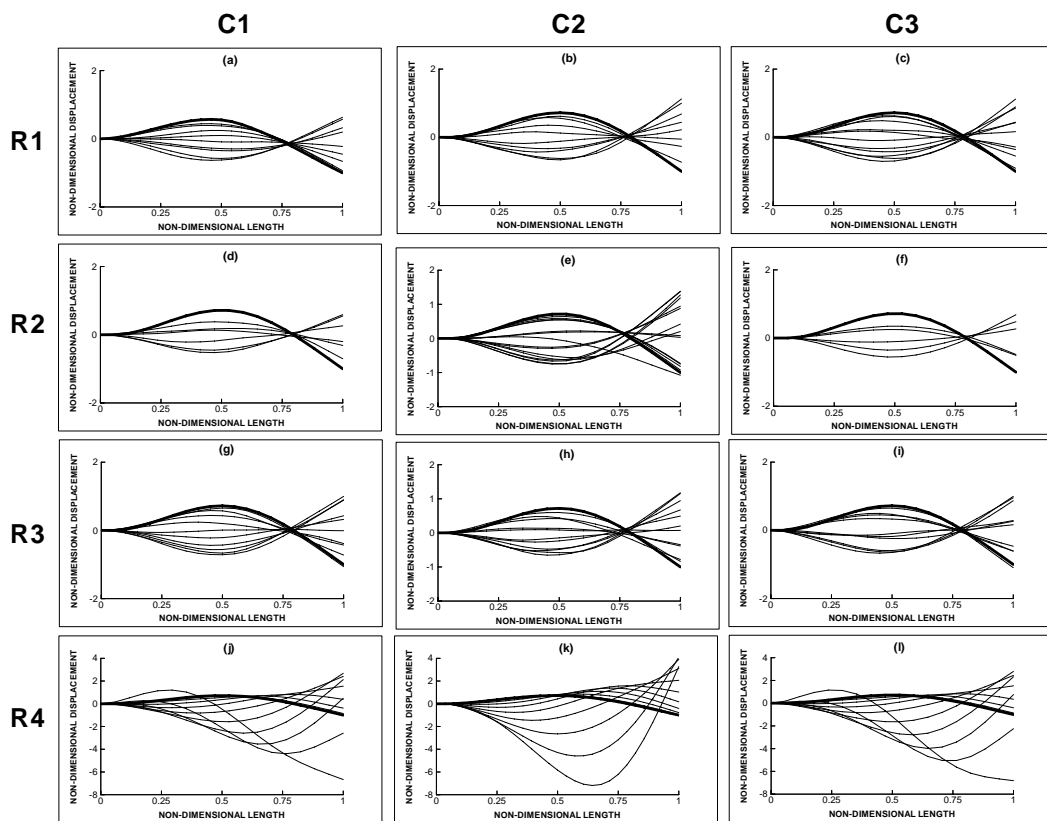


Figure 3.40: Flexible-plate oscillations. Variation of parameters, to demonstrate that dimensionless groups characterise palatal evolution. The relative importance of each dimensionless group to overall stability is also shown. Each row represents a set of dimensionless groups for comparison to determine the relative the importance of each. Cases (e, h and k) are for cases where Reynolds Number Re and of stiffness ratio Γ where varied showing significant changes to response. See Table 3.7 for specific dimensionless group values. Plate initial position thick line, displacement scale as shown in each case presented. Base cases for cases (a-i) considered neutrally stable oscillations and cases (j-l) unstable oscillations.

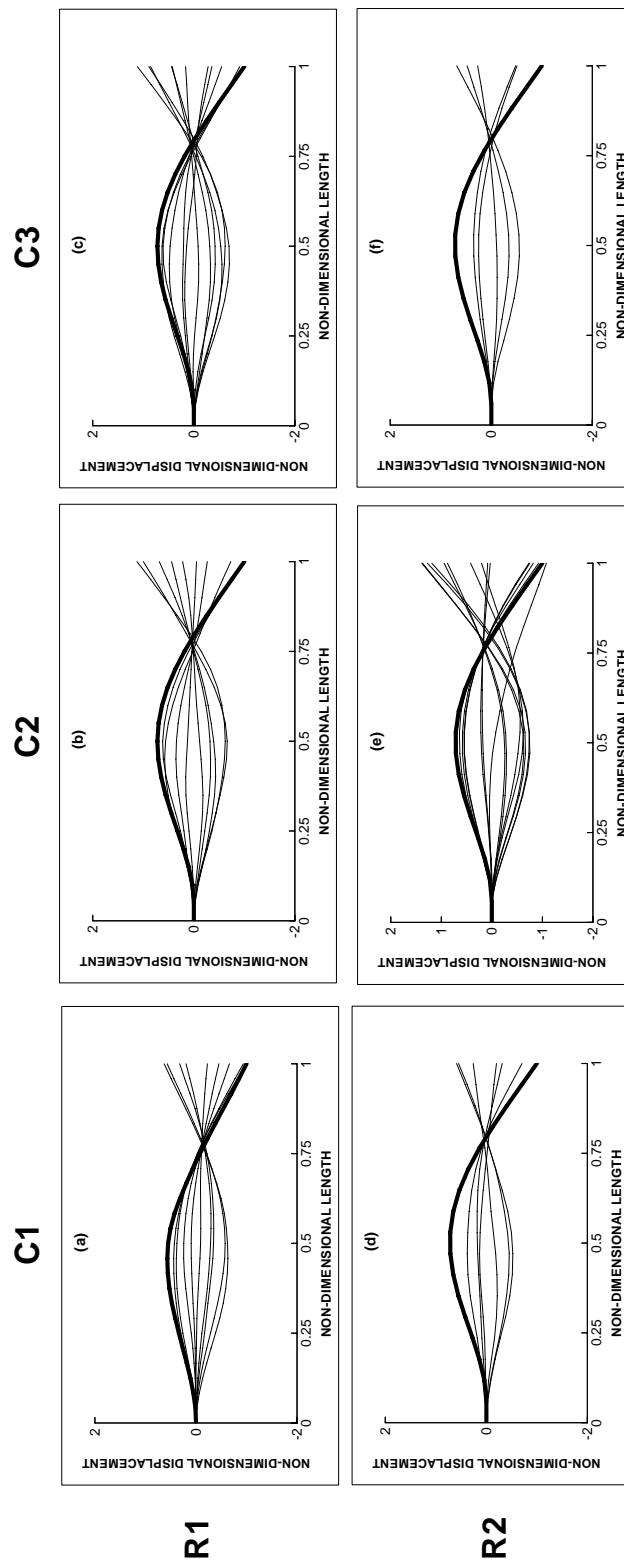


Figure 3.41: Enlarged view of Figure 3.40 showing Rows 1 and 2, Columns 1 to 3.

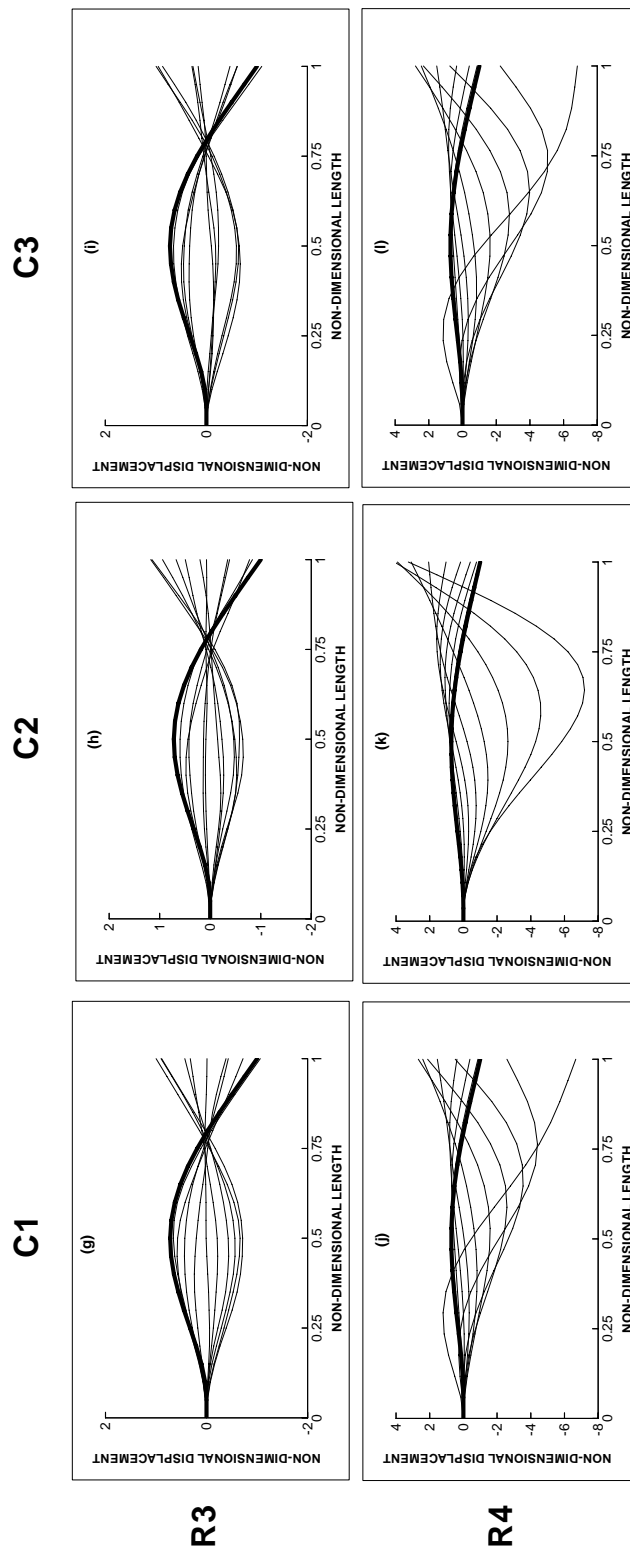


Figure 3.42: Enlarged view of Figure 3.40 showing Rows 3 and 4, Columns 1 to 3.

Cases (d-f) in Row 2 of Figure 3.40 show very similar critical mode shapes for (d & f) for the parameter variations investigated. However, case (e) had a stiffness ratio Γ a quarter (d & f) resulting in the visibly changed response. Note that while the Θ value is 10 times the value used in (d & f), this same differential was repeated in cases (j & l) of Row 4 here with stiffness ratio Γ effects removed, and shows only incremental change in response again demonstrating the response to be insensitive to manipulation of mass ratio Θ though a significant linkage between response and stiffness ratio Γ is noted.

Cases (g-i) in Row 3 of Figure 3.40 are comprised of combinations of parameter variations with similar dimensionless group values leading to good alignment between flexible-plate evolution for all. Case (h) show some minor tendency to deviate from the expected critical mode shape. Here Re and Γ were varied slightly and Θ by 50% when compared to cases (g & i), potentially all three dimensionless groups could be contributing to this small change. While there are some minor variations to the critical mode shape, Row 3 further serves to show the range of parameter variability for which the simulation and non-dimensional scheme yield consistent results.

Cases (j-l) in Row 4 of Figure 3.40 this time for unstable oscillations again yield results in close agreement with that of the above stable cases. Cases (j & l) produce unstable modes of great similarity with the small change here being due to the mass ratio, as all other groups were held constant further highlighting the minor role mass ratio contributes to flexible plate response. Note the travelling wave flutter exhibited in these unstable cases. Case (k) however, is vastly different from the response of (j & l), showing that Re and Γ were involved in this owing to their magnitude in change from the base cases. Moreover, cases (j-i) aid to extend the validity of the dimensionless scheme beyond just stable cases for the scheme to be of more general application.

In summary, for a range of parameter variations yielding equivalent dimensionless group values similar critical mode shapes have been generated further demonstrating the general applicability of the approach. The findings of Tetlow & Lucey (2009), Luo & Pedley (1998) & Huang *et al.* (2001) have been re-confirmed here, that structural inertia plays an essential part in the flutter instability as demonstrated in cases (j & i) whose origins lie in the phase shift between fluid pressure and plate velocity, for which mass ratio Θ has a limited effect on stability in

isolation. In contrast the groups of stiffness ratio Γ and Reynolds number Re result in significant changes to response. While the mass ratio Θ has been identified as being largely disassociated with palatal response the physical parameters comprising mass ratio were for the most part included in stiffness ratio Γ and Reynolds number Re . The extra term for the mass of the wall is accounted for in the natural frequency change in the simulation, which once non-dimensionalised presents minimal change to the corresponding palatal response in this analysis. For the purposes of this analysis, a compliant plate in isolation, the frequency of oscillation may be of little concern. Note however, that in more complex systems with significant interacting dynamics, manipulation of mass ratio Θ allows system tuning and would have many practical applications. For biological applications varying the mass of the wall may not be the most direct approach available.

3.8.7 Solution space for a 2-D flexible-plate in channel flow

This section builds upon the non-dimensional parametric study in Section 3.8.6. Following this work the results focus on the previously determined important non-dimensional groups of stiffness ratio Γ and Reynolds number Re and excludes mass ratio Θ as stability was demonstrated to be only weakly dependent on this group in Section 3.8.6. Figure 3.43 plots cases approaching neutral stability for the parameter ranges used in Table 3.3 on axis of Reynolds number Re versus stiffness ratio Γ . Figure 3.43 consists of 36 separate numerical simulations where stable motion was found, or approached, using a manually iterative approach involving up to six separate simulations to determine each result. Full details are provided in Appendix B. The solid red line was the line of best fit to these data points with equation of best fit determined as $\Gamma = 2.7 \times Re^{(-0.8)}$. Here neutrally stable means that the solution presents minimal bulk energy transfer between fluid flow and the flexible-plate, in the time period investigated.

The scatter of data points around the line of best fit of neutrally stable oscillation was expected due to the relatively short numerical simulation times. This made subsequent estimation of stable oscillation more prone to minor error particularly from modal realignment. However, given the numerical expense conducting significantly longer run times and the inability to account for transient modal realignment adequately masking some underlying overall trend, a compromise was made.

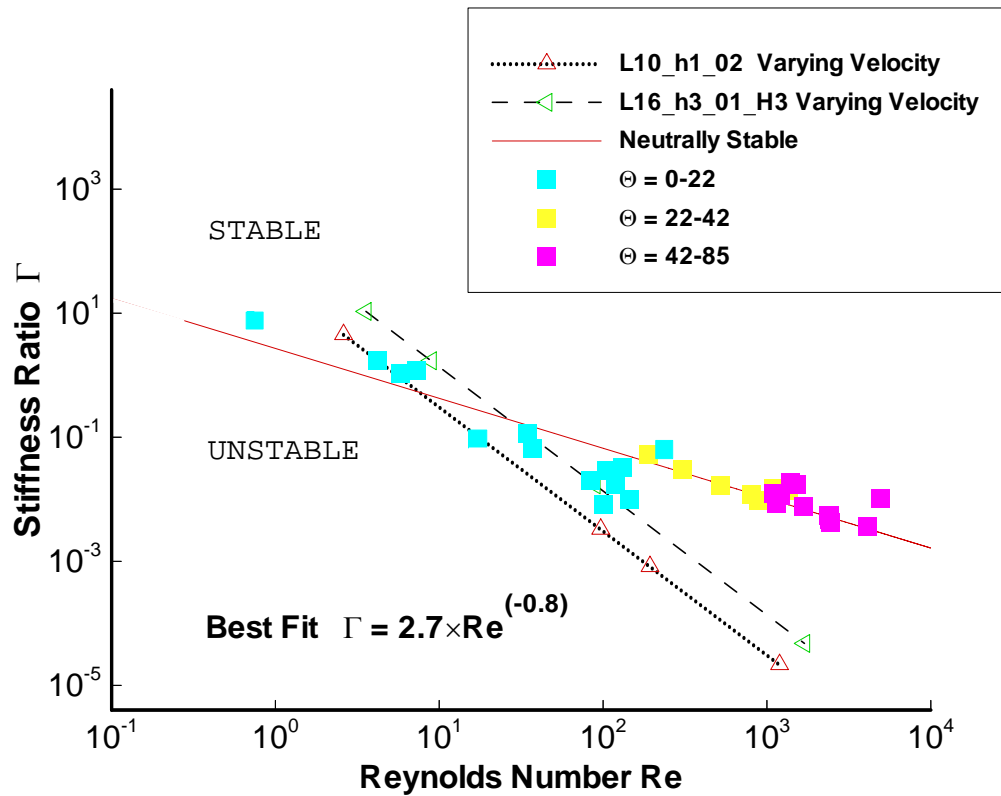


Figure 3.43: Stability space of Reynolds number Re versus stiffness ratio Γ . For numerical investigations of an undamped cantilevered, flexible plate, with one end fixed, symmetrically positioned in a 2-D channel subject to viscous fluid flow. Data points presented are for individual cases at or approaching stable conditions with red solid line of best fit and equation presented. The dotted and dashed lines represent two cases where plots for simulations with energy loss and gain to the fluid are also added. Below the solid red line energy is extracted by the flexible plate from the fluid, above loss of energy from the plate to the fluid. Note data points are coloured according to the dimensionless group of mass ratio Θ .

Figure 3.43 includes ranges of mass ratio Θ plotted in colour, which show a general trend aligning with the two primary dimensionless groups. Importantly ρ_m is the only parameter in Θ that was not present in Γ or Re and that this parameter (ρ_m) was not varied for the bulk of the results, thus this general trend is largely an artifice of the original parameters selected being for that of the pharynx. Section 3.8.6 was the only section that considered variation of ρ_m and it is these results that demonstrated Θ was not a governing dimensionless group.

Modal realignment was minimised through an initial study with second *in vacuo* mode-shape deformed plate and subsequent simulations to determine appropriate evolved plate deformations to reduce modal realignment effects. These evolved deformations consisting of a combination of 1st and 2nd modes which had partially undergone modal realignment and was conducted for each plate length L_p .

As both Reynolds number Re and stiffness ratio Γ are dependent on the mean velocity \bar{U} , varying the P_D varies both non-dimensional parameters. To determine the path such variations will take on Figure 3.43 two examples are presented moving about the best fit line from unstable (below) to stable (above), this trend is also demonstrated in (Luo *et al.*, 2008) which has a similar formulation of stiffness ratio. The two cases shown L10_h1_02 and L16_h3_01_H3, dotted and dashed respectively. These lines were generated by varying P_D and hence mean velocity \bar{U} to give successive points to show the power relationship (linear on these logarithmic axis) and each intersection point with the best fit line of neutral stability. Moreover, both lines have the same gradient to the red line which agrees with the dimensionless groups formulation. This enables the possibility for the inlet velocities and hence the P_D to be calculated directly from only one data point.

The underlying implicit simplifications permitting this solution space system to be presented have been discussed above. It has been demonstrated that the systems stability is not significantly dependent on mass ratio Θ apart from an actual frequency change and has been shown to be largely governed by the dimensionless groups of stiffness ratio Γ and Reynolds number Re . However, not considered here are the significant changes that will occur with change in ε , flow direction and the number of channels with flow present. The qualitative effect of these additional combinations have been dealt with throughout this chapter including Section 3.8.2 where indication has been provided regarding the relative effect on

stability in each combination of cases.

3.9 Summary

This chapter reported the development and use of analogue computational modelling to advance understanding of the dynamics of the soft palate within an idealised rigid pharynx. This system reveals the complex dynamics associated with a relatively simple geometry a flexible surface embedded in a fluid flow subject to a number of boundary conditions. Understanding of this system underpins the interpretation of results from geometrically more complex full anatomical models of the upper-airway system that would be specific to individual sufferers and the ultimate challenges for researchers.

Initial work, for example see Tetlow *et al.* (2006) & Tetlow & Lucey (2009), focused on understanding the underlying physics of the soft-palate with other channel walls (tongue and pharynx) considered rigid; a schematic of this simplified two-dimensional (2-D) model is shown in Figure 3.44. This analogue model of the upper airway reports a new approach because the mean flows in the oral and nasal inlets are not prescribed. Instead each was computed as functions of the applied pressure drop and the time-varying resistance of each channel, itself dependent upon the fluid-driven motion of the soft-palate for hydraulic resistance variations interacting with each other in a fully coupled fluid-structure interaction.

The model is rational as the system, driven by an applied pressure drop over the streamwise length of the channel, leads to fluctuating mean-flows above and below the flexible cantilever and through the domain as a whole. This approach contrasts with other modelling approaches that prescribe constant mean-flow through the individual channels, and thus the system, leading to a side-effect of fluctuating pressure gradients over the domain. These different modelling approaches result in significant material differences as has been reported in this chapter. Flow-volume curves which map the human breathing cycle show that the action of the lungs serves to maintain a relatively constant mass flux to the lungs or flow drafting Huang *et al.* (2001), during inhalation. A constant mass flux was of course achieved with a velocity-driven approach. However, despite the inlet channel variation of mass flux, the combined mass flux remains relatively

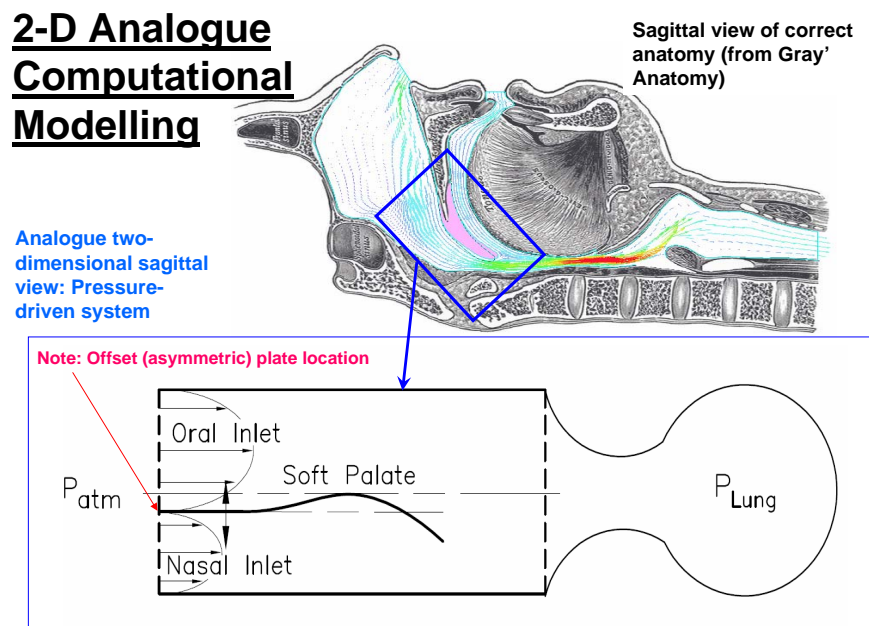


Figure 3.44: Development of 2-D model from anatomical midsagittal view.

constant for the pressure-driven model in the same way the biological system performs without necessitating varying external pressures to deliver this result. Thus, although the pressure boundary condition leads to very different soft-palate responses to that of imposing a constant downstream velocity boundary condition, pressure-driven predictions remain compatible with the clinical observations of flow drafting.

Flutter is a dynamic instability that involves coupling of fluid aerodynamic forces, and elastic and inertial forces of the structure. As the flow velocity increases around the flexible plate, the fluid dynamic forces interact with and alter the structural vibrations of the flexible wall. *Divergence* is a static instability, which occurs when the aerodynamic forces are greater than the elastic restoring forces of the flexible-plate. Divergence only occurs for cases with asymmetry, either, one inlet channel blocked or asymmetric placement of the flexible-plate for example the cases presented in Figure 3.35. However, this is not the usual way for divergence to be defined or found to occur in the literature, Kornecki (1978), Guo & Paidoussis (2000), Woodson (2003) & Paidoussis (2003) find divergence

to occur for plates with two ends fixed with flow to one side, not for cantilevered plates immersed in channel flow. Firstly, divergence would be encountered and at a velocity above a critical value flutter and travelling waves would evolve. The experiments devised by Kornecki (1978) applied an aerodynamic force to one side of the plate with an ambient constant pressure applied to the other. Clearly any resulting pressure differential, be that due to viscous or aerodynamic pressure forces, leads to motion of the flexible-plate towards the side of the flow (of lowest pressure). The one channel closed (or asymmetric) situation considered herein as Figure 3.35 presented a divergence instability leading to travelling waves and flutter, depending on flow direction. Thus for an initially unperturbed plate in a flow, ideally handled by the developed pressure-driven approach, leads to self-excitation previously not reported owing to the normal symmetric placement of compliant plates within channel flow.

The model developed herein also includes further flow structure coupling by inclusion of the full tension term $\frac{\partial T}{\partial x} \left(T \frac{\partial w}{\partial x} \right)$ due to skin friction within the flexible-plate 1-D equation Eq. (3.1). Although developed within a bio-mechanical context, the modelling of time-varying resistance due to strongly coupled fluid-structure interactions within a channel may find application in engineering systems.

Utilising parameters broadly appropriate to the study of human upper-airway dynamics the palatal response was dominated by the first and second modes of oscillation. As flow speeds increased, instability first occurred as a flutter dominated by downstream-travelling waves, caused by irreversible energy transfer from the mean-flow to the plate. The effect of tension was relatively small though cumulative and non-negligible, both postponing flutter and the onset of instability for typical inhalation cases.

The pressure-driven model developed in this thesis permits the study of a flexible-plate which can be asymmetrically positioned within the channel. Offsetting the plate was shown to have a marked effect on energy-transfer rates and reduced oscillating frequencies. Asymmetric positioning would be most common within real airways due to its three dimensional shape and curvature, an evolved response to walking upright. Accordingly the pressure-driven model yields insights permitting enhanced prediction and interpretation of more advanced and future anatomically correct models that will ultimately lead to improved clinical management of snoring and sleep apnoea.

Table 3.8: Relative stability for a range of model composition variations with two channel flow. The reference base case stable oscillation is noted as ‘=’ with increasing instability from boundary condition changes qualitatively indicated with ‘+’ where the greater the number the more unstable.

Composition	Inhalation	
	Pressure-driven	Velocity-driven
Symmetrical $\varepsilon = 0$	=	+
Offset $\varepsilon = 0.25$	+	++
Offset $\varepsilon = 0.5$	++	+++
Composition	Exhalation	
	Pressure-driven	Velocity-driven
Symmetrical $\varepsilon = 0$	++++	+++
Offset $\varepsilon = 0.25$	+++	++
Offset $\varepsilon = 0.5$	++	+

Table 3.9: Relative stability for a range of model composition variations for single channel flow for the configuration examined herein. Again increasing instability owing to boundary condition changes is qualitatively indicated with ‘+’ where the greater the number the more unstable

Composition	Inhalation	Exhalation
Offset $\varepsilon = 0.5$	++	+++
Offset $\varepsilon = 0.25$	+++	++++
Symmetrical $\varepsilon = 0$	++++	+++++
Offset $\varepsilon = -0.25$	+++++	+++++
Offset $\varepsilon = -0.5$	+++++	+++++

To summarise the findings of this chapter Table 3.8 gives an indication of the relative stability between the two models of pressure-driven and velocity-driven. Table 3.8 relates the base case stable oscillation noted as ‘=’ to the other possible boundary conditions for the two modelling approaches as instability was increased ‘+’. This provides a scale for the degree of relative instability from the base case with the more ‘+’ the more unstable the predicted result would be, for the reference base case.

Table 3.9 compares single channel flow and inhalation and exhalation for the pressure-driven model only. Note the sign change for ε now yields a different result as discussed in Section 3.8.4.

Part II

Three-Dimensional Duct Flow And Anatomically Correct Geometry

CHAPTER 4

Anatomically Correct 3-D Model

This chapter presents findings from a number of contributions towards greater understanding of upper-airway dynamics, translating concepts into numerical substance. Accordingly this comprises a combined effort between medical, imaging and engineering teams. As such the writer's involvement was limited to data acquisition, geometry reconstruction, model development, and developing numerical simulations that were faithful to upper airway function, it is these areas detailed herein. Owing to the obvious increases in complexities surrounding 3-D work, interfacing with specialist colleagues was required in delivering these advances.

Antecedent to numerical activities was attaining greater understanding of the actual human upper-airway giving an important *a priori* knowledge for subsequent model development. Accordingly the combined teams first studies were to explore snoring *in vivo*, with the aid of a bronchoscope, the outcomes of which are included in Appendix A. This increased understanding of the kinds of motion and vibrations that future modelling would be expected to mimic. Following this, a testing framework was formulated for which the outcomes are presented in this chapter. The aims to be achieved were structured to yield greater understanding of a human upper-airway, and are summarised below:

- Extract useful geometries using *in vivo* techniques with ability to account for variations throughout the breathing cycle
- Examine whether soft-palate and pharyngeal motions were linked

- Examine, for an anatomically correct geometry, if the pressure field was well accounted for through simplified models without curvature
- Examine effects on a flow field of airway narrowing
- Develop an understanding of what simplifications could be made, or more specifically what were the key elements of the overall model and what varies temporally and spatially
- What findings can be carried across from the 2-D work of Chapter 3.8 to real airways

Medical literature (Woodson, 2003) suggests soft-palate motion to be implicated in around 30% of OSA cases, the remainder being due to collapse of the pharynx or a combination of the two. The previously deployed two-dimensional modelling provides the potential for a degree of linkage between the dynamics of the soft-palate and pharynx. White (1995) cited medical literature indicating the tongue was well controlled by the comparative active *genioglossus muscle* so was unlikely to be implicated in pharyngeal collapse, whereas the action of the lateral wall dilator muscles was purely tonic and orthogonal to the line of action, further implicating this as the site of potential instability. One limitation to the 2-D model is that motion of soft-palate and pharyngeal side-walls are orthogonal requiring 3-dimensions to adequately model, the 2-D model is as such unsuited for this purpose. A three-dimensional analogue computational model was therefore devised and the various investigations pursued, presented herein. These investigations consider flow beyond the previously investigated laminar range now including turbulent flows.

Until recently researchers have examined, in isolation, the flow-driven dynamical behaviour of a flexible tube, studied with a Starling-resistor type of approach, or alternately the soft-palate problem with flow within a rigid-walled tube or channel. This was based on the assumption that the orthogonal motions of the soft-palate and the pharyngeal walls were largely subject to vastly different time scales and did not justify the additional numerical expense of coupling. In both types of study a simplified geometry was used that neglected curvature in the mean flow. The greater availability of computational resources now permits these problems to be considered together. The transition to three-dimensional modelling introduces many additional factors, with the inherent complexity this

implies. As for the 2-D modelling this necessitates efforts to reduce this complexity to limited changes allowing the effects of each to be fully examined and understood alone. This chapter sets out this research team's efforts to begin answering some of these questions.

4.1 Introduction

Firstly a model of an upper-airway with an anatomical 2-D model was modelled incorporating flow curvature effects. This is followed by a review of an analogue 3-D model incorporating soft-palate and pharyngeal compliance with no mean flow curvature. The results reported herein find a some linkage between the motion of the pharyngeal walls on the soft-palate. Moreover, the theories developed from the 2-D work of this thesis were re-confirmed in this 3-D model.

A recent study within our group of collaborative researchers utilised an endoscope to view the upper-airway while a subject produced forced snores through their nose with the mouth shut. While the results from this study were qualitative, findings made informed this 3-D work, the results from this study are presented in Appendix A. Not only did the soft-palate vibrate rapidly but side walls deflected inwards and also vibrated with the connecting tissue and pharynx. This indicates that the frequency of vibration could be of less use than other researchers have thought owing to the complex nature of vibration. Moreover, it highlights the need to understand the mechanism underlying channel narrowing and hence the catalyst for vibration. Another observation was that while breathing through both nasal and oral passages, upon commencement of heavy breathing the soft-palate shut off the nasal passage. This indicates the potential presence of some instability of the soft-palate that neuro-muscular activity seeks to prevent. Clearly under such heavy breathing critical velocities could be exceeded despite the other neuro-muscular systems being fully operable. While this is for future work, it is perhaps a measure of an individual's susceptibility to vibration of the soft-palate could be determined from the flowrate or velocities at which this occurs.

Customarily, it was thought that soft-palate motion was the main source of instability in the upper-airway. The transverse vibrations of the soft-palate were far faster than the motion of the surrounding upper airway walls, though linked

to neuro-muscular activity associated with the breathing cycle. For example, the pharynx has a typical oscillation time of 1 to 2 cycles per second thus an order of magnitude smaller than frequencies during snoring of between 20 and 320 Hz (De Backer *et al.*, 2008). This resulted in the assumption that, during snoring, the structural behaviour of the upper-airway could be modelled as one of a flexible structure in a rigid channel (Aurgan & Depollier, 1995). However, following the 2-D work in Chapter 3.8 and the findings in Appendix A, the interaction between the soft-palate and the compliant lateral pharyngeal walls appears to be more significant. Collapse of the pharynx would be related to the mean position of the soft-palate that would influence the downstream pressure. The 2-D model of Chapter 3.8 showed this mean position to be susceptible to large motions for one-inlet closed and with both-inlets open together with asymmetric positioning. Changes to the response of one and the influence this would have on the other's behaviour is therefore investigated in the following sections.

With these preliminary studies complete the target was now to build a full anatomically correct model, for which several techniques were examined including developing techniques to distinguish between various portions of the breathing cycle. The 3-D models developed were used to investigate flow conditions theorised in the previous chapter namely soft-palate mean motion as an indicator of bulk resistance found to be implicated with the start of inhalation or exhalation and separately the pressure reductions associated with reduction in caliber of the pharyngeal walls.

While this research advances the state-of-the-art one remaining element of research not fully pursued was biologically consistent material properties and techniques to mimic neuromuscular activity. These activities would be a logical next steps allowing full incorporation of FSI techniques into modelling.

4.2 Preliminary 2-D model with the inclusion of flow curvature

A preliminary two-dimensional study was conducted in order to provide an approximate description of the flow field in the upper-airway and guidance as to the expected flow-induced displacement of the soft-palate when flow curvature

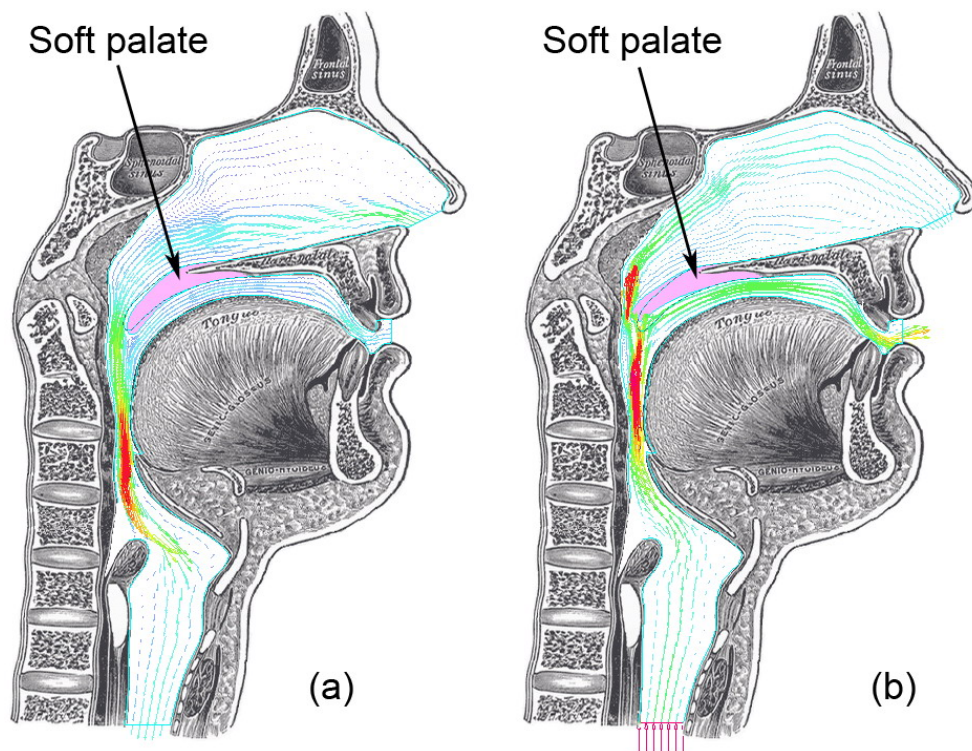


Figure 4.1: Two-dimensional calculation of the motion of the soft palate with a rigid anatomically valid upper-airway geometry during (a) inhalation, and (b) exhalation. (with the red peak values being 9.1 and 6.4 m/s, and blue indicating less than 1.5 and 1 m/s, in (a) and (b) respectively.) Adapted from Gray (1918a) "Anatomy of the human Body" online.

was included. Figure 4.1 shows a typical result using a model built from the geometry of Gray (1918b). The computation was performed using ADINA R & D. Inc (2006) to undertake a FSI (Fluid-Structure Interaction). The analysis used approximately 40,000 nodes. The material properties of the soft-palate were assumed linear with elastic modulus in the range 8-12 MPa. The driving pressure generated by the lungs was chosen such that laminar airflow occurred with peak airspeeds in the domain being, respectively, 9.1 and 6.4 m/s for inhalation and exhalation. Note that the turbinates in the nasal cavity were not included in this model. The turbinates promote turbulence to generate heat and mass-transference, importantly, also increase flow resistance. The gross flow-structure features in the simplified system show motion at the end of exhalation the soft-palate has moved so as to narrow the passage to the nasal airway (the velopharynx). Thus, there is the possibility of low-pressure intensification at this site during the commencement of inhalation. The simplification excluding the turbinates results in the nasal resistance being reduced, to the point that the bulk of flow was now through the nose rather than mouth and reverses the deflection of the soft-palate, for exhalation, to the nasal passage rather than the oral. The results were more representative of nasal breathing only rather than two channel flow and the influence of flow curvature appears subtle. The influence of soft-palate position on the pressure field was explored in the three-dimensional simulations developed and conducted below.

4.3 Analogue 3-D model with compliant palate and pharynx

With the aim of addressing some of the matters raised above regarding the interaction of orthogonal motions of the soft-palate and pharynx, a three-dimensional analogue computational model was developed; see Figure 4.2. This 3-D model was capable of capturing the essential dynamics of the soft-palate and pharynx while retaining simplicity and thus enabling representative phenomenology to be extracted. Again the Navier-Stokes equations were solved over the domain, fully coupled to the mechanics of the flexible surfaces.

The geometric configuration shown in Figure 4.2 (a) allowed simple numerical modelling while the bulk sizing and material properties reflect those of the human

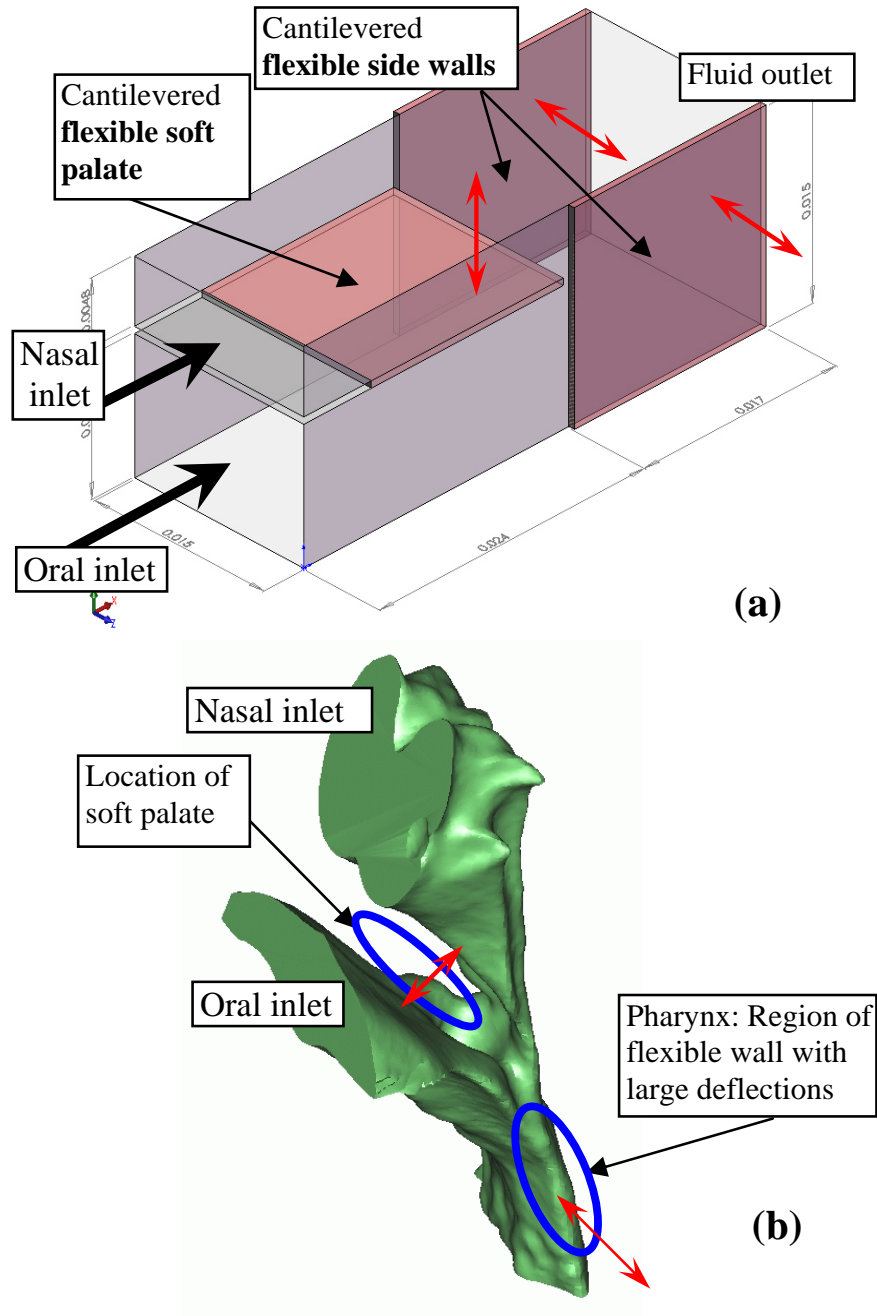


Figure 4.2: Upper-airway models, (a) 3-D analogue computational model, and (b) Anatomically correct reconstructed geometry (flexible regions circled in blue). Red arrows indicate principal directions of flexible-boundary motions.

upper-airway, similar to those used in the 2-D exemplar of Chapter 3. A notable departure from the real system was the representation of the pharyngeal side walls as cantilevered flexible-plates. This was a necessary assumption to overcome the difficulty of identifying rigid connection points for the pharyngeal walls in the airway (which in reality are not rigid or stationary) together with simplifying the overall geometry. Accordingly the inherent flexibility of the cantilevered arrangement permits the pharyngeal walls to collapse from the sides as clinically observed in airway narrowing and closure. The soft-palate cantilevered plate's initial position was neutral (straight), to develop motion this was asymmetrically positioned with $\varepsilon = 0.33$.

The commercial FSI software ADINA R & D. Inc (2006), a fully coupled finite-element solver, was used for this investigation. Before running a number of cases with manageable simulation run times a high-resolution preliminary simulation comprising 250,000 fluid tetrahedral elements and 30,000 solid brick elements, as described in Section 3.7.3 of Chapter 3. Accordingly, simulation run time were reduced with the level of discretisation down to 40,000 fluid plus 3,000 solid brick elements resulting with just a 3% reduction to the calculated maximum deflection of the soft-palate.

A series of numerical experiments were then performed for a range of soft-palate and side-wall material properties varying the Elastic modulus of the side walls (E_w) and palate (E_p). A single applied pressure load of 0.0028 Pa was used throughout and the properties of air were those at 20°C. A typical result, showing the ramp-up of pressure to maximum over 1 second then constant for the remaining 9 seconds, is shown schematically in Figure 4.3. The soft-palate deformed upward (y -displacement) and in the quantitative results that follow the position of Node A was tracked as being representative of soft-palate (maximum) deflection. This was reasonable since the deformation of the soft-palate was essentially planar. Correspondingly, (z -displacement) deformation of the side-walls was represented by Node B, at mid-channel height. In this case variation in the vertical direction was non-negligible, choosing the mid-point recorded the maximum displacement. This also indicated the presence of a pressure gradient in a plane orthogonal to the streamwise direction of flow, an explanation of this orthogonal pressure gradient will be revisited in Section 4.6.1.

The study used a combination of soft-palate properties that yield stable (damped)

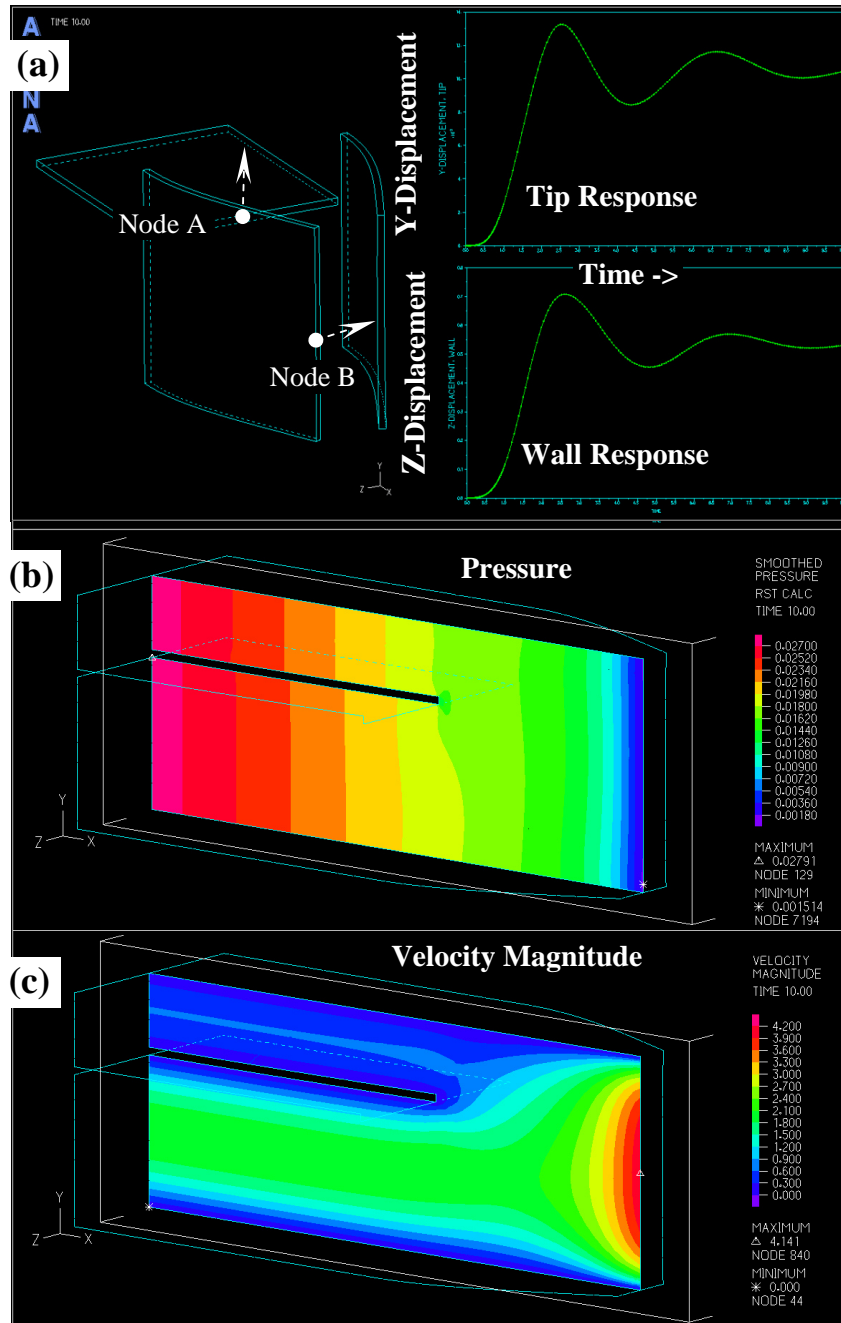


Figure 4.3: Illustrative simulation of the flow-structure interaction; (a) generation of a 10-second time series and centreline flow at final equilibrium, (b) pressure contours, and (c) velocity magnitude.

oscillatory behaviour, i.e. the mean flow speeds and Reynolds number were beneath those that would produce self-sustaining palatal flutter. Figure 4.4 shows illustrative time series for the palate-tip (a) and side-walls (b) for the case of side-wall elastic modulus (E_w) being 200 N/m^2 with a range of soft-palate elastic moduli (E_p). It was seen throughout that the soft-palate deflected upward into the narrower channel of greater resistance to a new static equilibrium position, as predicted by the two-dimensional model, exhibiting the same flow-curvature phenomena, while the side-walls moved inward with the downstream tip creating a partial closure of the channel. Soft-palate oscillations were seen to be attenuated in these sub-critical conditions. At the soft palate tip the upper and lower channel flows combine and a separated shear layer exists that must deflect towards the top rigid wall like the flow over a backward facing step, the extreme case of infinite upper-channel resistance. Resultant curvature of the isobars in the lower channel relative to those in the upper channel produced a net upwards force that deflects the soft-palate. As seen in Figure 4.4 (a), the lower the value of the soft-palate stiffness, the greater was the deflection.

Changes to E_p were found to generate only a negligible change to the final side-wall deflection see Figure 4.4 (b) even for large deflection (not shown here). Where soft-plate deflection were manually increased by 28% results in only a maximum change of 2.8% in the amplitude of side-wall movement. This signals the insensitivity of side-wall motion to the dynamics of the soft-palate for situations with two inlet channels open and thus may be predicted by assuming a rigid soft-palate. Again this reconfirms the 2-D model results that for two-channels, flow redistribution essentially holds mass flux constant as the soft-palate varies each channel's resistance. It is this mass flux that holds greatest influence over the deflections of the pharynx as the pressure gradient correlates most closely with mass flux.

However, palatal behaviour of both frequency and amplitude content is strongly dependent upon both soft-palate and side-wall material properties as shown in Figure 4.5. Here Palatal response was vastly changed as E_w varied including resonant amplifications in (b & c) as for $E_w = 150 \text{ Pa}$.

Importantly the response of the side-walls varies the mass flux through the domain. Whereas for two-channel-flow palatal motion results in a relatively constant mass flux as flow redistributes from the channel of higher resistance to that

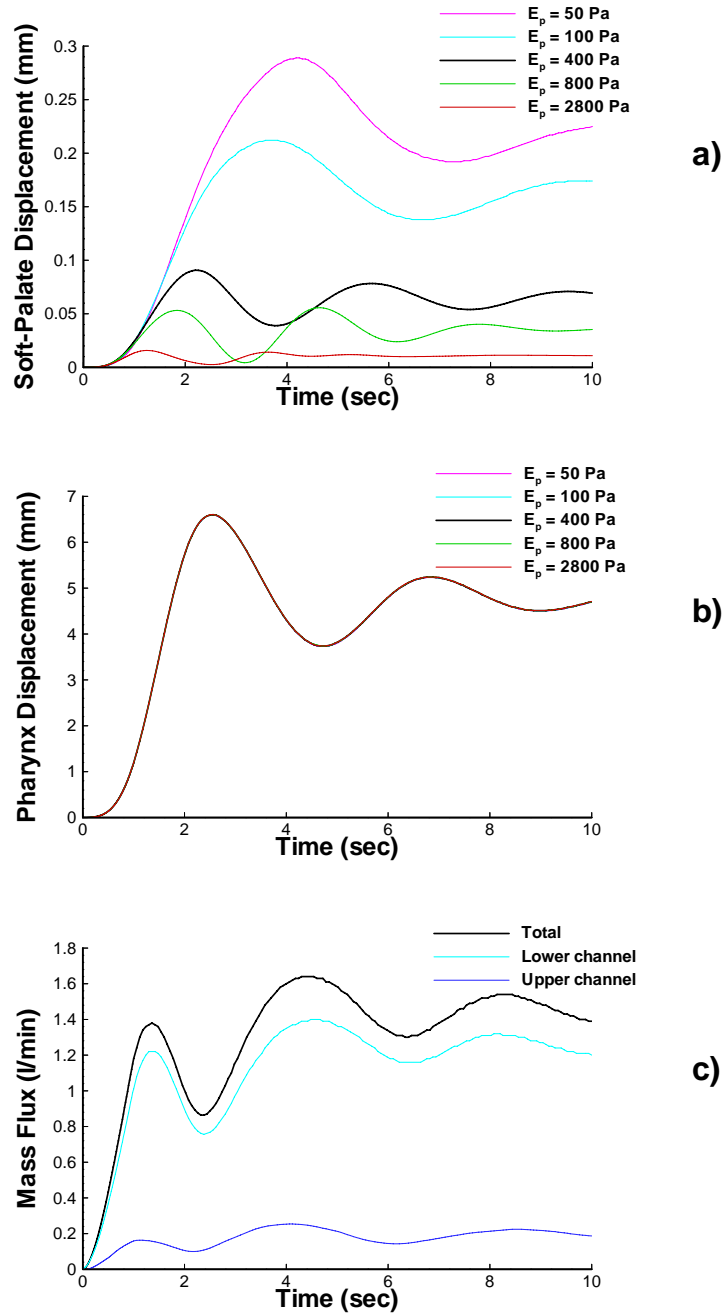


Figure 4.4: Dynamic response of palate tip and wall under various E_p - soft-palate stiffness, pharyngeal wall stiffness $E_w = 200$ Pa throughout. (a) Palatal response, (b) Pharyngeal Wall response & (c) Mass flux for a single case with $E_p = 400$ Pa.

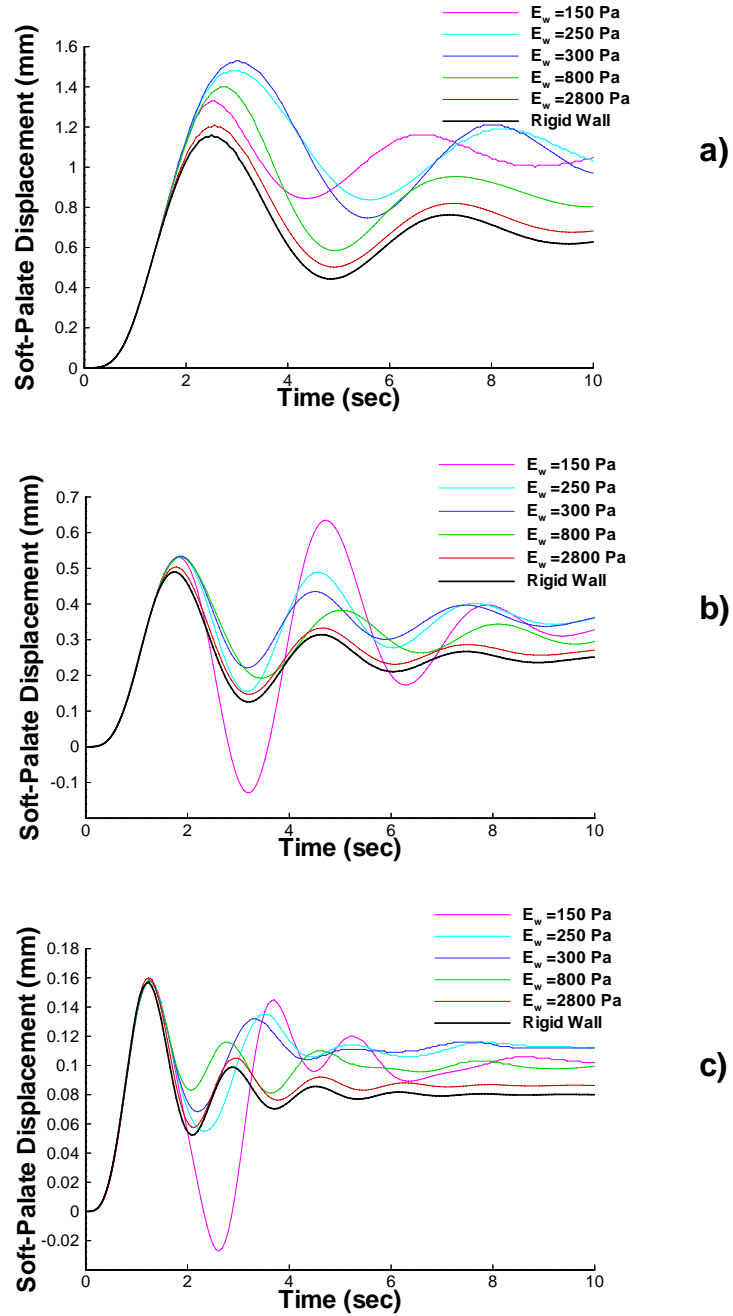


Figure 4.5: Dynamic response of palate tip, demonstrating effect of side-wall stiffness on tip motion for three different soft-palates: (a) $E_p=200$, (b) $E_p=800$, and (c) $E_p = 2800$ N/m².

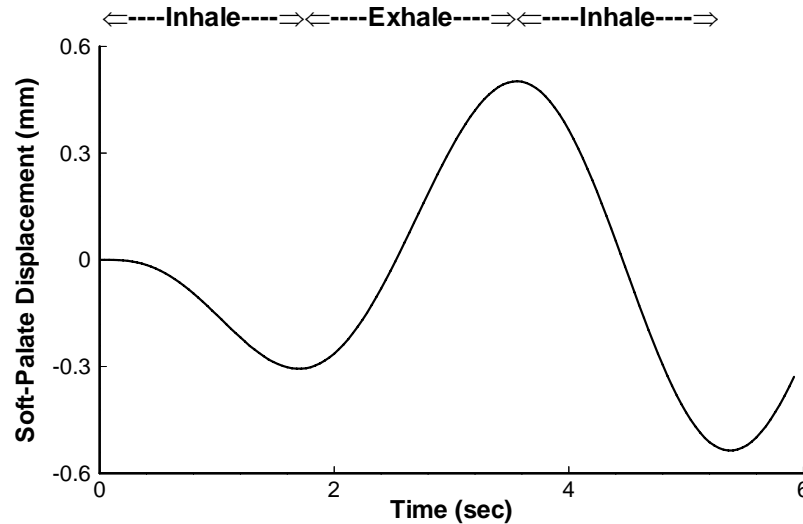


Figure 4.6: Soft-palate tip deflection versus time. Response of soft-palate asymmetrically positioned subject to sinusoidally varying pressure applied drop, $E_p=800$ and $E_w=1600$ N/m². Lower channel blocked as an example of the most extreme case of calibre imbalance. Note - increasing deformation of soft-palate over cycle.

of the lower. Figure 4.4 (c) shows the strong linkage with side wall deflection Figure 4.4 (b) resulting in the motion of the side walls coinciding with mass flow changes. Moreover, given the motion is a divergence 1st mode type, mass flux variations are in phase, without any lead or lag as a result of 2nd or higher mode complications.

Following on from Chapter 3.8 and the effect of single channel flow on breathing cycle, a sequence of inhalation, exhalation and then inhalation was modelled, applying a sinusoidal varying pressure drop across the domain. The period of oscillation, was set to 4 seconds (fairly rapid breathing) and the pressure-drop amplitude P_D was 0.0028 Pa. The elastic moduli of the soft-palate and side walls were 800 and 1600 N/m² respectively. The lower channel was closed at its left-hand end, thereby modelling nasal breathing only as performed in the 2-D simulations. Figure 4.6 presents the results of this simulation as a time series of the soft-palate tip. In the initial inhalation phase, the soft-palate deflects down-

wards into the channel of greater resistance (blocked in this case) as predicted in Chapter 3.8. In the following exhalation the palate then deflects upwards into the open channel so as to increase channel or pharyngeal resistance. With the return to inhalation, the soft-palate moves downwards once more, achieving a greater amplitude than that of the first inhalation, whereas for a constant mass flux attenuation was the response. Note that amplification was not due to conventional soft-palate flutter but to its interaction with a time-dependent mean flow and or coupling with the motion of the side walls. This result demonstrates that such interactions can yield an amplification of the soft-palate deflection into the open channel at sub-critical velocities thereby increasing its resistance or *resistance-peaks*. In an anatomical system, such *resistance-peaks* would be accompanied by increased lung suction and thus a greater likelihood of airway collapse and apnoea.

4.4 Anatomical 3-D model developed from CT scans

An anatomically correct 3-D geometry was required to examine these findings in greater detail. This step would customarily be fraught with difficulty owing to capturing data over an extended domain which moves during the breathing cycle. An established method combines traditional Computed Tomography (CT) scans to generate the raw data, which comprising a number of slices. This requires further postprocessing using software such as MIMICS to combine the 2-D slices into a 3-D geometry, producing a mesh-able geometry following some intervention and ‘cleaning up’ of the image. The need to clean up the data was a necessarily element to overcome the shortfalls of the CT method which fails to capture breathing cycle features and associated motion. For example, should a swallowing event occur the data set would otherwise be corrupted and may require to be recaptured.

With an anatomical geometry developed, a flow field was implemented through the upper-airway domain, illustrative cases were conducted for inhalation. The geometry of the CT model relates to the region spanning the velopharynx and oropharynx see Figure 4.7 and the oral opening. This geometry spans the region thought most prone to collapse and apnoea.

Computations for single channel and dual channel flow for inhalation were con-

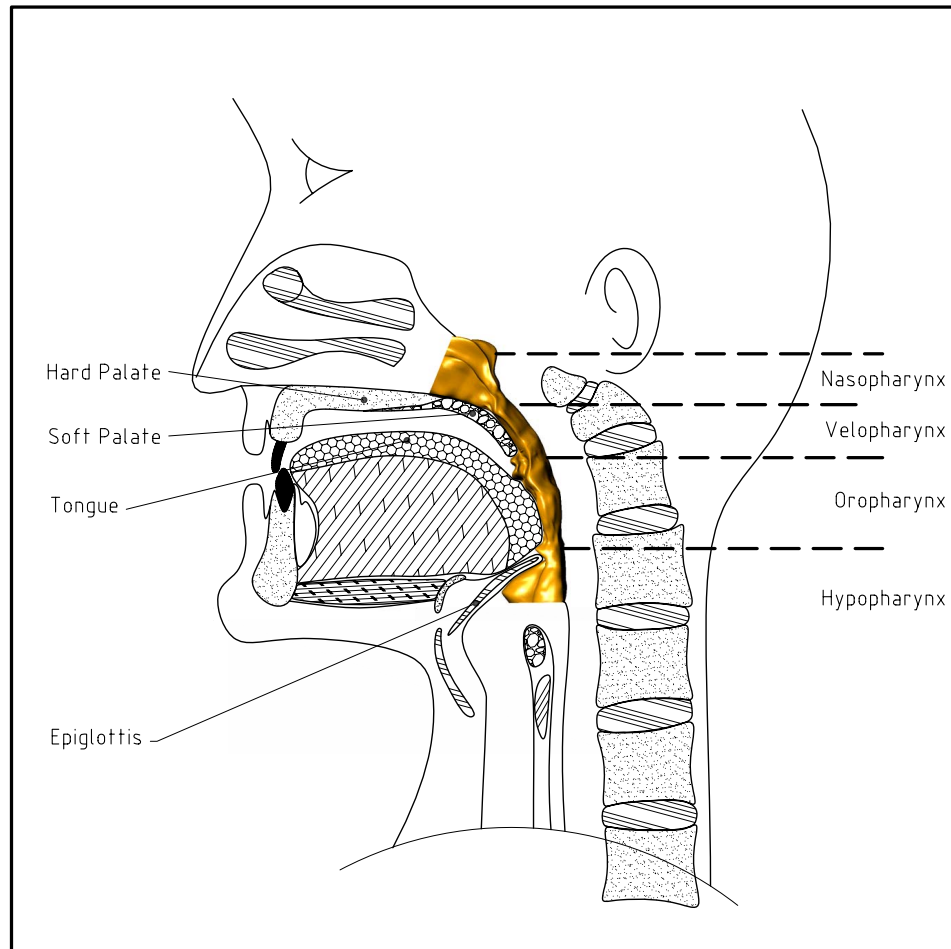


Figure 4.7: Schematic representation of a mid-sagittal view of the human head and neck highlighting the relevant upper-airway anatomy. The gold-coloured surface was the actual geometry that reconstructed in Section 4.5 using other methods to generate the geometric data.

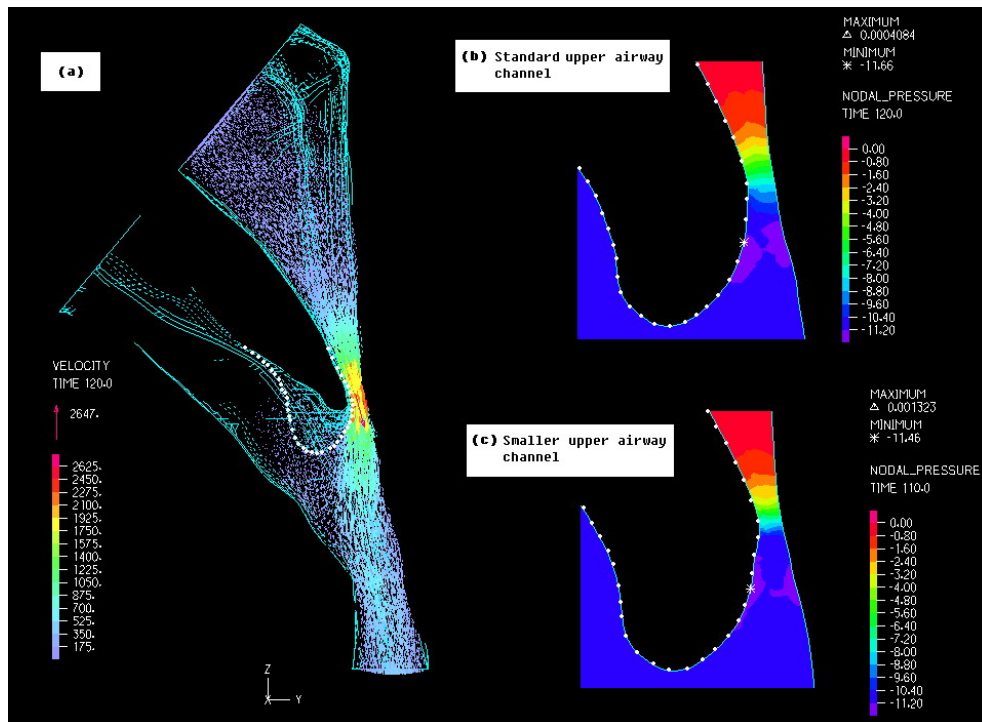


Figure 4.8: Computed flow field for inhalation only through the nasal inlet, (a) Three-dimensional plot of velocity vectors for standard case, (b) Pressure field for standard case, and (c) Pressure field for a case with the soft-palate slightly deformed, relative to the standard case, towards the posterior of the pharynx. (Note velocity and pressure scales are respectively in mm/s and dynes/mm².)

ducted. The finite-element solver of ADINA R & D. Inc (2006), with 160,000 tetrahedral linear elements, was used to carry out the solution of the Navier-Stokes equations without turbulence modelling. Laminar flow was deemed reasonable because the Reynolds number, based upon section hydraulic diameter, was in the range Re 330-350 at the point of maximum constriction. No-slip and no-flux boundary conditions were applied on the walls and the flow driven by a typical applied pressure drop of 110 Pa (Sung *et al.*, 2006) over the domain.

Figures 4.8 (a) (velocity vectors) and (b) (pressure contours in the palatal region) were obtained from a single computation with inhalation solely through the nasal entry. The white dots delimit the mid-sagittal extent of the soft-palate, otherwise obscured in the three-dimensional representation for Figures 4.8 (a, b & c). As expected the maximum velocity occurred where the passage, bounded on the anterior side by the soft-palate, was at its narrowest cross-sectional area of 23.8 mm². The peak velocity was 2.63 m/s and the flow rate, 28 ml/s. The

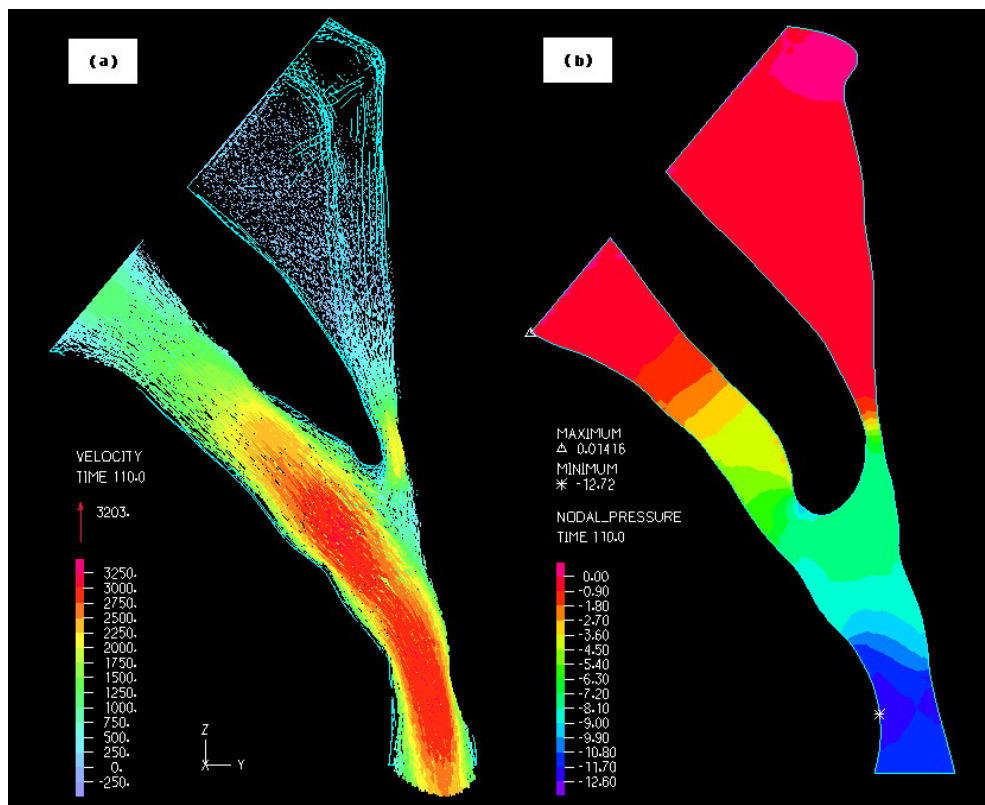


Figure 4.9: Computed flow field for inhalation through both oral and nasal inlets for standard case, (a) Three-dimensional plot of velocity vectors, and (b) Pressure field. (Note velocity and pressure scales are respectively in mm/s and dynes/mm².)

(streamwise) gradient of pressure drop was, similarly, most pronounced within this region. Figure 4.8 (c) presents pressure contours for a case where the soft-palate had been ‘artificially’ deflected towards the posterior wall narrowing down to 22.2 mm^2 . The maximum velocity for this case was 2.80 m/s while the flow rate was reduced to 23 ml/s . Importantly, a reduction in area of just 7% due solely to movement of the soft palate leads to a reduction in flow rate of 18%. Again this demonstrates the principle that without flow reassignment as was possible with the two open channel configuration instability will be more pronounced.

Comparing the pressure plots of Figure 4.8 (b & c), demonstrates the sensitivity of single channel flow to minor variations where the pressure gradient for the narrow channel was greatest at the site of narrowing, thus concentrated over a shorter streamwise extent. Had the soft-palate and pharyngeal walls been deformable this would have had two implications for possible airway closure. The first is the increased extent of the low-pressure region in the pharynx downstream of the channel’s narrowest point, thereby promoting collapse of the pharynx. The second, results from an increased net force across the palate upstream of the narrowest point, that would serve to deform the palate in the anterior direction thereby relaxing the constriction. Of interest here is that to maintain constant flow rate, the lungs would increase effort and a far lower pressure would be developed to overcome the 18% flow deficit, as a result of varying palatal position, increasing the possibility of airway-wall collapse.

Figure 4.9 shows flow field generated when inhaling through both oral and nasal inlets. The reduction of system resistance due to the open mouth led to a flow rate of 193 ml/s and a maximum velocity of 3.2 m/s with the bulk of inspiration occurring through the oral passage. The corresponding pressure field indicates higher pressures in the region of the soft-palate and uvula as compared with the nasal inhalation of Figure 4.8. Furthermore, the soft-palate would experience a net force that would move the soft-palate in the anterior direction thereby opening the nasal passage as predicted by the simplified 2-D model of Section 3.8. Both of these effects would serve to decrease the likelihood of airway-wall collapse.

Results for the 3-D anatomical model with steady airflow, showed the dependence of palatal position on the pressure within the pharyngeal region. This also strongly implicates palatal position with airway collapse during an apneic event.

Although the effect of palatal motion requires a full flow-structure-interaction analysis to determine how this occurs and under what circumstances, as illustrated in Section 4.3, the relationship is firstly dependent on number of channels open and then the variable dynamics at play as the competing constituent resonances interact in a highly non-linear fashion.

4.5 Anatomically accurate 3-D reconstructed geometry using anatomical optical coherence tomography (*a*OCT)

As a first attempt, the temporal problems with CT & MRI methods were overlooked in Section 4.4. The problems arising from these approaches are well understood and need resolution to address the final aim of models tailored to individual sufferers. Nithiarasu *et al.* (2008) related some of the problems associated with CT and MRI, principally relating to the amount of radiation the sufferer is exposed to and the inability to resolve temporal motion of the airway throughout the breathing cycle. Producing lower resolution, magnetic resonance-type imaging leaves the resulting model overly sensitive to temporal factors, such as patient motion inherent in normal breathing.

The special challenge lies in the need to measure a time-varying interior geometry, the access to which is highly restricted. These characteristics render the application of well-developed reverse engineering and profiling technologies wholly unsuitable. For longer duration sleep studies CT and MRI would be impractical as sleep would not be possible due to machinery noise and requirements to remain stationary together with the longer term considerations of extreme radiation exposure.

This section focuses on a method which overcomes these shortfalls establishing a technique that can be used over long periods such as sleep studies and is suitable for capturing temporal effects during normal airway motion. The method also requires later post-processing to construct an anatomically correct geometry for a sufferer's airway. The technique developed by our research partners (Armstrong *et al.*, 2006) satisfied or presented opportunity to satisfy these goals. Moreover, it being an experimental technique presented significant flexibility for customisation toward these ends.

The geometry of an upper-airway was measured using anatomical optical coherence tomography (*aOCT*), a variant of OCT specifically designed to map the internal anatomy of large hollow organs. For this investigation the optical probe was placed inside a transparent catheter (3.0mm outer diameter). Access to the airway was gained via the nares (of the nose) to the level of the mid-esophagus. Once in position, the catheter was taped to the external nares, see Figure 4.10. The probe was moved within the catheter without stimulating the airway mucosa. This method then permits awake or sleepful individuals to have measurements acquired, over an extended period without any significant morbidity. In this study the individual was resting in the supine position only.

Specifically, the system operated by directing a beam of light orthogonally to the catheter. The distance between the rotating probe head and the interface of the air and airway wall was determined from the reflected light using a low-coherence optical interferometer. The rotation of the probe captured quantitative cross-sectional images of the upper-airway recorded in image form. The probe head was controlled using a customised computer program, which precisely rotated and translated the probe head to various levels within the pharynx to record cross-sections of interest. These tomograms could be viewed graphically in real time or reconstructed in the form of a video. The rotation rate of the probe used herein was 1.25 Hz. Thus, for quiet breathing at 15 breaths per minutes, 5 full cross-sectional images were acquired within each breath.

A typical set of results for one ‘pullback scan’; as the probe translates slowly and progressively (0.2 mm/sec) upwards within the catheter from the esophagus to the nasal cavity while continuous recordings of airway dimensions was performed, is shown in Figure 4.11. One pullback scan, in which the entire geometry is captured, takes approximately 12 minutes to complete. The *aOCT* system has undergone testing, (Armstrong *et al.*, 2006), for both airway phantom and in vivo measurements against CT scans. The mean error in measured cross-sectional area (CSA) of circular phantoms was 0.5%, or 0.1 cm², which corresponded to a mean error in radius of 0.07 mm.

One *aOCT* data-set (measurements obtained from one pullback scan) produces more than 800 unique images for examples see Figure 4.11, each one being in a plane orthogonal to the catheter. In order to derive the CAD model, the catheter’s locus required to be known. This was obtained by use of a CT scan



Figure 4.10: Typical *a*OCT apparatus including mask to capture breathing related information and the catheter taped in position.

as shown in Figure 4.12 (a). This locus was assumed time-independent because the catheter was essentially rigid once taped in position at the external nares and held in place by contraction of esophageal muscle. This is shown as the locus OP in Figure 4.12 (d) and the plane, of dimensions 55.5 mm by 55.5 mm, in which the *a*OCT mapped out the airway cross-section, marked abcd. The 2-D geometry in the local coordinate system was then transformed into a global 3-D coordinate system seen in Figure 4.12 (e) giving form to the anatomical model. Forty six images were selected, away from swallowing events, at the same time point within the breathing cycle, which was assessed continuously by inductance pneumography see Figure 4.10 & 4.11 giving a lung-volume time series synchronised with the pullback scan.

For illustrative purposes from this one pullback scan, two three-dimensional models were built, representing the airway at the end of inhalation, Figure 4.13, and at the end of exhalation, Figure 4.14. On close examination these show that both lateral and anteroposterior dimensions of the airway change over the breathing cycle. The upper-airway geometries shown were for those of a healthy subject.

Clearly, the geometry at any intermediate time in the breathing cycle could

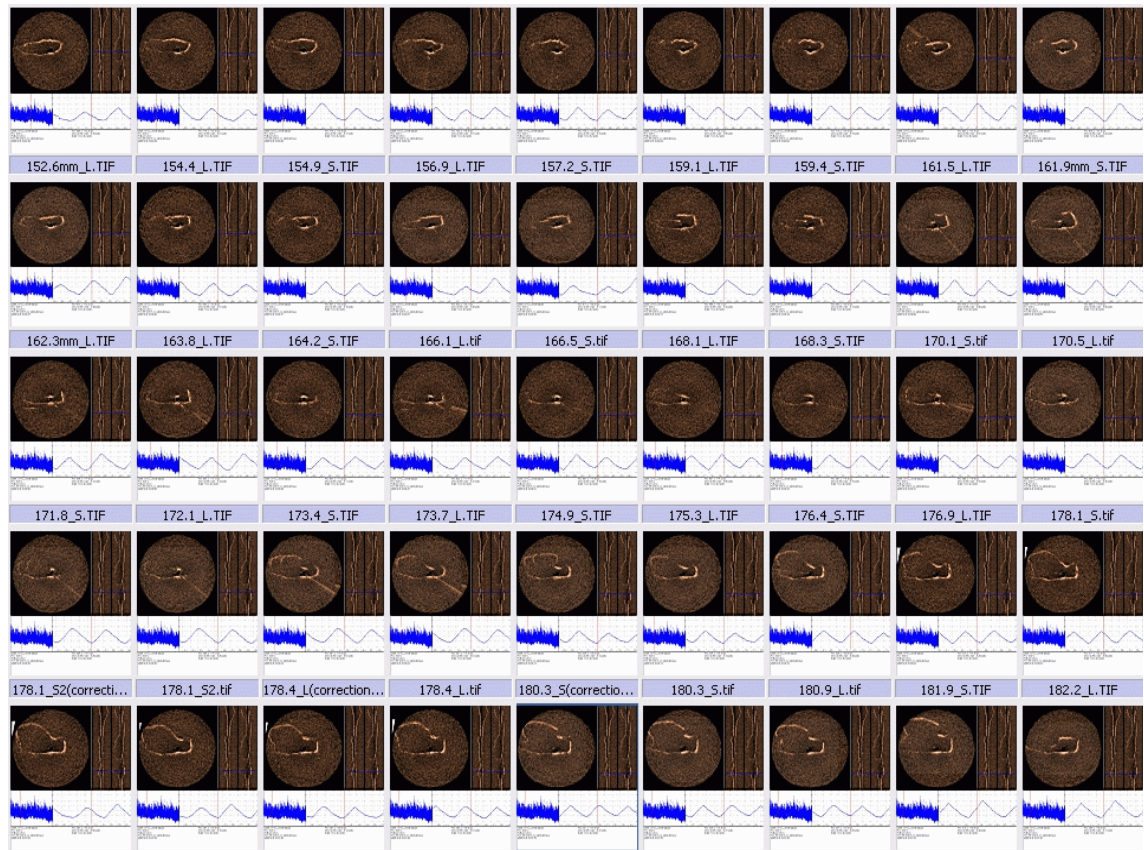


Figure 4.11: Series of slides generated by the *a*OCT system. Each slide captures geometry, location in breathing cycle and spacial information. Note an enlarged slide is included with in 4.12 demonstrating how the information was transposed into a 3-D model.

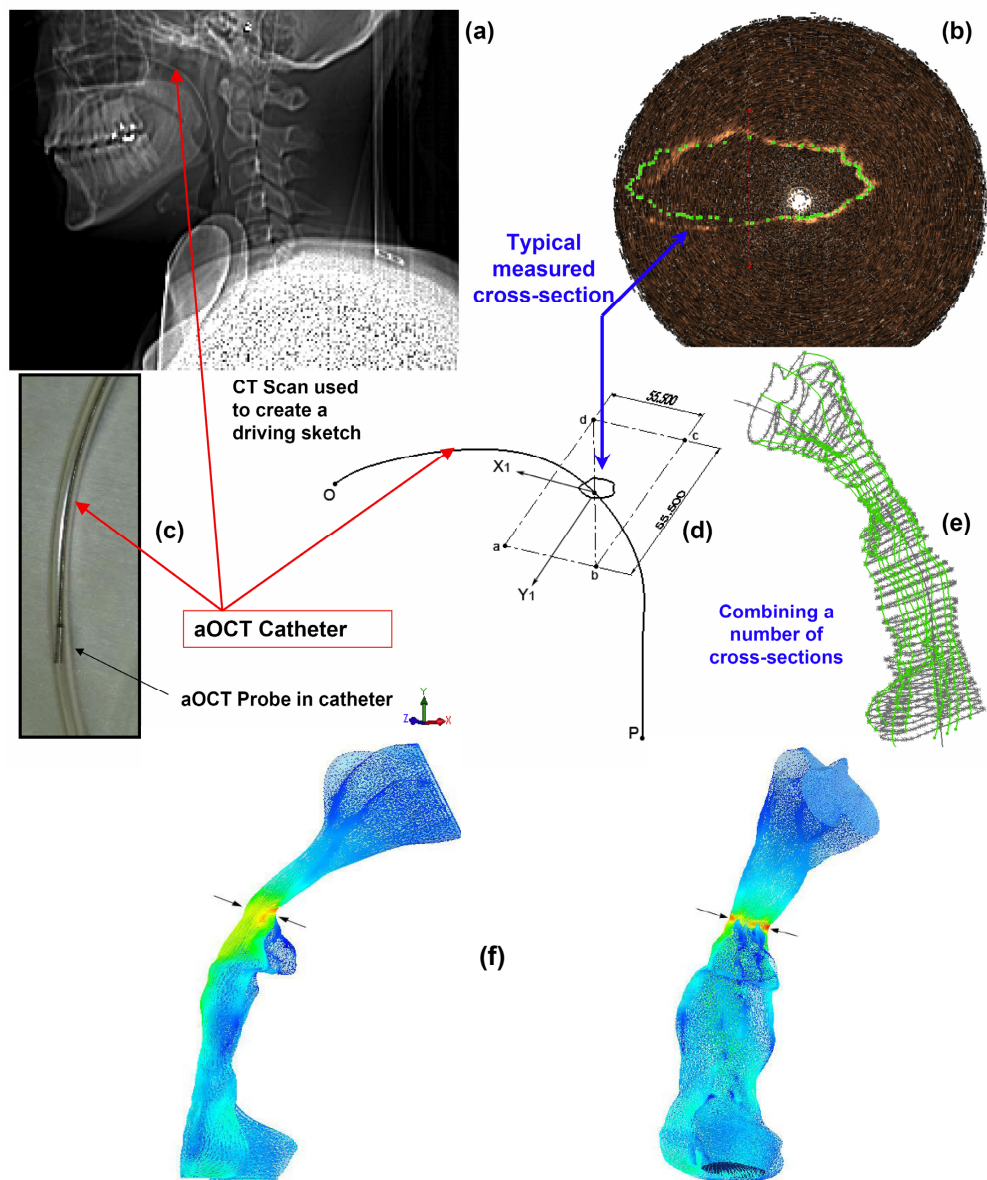


Figure 4.12: Progression from *a*OCT data acquisition to building an anatomical model of the upper-airway: (a) CT scan showing the locus of the catheter, (b) one *a*OCT geometry slice, (c) probe shown in the catheter, (d) one *a*OCT data set fitted to the catheter locus based on orientation and position from datum point, (e) 46 *a*OCT data sets added to the locus with the outline of the reconstructed geometry evident, (f) two images of velocity plots within the meshed model.

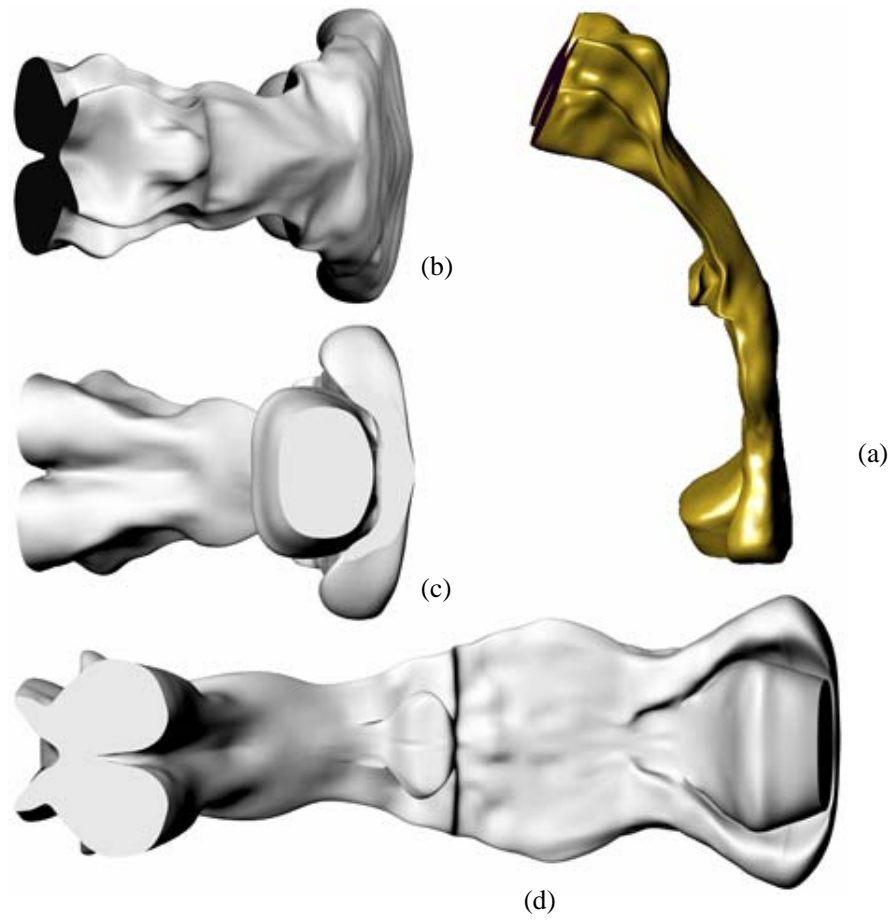


Figure 4.13: Various views of the upper-airway solid model at the end of inhalation (minimum volume): (a) from side, (b) from above, (c) from below, (d) from front.

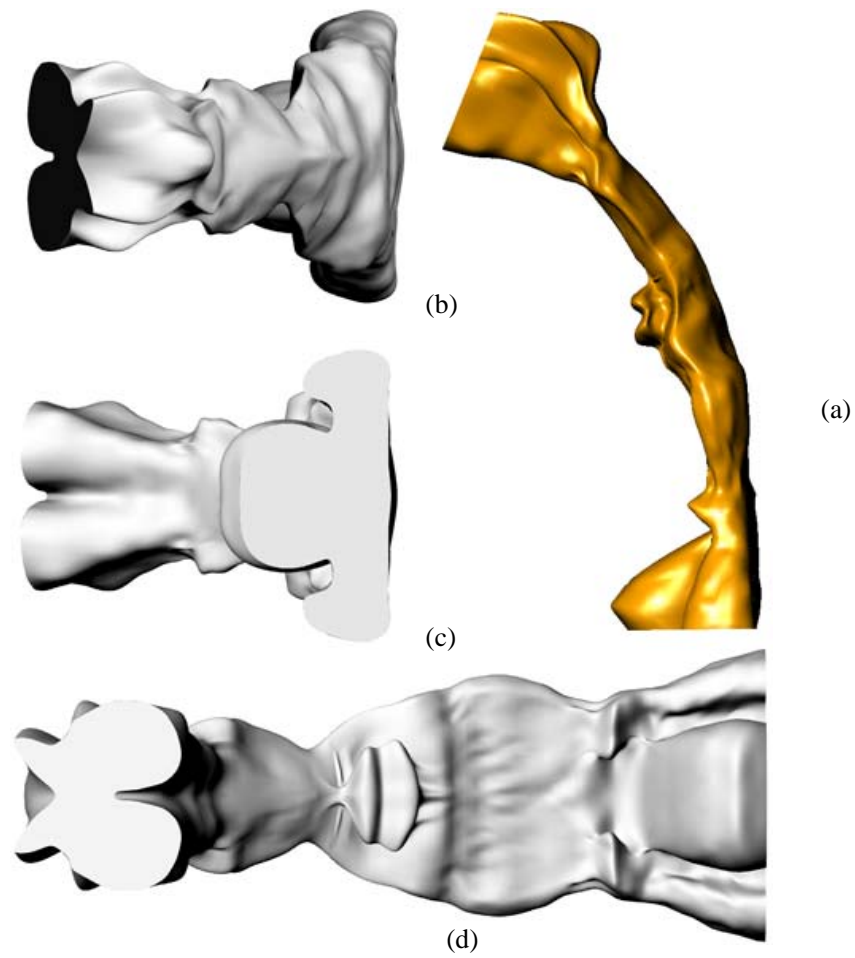


Figure 4.14: Various views of the upper-airway solid model at the end of exhalation (maximum volume): (a) from side, (b) from above, (c) from below, (d) from front.

equally be generated. Note that each normal section image was made symmetrical to axis Y1 in the local coordinate system, to reduce processing effort and data-storage requirements. No individual has a perfectly symmetric airway and geometric departures from the ‘naturally designed’ case would be present. However, asymmetry of the sectional geometry, and differences between the two nasal passages, can readily be accommodated using this *a*OCT technique and associated apparatus, although this would be more appropriate for later versions of the *a*OCT device that permit greater rotation speed than the current 1.25 Hz, further decreasing the period relative to that of the breathing cycle and reducing the time for a complete pullback scan. Efforts to increase the probes rotation to a more satisfactory speed of 4 Hz have thus far, been unsuccessful, suffering from a number of mechanical and instrumentation, implementation challenges. Another way to improve the linkage between the geometry captured and the breathing cycle is to progress in a contiguous manner, measuring discrete locations for an extended duration. This allows the data to be time averaged through an additional postprocessing step, decomposing each rotation into segments associated more closely to particular sections of the breathing cycle and thereby allowing variations between differences in the breathing cycle to be more effectively distinguished.

Having established the means by which the sequence of measurement, data-processing and solid-modelling was executed for a single case, this could equally be translated to any individual. Moreover, the procedure permits artificial variations to the reconstructed geometry, importantly allowing assessment of proposed interventions and their influence on stability of the upper-airway using numerical modelling. One such case is examined in Section 4.6.

In summary the procedure developed incorporates a non-contact measurement system, anatomical optical coherence tomography (*a*OCT), to generate a three-dimensional solid model of the entire upper-airway. The procedure has been used to capture the time-dependent geometry at the two extremes of the breathing cycle at the end of both inhalation and exhalation. Having demonstrated this, by extension, a record of the full history of the geometry as it varies through the breathing cycle now becomes attainable.

4.6 Flow-field modelling of a reconstructed human pharynx

This section reports on a number of numerical experiments for inhalation only, that were performed on the reconstructed geometry of Section 4.5. An investigation of the effect of soft-palate displacement and side-wall deformation on the pressure field for an airflow within the upper-airway was conducted. This utilised a number of solution methods to validate the novel phenomena found, for which the complete form may be viewed in Lucey *et al.* (2010).

Again the geometry, spanning the velopharynx and oropharynx seen in Figure 4.7 was used. Generally this would be where the airway has its narrowest caliber and, thus most prone to collapse during inhalation (Verbraecken & De Backer, 2009). However, it is acknowledged that in some OSA patients upper-airway collapse occurs at the end of expiration preceding the apnoeic event (De Backer, 2006).

Since the *a*OCT probe was nasally introduced in this application, the oral passage is hidden from view (by the soft-palate and uvula) and would, therefore, need to be reconstructed from CT scans. However the mouth is most often closed during sleep and/or the oral cavity occluded by apposition of tongue to palate. For healthy breathers nasal breathing offers a mechanical advantage, due to heat and mass transfer conditioning during inhalation and recovering products of respiration on exhalation. As a result the oral cavity has not been modelled in this analysis which was for inhalation through the nose only, maximising efficiency as would be expected from a biological system.

For the simulations, a quasi-static assumption was made for the flow-field computations. The absence of FSI complexities and fixing the value of pressure drop between inlet and outlet enables purely geometric parameters in this 3-D model to be explored that have been absent in the previous sections on this thesis. In reality, not only are the surfaces comprising the upper airway compliant but the pressure drop varies during the breathing cycle, and indeed reverses for exhalation; the geometric variations were evidenced by Figures 4.13 and 4.14.

Utilisation of the quasi-static assumption required the airflow timescale to be much shorter than that of the breathing cycle. Computations of velocity indicate typical residence times of the air between the velopharynx and hypopharynx to be on the order of 0.01 s whereas, an inhalation had a time period greater than

an order of magnitude than this. The results here for quiet breathing indicate Reynolds numbers (Re) in the range 1800-3300, based on mean flow speed and hydraulic diameter (D'_h), defined as $4(\text{area}/\text{perimeter})$ at the site of minimum cross-sectional area in the velopharynx. However, for dynamically deforming airway walls and soft-plate motions the structural timescales would also need to be taken into account.

4.6.1 Reconstructed human pharynx modelling method and validation

The flow field was computed using OpenFOAM software OpenCFD Ltd (2009) discretising the governing equations into finite-volume form. The Reynolds Averaged Navier-Stokes (RANS) equations were solved using a $k - \omega$ SST turbulence model appropriate to flows with curvature and adverse pressure gradients. An assessment of the pressure-field dependence and sensitivity to the selection of turbulence model was also considered for completeness. No-slip and no-flux boundary conditions were applied at the walls and the flow driven by a pressure drop between entry and exit of the domain applied as uniform traction across the two cross-sectional areas. This obviates the *a priori* assumption of entry and exit velocity fields, and their imposition as boundary conditions.

An unstructured tetrahedral mesh biased towards regions of most rapid change in fluid variables was used. The mesh contained 1.5 million cells to achieve convergence, to within 0.5% of the target flow rate, both on iterating towards the correct pressure drop, and on the velocity and pressure in the grid. This grid gave $y^+ < 1.5$ throughout the domain except for some isolated spots downstream of the velopharynx where values between 2.5 and 3 were noted. The accuracy of results was checked by conducting a run with 5 million cells that gave $y^+ < 1$ everywhere, with no discernible difference to the velocity and pressure values computed using 1.5 million cells. The properties of air at 35°C were used throughout because pharyngeal air temperature was considered to lie within the range of 33 - 37°C.

Figure 4.15 illustrates the three-dimensional flow field in the velopharynx and upper oropharynx for the measured geometry of Figure 4.14. The applied pressure drop, $P_D = -11$ Pa, was chosen to achieve a volumetric flow rate of 0.00025 m³/s (15 l/min). Fitzpatrick *et al.* (2003) Performed measurements of airway

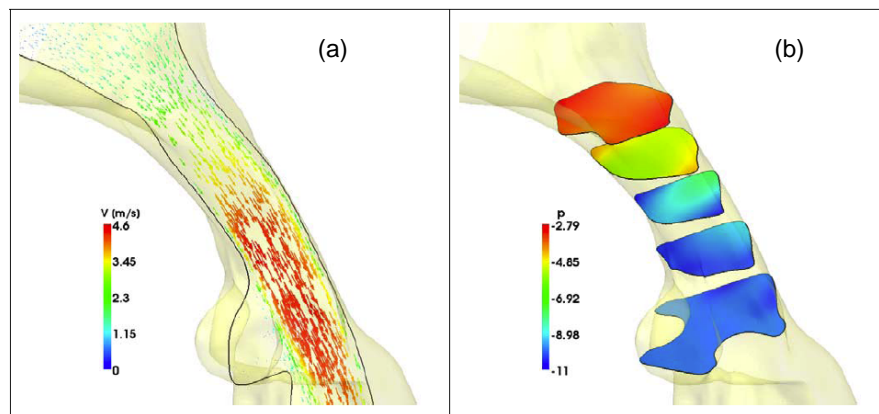


Figure 4.15: Computed flow field for the measured geometry in the velopharynx and upper oropharynx for inhalation through the nasal inlet, hence airflow direction is from top to bottom: (a) centerline velocity vectors, and (b) pressure values in five cross-sections of the airway, Note that the pressure legend denotes values of pressure divided by air density, (p/ρ) , in $(\text{m/s})^2$.

resistance for nasal breathing of healthy subjects in wakefulness suggesting a pressure drop of -60 Pa for the entire airway at 15 l/min. The smaller P_D utilised in this study was reasonable as only the contribution of the pharynx to the overall airway resistance was considered. Figure 4.15 (a) showed that a peak air velocity of 4.6 m/s was reached in the velopharynx where the soft palate effectively provides the anterior wall of the airway and yields the minimum cross-sectional area for the airway - the third cross-section identified in Figure 4.15 (b). The magnitude of this velocity aligns well with those of other computational studies for quiet breathing, for example both anatomically correct Mihaescu *et al.* (2007) and idealised Kleinstreuer (2003) studies respectively at 10 l/s and 15 l/s. Upstream of this minimum area location, the flow behaves like that in a pipe or duct of slowly varying cross-section. Downstream, the flow clearly separates at the tip of the soft-palate (uvula) past the tract to the oral inlet creating a free shear layer beneath which is a zone of recirculation. Figure 4.15 (b) shows the pressure contours in five cross-sections of the domain. The second and third sections were characterised by strong cross-flow pressure gradients. At the site of minimum area (the third section) the magnitude of the lateral side-wall pressure was approximately 50% greater than that of the posterior mid-line value. The cause of this phenomenon is the lateral variation in the airway cross-section and airway curvature, clearly seen in Figure 4.14 (a & d), which created a three dimensional streamline curvature whereby a cross-flow pressure gradient establishes to balance the centripetal effects on fluid elements. The lateral wall pressures were uniform owing to the symmetry introduced in the geometry reconstruction phase. Clearly, side-wall pressure could further reduce one side relative to the other should this symmetry be broken in the supine position or greater still should head or body rotation occur. Studies by Schwab *et al.* (1993) & Donnelly *et al.* (2003) suggest that airway closure may occur during normal quiet breathing and during apnoeic events due to the inward movement of the side walls. Thus, the existence and location of these low-pressure regions would be a significant component of the means by which inward motion of the side walls occurs when their degree of compliance is higher than some threshold value and symmetry of the airway broken.

The robustness of the sectional pressure field predicted with respect to the adopted flow modelling was assessed through a series of cases utilising different solution methods. Figure 4.16 (a-c) contrast pressure contours in the cross-section

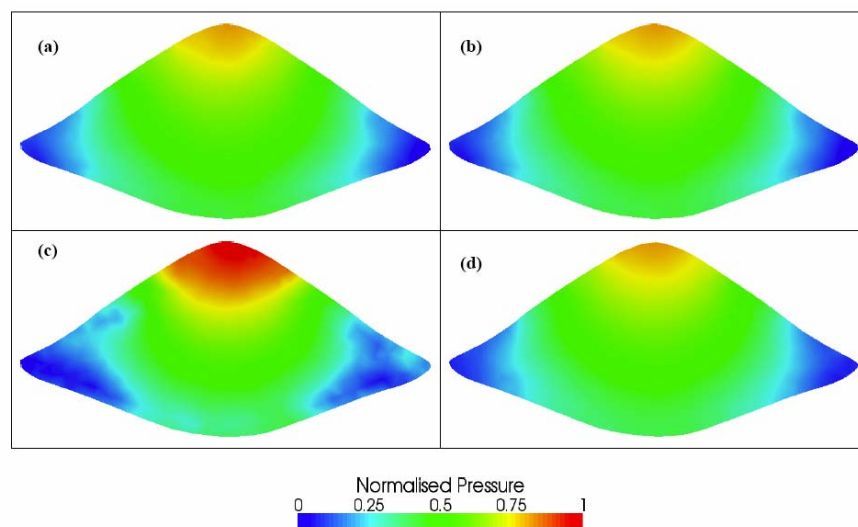


Figure 4.16: Comparison of the pressure fields in the measured pharyngeal cross-section of area of minimum area predicted by different flow models. For the standard stream-wise domain length depicted in Figure 4.14 and utilized throughout Figures 4.17 and 4.18: (a) unsteady laminar flow, and for turbulent flow, (b) $k - \omega$ SST model, (c) $k - \epsilon$ model, and (d) using the $k - \omega$ SST model for a domain extended by 30% in both upstream and downstream directions.

of minimum area as predicted by an extreme assumption of unsteady laminar flow and then two turbulence models, these being $k - \omega$ SST and $k - \epsilon$. This demonstrated that the phenomenon to be largely independent of flow model and that the $k - \epsilon$ model over-predicts the cross-flow pressure gradient as compared with the $k - \omega$. For an idealised geometry, Kleinstreuer (2003) and Zhang & Kleinstreuer (2003) show that the low Reynolds number (LRN) variant of the $k - \omega$ model was appropriate for upper-airway flows. Thus, while LES predicts the flow field with the greatest fidelity, the less computationally intensive $k - \omega$ SST model used herein captures the essential phenomenology that underlies the pressure field upstream of the flow separation seen in Figure 4.15 (b). Figure 4.16 (d) presents the computed pressure field using the $k - \omega$ SST model but with the streamwise domain extended by 30% in the upstream and downstream directions. Comparison with Figure 4.16 (c) demonstrates that the effect on the predicted pressure field in the velopharynx due to the choice of inlet and outlet locations in the model to be negligible.

4.6.2 Reconstructed human pharynx modelling results and Discussion

The preliminary results from Section 4.6.1 were used as the base case for comparison of geometric changes in the region of the velopharynx affecting flow and pressure fields. These variations were foreshadowed previously as being advantageous to model the effectiveness of corrective surgery. In this case what was being investigated was quite the opposite, although it does hold key information regarding the onset of pharyngeal collapse. The particular focus was in localised changes in flow curvature around constrictions and the manner these affected the cross-flow pressure gradient. These geometric changes were characterised by variation of the soft-palate location and side-wall deformation which were considered to be a function of physiology, neuromuscular and/or aerodynamic loading. Potential fluid-structure interaction mechanisms for soft-palate and side-wall motions were described in Section 4.3 and the deformation of a fluid-conveying tube flexible tube comprehensively reviewed by Bertram (2003).

The base geometry was deformed to model separately each of the effects of soft-palate movement into the velopharynx and the inward deformation of the side-walls of the velopharynx, the key motions linked with apnoea and an under-

standing for which resultant pressure contours provided a self-sustaining collapse or apnoea of the airway. The quasi-static approach and occluded oral entry remain boundary conditions for the range of orthogonal palatal and pharyngeal deformations, the results for which were presented in Figures 4.17 and 4.18.

Figures 4.17 and 4.18 present soft-palate and side-wall deformation respectively with Case 0 being the base case measured and modelled in Section 4.6.1. For each of the geometric cases in Figures 4.17 and 4.18, the applied pressure drop required to maintain the volumetric flow rate of $0.00025 \text{ m}^3/\text{s}$ (15 l/min) which was obtained by an iterative process. This approach was considered more faithful to reality than artificially applying a velocity boundary condition either at the entry or exit to the airway system.

The velocity and pressure fields for the most extreme cases of soft-palate and side-wall deformation, Case P4 in Figure 4.17 and Case W4 in Figure 4.18, are presented in Figures 4.19 and 4.20 respectively, these contrast with the results of Figure 4.15. In addition to detailing the geometric variations studied, Figures 4.17 & 4.18 also show the resulting pressure fields in the sectional plane at the location of minimum cross-sectional area. The applied pressure drop over the airway required to maintain the volumetric flow rate is presented together with the pressure values both on the surface of soft-palate and at the side-walls of the pharynx. The pressure contours in Figures 4.17 & 4.18 for the mid-sagittal plane showed that increasing either the soft-palate displacement or side-wall deformation generates a sharper pressure drop in the velopharynx, in line with the additional constriction experienced. Clearly, the increased resistance at the site of reduced cross-sectional area contributes a greater part of the overall hydraulic resistance of the airway. The pressure contours in the cross-sections of minimum area demonstrate the cross-flow pressure gradient, also visible in Case 0. These not only continued to exist but steepened as the airway was narrowed by the side walls in Figures 4.17 & 4.18. Soft-palate deformation exercises a similar effect until Case P4 is reached as seen in Figure 4.17. Case P4 presents a different flow field with the deformation a more gradual pressure recovery occurred downstream of minimum cross-sectional area with the flow remaining attached as seen in Figure 4.19.

Overall intensification of cross-flow pressure gradient is explained by the increase in flow speed required to maintain the fixed volumetric flow rate. The cross-

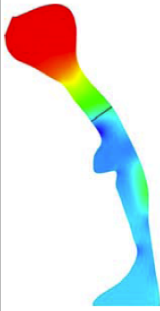
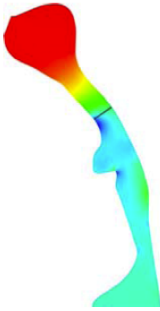
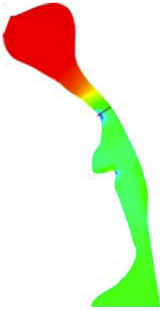
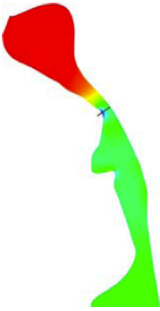
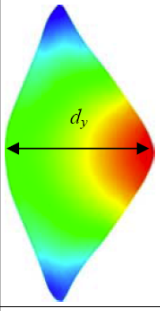
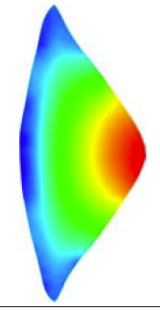
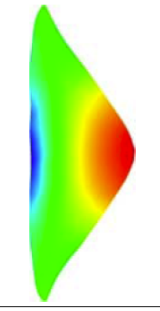
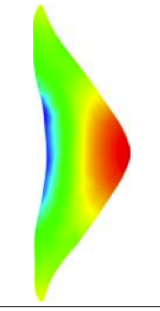
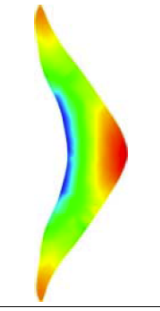
	Case 0	Case P1	Case P2	Case P3	Case P4
Pressure in mid-sagittal plane (red-maximum to blue-minimum for each case)					
Exit minus entry pressure, P_D/ρ (m/s) ²	-9.38	-11.20	-14.50	-21.30	-35.10
Geometric properties of the velopharynx at the cross-section of minimum area (marked above)					
d_y (mm)	7.75	6.38	5.25	4.20	3.13
Area, A (mm ²)	66.20	56.63	47.33	38.17	28.63
Perimeter (mm)	34.67	33.95	33.72	33.39	33.85
Hydraulic Diameter, D_h (mm)	7.64	6.67	5.61	4.57	3.38
Flow-field characteristics in the velopharynx at the cross-section of minimum area					
Pressure in section of minimum area					
Pressure range (red-to-blue), p/ρ (m/s) ²	-7.7 to -11.0	-9.9 to -14.0	-13.6 to -22.4	-20.9 to -36.3	-37.5 to -65.4
Mean flow speed (m/s)	3.77	4.41	5.28	6.55	8.73
Pressure at lateral extents, p_{lat}/ρ (m/s) ²	-10.9	-13.6	-17.5	-25.2	-47.2
Pressure on soft palate section, p_{pal}/ρ (m/s) ²	-9.4	-14.0	-20.9	-35.7	-64.4

Figure 4.17: Summary of variations to airway geometry generated by the model of soft-palate deflection; Case 0 is the actual (un-deformed) geometry measured.

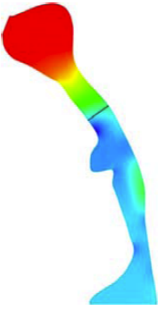
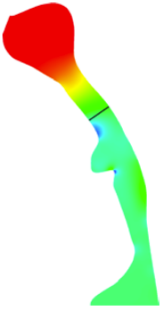
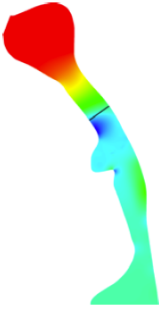
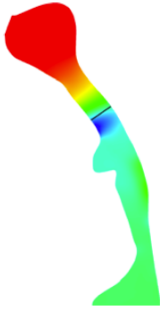
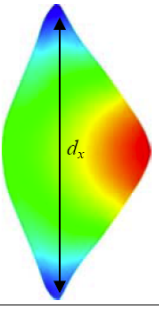
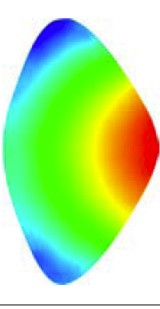
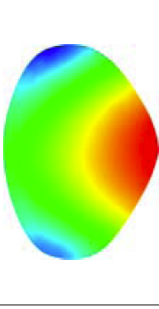
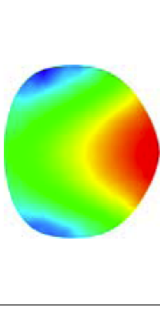
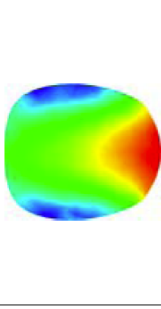
	Case 0	Case W1	Case W2	Case W3	Case W4
Pressure in mid-sagittal plane (red-maximum to blue-minimum for each case)					
Exit minus entry pressure, P_D/ρ (m/s) ²	-9.38	-9.50	-10.51	-13.00	-21.00
Geometric properties of the velopharynx at the cross-section of minimum area (marked above)					
d_x (mm)	15.01	10.99	8.97	6.83	5.33
Area, A (mm ²)	66.20	63.27	56.21	47.59	37.27
Perimeter (mm)	34.67	26.92	24.01	20.87	19.23
Hydraulic Diameter, D_h (mm)	7.64	9.40	9.36	9.12	7.75
Flow-field characteristics in the velopharynx at the cross-section of minimum area					
Pressure in section of minimum area					
Pressure range (red-to-blue), p/ρ (m/s) ²	-7.7 to -11.0	-8.1 to -11.9	-9.9 to -15.0	-13.8 to -21.1	-21.2 to -31.6
Mean flow speed (m/s)	3.77	3.95	4.45	5.25	6.71
Pressure at lateral extents, p_{lat}/ρ (m/s) ²	-10.9	-11.1	-14.5	-19.2	-28.3
Pressure on soft palate section, p_{pal}/ρ (m/s) ²	-9.4	-10.0	-12.6	-17.2	-25.1

Figure 4.18: Summary of variations to airway geometry generated by the model of side-wall deflection; Case 0 is the actual (un-deformed) geometry measured.

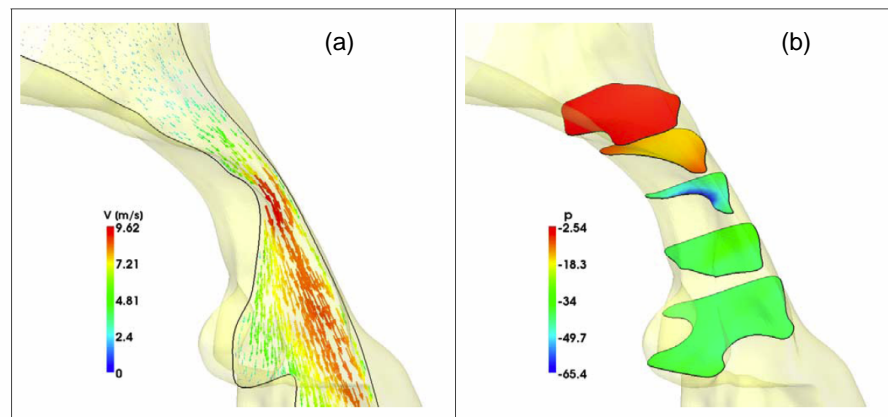


Figure 4.19: Computed flow field in the airway section of Figure 4.15 but with the soft-palate displaced into the velopharynx giving Case P4 of Figure 4.17: (a) centerline velocity vectors, and (b) pressure values in five cross-sections of the airway, Note that the pressure legend denotes values of pressure divided by air density, (p/ρ) , in $(m/s)^2$.

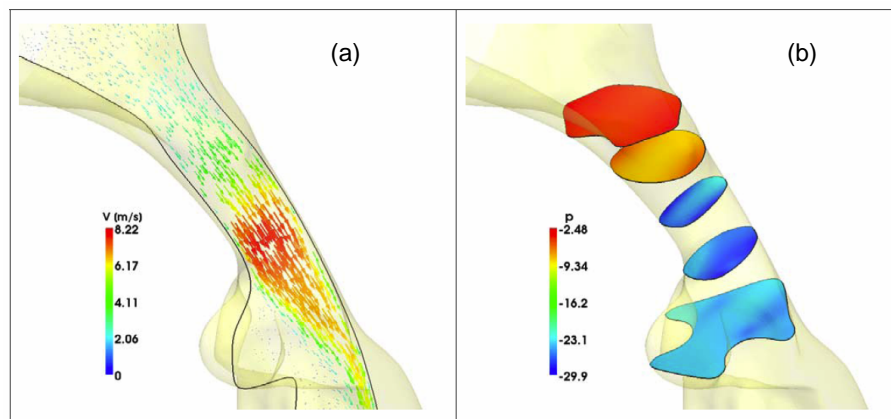


Figure 4.20: Computed flow field in the airway section of Figure 4.15 but with the side walls of the velopharynx deformed inwards giving Case W4 of Figure 4.18: (a) centerline velocity vectors, and (b) pressure values in five cross-sections of the airway, Note that the pressure legend denotes values of pressure divided by air density, (p/ρ) , in $(\text{m/s})^2$.

flow pressure gradient is also generated as a consequence of the centripetal forces (proportional to the square of flow speed) experienced by fluid elements as they travel the laterally curved path through the section of minimum cross-sectional area. It is also noted that curvature in the orthogonal anteroposterior plane was implicated. This effect is additional to the expected pressure reduction caused by area reduction and one-dimensional mass-conservation principles applied in the axial direction. For the case of side-wall deformation the lateral curvature was also increased. Also evident in the sectional plots of Figures 4.17 & 4.18 where significant cross-flow pressure gradients in the mid-sagittal plane. Low-pressure intensification on the surface of the soft-palate occurs as deformation into the airway proceeded with increased localised flow curvature. This contributes to a net pressure difference across the soft-palate generating a force that in a FSI analysis would tend to move it so that further airway narrowing occurs, effectively the beginnings of a self sustained collapse of the airway or apnoea. The present results, therefore, provide a preliminary explanation of how the soft-palate can contribute to airway collapse and why collapse should occur principally in the lateral direction where minimum pressures are predicted.

Quantitatively the effect of soft-palate position and side-wall deformation on key pressure quantities within the airway are further examined. using the parameters and results of Figures 4.17 & 4.18 in non-dimensional form to lend generality. Time and mass scales were obtained from the fluid density, ρ , and volumetric flow rate, Q but the determination of a suitable length scale is not as obvious. Ball *et al.* (2008) used cross-sectional area of the airway for the latter and this was adopted here. A_0 , was chosen at the site of minimum area for the base geometry denoted Case 0 since this is the area of interest and where the area was varied. However, deformations also needed to be quantified separately through the variation of the section dimensions d_y and d_x used in Figures 4.17 & 4.18. These represented soft-palate and side-wall displacements respectively relative to their values for Case 0. Thus, the magnitude of the non-dimensional pressure (below that of the zero datum taken at entry to the pharyngeal region studied), cross-sectional area and displacements were defined as;

$$P'_D = \frac{-p}{(1/2)\rho(Q/A_0)^2} \quad (4.1)$$

$$A' = \frac{A}{A_0} \quad (4.2)$$

$$\Delta d_y = \frac{d_y - d_{y0}}{d_{y0}} \quad (4.3)$$

$$\Delta d_x = \frac{d_x - d_{x0}}{d_{x0}} \quad (4.4)$$

Figure 4.21 (a) depicts the dependence of non-dimensional pressure values on soft-palate displacement for the applied pressure drop, P'_D , to maintain the inhalation mass flux, and the values of pressure on the side walls, p'_{lat} , and soft-palate, p'_{pal} . Again, the values for the velopharynx at the site of minimum cross-sectional area. Also plotted are the two values of P'_D obtained from computations with the much higher volumetric flow rate of 50.4 l/min. The non-dimensionalisation is seen to bring these into alignment with the main results obtained at 15 l/min, thereby suggesting the flow dynamics modelled also hold at higher, rapid-breathing, flow rates.

Figure 4.21 (b) demonstrates corresponding results for displacement though this time for the side walls. Since the system pressure drop comprised a dominant contribution from the velopharynx, the divergence of the side-wall and soft-palate pressure curves from the pressure-drop curve as displacements were increased indicated the substantial contribution to minimum pressure by the lateral flow-curvature effects discussed above. The logarithmic plot of Figure 4.22 shows the correlation of the required system pressure drop with airway deformation, due to soft-palate displacement and side-wall deformation. Note that the un-deformed geometry, Case 0, is represented by results for zero on the abscissa. Deformations were again characterised by the resulting minimum cross-sectional area for those due the soft-palate displacement, or hydraulic diameter, non-dimensionalised relative to Case 0. The mid-sagittal-plane pressure contours in Figure 4.17 show a concentration of system pressure loss within the region of the velopharynx as soft-palate displacement was increased. This explained the index-law correlations in Figure 4.22 that give $P'_D \propto (D'_h)^{-1.70}$ and $P'_D \propto (A')^{-1.61}$ when deformation was caused by the soft-palate. The airway constriction provides an effect analogous to that caused by a combination of a Venturi and orifice-plate in a duct

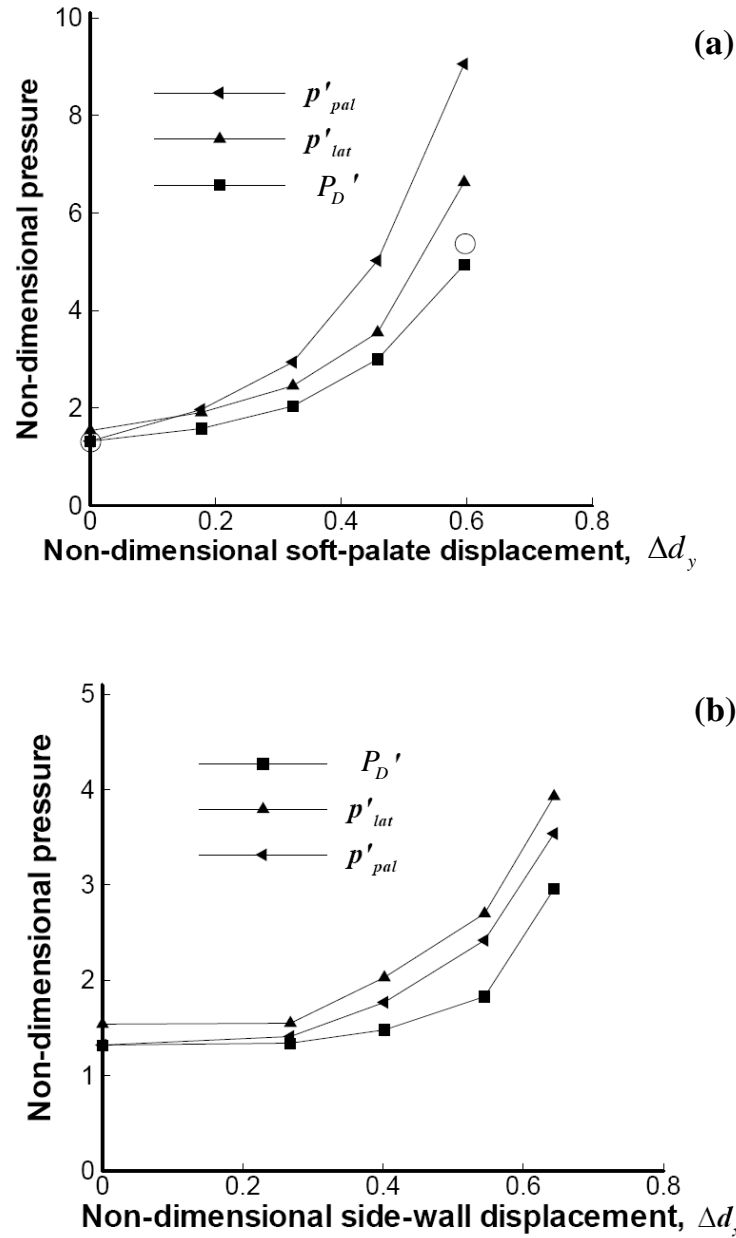


Figure 4.21: Effect of airway deformation on magnitudes of non-dimensional pressure drop (P'_D), and pressures on the side-wall (p'_{lat}) and the soft-palate (p'_{pal}) surfaces, at the site of minimum cross-sectional area, due to: (a) non-dimensional soft-palate displacement, (Δd_y), and: (b) non-dimensional side-wall displacement into the airway, (Δd_x). The data points plotted as circles in (a) indicate results obtained at higher breathing rates of 50.4 l/min.

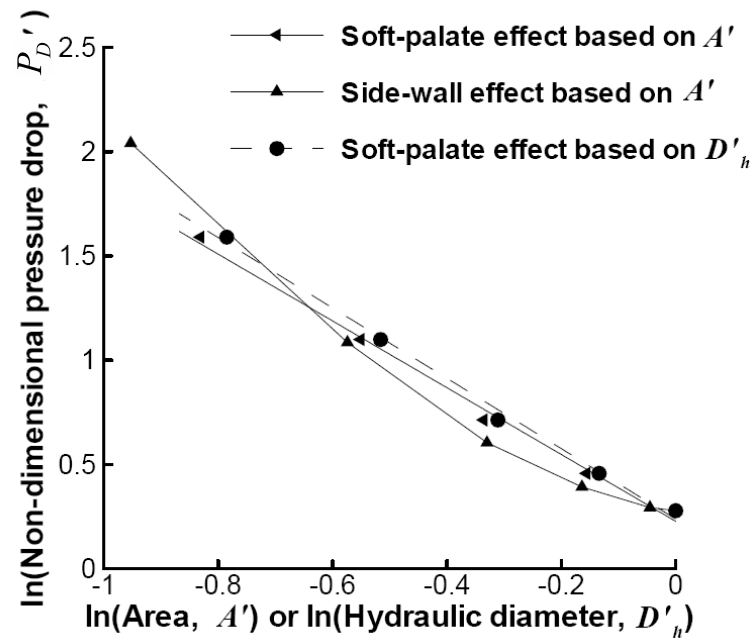


Figure 4.22: Non-dimensional logarithmic plot of the dependence of required pressure drop (P'_D) to maintain quiet breathing in an airway deformed due to soft-palate deflection characterised by non-dimensional hydraulic diameter (D'_h) and area (A'), and side-wall deformation characterised by non-dimensional area, at the site of minimum cross-sectional area in the velopharynx.

flow.

When changes to the airway geometry were caused by side-wall deformation, Figure 4.22 shows that a clear index law does not emerge. This is due to area reduction and increasing hydraulic efficiency of the cross-section from Case 0 to Case W2 have opposing effects on the airway's resistance; for further deformation, the hydraulic efficiency decreases. However, the nonlinearity of the curve in Figure 4.22 was fairly weak and, for practical purposes, the relationship between system pressure drop and side-wall deformation could be expressed approximately as an index law. For patients with OSA, clinicians often relate the level of flow to the critical closing pressure and upstream resistance (Boudewyns *et al.*, 2000) with the latter determined from an empirical pressure-flow relation, for which the non-dimensional pressure drop, defined in Eq. (4.1), is effectively such a correlation.

Figure 4.23 correlates the pressures experienced by the side walls and the soft palate with the value of minimum cross-sectional area, as this varies with soft-palate side-wall displacement. This represents the pressure that would principally cause the deformation and lead to a self-sustaining mechanism for dynamic collapse of the pharynx. The straight broken lines in Figure 4.23 (a & b) show the results from a one-dimensional inviscid theory, utilising Bernoulli equation and mass-conservation following a notional streamline from entry (where the flow speed was approximated as zero) through to the section of minimum area. All numerical data-sets clearly evidence the relationship $P'_D \propto (A')^{-n}$. When the cause of deformation is the soft-palate, Figure 4.23 (a) gives $n = 1.74$ and 2.30 for the cases of pressure acting on the side-walls, p'_{lat} , and soft-palate, p'_{pat} , respectively. This difference was anticipated as the geometric deformation most significantly increased the streamwise curvature close to the section of minimum area. In contrast, side-wall deformation increases lateral curvature and the corresponding indices from Figure 4.23 (b) were $n = 1.71$ and 1.73 . The inviscid theory gave an index of exactly 2 and thus even this simple model bears a modest level of agreement with those of the full simulations.

The vertical offset between the inviscid-theory results and the full data was not explained by the multiplicative loss factor that should be applied to inviscid theory to account for frictional and turbulence losses through a constriction. The inclusion of a loss factor would actually increase the difference. The cause of

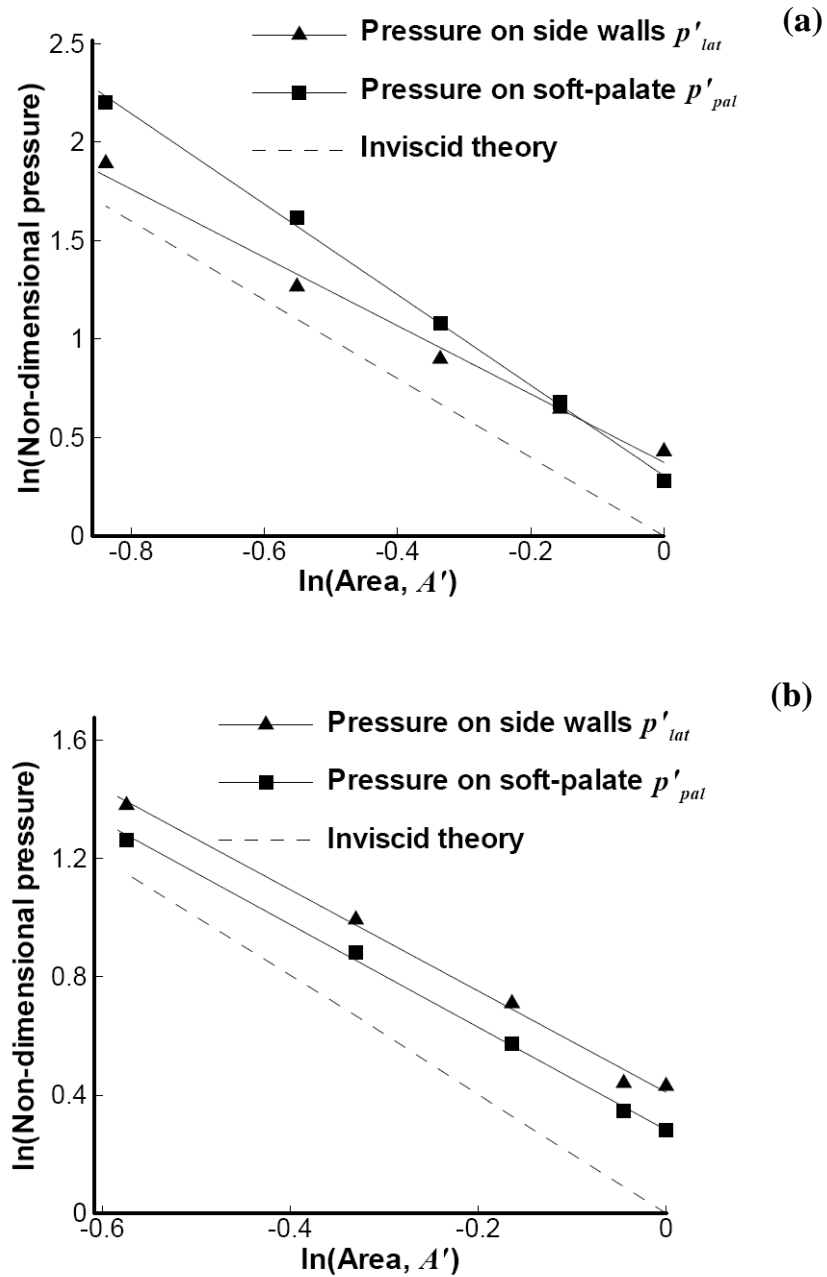


Figure 4.23: Variation of the magnitude of non-dimensional pressure on the lateral extremes of airway side-wall (p'_{lat}), and the soft-palate surface (p'_{pat}), with the non-dimensional minimum cross-sectional area (A') in the velopharynx varied by (a) soft-palate displacement, and (b) side-wall displacement into the airway. Broken lines indicate predictions based on a inviscid theory and mass continuity approach.

the difference is streamline curvature that leads to the pressure gradient across the cross-sectional area, an effect absent from the one-dimensional inviscid theory that can only yield a uniform pressure for the section. Correlations such as those of Figure 4.23 may be useful for the prediction of the low pressures on the side-walls and soft palate of an individual, provided that just one pressure reading at each of these two locations (e.g., in the state of Case 0) was available to determine the multiplicative constant, C , in the correlation $P'_D = C(A')^{-n}$. For the airway studied in this paper $n \cong 1.7$ for the side-wall pressure changes due to constriction of the velopharynx, while soft-palate pressure changes have the same value for side-wall deformations but $n \cong 2.3$ when the constriction was caused by displacement of the soft-palate. The robustness of these values across a wider population still require further research.

4.6.3 Reconstructed 3-D human pharynx modelling - conclusion

Chapter 4 has reported the research effort undertaken towards greater understanding of the upper-airway culminating the procedurelisation of the geometry acquisition, reconstruction finally culminating in reporting a new adverse pressure distribution within the airway leading to collapse of the pharynx. This comprised development of a non-contact measurement system, anatomical optical coherence tomography (*a*OCT), which was used to generate a three-dimensional geometric model of the upper-airway. The procedure importantly permitted the time-dependent geometry to be captured for which two extremes of airway volume were post-processed and rendered. Having demonstrated this, a record of the full history of the geometry as it varies through the breathing cycle becomes attainable. The advantages of the examined method are that the airway data can be acquired quickly (typically 12 minutes scanning time for a complete pull-back scan), during sleep or wakefulness, and, if necessary, repeatedly without harmful effects associated with other techniques, such as ionizing radiation in the case of CT scans from which airway geometries have previously been constructed. Calculations of steady flow through the system have been performed for inhalation using a quasi-static assumption.

A characterisation of the flow and pressure field has been undertaken. A significant feature uncovered in the present study was that of a strong cross-flow pressure gradients situated in the region of the pharynx effectively bounded by

the soft-palate at the site of minimum cross sectional area. This generated regions on both the soft-palate and side walls of the pharynx where the pressure was significantly lower than that of the section's mean pressure. Accordingly, both the soft-palate and side walls of the pharynx would have a propensity for flow-induced inward motion leading to self sustained airway closure and apnoea. This prediction is supported by studies Schwab *et al.* (1993) and Donnelly *et al.* (2003) showing that the changes in upper-airway dimensions during normal quiet breathing and during obstructive events were greater in the lateral, than in the anteroposterior, direction.

The effect of soft-palate displacement and side-wall deformation on the velocity and pressure fields were studied. Soft-palate motion can occur due to fluid-structure interactions during the breathing cycle as demonstrated in Chapter 3.8 and in the literature (Tetlow & Lucey, 2009) and (Tetlow *et al.*, 2008). The results presented herein demonstrate that palatal displacement into the velopharynx leads to both increased respiratory effort, to maintain the airflow through the system and localised regions of pressures that are significantly lower than those that expected simply on the basis of area reduction. Similar, but less dramatic, effects were found when airway area reduction was caused by the inward deformation of the side walls. For the individual geometry studied, the computed values of low pressure on the side walls and soft palate were found to correlate with the cross-sectional area at the site of greatest constriction following the non-dimensional index law $P'_D = C(A')^{-n}$, where the value of n was close to that predicted by a simplified inviscid-theory approach. The non-dimensional pressure drop applied by the respiratory muscles via the lungs maintaining constant flow rate correlated well with the minimum cross-sectional area in the velopharynx. Clearly, suitable population-based studies would be required to confirm that these correlations are generally applicable and, if so, to determine the range, sensitivity and distribution of index values. The value of such correlations lies in the ability to make approximate, but very quick, predictions of potential lowest pressures within the airway and its cross-section in the soft-palate region. Of course, complete and more exact flow and pressure fields for an individual could be generated by the full application of the methods developed and demonstrated here. Whether the pressure field so-predicted, with its dependence upon soft-palate position and side-wall deformation, was sufficient to trigger airway collapse requires a computational model that includes the key dynamics of the flow,

pharyngeal-wall and soft-palate. In addition to this there is the complementary indicator seen in the endoscopic study, though not further investigated, where the soft palate occluded the nasal passage once heavy breathing was instigated. Determining the onset of this could be an equally important or complementary readily obtainable measure though set aside for future work.

Future investigations will also further examine the dynamics of three dimensional streamline curvature evaluated herein, whereby a cross-flow pressure gradient was established to balance the centripetal effects on fluid elements. However, now symmetry would be broken allowing the lateral pressures to fluctuate independently in a similar way to that of the anteroposterior direction visualised here. Clearly side-wall pressure could further reduce one side relative to the other once the symmetry introduced in the current approaches geometry reconstruction phase, was removed, especially in the light of the results showing local curvature to be implicated in large pressure reductions.

The key achievement of the present work was in establishing a practicable process comprising time-dependent data capture, geometric reconstruction and numerical simulation that can be used to predict airflow in the upper-airway for any individual. The next step towards assembling a full dynamic flow-structure interaction model will be to incorporate the airway-wall dynamics along with those of the soft-palate, pharynx and tongue. The complete dynamic model could be built using the modelling approach presented in this paper.

4.7 Summary

This Chapter has reported on the activities of the research group directed towards understanding the dynamics of the human upper airway. Two examples obtaining anatomically correct geometry were reported in Sections 4.4 and 4.5. These both proved able to extract useful geometries although only 4.5, used *in vivo* techniques, that have the ability to account for geometric variations through the breathing cycle. Section 4.4 details a conventional geometry acquisition method for individuals using CT. However this external method together with MRI suffer from a number of limitations when studying the upper-airway, principally relating to the amount of radiation the sufferer would be exposed to in a full airway sleep study and the inability to resolve temporal motion of the airway throughout the

breathing cycle.

Section 4.5 describes the efforts to overcome the challenges that lie in the need to measure a time-varying interior geometry, the access to which is highly restricted for which *a*OCT was proposed and utilised to this end.

A examination of the linkage between the soft-palate and pharyngeal motions was conducted using a three-dimensional analogue computational and study of the fluid-structure interaction that resulted from such a system. This 3-D model reported findings similar in nature to that of the 2-D investigation of Section 3.8 namely that the presence of low pressure regions in the airway and that over a succession of breathing cycles collapse of the airway and apnoea can occur. Central to such events was an imbalance between the resistances of the nasal and airway passages and the effect this has on soft-palate deflection and destabilisation. In the extreme case of a closed oral airway undergoing a breathing cycle, presented in Section 3.8.5, the three-dimensional model with flexible side walls corroborates these 2-D findings and demonstrates that side-wall motion exercises an additional strong influence on soft-palate motion that could add to the partial-blockage effect.

Curvature in the upper-airway was examined in an anatomically correct geometry in Section 4.6.2 and showed that inclusion of flow curvature was critical in producing a cross channel pressure gradient. At the site of minimum area the magnitude of the lateral side-wall pressure was approximately 50% greater than that of the posterior mid-line value with the centripetal effects on the fluid elements producing the crossflow pressure gradient.

An assessment of the pressure-field dependence and sensitivity to the selection of turbulence model and an extreme assumption of unsteady laminar flow demonstrated that the cross flow pressure gradient phenomenon was largely independent of flow model though the accuracy of the predicted magnitude did vary.

Airway narrowing was examined in Section 4.4 and showed that for single channel flow, as was predicted in the 2-D work of Section 3.8.5, the sensitivity of single channel flow to minor variations was increased. These materialised in the pressure contour gradient as being elevated at the site of narrowing, thus concentrated over a shorter streamwise extent.

CHAPTER 5

Application To Obstructive Sleep Apnoea

Obstructive Sleep Apnoea (OSA) is a common disease with important neurocognitive and cardiovascular sequelae. Existing therapies are unsatisfactory on the basis of addressing the causal factors, leading investigators to seek alternative forms of anatomic manipulation to influence pharyngeal mechanics such as nasal CPAP. This chapter reports the key contributions of this thesis' research towards developing a greater understanding of obstructive sleep apnoea and its causes.

5.1 Airway geometry

From Chapters 3 and 4 the key focus was to enable modelling of individual sufferers airway geometry and material properties as the gold standard in diagnosis. These chapters very clearly make the case against population based analysis, in the first instance, from the practical point of view that it is subtle variations that lead to the onset of OSA. Therefore it is understanding at an individual level which needs understanding first to enable population based characterisations to be correctly classified, and then measured. Accordingly it is the need to understand these variations that numerical modelling offers, permitting proposed interventions to be modelled and their effectiveness evaluated. Once this work has been completed then population based conclusions might be drawn from an informed set of criteria.

For *heathy breathers* the mouth is most often closed during sleep and/or the oral cavity occluded by apposition of tongue to palate, so the modelling approach in Section 4.6.1 is appropriate. For healthy breathers nasal breathing offers a mechanical advantage, due to heat and mass transfer conditioning during inhalation and recovering products of respiration on exhalation. In contrast for unhealthy subjects, obstructive sleep apnoea can often be associated with oral breathing Woodson (2003). This would likely be as a result of higher hydraulic resistances in the nasal passage and or the pharynx providing insufficient mass-flow even for light breathing through the nasal passage alone, requiring breathing through the mouth as well. This point was often not clearly distinguished in the literature as for a number of other reasons healthy breathers would breath through their mouth. The view presented in this thesis is that oral breathing is a precursor to OSA and as such modelling should be directed towards nasal breathing in the first instance to determine stability thresholds.

A focus on healthy breathers should examine the necessary conditions permitting unobstructed breathing during sleep for purely nasal breathing. Pathological deviations from this state would then by extension be unhealthy persons, that then resort to oral breathing in an attempt to maintain mass flux to sustain respiration without the onset of debilitating hypoxia. Oral breathing by this reasoning can be a symptom of obstruction rather than a separate set of initial conditions to be solved for, noting that some will breathe via the mouth for other reasons. Section 3.8.4 and 3.8.5 clearly demonstrate the additional complexities associated with two channel flow where the palate would be asymmetrically positioned in the flow field with added curvature as would be the case in anatomical reality.

Our experimental research with an endoscope and a subject producing a forced through the nose with the mouth shut as seen in Appendix A, showed that not only did the soft-palate vibrate rapidly but the side walls moved in and also vibrated with the connecting tissue and pharynx. This indicates that the frequency of vibration could be of less use than other researchers have thought owing to the complex nature of vibration. Moreover, this finding highlights the need to understand the mechanism underlying channel narrowing and hence the catalyst for vibration.

Another observation from the endoscopic experimentation was that with both nasal and oral breathing, upon increased or heavy breathing, the soft-palate shut

off the nasal passage. This indicates some instability of the soft-palate that in the wakeful state the body acts to control. While this aspect has not been pursued within the current research this could be a meaningful measure of an individuals susceptibility to OSA that could be determined from the flowrate or velocities this occlusion of the nasal passage occurs, as such is left for future work.

The computational results for the 2-D offset cases from Section 3.8.5 with the flexible-plate drifting towards the narrower channel mirror the *in vivo* observations in Appendix A. This was seen for cases of normal respiration when only one of the airways was used, and cases with both. The exhalation-inhalation sequences with one airway closed produces a time-varying resistance, resulting in cyclic motion of the soft-palate; collapse of the pharynx is therefore plausible under adverse conditions. Furthermore, the OSA dysfunctions random occurrence of 200-500 times per night makes full understanding dependent on other factors - perhaps two or more are required to bring about an apnea, how these parameters interact will only be understood following further research. Tetlow & Lucey (2006) postulated a dysfunction mechanism illustrated in Appendix D for an idealised breathing cycle leading to apnea. For this phenomenon the soft-palate initiates the apnea owing to its cyclic motion over the respiratory cycle which has now been further confirmed with independent 2-D and 3-D modelling approaches predicting the potential for this excitation to be possible. The resultant dynamic pressure fluctuations were most adverse at the beginning of inhalation. From time to time the pressure drop could reach some threshold value where the pharynx is unable to maintain caliber and apnea ensues. The illustration in Appendix D of how this phenomenon may occur is shown in a series of schematics covering an illustrative respiratory cycle, with one inlet closed. An example of first mode flexible-plate motion was depicted demonstrating how the flexible-plate position changes over the cycle. Resultant large changes in pressure gradient along the flexible-plate are shown. Noting that pressure drop is a function of the channel height squared, the extremely low pressure that may lead to apnea are illustrated in the final schematic.

Pursuant to this, the greatest amplitude motion of the mean position of the flexible-plate is for one channel blocked or to a lesser extent both inlets open and asymmetric positioning of the flexible-plate. For the latter a relatively simple test measuring the flow-ratio for combined breathing could be simply implemented. Results significantly far from unity, i.e. equal flow, represent the conditions for

largest motions of the soft-palate and potential for instability.

The current 3-D modelling did not include full implementation of FSI, when anatomically correct geometries were used, considering the soft-palate to be resting against (effectively connected to) the tongue. If this is the case it serves to restrain the soft-palate from amplified motion during the breathing cycle, evidenced during the 2-D breathing cycle work of Section 3.8.3. This aspect has not been fully addressed in the current research and is listed below for further investigations.

The results of Section 4.3 confirm the likelihood that the soft-palate does not play a significant role in pharyngeal collapse for dual inlet flow. This is due to the nil effect on the side wall tip deflections as soft-palate dynamics and amplitude changed. For dual inlet flow as the overall flowrates remain essentially constant this was unsurprising. However, it must be stressed further work is required to prove this postulation and extended to single channel flow where flow fluctuations would have a more deleterious affect on pharynx stability. The main findings from the 3-D results of Section 4.6.2 were that large pressure variations were required to maintain flow through an increasingly narrowing channel and the lateral pressure variations identified had the lowest pressures predicted on the pharynx walls. Flow curvature in the anteroposterior direction was expected though lateral pressure fluctuation due to lateral curvature have not previously been reported. Moreover, this finding of a lateral pressure gradient was confirmed using a number of flow solution methods indicating the robustness of this finding.

5.2 Future biomechanical related work

For future investigators this section poses a number of questions and proposals. Now that the direction for research clearly points towards 3-D anatomical modelling, ability to answer or prove/disprove the issues below will provide a strong foundation for tackling this complex multidisciplinary biological problem.

5.2.1 Anatomical understanding

Length reduction of soft-palate has been listed in the literature as a relatively common procedure. The findings reported in Appendix A and Section 4.6.2

implicate the pharynx in narrowing of the airway so further work is required here to determine to what extent the pharynx geometry governs collapse. What are the key parameters that control this aspect of disfunction and secondly what form of mitigation maybe implemented against collapse of the pharynx. Some proposals for consideration would be: Laser scaring to increase stiffness, fat pad reduction, insertion of lateral stiffeners or simply and more sensibly an exercise regime improving the degraded function of the already existing biological system.

Chapter 3.8 finds that collapse of the airway is likely more dependent on motion and instability of lateral walls than the soft-palate though there is likely some combination at work. Previously the soft-palate was thought to be the main instability driver through the interaction between the soft-palate and lateral pharyngeal walls. However the pharynx trans-lumen pressure acting across the pharynx walls is governing in OSA where any significant obstruction present, results in higher resistance and lower internal pressures. While dysfunctions of the two structures are related as airway resistance changes influencing the other's behaviour, identification of some relationship with the pharynx causing the soft-palate to deflect via an amplifying feedback mechanism would be required to merit inclusion of the soft-palate in 3-D modelling. Considering one-inlet breathing provides the boundary condition for the onset of OSA. The challenge here is to demonstrate how the soft-palate becomes disengaged from the tongue through purely nasal breathing, noting that apnoea only occurs occasionally. If this is not *ever* the case computational expense would be deployed for modelling a symptom rather than an initiator of the dysfunction.

It is proposed that swallowing can be discounted as an initiation mechanism during sleep as it is thought that a period of wakefulness is required to perform this action. Moreover, the airway opens to its widest point immediately following a swallow, similar to following a snore as shown in Appendix A as muscular control is reinstated. One aspect not considered in the present research is the affect that sleeping position plays on OSA currently, only the supine position has been imaged, flow curvature effects could be exasperated when the head and or body are rotated to the side.

Another aspect of OSA worthy of further study is could neuromuscular delay aid instability? This factor is present in the awake state with the soft-palate moving through the breathing cycle retracting during inhalation and the pharynx

know to vary as presented in 4.5 showing plots at the end of exhalation and inhalation. This could yield some crucial information that is easily obtainable from individuals - for example the point in the breathing cycle when the soft-palate retracts and then relaxes and the velocities associated with this.

CHAPTER 6

Conclusions & Future Work

This thesis has delivered a framework and methodology for understanding the solution space for a one-dimensional cantilevered plate immersed within a two-dimensional viscous channel flow adopting pressure-driven boundary conditions. Furthermore three-dimensional anatomical geometries have been successfully captured *in vivo*, reconstructed and with viscous and turbulent flow fields modelled to explore pharynx collapse.

While the original aims of this thesis have been met, as with any worthwhile research the journey to reach these goals generated a number of additional questions and lines of enquiry. The principle outcome of this thesis was establishing the stability solution space for one set of boundary conditions, reported as the base case. However, during development and collaboration with medical practitioners it became increasingly apparent that a range of parameters and combination of boundary conditions affected stability greatly, for which the newly developed pressure-driven model was well suited to investigate. Furthermore, the base case with two inlets and symmetric positioning of the soft-palate was probably the least directly applicable configuration relevant to Obstructive Sleep Apnoea (OSA). This led to an extensive examination of the other boundary conditions determining their relative stabilities when compared to the extensively examined base case.

Three-dimensional studies further confirmed the two-dimensional findings and presented potential for flow curvature to develop a further destabilising cross flow pressure gradient when considering an anatomically correct model.

6.1 2-D modelling

The pressure-driven model developed in this thesis is presented as a more faithful prediction of the action of human breathing, whereby velocities through the nose and mouth are permitted to vary according to each passage's resistance and the applied pressure drop over the system. Comparison of velocity and pressure-driven models found that flexible-plate stability was sensitive to the choice of model which was supported by the literature (Luo & Pedley, 2000). Moreover, flow direction played an important role on which modelling approach predicted the most stable result being pressure-driven for inhalation and velocity-driven for exhalation.

Mapping the non-dimensional parameter space with pressure-driven boundary conditions, permitted modelling hydraulic resistance variations as a function of palatal oscillation. A study of the solution space was presented in the context of the derived dimensionless scheme, noting this stability solution space only pertains to symmetrically positioned configurations for inhalation. Six dimensionless groups were defined that fully described the system, adopting appropriate assumptions permitted the system to be reduced to just two key non-dimensional terms useful for engineering and clinical purposes. These two groups, of stiffness ratio (Γ) and Reynolds number (Re) yielded the most significant changes effect on system behaviour, whereas mass ratio (Θ) had a limited effect on stability when considered in isolation.

One element of the present research where reality is likely to be different, in a biological sense, from that being modelled was breathing through the mouth and nose simultaneously. It is known that quiet breathing occurs through the nose only. Pierce & Worsnop (1999) state that opening the mouth markedly reduces upper-airway resistance but heating, humidification and filtering of the inspired air is less efficient. In general it requires approximately 580-750ml/s of flow to necessitate the mouth and nose to be open together. This led to examining the boundary conditions of one channel closed, that revealed stark differences compared to flow through two channels. Single channel flow had a significant destabilising effect including the occurrence of a divergence-type instability for both exhalation and inhalation in addition to a travelling-wave flutter instability.

When considering asymmetric positioning of the soft-plate and for nasal breath-

ing (single channel flow) modelled the breathing cycle yielded an amplification mechanism where the soft-palate amplitude was found to increase, leading to a reduction in airway size on exhalation. This mechanism provides a explanation for increased likelihood of obstruction on ‘occasional’ inspiratory breaths, similar to that reported by Woodson (2003), whom also reported OSA was not only implicated with inhalation, but developed over the exhalation portion of the breathing cycle.

Development of the pressure-driven model allowed realistic treatment of asymmetric positioning of the cantilevered plate within channel flow, permitting one channel to be closed and the exhalation-inhalation cycle to be studied. This highlighted the enhanced functionality of the numerical model to predict the biological systems behaviour. In the human upper-airway irregularity and variability dominate whether this be through; compliant materials with changing mechanical properties, muscle activity constantly changing geometry, the vastly differing geometries of the nasal and oral passages or simply flow direction changes over the breathing cycle. The simple symmetrical model solution space fails to capture any of this realism. While each set of boundary conditions stability solution space was not explicitly determined, comparative stability was determined using candidate simulations, permitting relative stability to be determined. Despite not attempting to identify each combination of boundary condition’s stability solutions space, this work provides a great detail of insight into the function and dysfunction of the human upper airway. In the end collapse of the pharynx may not be linked to the soft-palate in any way, but the understanding developed and postulated failure mechanisms developed as a result of this research are fundamental elements of the overall research effort, moving towards the end goal of improving individual sufferer’s condition and life. This thesis does however identify a mechanism for occlusion of the pharynx by the soft-palate during exhalation which can occur during single channel flow.

6.2 3-D anatomically correct modelling

As a starting point a study was conducted where a 3-D version of the 2-D study, detailed above, was presented. The 3-D model here, while being a simple rectangular duct, included orthogonal motions of the pharynx walls. The results

indicated that the pharynx has an effect on soft-palate response but the reverse was not true as these studies were for two-inlet channel flow. It was postulated that mass-flux remaining essentially unchanged by palatal motion was the governing factor in this case as opposed to single channel flow where mass flow does vary significantly with palatal motion.

The primary challenge with 3-D modelling of the human upper-airway was and remains obtaining data to create an anatomically correct geometry. The challenge here being the need to measure a time-varying interior geometry, with limited access. Normal methods such as CT or MRI scans were not appropriate for capturing airway motion over a series of breathing cycles without significant radiological exposures to the participant undergoing measurement. This was overcome using anatomical optical coherence tomography *aOCT* a technique developed locally for this purpose. Details of the *aOCT* technique and the process to reconstruct the geometry were reported. Findings revealed that the geometry of the pharynx results in the formations of an adverse lateral pressure gradient, where the lowest pressures were situated on the lateral pharyngeal walls at the typical site of pharynx collapse. These low pressure regions were attributed to flow curvature effects in the lateral orientation of the airway. This extends understanding of the dysfunction and also points efforts towards alleviating this site of narrowing or strategies for stiffening the pharynx lateral walls such as targeted exercise.

6.3 Future work: 2-D modelling

While the principal contribution from this thesis was the development of a non-dimensional scheme for a cantilevered flexible plate immersed in viscous channel flow and defining its stability solution space with symmetrical positioning of the flexible-plate. This enhanced understanding led to the realisation that OSA does not lie with symmetrically positioned soft-palates but irregularity and asymmetry, as in the real world case. One aspect that remains to be finalised is extension of these findings from the explored symmetrical case of inhalation to the remaining boundary conditions of asymmetric position of the flexible-plate, one channel closed, exhalation and inhalation. Moreover, the destabilising case of one channel closed, presents further opportunity to understand the stability constraints for an

important set of boundary conditions proposed within this thesis, being closely linked with the instability of the upper-airway. Central to this understanding of the dysfunction was the proposition of two-channel breathing to be implicated in apnoea, not as traditionally thought, but as a response to the significant morbidity of apnoea brought on from single-channel breathing through the nose. It follows that if breathing through the nose is to be obstructed then oral breathing would then commence and if both were obstructed two-channel breathing would then be implicated with apnoea. Here single-channel flow through the nose was identified as the primary dysfunction to be resolved and dual flow decoupled from this completely as a first step. The present results clearly demonstrate that single channel flow is the most unstable mode of breathing and by extension greater understanding here will lead to unlocking the principal features and aid remediation of sufferers debilitating apnoea and hypoxia.

While most research has been directed towards the 3-D application of FSI to the subject of understanding and cure of OSA, an important feature in this thesis has been the simplified 2-D work. Direction of research effort towards simplified models has delivered a far greater degree of understanding of the modes of breathing and their interactions than could be obtained from a full 3-D modelling approach alone. This approach enables controlled changes to be made and these effects to be analysed in isolation, without the need to attempt to decouple areas of change from secondary interrelated influences which may not be directly not been fully understood by inspection.

6.4 Future work: 3-D modelling

The preliminary simplified FSI study of a rectangular duct flow incorporating the orthogonal motions of the soft-palate together with lateral pharynx walls led to a finding that some linkage between the two was possible when mass flux was altered as a result of their motions. Future work should determine governing parameters that, in addition to the length of the narrow entry duct and magnitude of palatal deflection, control system behaviour. Investigation of clamped-clamped boundary conditions for the pharyngeal walls may be worth investigating to increase the level of realism in the approach. However the study of Appendix A. detailed in Figure f) of the first slide titled *key features of the*

upper airway, provides guidance to future studies where a rectangular duct with longitudinal edges are fixed with three walls being compliant. These compliant walls consist of the two lateral pharyngeal walls and the soft palate which combines elements of the side walls panel divergence together with cantilevered motion sliding over the pharynx walls.

For anatomically correct models, obtaining a satisfactory temporal geometry capable of distinguishing wall motion throughout the whole breathing cycle is still an ongoing effort. While *a*OCT offers many advantages over traditional CT and MRI techniques, the speed of data acquisition remains an area for improvement. Once the means by which a reconstructed geometry for individual sufferers has been established, the next challenge lies with implementing FSI to an anatomically correct geometry in a meaningful manner. Clearly, 2-D channel and 3-D duct studies are only useful to a point, where findings could be used, for example, as general rules for groups of sufferers though not directly applicable to individuals. It is the inherent complexity in the 3-D anatomical modelling that holds the key for individuals underlying airway dysfunction.

The materials of the soft-palate and particularly the pharynx walls, are composed of several layers coupled with supporting muscles, bone and flesh that once classified require sophisticated techniques to model. An additional challenge will be to model faithfully the motion that results from shear forces lengthening or shortening the soft-palate and lateral walls during heavy breathing and snoring, potentially further destabilising elements.

Future investigations should also examine the dynamics of three dimensional streamline curvature, whereby a cross-flow pressure gradient is established to balance the centripetal effects on fluid elements. Asymmetry should be considered, allowing the lateral pressures to fluctuate independently in a similar way to that of the anteroposterior direction including head and body rotation from the supine position.

Bibliography

- ADINA R & D. Inc (2006). *Software, ADINA version 8.2/8.3*, ADINA R & D, Inc, 71 Elton Avenue, Watertown, MA 02472, USA.
- Aittokallio, T., Gyllenberg, M. & Polo, O. (2001). A model of a snorer's upper airway, *Mathematical Biosciences* **170**(1): 79 – 90.
- Allen, J. J. & Smits, A. J. (2001). Energy harvesting eel, *Journal of Fluids and Structures* **15**(3-4): 629 – 640.
- Armstrong, J. J., Leigh, M. S., Sampson, D. D., Walsh, J. H., Hillman, D. R. & Eastwood, P. R. (2006). Quantitative upper airway imaging with anatomic optical coherence tomography, *Am. J. Respir. Crit. Care Med.* **173**(2): 226–233.
- Aurgan, Y. & Depollier, C. (1995). Snoring: linear stability analysis and in-vitro experiments, *Journal of Sound and Vibration* **188**(1): 39 – 53.
- Balint, T. (2001). *Dynamics of the Upper Airway*, PhD thesis, University of Warwick.
- Balint, T. & Lucey, A. (2005). Instability of a cantilevered flexible plate in viscous two-dimensional channel flow, *Journal of Fluids and Structures* **20**: 893–912.
- Ball, C., Uddin, M. & Pollard, A. (2008). Mean flow structures insider the human upper airway, *Flow Turbulence Combustion* **81**: 155–188.
- Bathe, K.-J. (1996). *Finite Element Procedures*, Prentice-Hall, Inc.
- Bertram, C. (1986). An adjustable hydrostatic-head source using compressed air, *Journal of Physics & Scientific Instruments* **19**: 201–202.

- Bertram, C. (2003). Flows in deformable tubes and channels, in P. Carpenter & T. Pedley (eds), *Flow Past Highly Compliant Boundaries and in Collapsible Tubes*, Kluwer, pp. 51–65.
- Bisplinghoff, R. L., Ashley, H. & Halfman, R. L. (1956). Aeroelasticity ix, *ZAMM - Journal of Applied Mathematics and Mechanics / Zeitschrift fr Angewandte Mathematik und Mechanik* **36**(7-8): 316–316. Cambridge 1955. Addison-Wesley Publishing Company, Inc.
- Boudewyns, A., Punjabi, N., Van de Heyning, P. H., De Backer, W. A., O'Donnell, C. P., Schneider, H., Smith, P. L. & Schwartz, A. R. (2000). Abbreviated method for assessing upper airway function in obstructive sleep apnea, *Chest* **118**(4): 1031–1041.
- British Lung Foundation (1999). Snoring and sleep apnoea the facts, London. Fact sheet.
- Carpenter, P. & Garrad, A. (1985). The hydrodynamic stability of flow over kramer-type compliant surfaces: Part 1: Tollmien-schlichting instabilities, *Journal of Fluid Mechanics* **155**: 465–510.
- Carpenter, P., Lucey, A. & Davies, C. (2001). Progress on the use of compliant walls for laminar-flow control, *AIAA: Journal of Aircraft* **38**: 504–512.
- Chouly, F., Hirtim, A. V., Lagre, P.-Y., Paoli, J.-R. & Payan, Y. (2006). Simulation of the retroglottal fluid-structure interaction during obstructive sleep apnea, *Lecture Notes in Computer Science* **4072**: 48–57.
- Chouly, F., Hirtim, A. V., Lagre, P.-Y., Peloson, X. & Payan, Y. (2008). Numerical and experimental study of expiratory flow in the case of major airway obstructions and fluid structure interactions, *Journal of Fluids and Structures* **24**: 250–269.
- Crossman, A. & Neary, D. (2001). *Neuroanatomy: An illustrated colour text*, Churchill Livingstone.
- Cuvelier, C., Segal, A. & Steenhoven, A. A. v. (1986). *Finite element methods and Navier Stokes equations*, D. Reidel, Dordrecht.

- Davies, C. & Carpenter, P. (1997). Numerical simulation of the evolution of tollmien-schlichting waves over finite compliant panels, *Journal of Fluid Mechanics* **335**: 361–392.
- De Backer, J., Vanderverken, O., Vos, W., Devolder, A., Verhulst, S., Verbraecken, J., Parizel, P., Braem, M., de Heyning, P. V. & De Backer, W. (2007). Functional imaging using computational fluid dynamics to predict treatment success of mandibular advancement devices in sleep-disordered breathing, *Journal of Biomechanics* **40**: 3708–3714.
- De Backer, J., Vos, W., Verhulst, S. & De Backer, W. (2008). Novel imaging techniques using computer methods for the evaluation of the upper airway in patients with sleep disordered breathing: A comprehensive review, *Sleep Medicine Reviews* **12**: 437–447.
- De Backer, W. (2006). Obstructive sleep apnea-hypopnea syndrome, *Sleep Apnea: Current Diagnosis and Treatment* **35**: 90–96.
- Donnelly, L., Surdulescu, V., Chin, i. B., Casper, K., Poe, S. & Amin, R. (2003). Upper airway motion depicted at cine mr imaging performed during sleep: comparison between young patients with and those without obstructive sleep apnea, *Radiology* **227**: 239–245.
- Douglas, J. F. (1969). *An introduction to dimensional analysis for engineers*, Isaac Pitman and Sons, London, U.K.
- Dowell, E. (1975). Vibration and flutter analysis of reusable surface insulation panels, *Journal of Spacecraft and Rockets* **12**: 44–+.
- Dowell, E. H. & Hall, K. C. (2001). Modeling of fluid-structure interaction, *Annual Review of Fluid Mechanics* **33**(1): 445–490.
- Elliott, N., Lucey, A. & Heil, M. (2010). Large-amplitude oscillations of a finite-thickness cantilevered flexible plate in viscous channel flow, *Proc. ASME 3rd Joint US-European Fluids Engineering Summer Meeting and 8th International Conference on Nanochannels, Microchannels and minichannels*, number 30348 in ISBN 978-0-7918-3880-8, Montreal, Canada.
- Fitzpatrick, M., McLean, H., Urton, A., Tan, A., O'Donnell, D. & Driver, H. (2003). Effect of nasal or oral breathing route on upper airway resistance, *European Respiratory Journal* **22**: 827–832.

- Fung, Y. C. (1955). *An introduction to the theory of aeroelasticity*, number 2460351, Wiley, New York.
- Galerkin, B. (1915). Series development for some cases of equilibrium of plates and beams (in russian) translation 6318924, *Wjestnik Ingenerow Petrograd* **19**: 897–908. Translation 6318924.
- Gavriely, N. & Jensen, O. (1993). Theory and measurements of snores, *Journal of Applied Physiologists* **74**: 2828–2837.
- Gere, J. & Timoshenko, S. P. (1999). *Mechanics of Materials*, 3rd edn, Boston : PWS-Kent Pub. Co.
- Gray, H. (1918a). Anatomy of the human body, Retrieved March 8, 2006.
URL: <http://www.bartleby.com/107/illus994.html>
- Gray, H. (1918b). *Anatomy of the human body*, 20th edn, Lea & Febiger, Philadelphia.
- Gresho, P. & Sani, P. (2000a). *Incompressible Flow and the Finite Element Method, Volume One, Advection-Diffusion*, John Wiley and Sons, Ltd., New York.
- Gresho, P. & Sani, P. (2000b). *Incompressible Flow and the Finite Element Method, Volume Two, Isothermal Laminar Flow*, John Wiley and Sons, Ltd., New York.
- Grotberg, J. B. & Jensen, O. E. (2004). Biofluid mechanics in flexible tubes, *Annual Review of Fluid Mechanics* **36**(1): 121–147.
- Guo, C. Q. & Paidoussis, M. P. (2000). Stability of rectangular plates with free side-edges in two-dimensional inviscid channel flow, *Journal of Applied Mechanics* **67**(1): 171–176.
- Howell, R., Lucey, A., Carpenter, P. & Pitman, M. (2009). Interaction between a cantilevered-free flexible plate and ideal flow, *Journal of Fluids and Structures* **25**: 544–546.
- Huang, L. (1995). Flutter of cantilevered plates in axial flow, *Journal of Fluids and Structures* **9**: 127–147.

- Huang, L. & Ffowcs Williams, J. (1999). Neuromechanical interaction in human snoring and upper airway obstruction, *Journal of applied physiology* **86**: 1757–1763.
- Huang, Y., Malhotra, A., Fogel, R., Pillar, G., Kikinis, R., Loring, S. & White, D. (2001). A finite element analysis of gender differences in upper airway structure, *Am J Respir Crit Care Med* **163**: A635.
- Huang, Y., Malhotra, A. & White, D. P. (2005). Computational simulation of human upper airway collapse using a pressure-/state-dependent model of genioglossal muscle contraction under laminar flow conditions, *Journal of Applied Physiology* **99**: 1138–1148.
- Huang, Y., White, D. P. & Malhotra, A. (2005). The impact of anatomic manipulations on pharyngeal collapse: Results from a computational model of the normal human upper airway, *CHEST* **128**: 1324–1330.
- Huang, Y., White, D. P. & Malhotra, A. (2007). Use of computational modeling to predict responses to upper airway surgery in obstructive sleep apnea, *Laryngoscope* **117**: 648653.
- Hudgel, D. (1998). Availability of a meta-analysis of the surgical treatment of obstructive sleep apnoea, *CHEST* **111**: 265–268.
- Hukins, C., Mitchell, I. & Hillman, D. (2000). Radiofrequency tissue volume reduction of the soft palate in simple snoring, *Arch Otolaryngol Head Neck Surg* **126**: 602–606.
- Jensen, O. (1990). Instabilities of flow in a collapsed tube, *J. Fluid Mech.* **220**: 623.
- Kleinstreuer, C. (2003). *Two-phase flow: theory and applications*, number ISBN: 1-59169-000-5, Taylor and Francis, 29 West 35th Street, New York, NY 10001.
- Kornecki, A. (1978). Aeroelastic and hydroelastic instabilities of infinitely long plates, *Solid Mechanics Archives* **3**: 381–440.
- Kornecki, A., Dowell, E. & O'Brien, J. (1976). On the aeroelastic instability of two-dimensional panels in uniform incompressible flow, *Journal of Sound and Vibration* **47**(2): 163–178.

- Larose, P. & Grotberg, J. (1997). Flutter and long-wave instabilities in compliant channels conveying developing flows, *Journal of Fluid Mechanics* **331**: 37–58.
- Lucey, A., King, A., Tetlow, G., Wang, J., Armstrong, J., Leigh, M., Paduch, A., Walsh, J., Sampson, D., Eastwood, P. & Hillman, D. (2010). Measurement, reconstruction and flow-field computation of the human pharynx with application to sleep apnea, *Transactions on Biomedical Engineering* **57**(10): 2535–2548.
- Luo, X., Cai, Z., Li, W. & Pedley, T. (2008). The cascade structure of linear instability in collapsible channel flows, *Journal of Fluid Mechanics* **600**: 45–76.
- Luo, X. & Pedley, T. (1996). A numerical simulation of unsteady flow in a two-dimensional collapsible channel, *Journal of Fluid Mechanics* **314**: 191–225.
- Luo, X. & Pedley, T. (1998). The effects of wall inertia on flow in a two-dimensional collapsible channel, *Journal of Fluid Mechanics* **363**: 253–280.
- Luo, X. & Pedley, T. (2000). Multiple solutions and flow limitation in collapsible channel flows, *Journal of Fluid Mechanics* **420**: 301–324.
- Malhotra, A., Huang, Y., Fogel, R., Pillar, G., Edwards, J., Kikinis, R., Loring, S. & White, D. (2002). The male predisposition to pharyngeal collapse: Importance of airway length, *Am J Respir Crit Care Med* **166**: 1388–1395.
- Malhotra, A., Pillar, G., Fogel, R., Edwards, J., Ayas, N., Akahoshi, T., Hess, D. & White, D. (2002). Pharyngeal pressure and flow effects on genioglossus activation in normal subjects, *Am J Respir Crit Care Med* **165**: 71–77.
- Mihaescu, M., Murugappan, S., Gutmark, E., Donnelly, M. & Kalra, M. (2007). Computational modeling of upper airway before and after adenotonsillectomy for obstructive sleep apnea, *Laryngoscope* **117**: 1–3.
- Moretti, P. (2003). Tension in fluttering flags, *10th Intl. Conf. Sound and Vibration*, Stockholm, Sweden.
- Nithiarasu, P., Hassan, O., Morgan, K., Weatherill, N., Fielder, C., Whittet, H., Ebdon, P. & Lewis, K. (2008). Steady flow through a realistic human upper airway geometry, *International Journal for Numerical Methods in Engineering* **57**: 631–651.

- Nowacki, W. (1963). *Dynamics of Elastic Systems*, Chapman & Hall Ltd., London.
- Oden, J. T., e. a. (1975). Computational methods in nonlinear mechanics, Vol. 9, Texas Institute for Computational Mechanics, John Wiley & Sons, Ltd, The University of Texas at Austin, Austin, Texas 78712, 1974, pp. 492–492.
- OpenCFD Ltd (2009). *Software, OpenFOAM, the Open Source CFD Toolbox: User Guide, Version 1.6*, OpenCFD Ltd.
- Paidoussis, M. P. (1998). Fluid-structure interactions, in M. P. Paidoussis (ed.), *Slender Structures and Axial Flow*, Vol. 1 of *Fluid-Structure Interactions*, Elsevier Science Publishing Co Inc, United States.
- Paidoussis, M. P. (2003). Fluid-structure interactions, in M. P. Paidoussis (ed.), *Slender Structures and Axial Flow*, Vol. 2 of *Fluid-Structure Interactions*, Academic Press.
- Pierce, R. & Worsnop, C. (1999). Upper airway function and dysfunction in respiration, *Clinical and Experimental Pharmacology and Physiology* **26**(1): 1–10.
- Rayleigh (1879). On the stability of jets, *Proceedings of the London Mathematical Society* **10**: 4–12.
- Reddy, J. N. & Gartling, D. K. (1994). *The Finite Element Method in Heat Transfer and Fluid Dynamics*, CRC Press, Inc.
- Reddy, J. N. and Gartling, D. K. (2001). *The finite element method in heat transfer and fluid dynamics*, 2nd edn, CRC Press, Boca Raton, FL.
- Saladin, K. (2001). *Anatomy and physiology: The unity of form and function*, McGraw Hill.
- Schwab, R., Geftter, W., Pack, A. & Hoffman, E. (1993). Dynamic imaging of the upper airway during respiration in normal subjects, *Journal of Applied Physiology* **74**: 1504–1514.
- Shome, B., Wang, L., Santare, M., Prasad, A., Szeri, A. & Roberts, D. (1998). Modeling of airflow in the pharynx with application to sleep apnea, *J Biomech Eng* **120**: 416422.

- Sun, X., Yu, C., Wang, Y. & Liu, Y. (2007). Numerical simulation of soft palate movement and airflow in human upper airway by fluid-structure interaction method, *Acta Mechanica Sinica* **23**: 359–367.
- Sung, S., Jeong, S., Yu, Y., Hwang, C. & Pae, E. (2006). Customized three-dimensional computational fluid dynamics simulation of the upper airway of obstructive sleep apnea, *Angle Orthodontist* **76**: 791–799.
- Tetlow, G. A. & Lucey, A. D. (2009). Motions of a cantilevered flexible plate in viscous channel flow driven by a constant pressure drop, *Communications in Numerical Methods in Engineering* **25**(5): 463–482.
- Tetlow, G. & Lucey, A. (2006). Motions of an offset plate in viscous channel flow: A model for flutter of the soft palate, *World Congress on Medical Physics and Biomechanical Engineering*, IFMBE.
- Tetlow, G., Lucey, A. & Balint, T. (2006). Instability of a cantilevered flexible plate in viscous channel flow driven by constant pressure drop, number ASME Paper PVP2006-ICPVT11-93943.
- Tetlow, G., Lucey, A. & Wang, J. (2008). Analogue computational modelling of upper airway dynamics, in Zolotarev & Horacek (eds), *Proc. of 9th International Conference on Flow Induced Vibrations - FIV2008*.
- The Boston Consulting Group (2003). Proposal for a national sleep health agenda, *Technical report*, Australasian Sleep Association.
- Thoma, S. (1939). Why does the flag flutter, *Technical report*, Mitteilungen des Hydraulischen, Institut der Technischen Hochschule, Munich.
- Verbraecken, J. A. & De Backer, W. A. (2009). Upper airway mechanics, *Respiration* **78**(2): 121–133.
- Vos, W., Backer, J. D., Devolder, A., Vanderveken, O., Verhulst, S., Salgado, R., Germonpre, P., Bartoens, B., Wuyts, F., Parizel, P. & Backer, W. D. (2007). Correlation between severity of sleep apnea and upper airway morphology based on advanced anatomical and functional imaging, *Journal of Biomechanics* **40**: 2207–2213.
- Watanabe, Y., Isogai, K., Suzuki, S. & Sugihara, M. (2002). A theoretical study of paper flutter, *Journal of Fluids and Structures* **16**: 543–560.

- Watanabe, Y., Suzuki, S., Sugihara, M. & Sueoka, Y. (2002). An experimental study of paper flutter, *Journal of Fluids and Structures* **16**(4): 529–542.
- White, D. (1995). Sleep-related breathing disorder: II. pathophysiology of obstructive sleep apnoea, *Thorax* **50**(7): 797–804.
- Woodson, B. T. (2003). Expiratory pharyngeal airway obstruction during sleep: A multiple element model, *The Laryngoscope* **113**: 1450–1459.
- Yamaguchi, N., Ito, K. & Ogata, M. (2003). Flutter limits and behaviors of flexible webs having a simplified basic configuration in high-speed flow, *Journal of Fluids Engineering* **125**: 345–353.
- Yandykin, Y., Tenetov, V. & Levin, D. (2001). The flow-induced vibration of a flexible strip hanging vertically in a parallel flow part 1: Temporal aeroelastic instability, *Journal of Fluids and Structures* **15**: 1167–1185.
- Zhang, Z. & Kleinstreuer, C. (2003). Low-reynolds-number turbulent flows in locally constricted conduits: A comparison study, *AIAA Journal* **41**: 831–840.

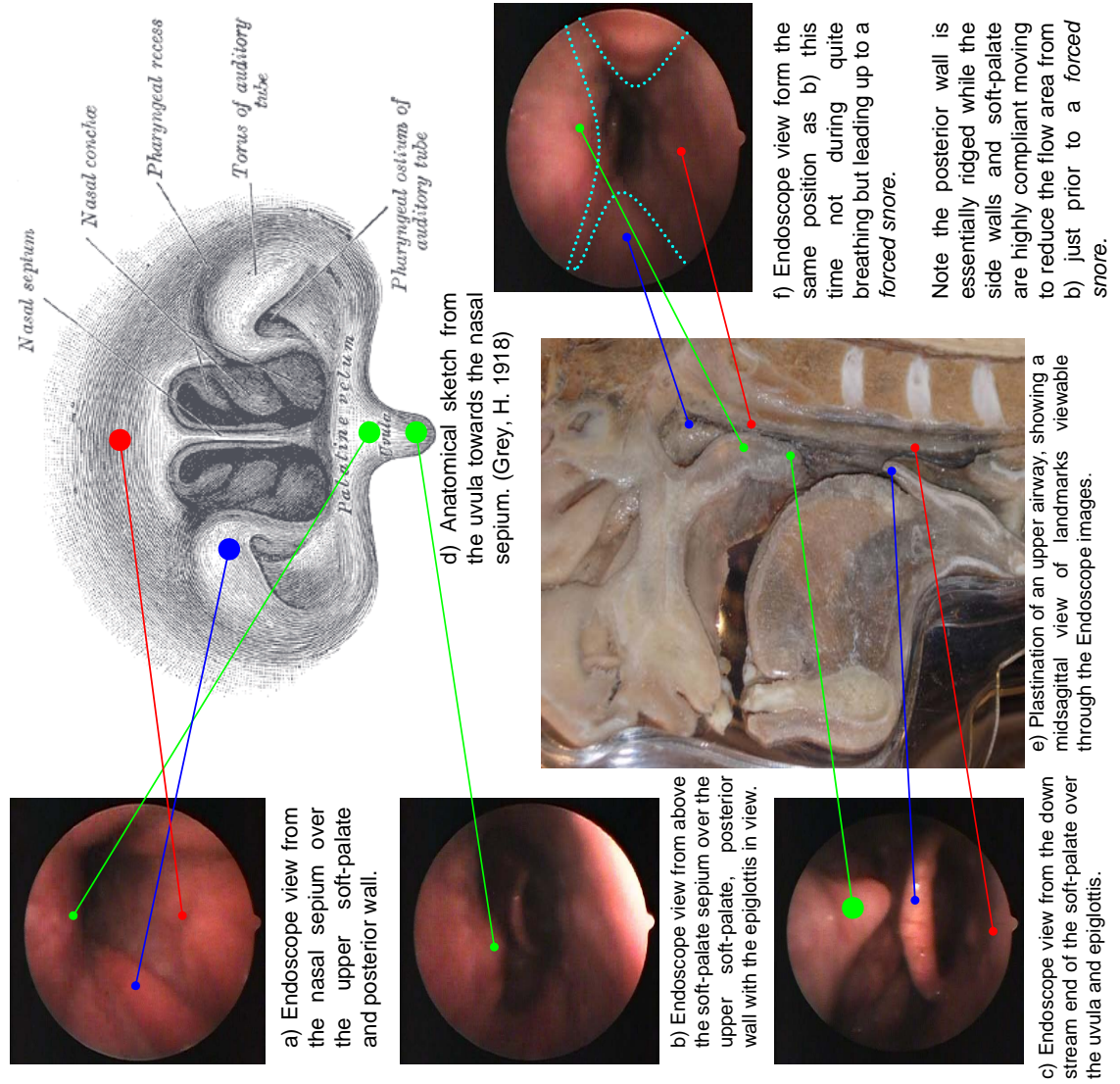
.
.
Every reasonable effort has been made to acknowledge the owners of copyright material. I would be pleased to hear from any copyright owner who has been omitted or incorrectly acknowledged.

Part III

Appendices

APPENDIX A

Bronchoscope Images Of Forced Snores



Key features of the upper airway:
Through this slide Endoscope snapshots will be compared with typical representations of the upper airway to aid in later landmark identification during several breathing cycle scenarios.

In a) the upstream (during inhalation) region of the soft-palate is shown along with the other structures including the torus of auditory tube. Note the view is through the nose and the palate is at the top of screen in each case.

Moving further downstream b) views the area where the torus of auditory tube is no longer visible but shows the open area during normal quite breathing.

The final image in this series c) shows the section of the soft-palate (uvula) without lateral connections to other structures whereby flow leakage would be expected.

Image f) shows the level of compliance in this region of the upper airway when contrasted with b) taken in a similar position. Here the torus of auditory tube and soft-palate are clearly moved inwards obstructing/limiting flow. The dotted lines give an indication of the sliding surfaces, bottom of view, the posterior wall is essentially ridged.

a) Endoscope view from the nasal septum over the upper soft-palate and posterior wall.

b) Endoscope view from above the soft-palate septum over the upper soft-palate, posterior wall with the epiglottis in view.

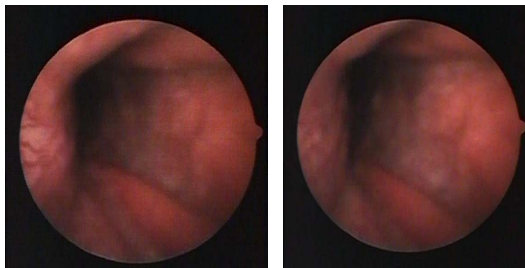
c) Endoscope view from the downstream end of the soft-palate over the uvula and epiglottis.

e) Plastination of an upper airway, showing a midsagittal view of landmarks viewable through the Endoscope images.

d) Anatomical sketch from the uvula towards the nasal septum. (Grey, H. 1918)

f) Endoscope view from the same position as b) this time not during quite breathing but leading up to a forced snore.

Note the posterior wall is essentially ridged while the side walls and soft-palate are highly compliant moving to reduce the flow area from b) just prior to a forced snore.



a) Endoscope view from the nasal septum over the upper soft-palate and posterior wall during heavy exhalation via nose only

Heavy breathing - Exhalation:

During exhalation as view in a) the airway upstream the soft-palate is seen to open from its mean position (quite breathing). Additionally the shear stress exerted by the fluid flow on the physical boundary causes a small motion in the exhalation streamwise direction. The increased opening in the airway was just prior to exhalation so attributed to neuromuscular activity. This dynamic opening and stiffening of the airway supports the 1 channel closed exhalation findings where the soft-palate would otherwise be driven into the flowing passage (for this case the nasal passage shown).

The structural shear stress induced tension can be best visualised by tracking the positions of the soft-palate from a) prominent to c) taut and elongated.

Heavy breathing - Inhalation:

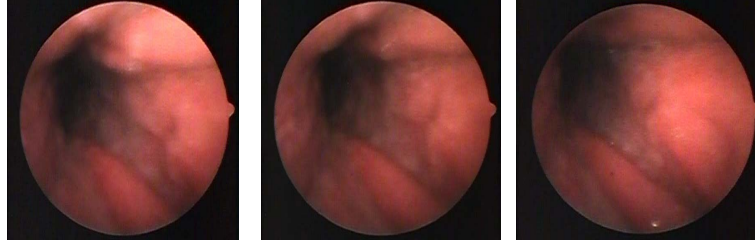
The series of snapshots in c) show the relative airway opening for the inhalation case similar to a). This time owing to the relatively higher velocities the shear stress exerted on the boundary is greater leading to greater motion of the wall in the inhalation streamwise direction, observe the position of soft-palate from a) to c) where it's taut & noticeably elongated.

Heavy breathing - mouth:

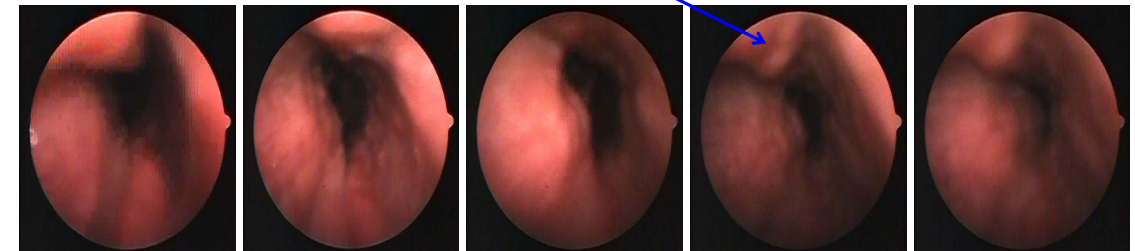
The series in b) viewed from the same position as a) & c) though subject to heavy breathing through the mouth. The nasal airway closes which appears as suitable response as predicted by offset channel simulations where a free soft-palate would undergo large amplitude motions from inhalation to exhalation and likely flutter instability as for a forced snore through the mouth.



b) Endoscope view from the nasal septum during heavy breathing through the mouth



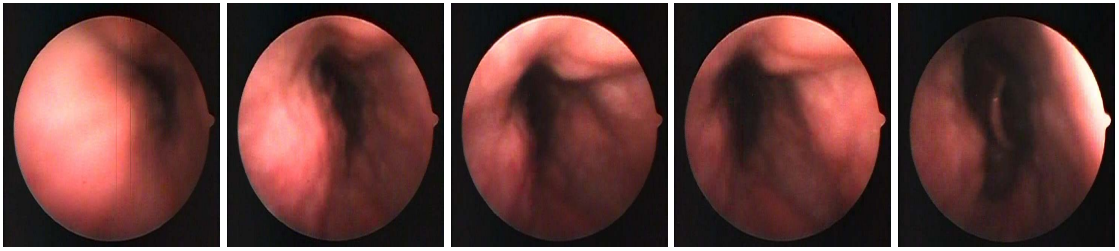
c) Endoscope view from the nasal septum over the upper soft-palate and posterior wall during heavy inhalation via nose only



Forced snore - Nose:

During inhalation through the nose only a forced snore was achieved by restricting the airway in the region of the soft-palate by conscious muscle control and breathing heavily.

This series of snapshots show, a) initiating the snore and b) recovery to normal breathing. Initiation of the snore can be characterised by a rapid reduction in area of the airway (2 frames at 24fps) and through a shear stress induced motion in the streamwise direction of the compliant lateral walls and soft-palate from the fluid moving through the restriction. The snore instability took the form of panel flutter of the walls and what looks like small amplitude flutter of the trailing edges. The panel flutter seen was in the top or mucous layer of pharynx structure localised around lumpy protrusions from the mean geometry.

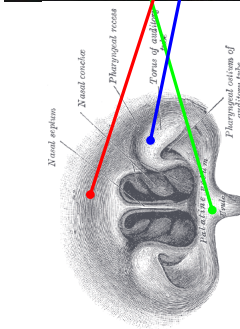
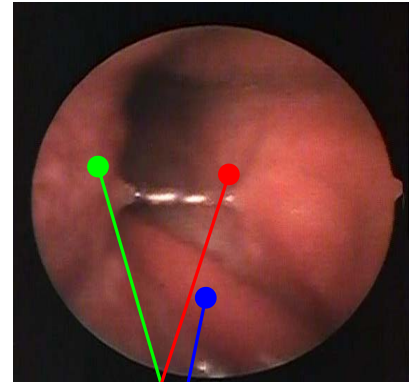


During the recovery conscious muscular effort was unable to regain stability, cessation of flow was required to allow the airway to stabilised. The recovery was characterised by a rapid returned to normal size or slightly larger taking a similar time as the initial collapse .

Note this takes place prior to inhalation commencing.

b) Endoscope view from above the soft-palate during recovery (when viewed from top to bottom) from a forced snore through the nose

Below: The anatomical landmarks repeated, this was following a swallow where saliva is still visible.



a) Endoscope view from above the soft-palate during initiation (when viewed top to bottom) of a forced snore through the nose

Structure.—The pharynx is composed of three coats: **mucous, fibrous, and muscular**

Forced snore - Mouth:

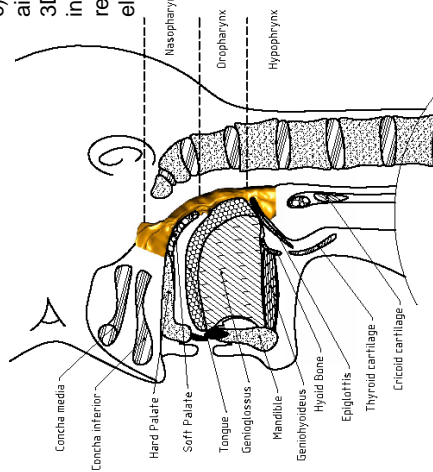
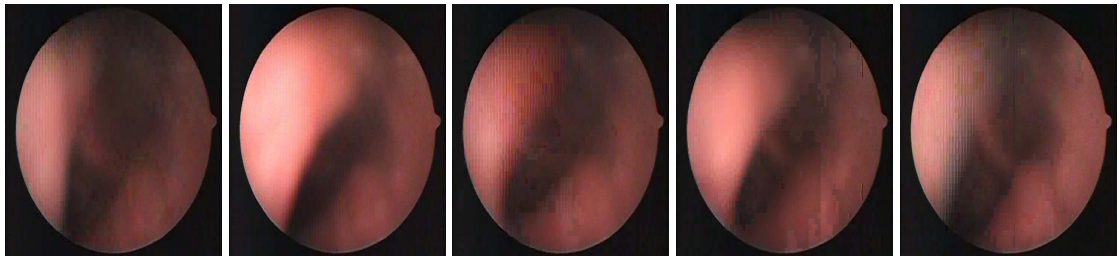
The burliness of this series of snapshots is due to the rapid motion flutter instability being viewed.

In this case the force snore was brought on by opening the passage to the nasal airway by conscious muscular activity as opposed to the heavy oral breathing previously where the soft-palate was permitted to stiffen and close.

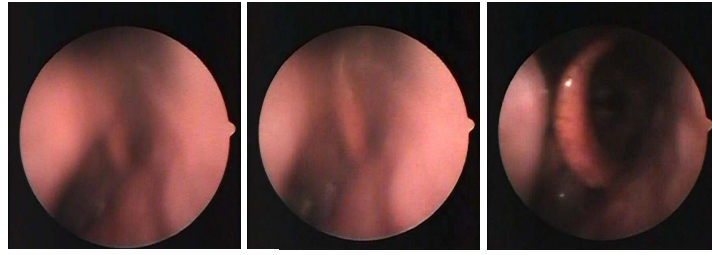
The free soft-palate was then exposed to the forces expected from the offset plate modelling where the compliant surface moves into the passage with the greater resistance (nasal). Clearly visible in a) is the position of the uvula deflected almost to the posterior ridged surface, contrast this against the final snapshot in b) with the palate in a normal position and the uvula out of view.

In contrast to the motion of the nasal forced snore the oral forced snore was characterised with large amplitude flutter moving rapidly from a neutral position to impacting the posterior wall

a) Endoscope view from the down stream end of the soft-palate over the uvula and epiglottis during a forced snore through the mouth.



c) Illustration of the upper airway overlaid with a 3D reconstruction of an individuals airway referencing the 3 major elements of the pharynx



b) Endoscope view from the down stream end of the soft-palate over the uvula and epiglottis at the conclusion of a forced snore through the mouth.

Shear stress induced tension does not appear to have any visually significant role potentially owing to the larger flow area, however any elongation (which appeared to be significant in the nasal forced snore) of the soft-palate as a result of flow induced tension would have an additional destabilising effect from increasing the length of the compliant section in opposition to the normally attributed stabilising restorative force.

Illustration c) shows the visible area from the endoscope being the nasopharynx, and also highlights the areas not visible that are of importance such as the oropharynx and the oral side of the soft-palate which is not imaged currently.

APPENDIX B

Simulation Parameter Data Set

B.1 Solved cases within the viscous range

The variable tags listed in the following table have the following physical interpretations:

Table B.1: Parameter data set expanded descriptions

Parameter	Expanded parameter description
SBS	Simulation Breakdown Structure
REF_DOMAIN(1)	x position (m), Start of split channel
REF_DOMAIN(2)	x position (m), End combined channel
REF_DOMAIN(3)	y position (m), Bottom wall
REF_DOMAIN(4)	y position (m), Top wall
NS_OPT	For a Stokes problem 1; for Navier-Stokes 2
N_BLOCK_X	The number of element blocks along the x axis
N_BLOCK_Y	The number of element blocks along the y axis
N_BLOCK_XST	The number of blocks to the free end of the cantilevered plate in the x direction measured from the back end of the combined channel
N_BLOCK_YST	The number of blocks to the split plate in the y direction measured from the top wall
N_CPLATE_DISPL	The number of blocks for the flexible cantilever
INLETS	Number of inlets to the split duct
DAMPING	Damping (kg/sm ²)
PLATE THICKNESS (h)	Plate thickness (m)
RHO_FLUID	Density of the fluid (kg/m ³)
Youngs Mod (Pa)	elastic (Young's) modulus (N/m ²)
RHO_WALL	Density of the flexible cantilever (kg/m ³)
Dynamic viscosity (μ)	Dynamic viscosity (N.s/m ³)
Plate Stiffness (B)	Flexural rigidity (Nm)
Frequency Theory 2nd mode (Rad/sec)	Second fundamental <i>in vacuo</i> mode
Re Reynolds number	Reynolds number dimensionless
$Zeta$ Mass ratio	Mass ratio dimensionless
EXIT VELOCITY	Average velocity (m/s) combined channel
Γ Stiffness ratio	Stiffness ratio dimensionless

Simulation Breakdown Structure (SBS)	REF_DOMAIN(1)	REF_DOMAIN(2)	REF_DOMAIN(3)	REF_DOMAIN(4)	NST_OPT	N_BLOCK_X	N_BLOCK_Y	N_BLOCK_XST	N_BLOCK_YST	N_PLATE_DISPL	INLETS	DAMPING	PLATE THICKNESS (h)	RHO_FLUID	Youngs Mod (Pa)	RHO_WALL	Dynamic viscosity (mu)	Plate Stiffness (B)	Frequency Theory 2nd mode (Rad/sec)	Re Reynolds number	Zeta mass ratio	EXIT VELOCITY	Gamma stiffness ratio
L10_h1_01	0	0.0405	-0.0050	0.0050	2	81	16	35	8	21	2	0	5.0E-04	1.1774	8.8E+03	1000	1.98E-05	1.0E-07	100.1	2392	42.5	4.0	5.4E-03
a	0	0.0405	-0.0050	0.0050	2	81	16	35	8	25	2	0	6.0E-04	1.1774	8.8E+03	1000	2.38E-05	1.8E-07	83.4	1702	42.5	3.4	7.4E-03
b	0	0.0405	-0.0050	0.0050	2	81	16	35	8	21	2	0	1.0E-03	2.3548	1.1E+03	1000	2.80E-05	1.0E-07	70.8	2405	42.5	2.9	5.4E-03
c	0	0.0405	-0.0050	0.0050	2	81	16	35	8	21	2	0	1.0E-03	2.3548	1.1E+03	500	2.80E-05	1.0E-07	100.1	2405	21.2	2.9	5.4E-03
d	0	0.0405	-0.0025	0.0025	2	81	16	50	8	18	2	0	1.0E-05	1.1774	2.0E+08	2477	1.98E-05	1.9E-08	265.3	257	2.5	0.9	3.5E-02
e	0	0.0405	-0.0025	0.0025	2	81	16	50	8	18	2	0	1.0E-04	1.1774	5.0E+04	2477	1.98E-05	4.7E-09	42.0	255	24.8	0.9	8.8E-03
f	0	0.0405	-0.0025	0.0025	2	81	16	50	8	18	2	0	1.0E-05	1.1774	2.0E+08	2477	1.98E-05	1.9E-08	265.3	256	2.5	0.9	3.5E-02
g	0	0.0405	-0.0050	0.0050	2	81	16	35	8	21	2	0	5.0E-04	1.1774	8.8E+03	1000	1.98E-05	1.0E-07	100.1	2438	42.5	4.1	5.2E-03
h	0	0.0405	-0.0050	0.0050	2	81	16	35	8	21	2	0	1.0E-03	2.3548	1.1E+03	500	2.80E-05	1.0E-07	100.1	2405	21.2	2.9	5.4E-03
i	0	0.0405	-0.0050	0.0050	2	81	16	35	8	21	2	0	2.3E-04	1.1774	8.8E+04	2154	1.98E-05	1.0E-07	99.2	2438	42.1	4.1	5.1E-03
j	0	0.0405	-0.0025	0.0025	2	81	16	50	8	18	2	0	1.0E-05	1.1774	5.0E+06	2477	1.98E-05	4.7E-10	42.0	247	2.5	0.8	9.4E-04
k	0	0.0405	-0.0025	0.0025	2	81	16	50	8	29	2	0	1.0E-04	1.1774	5.0E+04	2477	1.98E-05	4.7E-09	15.5	514	15.0	1.7	4.8E-04
l	0	0.0405	-0.0025	0.0025	2	81	16	50	8	18	2	0	1.0E-04	1.1774	5.0E+03	2477	1.98E-05	4.7E-10	13.3	242	24.8	0.8	9.8E-04
L12_h1_01	0	0.0405	-0.0050	0.0050	2	81	16	35	8	25	2	0	5.0E-04	1.1774	8.8E+03	1000	1.98E-05	1.0E-07	69.5	1095	35.4	1.8	1.5E-02
L14_h1_01	0	0.0405	-0.0050	0.0050	2	81	16	35	8	29	2	0	5.0E-04	1.1774	8.8E+03	1000	1.98E-05	1.0E-07	51.1	1138	30.3	1.9	8.7E-03

Simulation Breakdown Structure (SBS)	REF_DOMAIN(1)	REF_DOMAIN(2)	REF_DOMAIN(3)	REF_DOMAIN(4)	NST_OPT	N_BLOCK_X	N_BLOCK_Y	N_BLOCK_XST	N_BLOCK_YST	N_CPLATE_DISPL	INLETS	DAMPING	PLATE THICKNESS (h)	RHO_FLUID	Youngs Mod (Pa)	RHO_WALL	Dynamic viscosity (mu)	Plate Stiffness (B)	Frequency Theory 2nd mode (Rad/sec)	Re Reynolds number	Zeta mass ratio	EXIT VELOCITY	Gamma stiffness ratio
L16_h1_01	0	0.0405	-0.0050	0.0050	2	81	16	35	8	33	2	0	5.0E-04	1.1774	8.8E+03	1000	1.98E-05	1.0E-07	39.1	884	26.5	1.5	9.7E-03
L10_h2_01	0	0.0405	-0.0050	0.0050	2	81	16	35	8	21	2	0	1.0E-03	1.1774	8.8E+03	1000	1.98E-05	8.2E-07	200.1	4915	84.9	8.3	1.0E-02
L16_h2_01	0	0.0405	-0.0050	0.0050	2	81	16	35	8	33	2	0	1.0E-03	1.1774	8.8E+03	1000	1.98E-05	8.2E-07	78.2	4096	53.1	6.9	3.6E-03
L10_h3_01	0	0.0405	-0.0050	0.0050	2	81	16	35	8	21	2	0	1.0E-04	1.1774	8.8E+03	1000	1.98E-05	8.2E-10	20.0	120	8.5	0.2	1.7E-02
L12_h3_01	0	0.0405	-0.0050	0.0050	2	81	16	35	8	25	2	0	1.0E-04	1.1774	8.8E+03	1000	1.98E-05	8.2E-10	13.9	84	7.1	0.1	2.0E-02
L14_h3_01	0	0.0405	-0.0050	0.0050	2	81	16	35	8	29	2	0	1.0E-04	1.1774	8.8E+03	1000	1.98E-05	8.2E-10	10.2	37	6.1	0.1	6.6E-02
L10_h1_01_H2	0	0.0405	-0.0025	0.0025	2	81	16	35	8	21	2	0	5.0E-04	1.1774	8.8E+03	1000	1.98E-05	1.0E-07	100.1	808	42.5	2.7	1.2E-02
L12_h1_01_H2	0	0.0405	-0.0025	0.0025	2	81	16	35	8	25	2	0	5.0E-04	1.1774	8.8E+03	1000	1.98E-05	1.0E-07	69.5	520	35.4	1.7	1.7E-02
L14_h1_01_H2	0	0.0405	-0.0025	0.0025	2	81	16	35	8	29	2	0	5.0E-04	1.1774	8.8E+03	1000	1.98E-05	1.0E-07	51.1	306	30.3	1.0	3.0E-02
L16_h1_01_H2	0	0.0405	-0.0025	0.0025	2	81	16	35	8	33	2	0	5.0E-04	1.1774	8.8E+03	1000	1.98E-05	1.0E-07	39.1	188	26.5	0.6	5.3E-02

Simulation Breakdown Structure (SBS)	REF_DOMAIN(1)	REF_DOMAIN(2)	REF_DOMAIN(3)	REF_DOMAIN(4)	NST_OPT	N_BLOCK_X	N_BLOCK_Y	N_BLOCK_XST	N_BLOCK_YST	N_PLATE_DISPL	INLETS	DAMPING	PLATE THICKNESS (h)	RHO_FLUID	Youngs Mod (Pa)	RHO_WALL	Dynamic viscosity (mu)	Plate Stiffness (B)	Frequency Theory 2nd mode (Rad/sec)	Re Reynolds number	Zeta mass ratio	EXIT VELOCITY	Gamma stiffness ratio
L12_h2_01_H2	0	0.0405	-0.0025	0.0025	2	81	16	35	8	25	2	0	1.0E-03	1.1774	8.8E+03	1000	1.98E-05	8.2E-07	139.0	1384	70.8	4.7	1.9E-02
L16_h2_01_H2	0	0.0405	-0.0025	0.0025	2	81	16	35	8	33	2	0	1.0E-03	1.1774	8.8E+03	1000	1.98E-05	8.2E-07	78.2	1096	53.1	3.7	1.3E-02
L10_h3_01_H2	0	0.0405	-0.0025	0.0025	2	81	16	35	8	21	2	0	1.0E-04	1.1774	8.8E+03	1000	1.98E-05	8.2E-10	20.0	7	8.5	0.0	1.2E+00
L12_h3_01_H2	0	0.0405	-0.0025	0.0025	2	81	16	35	8	25	2	0	1.0E-04	1.1774	8.8E+03	1000	1.98E-05	8.2E-10	13.9	6	7.1	0.0	1.1E+00
L12_h1_01_H3	0	0.0405	-0.0075	0.0075	2	81	16	35	8	25	2	0	5.0E-04	1.1774	8.8E+03	1000	1.98E-05	1.0E-07	69.5	1517	35.4	1.7	1.8E-02
L14_h1_01_H3	0	0.0405	-0.0075	0.0075	2	81	16	35	8	29	2	0	5.0E-04	1.1774	8.8E+03	1000	1.98E-05	1.0E-07	51.1	1360	30.3	1.5	1.4E-02
L16_h1_01_H3	0	0.0405	-0.0075	0.0075	2	81	16	35	8	33	2	0	5.0E-04	1.1774	8.8E+03	1000	1.98E-05	1.0E-07	39.1	1211	26.5	1.4	1.2E-02
L10_h3_01_H3	0	0.0405	-0.0075	0.0075	2	81	18	35	9	21	2	0	1.0E-04	1.1774	8.8E+03	1000	1.98E-05	8.2E-10	20.4	131	8.5	0.1	3.3E-02
L12_h3_01_H3	0	0.0405	-0.0075	0.0075	2	81	18	35	9	25	2	0	1.0E-04	1.1774	8.8E+03	1000	1.98E-05	8.2E-10	14.1	105	7.1	0.1	2.9E-02

Simulation Breakdown Structure (SBS)	REF_DOMAIN(1)	REF_DOMAIN(2)	REF_DOMAIN(3)	REF_DOMAIN(4)	NST_OPT	N_BLOCK_X	N_BLOCK_Y	N_BLOCK_XST	N_BLOCK_YST	N_CPLATE_DISPL	INLETS	DAMPING	PLATE THICKNESS (h)	RHO_FLUID	Youngs Mod (Pa)	RHO_WALL	Dynamic viscosity (mu)	Plate Stiffness (B)	Frequency Theory 2nd mode (Rad/sec)	Re Reynolds number	Zeta mass ratio	EXIT VELOCITY	Gamma stiffness ratio
L14_h3_01_H3	0	0.0405	-0.0075	0.0075	2	81	18	35	9	29	2	0	1.0E-04	1.1774	8.8E+03	1000	1.98E-05	8.2E-10	10.3	144	6.1	0.2	9.8E-03
L16_h3_01_H3	0	0.0405	-0.0075	0.0075	2	81	16	35	8	33	2	0	1.0E-04	1.1774	8.8E+03	1000	1.98E-05	8.2E-10	7.9	35	5.3	0.0	1.1E-01

B.2 Un-Solved cases with stability points in the turbulent range

The variable tags listed in the following table have the following physical interpretations:

Table B.2: Parameter data set expanded descriptions

Parameter	Expanded parameter description
SBS	Simulation Breakdown Structure
REF_DOMAIN(1)	x position (m), Start of split channel
REF_DOMAIN(2)	x position (m), End combined channel
REF_DOMAIN(3)	y position (m), Bottom wall
REF_DOMAIN(4)	y position (m), Top wall
NS_OPT	For a Stokes problem 1; for Navier-Stokes 2
N_BLOCK_X	The number of element blocks along the x axis
N_BLOCK_Y	The number of element blocks along the y axis
N_BLOCK_XST	The number of blocks to the free end of the cantilevered plate in the x direction measured from the back end of the combined channel
N_BLOCK_YST	The number of blocks to the split plate in the y direction measured from the top wall
N_CPLATE_DISPL	The number of blocks for the flexible cantilever
INLETS	Number of inlets to the split duct
DAMPING	Damping (kg/sm ²)
PLATE THICKNESS (h)	Plate thickness (m)
RHO_FLUID	Density of the fluid (kg/m ³)
Youngs Mod (Pa)	elastic (Young's) modulus (N/m ²)
RHO_WALL	Density of the flexible cantilever (kg/m ³)
Dynamic viscosity (μ)	Dynamic viscosity (N.s/m ³)
Plate Stiffness (B)	Flexural rigidity (Nm)
Frequency Theory 2nd mode (Rad/sec)	Second fundamental <i>in vacuo</i> mode

SBS Simulation Breakdown Structure	REF_DOMAIN(1)	REF_DOMAIN(2)	REF_DOMAIN(3)	REF_DOMAIN(4)	NST_OPT	N_BLOCK_X	N_BLOCK_Y	N_BLOCK_XST	N_BLOCK_YST	N_PLATE_DISPL	INLETS	DAMPING	PLATE THICKNESS (h)	RHO_FLUID	Youngs Mod (Pa)	RHO_WALL	Dynamic viscosity (mu)	Plate Stiffness (B)	Frequency Theory 2nd mode (Rad/sec)
L4_h1_01	0	0.0405	-0.0050	0.0050	2	81	16	35	8	9	2	0	5.0E-04	1.1774	8.8E+03	1000.0	1.98E-05	1.0E-07	625.4
L6_h1_01	0	0.0405	-0.0050	0.0050	2	81	16	35	8	13	2	0	5.0E-04	1.1774	8.8E+03	1000.0	1.98E-05	1.0E-07	278.0
L8_h1_01	0	0.0405	-0.0050	0.0050	2	81	16	35	8	17	2	0	5.0E-04	1.1774	8.8E+03	1000.0	1.98E-05	1.0E-07	156.3
L4_h2_01	0	0.0405	-0.0050	0.0050	2	81	16	35	8	9	2	0	1.0E-03	1.1774	8.8E+03	1000.0	1.98E-05	8.2E-07	1250.8
L6_h2_01	0	0.0405	-0.0050	0.0050	2	81	16	35	8	13	2	0	1.0E-03	1.1774	8.8E+03	1000.0	1.98E-05	8.2E-07	555.9
L8_h2_01	0	0.0405	-0.0050	0.0050	2	81	16	35	8	17	2	0	1.0E-03	1.1774	8.8E+03	1000.0	1.98E-05	8.2E-07	312.7
L10_h2_01	0	0.0405	-0.0050	0.0050	2	81	16	35	8	21	2	0	1.0E-03	1.1774	8.8E+03	1000.0	1.98E-05	8.2E-07	200.1
L4_h3_01	0	0.0405	-0.0050	0.0050	2	81	16	35	8	9	2	0	1.0E-04	1.1774	8.8E+03	1000.0	1.98E-05	8.2E-10	125.1
L6_h3_01	0	0.0405	-0.0050	0.0050	2	81	16	35	8	13	2	0	1.0E-04	1.1774	8.8E+03	1000.0	1.98E-05	8.2E-10	55.6
L8_h3_01	0	0.0405	-0.0050	0.0050	2	81	16	35	8	17	2	0	1.0E-04	1.1774	8.8E+03	1000.0	1.98E-05	8.2E-10	31.3
L4_h1_01_H2	0	0.0405	-0.0025	0.0025	2	81	16	35	8	9	2	0	5.0E-04	1.1774	8.8E+03	1000.0	1.98E-05	1.0E-07	625.4
L6_h1_01_H2	0	0.0405	-0.0025	0.0025	2	81	16	35	8	13	2	0	5.0E-04	1.1774	8.8E+03	1000.0	1.98E-05	1.0E-07	278.0

SBS Simulation Breakdown Structure	REF_DOMAIN(1)	REF_DOMAIN(2)	REF_DOMAIN(3)	REF_DOMAIN(4)	NST_OPT	N_BLOCK_X	N_BLOCK_Y	N_BLOCK_XST	N_BLOCK_YST	N_PLATE_DISPL	INLETS	DAMPING	PLATE THICKNESS (h)	RHO_FLUID	Youngs Mod (Pa)	RHO_WALL	Dynamic viscosity (mu)	Plate Stiffness (B)	Frequency Theory 2nd mode (Rad/sec)
L8_h1_01_H2	0	0.0405	-0.0025	0.0025	2	81	16	35	8	17	2	0	5.0E-04	1.1774	8.8E+03	1000.0	1.98E-05	1.0E-07	156.3
L4_h2_01_H2	0	0.0405	-0.0025	0.0025	2	81	16	35	8	9	2	0	1.0E-03	1.1774	8.8E+03	1000.0	1.98E-05	8.2E-07	1250.8
L6_h2_01_H2	0	0.0405	-0.0025	0.0025	2	81	16	35	8	13	2	0	1.0E-03	1.1774	8.8E+03	1000.0	1.98E-05	8.2E-07	555.9
L8_h2_01_H2	0	0.0405	-0.0025	0.0025	2	81	16	35	8	17	2	0	1.0E-03	1.1774	8.8E+03	1000.0	1.98E-05	8.2E-07	312.7
L10_h2_01_H2	0	0.0405	-0.0025	0.0025	2	81	16	35	8	21	2	0	1.0E-03	1.1774	8.8E+03	1000.0	1.98E-05	8.2E-07	200.1
L4_h3_01_H2	0	0.0405	-0.0025	0.0025	2	81	16	35	8	9	2	0	1.0E-04	1.1774	8.8E+03	1000.0	1.98E-05	8.2E-10	125.1
L6_h3_01_H2	0	0.0405	-0.0025	0.0025	2	81	16	35	8	13	2	0	1.0E-04	1.1774	8.8E+03	1000.0	1.98E-05	8.2E-10	55.6
L4_h1_01_H3	0	0.0405	-0.0075	0.0075	2	81	16	35	8	9	2	0	5.0E-04	1.1774	8.8E+03	1000.0	1.98E-05	1.0E-07	625.4
L6_h1_01_H3	0	0.0405	-0.0075	0.0075	2	81	16	35	8	13	2	0	5.0E-04	1.1774	8.8E+03	1000.0	1.98E-05	1.0E-07	278.0
L8_h1_01_H3	0	0.0405	-0.0075	0.0075	2	81	16	35	8	17	2	0	5.0E-04	1.1774	8.8E+03	1000.0	1.98E-05	1.0E-07	156.3
L10_h1_01_H3	0	0.0405	-0.0075	0.0075	2	81	16	35	8	21	2	0	5.0E-04	1.1774	8.8E+03	1000.0	1.98E-05	1.0E-07	100.1

SBS Simulation Breakdown Structure	REF_DOMAIN(1)	REF_DOMAIN(2)	REF_DOMAIN(3)	REF_DOMAIN(4)	NST_OPT	N_BLOCK_X	N_BLOCK_Y	N_BLOCK_XST	N_BLOCK_YST	N_PLATE_DISPL	INLETS	DAMPING	PLATE THICKNESS (h)	RHO_FLUID	Youngs Mod (Pa)	RHO_WALL	Dynamic viscosity (mu)	Plate Stiffness (B)	Frequency Theory 2nd mode (Rad/sec)
L4_h2_01_H3	0	0.0405	-0.0075	0.0075	2	81	16	35	8	9	2	0	1.0E-03	1.1774	8.8E+03	1000.0	1.98E-05	8.2E-07	1250.8
L6_h2_01_H3	0	0.0405	-0.0075	0.0075	2	81	16	35	8	13	2	0	1.0E-03	1.1774	8.8E+03	1000.0	1.98E-05	8.2E-07	555.9
L8_h2_01_H3	0	0.0405	-0.0075	0.0075	2	81	16	35	8	17	2	0	1.0E-03	1.1774	8.8E+03	1000.0	1.98E-05	8.2E-07	312.7
L10_h2_01_H3	0	0.0405	-0.0075	0.0075	2	81	16	35	8	21	2	0	1.0E-03	1.1774	8.8E+03	1000.0	1.98E-05	8.2E-07	200.1
L12_h2_01_H3	0	0.0405	-0.0075	0.0075	2	81	16	35	8	25	2	0	1.0E-03	1.1774	8.8E+03	1000.0	1.98E-05	8.2E-07	139.0
L14_h2_01_H3	0	0.0405	-0.0075	0.0075	2	81	16	35	8	29	2	0	1.0E-03	1.1774	8.8E+03	1000.0	1.98E-05	8.2E-07	102.1
L16_h2_01_H3	0	0.0405	-0.0075	0.0075	2	81	16	35	8	33	2	0	1.0E-03	1.1774	8.8E+03	1000.0	1.98E-05	8.2E-07	78.2
L4_h3_01_H3	0	0.0405	-0.0075	0.0075	2	81	20	35	10	9	2	0	1.0E-04	1.1774	8.8E+03	1000.0	1.98E-05	8.2E-10	125.1
L6_h3_01_H3	0	0.0405	-0.0075	0.0075	2	81	18	35	9	13	2	0	1.0E-04	1.1774	8.8E+03	1000.0	1.98E-05	8.2E-10	55.6

APPENDIX C

Dimensionless Scheme Derivation

Two-Dimensional Dimensionless Scheme Derivation:

x direction

$$\rho \left(\frac{\partial u}{\partial t} + \frac{u \partial u}{\partial x} + \frac{v \partial u}{\partial y} \right) = -\frac{\partial p}{\partial x} + \mu \left(\frac{\partial^2 u}{\partial x^2} + \frac{\partial^2 u}{\partial y^2} \right)$$

y direction

$$\rho \left(\frac{\partial v}{\partial t} + \frac{u \partial v}{\partial x} + \frac{v \partial v}{\partial y} \right) = -\frac{\partial p}{\partial y} + \mu \left(\frac{\partial^2 v}{\partial x^2} + \frac{\partial^2 v}{\partial y^2} \right)$$

Continuity equation incompressible fluid

$$\frac{\partial u}{\partial x} + \frac{\partial v}{\partial y} = 0$$

Non-dimensionalised with the following;

Use for scaling:

The combined channel height H_3
The mean input velocity \bar{U}

Gives a time scale $T = \frac{H_3}{\bar{U}}$

Now a dimensionless scheme for the variables of the Navier-Stokes equation

$$\bar{u} = \frac{u}{\bar{U}}, \quad \bar{v} = \frac{v}{\bar{U}}, \quad \bar{t} = \frac{t}{\frac{H_3}{\bar{U}}}, \quad \bar{x} = \frac{x}{H_3}, \quad \bar{y} = \frac{y}{H_3}$$

Substituting into the x component of the Navier-Stokes (N-S) equation gives the following;

$$\rho \left(\frac{\partial (\bar{u}\bar{U})}{\partial (\bar{t} H_3 / \bar{U})} + \frac{\bar{u}\bar{U} \partial (\bar{u}\bar{U})}{\partial (H_3 \bar{x})} + \frac{\bar{v}\bar{U} \partial (\bar{u}\bar{U})}{\partial (H_3 \bar{y})} \right) = -\frac{\partial p}{\partial (H_3 \bar{x})} + \mu \left(\frac{\partial^2 (\bar{u}\bar{U})}{\partial (H_3 \bar{x})^2} + \frac{\partial^2 (\bar{u}\bar{U})}{\partial (H_3 \bar{y})^2} \right)$$

Multiplying through by $\frac{H_3}{\rho \bar{U}^2}$ gives;

$$\frac{\partial \bar{u}}{\partial \bar{t}} + \frac{\bar{u} \partial \bar{u}}{\partial \bar{x}} + \frac{\bar{v} \partial \bar{u}}{\partial \bar{y}} = -\frac{\partial \left(\frac{p}{\rho \bar{U}^2} \right)}{\partial \bar{x}} + \left(\frac{\mu}{\rho \bar{U} H_3} \right) \left(\frac{\partial^2 \bar{u}}{\partial \bar{x}^2} + \frac{\partial^2 \bar{u}}{\partial \bar{y}^2} \right)$$

Simplifying gives;

$$\frac{\partial \bar{u}}{\partial \bar{t}} + \frac{\bar{u}\partial \bar{u}}{\partial \bar{x}} + \frac{\bar{v}\partial \bar{u}}{\partial \bar{y}} = -\frac{\partial \bar{p}}{\partial \bar{x}} + \left(\frac{1}{\text{Re}}\right) \left(\frac{\partial^2 \bar{u}}{\partial \bar{x}^2} + \frac{\partial^2 \bar{u}}{\partial \bar{y}^2}\right)$$

Where;

$$\bar{p} = \frac{p}{\rho \bar{U}^2} \quad \text{and} \quad \text{Re} = \frac{\rho \bar{U} H_3}{\mu}$$

Similarly y direction and continuity give

y direction

$$\frac{\partial \bar{v}}{\partial \bar{t}} + \frac{\bar{u}\partial \bar{v}}{\partial \bar{x}} + \frac{\bar{v}\partial \bar{v}}{\partial \bar{y}} = -\frac{\partial \bar{p}}{\partial \bar{y}} + \frac{1}{\text{Re}_{H_3}} \left(\frac{\partial^2 \bar{v}}{\partial \bar{x}^2} + \frac{\partial^2 \bar{v}}{\partial \bar{y}^2}\right)$$

Continuity equation incompressible fluid

$$\frac{\partial \bar{u}}{\partial \bar{x}} + \frac{\partial \bar{v}}{\partial \bar{y}} = 0$$

Now considering the flexible plate equations of motion

$$\rho_m h \frac{\partial^2 w}{\partial t^2} + d \frac{\partial w}{\partial t} + B \frac{\partial^4 w}{\partial x^4} = -\Delta p$$

$$\text{Where} \quad B = \frac{Eh^3}{12(1-\nu^2)}$$

Using the same non-Dimensional scheme with the addition of now using L_p for the length scale.

$$\bar{w} = \frac{w}{L_p}$$

Substitution gives

$$\rho_m h \frac{\partial^2 (\bar{w} L_p)}{\partial (\bar{t} L_p / \bar{U})^2} + d \frac{\partial (\bar{w} L_p)}{\partial (\bar{t} L_p / \bar{U})} + B \frac{\partial^4 (\bar{w} L_p)}{\partial (\bar{x} L_p)^4} = -\Delta p \rho \bar{U}^2$$

Multiplying through by $\frac{1}{\rho\bar{U}^2}$ gives

$$\left(\frac{\rho_m h}{\rho L_p}\right) \frac{\partial^2 \bar{w}}{\partial \bar{t}^2} + \left(\frac{d}{\rho \bar{U}}\right) \frac{\partial \bar{w}}{\partial \bar{t}} + \left(\frac{B}{\rho \bar{U}^2 L_p^3}\right) \frac{\partial^4 \bar{w}}{\partial \bar{x}^4} = -\Delta \bar{p}$$

So we have the following non-dimensional flow structure system with the choice of Reynolds number based on H_3 (length of the plate)

$$\frac{\partial \bar{u}}{\partial \bar{t}} + \bar{u} \frac{\partial \bar{u}}{\partial \bar{x}} + \bar{v} \frac{\partial \bar{u}}{\partial \bar{y}} = -\frac{\partial \bar{p}}{\partial \bar{x}} + \left(\frac{1}{\text{Re}_{L_p}}\right) \left(\frac{\partial^2 \bar{u}}{\partial \bar{x}^2} + \frac{\partial^2 \bar{u}}{\partial \bar{y}^2}\right)$$

$$\frac{\partial \bar{v}}{\partial \bar{t}} + \bar{u} \frac{\partial \bar{v}}{\partial \bar{x}} + \bar{v} \frac{\partial \bar{v}}{\partial \bar{y}} = -\frac{\partial \bar{p}}{\partial \bar{y}} + \left(\frac{1}{\text{Re}_{L_p}}\right) \left(\frac{\partial^2 \bar{v}}{\partial \bar{x}^2} + \frac{\partial^2 \bar{v}}{\partial \bar{y}^2}\right)$$

$$\frac{\partial \bar{u}}{\partial \bar{x}} + \frac{\partial \bar{v}}{\partial \bar{y}} = 0$$

$$\left(\frac{\rho_m h}{\rho L_p}\right) \frac{\partial^2 \bar{w}}{\partial \bar{t}^2} + \left(\frac{d}{\rho \bar{U}}\right) \frac{\partial \bar{w}}{\partial \bar{t}} + \left(\frac{B}{\rho \bar{U}^2 L_p^3}\right) \frac{\partial^4 \bar{w}}{\partial \bar{x}^4} = -\Delta \bar{p}$$

This analysis gives 4 control parameters being

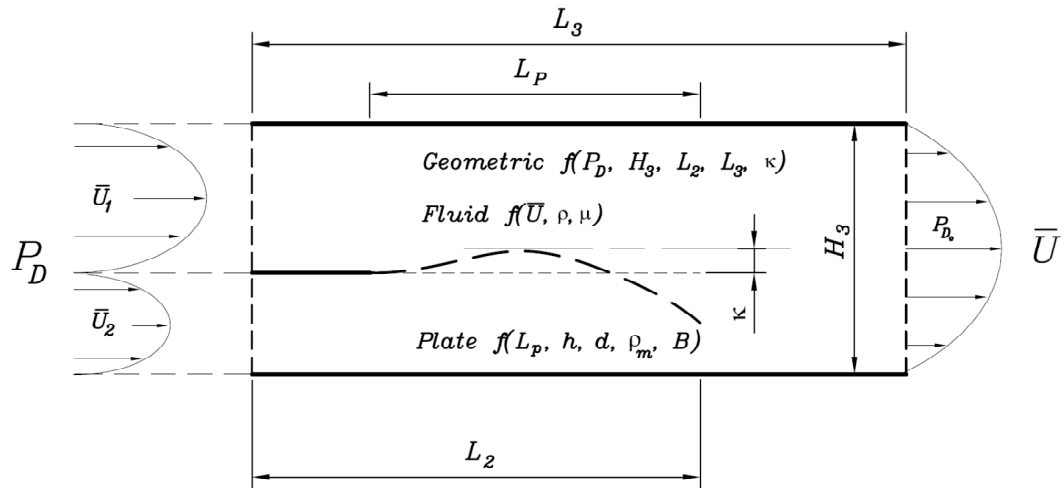
$$\text{Reynolds Number} \quad \text{Re}_{L_p} = \frac{\rho \bar{U} H_3}{\mu}$$

$$\text{Mass ratio} \quad \Theta = \frac{\rho_m h}{\rho L_p}$$

$$\text{Damping ratio} \quad \xi = \frac{d}{\rho \bar{U}}$$

$$\text{Stiffness ratio} \quad \Gamma = \frac{B}{\rho \bar{U}^2 L_p^3}$$

The above excludes the effect of any channel geometrical control parameter/s so applying boundary conditions to a plate within a channel



Positioning the flexible plate between two ridged channel walls as shown above and extracting the following dimensionless geometrical control parameters

Eccentricity $\varepsilon = \frac{2\kappa}{H_3}$

Aspect ratio $\bar{H} = \frac{H_3}{L_2}$

APPENDIX D

Breathing Cycle Instability Mechanism

